Author:
Topliss, Margaret E

Title:
Water wave impact on structures.

Water Wave Impact on Structures

Margaret E Topliss

School of Mathematics

University of Bristol

A Thesis submitted to The University of Bristol

for the degree of Doctor of Philosophy

in the Faculty of Science

September 1994

Abstract

This thesis presents an analytical and numerical study of water-wave impact on structures which builds on a long history of study in the area of coastal hydrodynamics. During the course of the project, the scope was widened to include liquid impacts in containers where the physics of the problem is essentially the same. Chapter 1 presents a general introduction describing the outlay of the thesis.

The theory of pressure impulse is applied in chapter 2 to wave impact in several two-dimensional geometries and a three-dimensional rectangular domain. This is an extension of work developed by Cooker & Peregrine (1990) for wave impact on a sea wall.

Experimental studies of wave impact on a vertical wall have recorded pressure oscillations, believed to be due to the presence of trapped air. Chapter 3 investigates how to model entrained air found in water-wave impacts. A numerical boundary-integral method originally due to Dold & Peregrine (1986) is used to model an overturning wave against a vertical wall trapping an air pocket. This provides detailed initial data for simple theoretical models. Comparisons are made with experimental data, in particular, with Hattori & Arami (1992 and private communications) and Hattori, Arami & Yui (1994). A discussion of how to model peak pressures follows.

Chapter 4 involves the numerical study of large amplitude 'standing' waves inside a rectangular tank to simulate the sloshing motions found inside confined spaces. This uses a periodic version of the boundary-integral method described in chapter 3, discussed in Dold (1992), and includes the evaluation of the forces on the side walls of a container.

The response of a vertical wall to some of the wave impacts described in the previous chapters is investigated in chapter 5. The impact wall is modelled as a two-dimensional elastic plate and the transverse displacements and amplitudes are evaluated. Comparisons are made with Kirkgöz & Mengi (1986) for a vertical breakwater and with Corrignan (1993) for a thin tank wall.

The thesis is concluded in chapter 6, discussing the results for the work presented and giving suggestions for further research in this area.

Acknowledgements

I thank Prof. Howell Peregrine for all his guidance, encouragement and patience over the last three years. I also thank Dr Mark Cooker, Dr Quentin Vaughan and Dr Ross Hughes. I acknowledge the financial support of the Engineering and Physical Sciences Council (formerly Science Engineering Research Council) and British Aerospace plc, and the E.E.C. under the research program MAST II (contract MAS 2-CT92-0047) for supporting travel and providing valuable contributions.

Author's Declaration

The work described in this thesis was carried out in the School of Mathematics at Bristol University and has not been submitted for any other degree or diploma of any examining body. Part of the work in chapter 3 has been published in Topliss, Cooker & Peregrine (1992). All the material described herein is the original work of the author unless otherwise acknowledged.

Maggie Topliss

Contents

List of Figures

List of Tables

Chapter 1

Introduction

In the context of coastal hydrodynamics, the impact of steep water waves with structures can result in damage or collapse of breakwaters. This leads to the need for the modelling of water-wave impacts and has been the subject of extensive research. Sea defences need to withstand storms with successive attacks of large waves. Failures of vertical breakwaters along coastal defences have led to much attention being given to the pressure distributions which occur when storm waves meet sea walls. For industrial applications, the importance of the stability of a vehicle or vessel transporting liquids in partially full tanks has led to the need for a good understanding of the violent liquid motion inside confined spaces. Tank accelerations can set the liquid into relative motion leading to large scale motion. The aim of this thesis is to study and model some of the liquid motions and pressure distributions which occur due to the impact of breaking or near breaking steep water-waves on structures with emphasis on problems of practical interest. The pressure fields resulting from a moderately severe wave impact have been divided into three overlapping areas of study: i) the initial violent brief impact pressure peak, ii) the somewhat longer duration oscillatory pressures and iii) the longer lasting, more moderate, reflected pressures. All three types can occur in one impact. This thesis contains three separate chapters investigating an aspect of the pressure field resulting from wave impact on a structure and relating to a particular application. A fourth chapter models the response of a non-rigid vertical wall to wave impact. Finally a fifth concluding chapter summarises the results of the preceeding work and indicates future areas for research.

A review of the relevant literature occurs in the individual chapters. The work described in this thesis has been undertaken using either detailed two-dimensional com-

putations describing the motion of unsteady nonlinear water-waves in time or simple theoretical models. Where appropriate, comparisons are made with experimental data available in the literature. The numerical computations used to describe the wave motion are for incompressible, irrotational, inviscid flow on a finite depth.

1.1 Impact Pressures

Large water-waves can give exceptionally high impact pressures on walls as they break. The first aspect of the pressure distribution resulting from a wave impact to be studied is this initial brief large pressure peak. For example, figure 1.1 shows the surface profiles

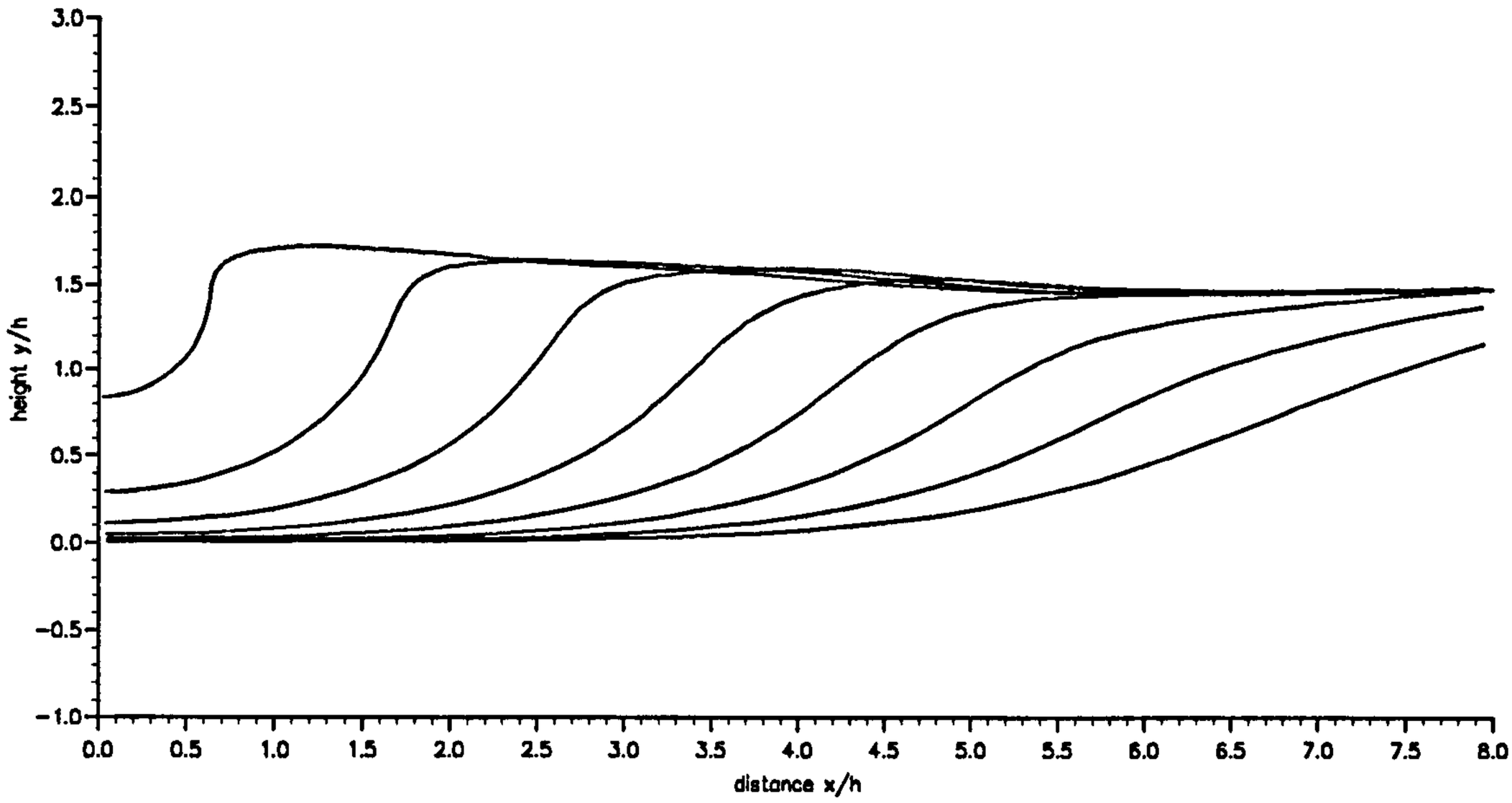

Figure 1.1: Surface profiles of a wave of initial amplitude $1.5h$ on a depth $1.0h$ approaching a vertical wall from the right from an initial distance of $7.5h$.

of a large wave of amplitude $1.5h$ on a finite depth of $1.0h$ moving left towards a vertical wall from an initial distance of $7.5h$, where h is the still water depth. This example is taken from the numerical program described in section 3.3 in chapter 3. The wavefront steepens in time and the waterline at the wall rises.

Figure 1.2 portrays the surface profiles at a later time, in smaller timesteps than the

previous figure for the same wave, where the wave front is now much closer to the wall. As the almost vertical wavefront approaches the wall from the right, the waterline at the wall now begins to rise very rapidly up the wall. This results in a thin vertical jet of water. The final computed timestep occurs when the top of the jet is at its maximum position.

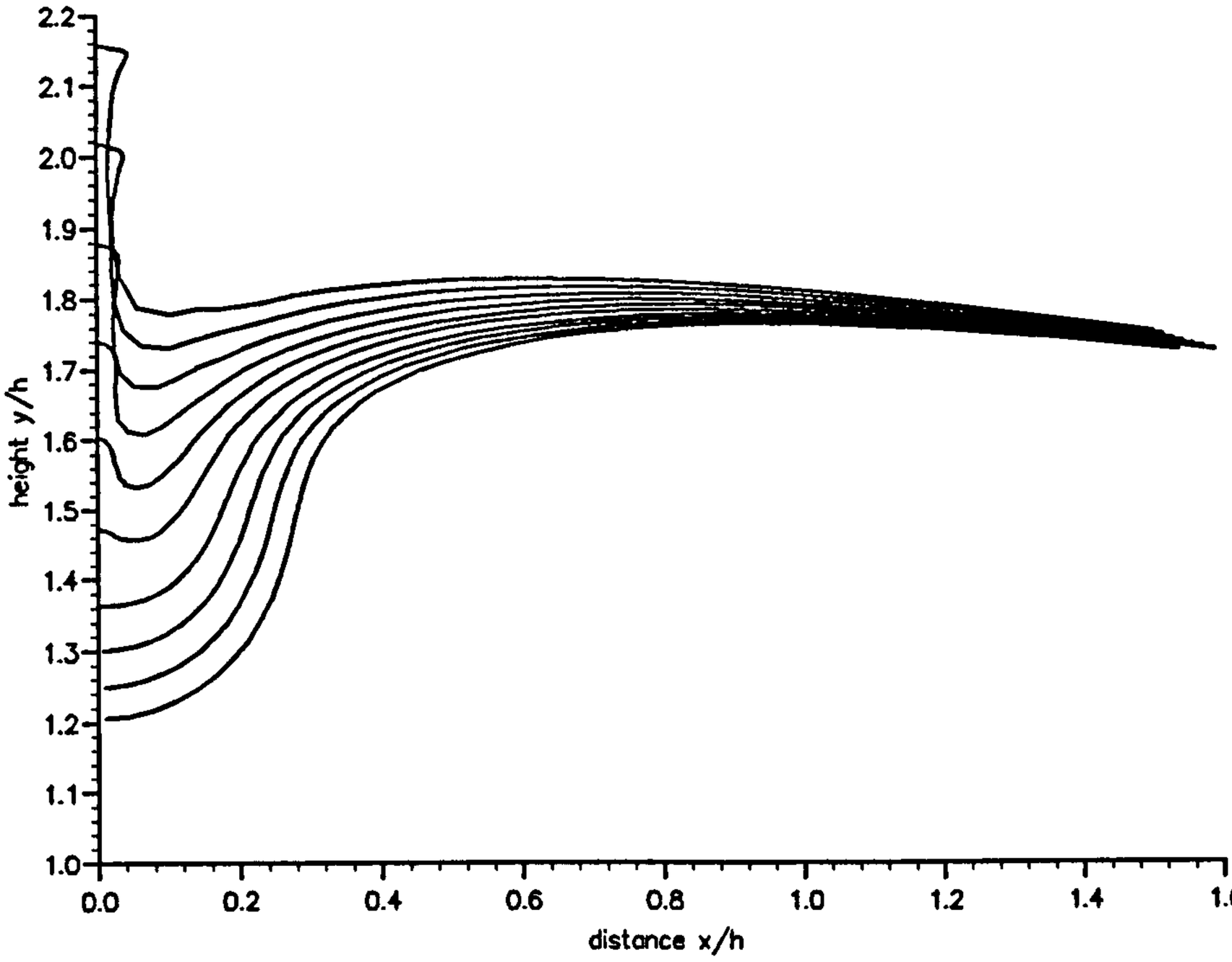

Figure 1.2: Surface profiles of the final stages of motion of a wave of initial amplitude $1.5h$ on a depth $1.0h$ approaching from an initial distance of $7.5h$ impacting on a vertical wall.

Figure 1.3 shows the pressure $P/\rho gh$ on the wall, at three positions, during the final stages of motion t=4.17-4.23 $\sqrt{h/g}$. Here ρ is the density of the water and g is the gravitational constant. The computations commenced at t=0.0. At the third position shown, y/h=1.55, the water does not come into contact with the wall until t=4.183 $\sqrt{h/g}$. A rapid increase in pressure at this point is then shown rising to a peak of 28.8 ρgh and subsequently decaying. This occurs over a short time duration of approximately 0.05 $\sqrt{h/g}$ in total.

The markers on the three curves for each small timestep of 0.0005 $\sqrt{h/g}$ have been shown to highlight this rapid change in pressure on the third curve, with the larger separation between the points indicating the greatest pressure change. Thus the peak

pressure is just below the waterline.

The subject of the second chapter concerns this high peak pressure of short duration from the initial impact against the structure. Peak pressures and pressure distributions due to wave impact have been extensively investigated. Studies of water waves breaking against walls have shown that violent free surface motion can cause severe impacts upon structures. The impact is assumed to be of sufficiently short time duration so that it

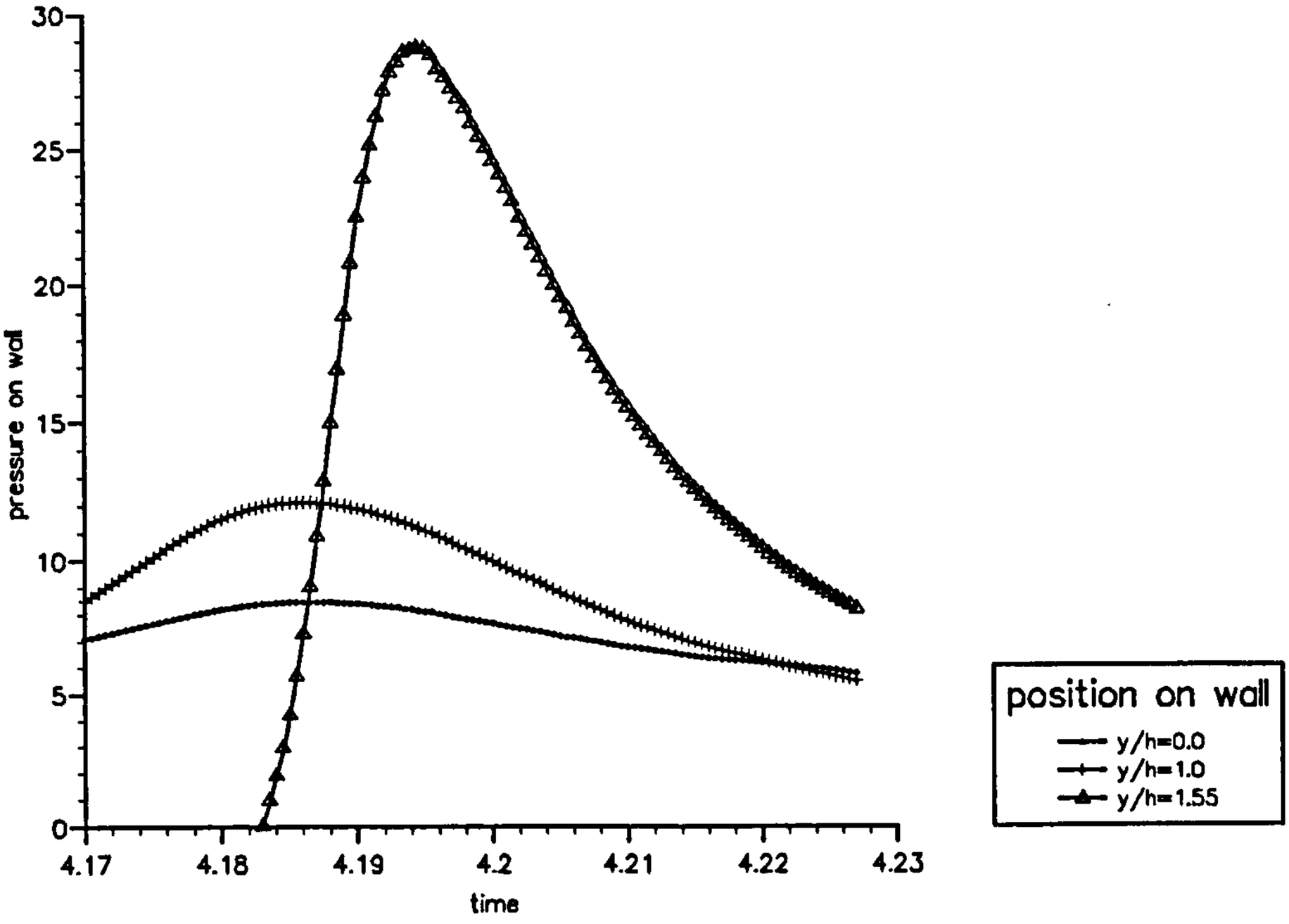

Figure 1.3: Pressure $P/\rho gh$ on impact wall for a short period of the final motion for a wave of initial amplitude $1.5h$ on a depth $1.0h$ approaching from an initial distance of $7.5h$.

may be described in terms of pressure impulse; the integrated pressure over the short timescale. As previous authors (e.g. Bagnold (1939) and Zhou, Chan & Melville (1991)) have noted, the pressure impulse is more repeatable despite the wide variability of the peak pressures. The simple analytical theory of the two-dimensional pressure impulse applied to wave impact on sea walls has been developed by Cooker & Peregrine (1990). Work by Cooker & Peregrine (1994) has shown the pressure impulse distribution to be increased in confined spaces. The second chapter contains the application of this theory to the study of the characteristics of localised liquid impacts on one or two sides of a partly filled container. The pressure impulse model involves the solution of Laplace's equation in

an idealised domain. Hence, although less precise than detailed numerical computations, more general results for wave impact in a confined space can be found. The model is used to describe the motion of the fluid in a two-dimensional rectangular domain and is then applied to circular and elliptical containers. The total impulse imparted to a container and the change in the normal velocity of the free surface due to the impact can be evaluated. Conformal transformations are used in section 2.4.2 to describe the motion in the more complex geometry of a nearly full circular container and in section 2.5 to enable the total resultant force on a small baffle on the bed of the tank to be studied. Examples are presented in section 2.6 to indicate how the motion of vehicles or ships may be affected by such short interval impacts. The work is extended in section 2.7 to study the effects in the three-dimensional geometry of a rectangular tank, of interest since fully nonlinear three-dimensional computations are more difficult to achieve.

1.2 Oscillating Pressures

The second feature in the time evolution of the pressure distribution due to wave impact on a wall concerns the decaying oscillatory pressures thought to be due to the oscillations of trapped air. Natural wave impacts contain significant amounts of air entrained in the water which could cushion the impact resulting in a longer duration of high pressure distributions. The third chapter studies the role entrained air plays in the generation of pressure distributions and discusses how the trapped air could be modelled. A review provides important background material of the experimental studies undertaken to investigate entrained air. These studies show how aeration in wave impacts has been described in the laboratory experiments as either a cloud of small air bubbles in the water adjacent to the vertical structure or as a single air pocket trapped between the overturning wave and the impact wall. The new work presented here involves numerical and analytical modelling of the entrained air, followed by detailed comparisons with available experimental data.

There are several numerical models available for the violent motion of a liquid with a free surface which can describe incompressible two-dimensional motion. However they are of limited value once air is entrained. A boundary-integral method, used in section 1.1 to produce the computations shown in figures 1.1 and 1.2, for computing the unsteady

motion of a water surface, including that describing breaking waves, has been initially described by Dold & Peregrine (1986) and later by Dold (1992). The method allows the simulation of an overturning water-wave on finite depth in front of a vertical wall. The computations are used to describe the steepening and overturning of a plunging water wave immediately before a vertical wall up until the moment of impact, trapping a cylindrical pocket of air against the structure. The internal wave characteristics can then be found from the surface values and the pressure field evaluated. Several examples from the numerical results are presented. These include different sizes of trapped air pockets to see how the characteristics of the resulting motion might change in relation to the amount of air trapped. Comparisons are made with the final motions from different incident waves.

The detailed computations provide suitable initial parameters for a simple theoretical model. In Topliss (1991), the natural frequency for a two-dimensional bubble under a free surface was evaluated. This was compared with a three-dimensional bubble under a free surface and shown to produce lower frequencies, in the range of those given by experimental data for trapped air pockets. Using a conformal mapping, the trapped air pocket is modelled in section 3.4 as a two-dimensional semi-circular bubble, taking into account the effect of the free surface and rigid bed. The method of images allows the potential of the flow due to the free oscillations of the air pocket to be evaluated. The entrained air can also be modelled as a bubbly mixture next to the impact wall. The sound speed in this region is considerably reduced due to the bubbles and trapped modes of oscillation can be found where the fundamental frequencies are in the range of those given by the single bubble.

Video frames of small model experiments by Hattori & Arami (1992 and private communications) and Hattori, Arami & Yui (1994) of overturning waves are examined to measure the dimensions of the trapped air pockets. Three experimental data sets have been studied in detail and compared with computations that provide the same size air pocket. The resulting peak pressures are estimated using the analytic theory. The comparison with experimental studies is followed by a discussion on how the peak pressures for wave impacts involving trapped air may be estimated using the pressure impulse theory for wave impact on sea walls in Cooker & Peregrine (1990).

This study is concluded with section 3.9 concerning scaling. The majority of the ex-

periments undertaken to study wave impact are performed in small-scale tanks. Scaling from model to prototype remains a complex problem. Compressibility, strongly influenced by the presence of bubbles is an important factor. Peregrine (1994) has suggested simple dimensional formulae for estimating the order of magnitude of the frequencies and maximum pressures. Comparisons of these estimates are made with the analytic results.

1.3 Reflecting Pressures

The fourth chapter is concerned with the final aspect of the pressure distributions, the "reflected" pressure, which has the longest duration and the lowest values. For example,

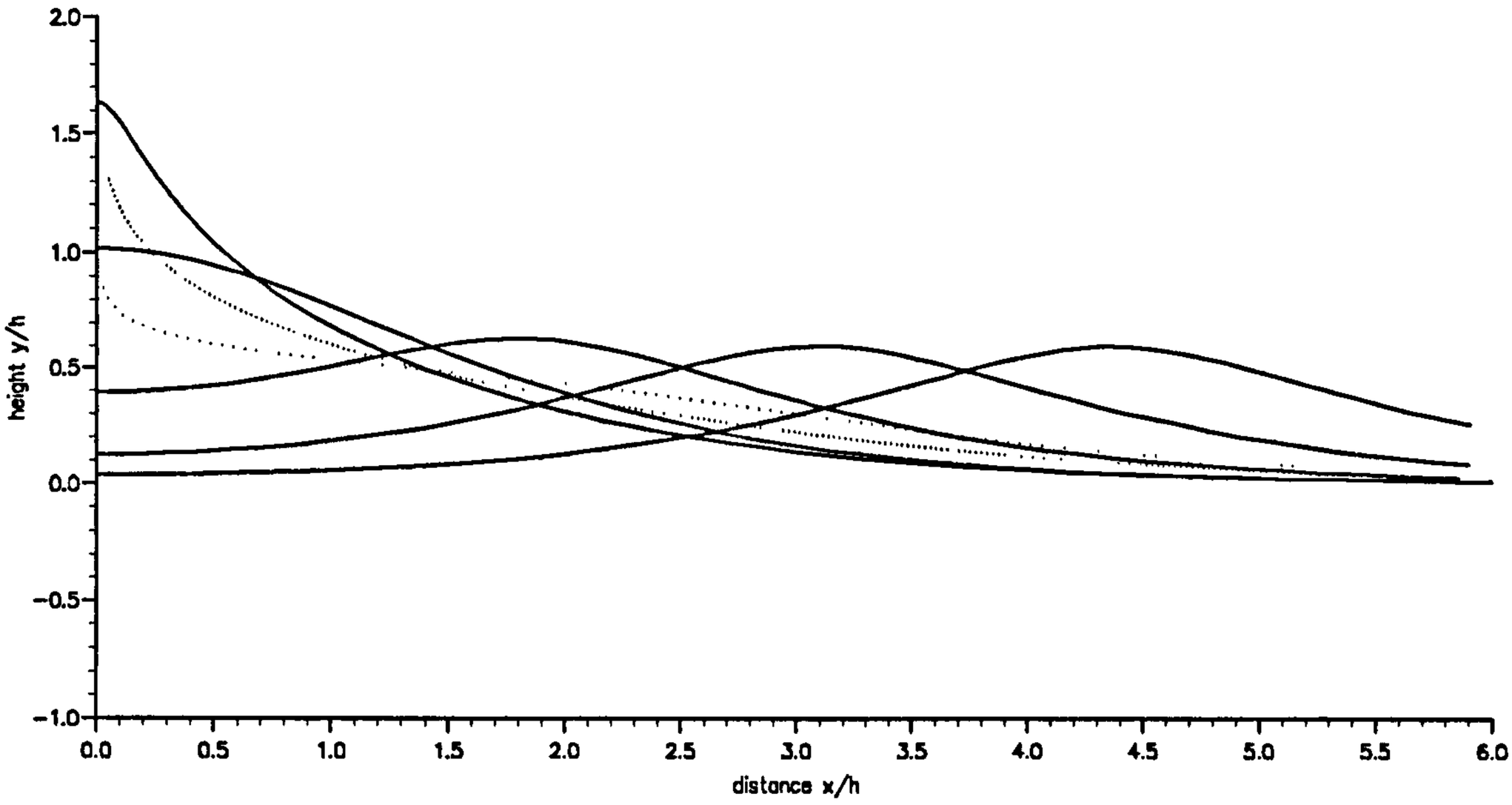

Figure 1.4: Surface profiles of a solitary wave of amplitude $0.6h$ on a finite depth of $1.0h$ colliding with a vertical wall. The dotted lines represent the reflecting profiles.

in figure 1.4, the surface profiles are drawn for a solitary wave of amplitude $0.6h$ on a finite depth of $1.0h$, approaching a wall from an initial distance of $18.1h$. The waterline rises up the wall, reaching a maximum height of $1.63h$ and then returns down the wall. The dotted lines in the figure represent the descending profiles. The pressures on the impact wall at the bed $y = -1.0h$ and at $y = 0.3h$ for this wave, shown in figure 1.5 for t=8.0-17.0 $\sqrt{h/g}$, indicate much longer rise and decay times of the maximum pressures. Unlike the

pressures for the wave impact discussed previously in section 1.1, the maximum pressures are much lower and lie on the bed of the domain. The peak value rises from 1.0 ρgh at hydrostatic pressure to approximately 1.8 ρgh.

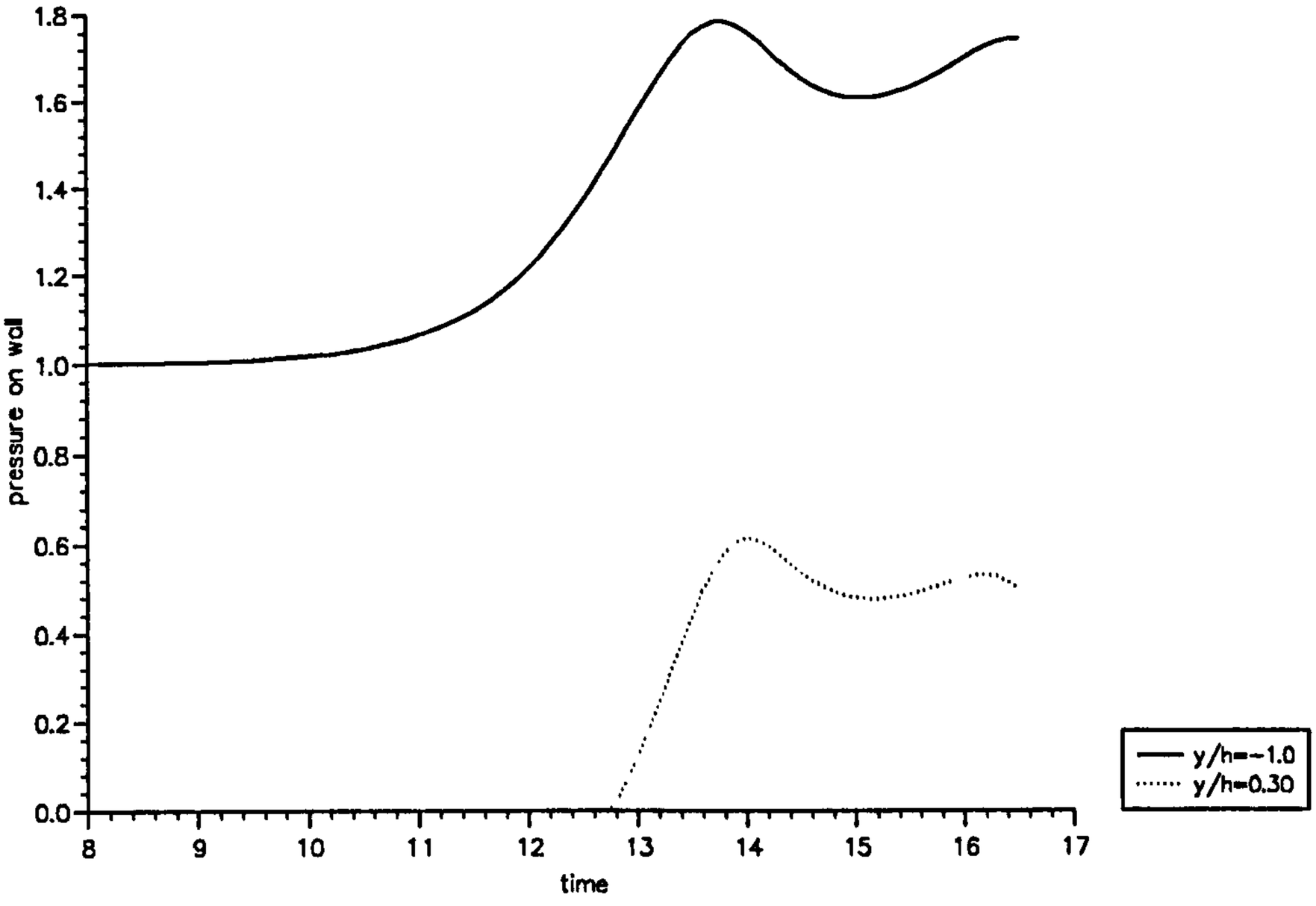

Figure 1.5: Pressure history at two positions on the impact wall for a solitary wave of amplitude $0.6h$ of initial distance $18.1h$ on a depth of $1.0h$ colliding with a vertical wall.

These moderate pressures can also arise due to the existence of standing waves which occur inside confined areas and can be used to model the wave generation in partially full tanks. The phenomenon of sloshing liquid in containers as a response to external excitation is of importance in maritime, road, air, rail and space transport applications. The ability to design safe and reliable tanks is required. Using the numerical program described in section 3.3 chapter 3 for calculating the two-dimensional motion of the free surface, computations of large amplitude 'standing' water waves are used in section 4.2 in chapter 4 to simulate sloshing motions inside two-dimensional rectangular domains. With appropriate initial conditions, these can be used to represent tanks. A selection of figures in subsection 4.2.1 demonstrates different surface profiles resulting from the initial conditions.

The pressure distributions due to the reflection of these large water waves on vertical walls can be evaluated and are presented in subsection 4.2.2 at instances of minimum and maximum kinetic energy. Finally the force on the side walls is evaluated and discussed.

1.4 Response of a Vertical Wall to Wave Impact

Wave impacts on sea walls or walls of a container result in forces perpendicular to the structures. Severe wave impacts can result in damaged breakwaters or can cause the structure to slide. For thin walls, such as those found in aircraft or the sectioning of large tanks, the elasticity has to be taken into account. The final chapter investigates how to study the response of a vertical wall to wave impact. The impact wall is modelled as a two-dimensional flexible plate. This allows the evaluation of small deflections of a non-rigid wall either from wave impact on a breakwater or from wave impact inside a tank. The computations from the numerical program described in section 3.3 in chapter 3 and section 4.2 in chapter 4 are used to provide the pressure distribution as a function of time on the wall.

This is followed by a discussion and comparison of the experimental work in section 5.3.1 given by Kirkgöz & Mengi (1986) for wave impact on a concrete caisson and in section 5.4.1 by Corrignan (1993) for wave impact on a thin steel wall in a tank.

This final aspect of the thesis is the subject of current research and as yet has not been fully analysed. However, this chapter is included to indicate how some of the previous work can be used, in applications particularly relevant to the transportation industries.

Chapter 2

Impact Pressures in a Container

2.1 Introduction

Violent motion of a liquid inside a moving container can lead to high impact pressures on the enclosing structures which may affect the stability of the host vehicle or vessel. This situation occurs in a wide range of tank geometries including rectangular, circular and elliptical configurations. An extensive literature survey of early research on the dynamics of liquids in moving containers was undertaken by Cooper (1960). Abramson (1966) produced a wide review of the dynamic behaviour of fluid motion inside moving containers including the non-linear effects due to large amplitude excitation and later Faltinsen (1974) studied the non-linear effects of large motion inside a rectangular tank. The rectilinear and rolling motion of a fluid-tank system has been studied by Lui & Lou (1990) for small amplitude motions to compare the response between a fluid-tank system and an equivalent rigid-cargo system undergoing an oscillatory type motion. The differences in the two responses were shown to be dependent on the ratio of the fundamental frequency of the fluid and the equivalent rigid-cargo system, with discrepancies when this ratio is close to unity. The stability of vessels undergoing a turning or braking manoeuvre has been studied by both Popov, Sankar, Sankar & Vatistas (1992) and Popov, Sankar & Sankar (1993) for rectangular containers.

Tank accelerations leading to violent free surface motions can cause localised fluid impacts with brief high pressures. Peak pressures and pressure distributions due to wave impact have been extensively studied. However previous authors (e.g. Bagnold (1939) and

Zhou, Chan & Melville (1991)) have noted that the pressure impulse is more repeatable. In this chapter, the pressure distributions due to a sudden large pressure on one rigid side of a partly-filled rigid open container are studied for simple two-dimensional geometries. This is extended in section 2.7 to a three-dimensional rectangular domain for impacts on two rigid sides.

Sudden large pressures acting upon fluid and bodies are described by Lamb (§11, 1932) and are modelled by an extension of the concept of impulse in elementary mechanics of rigid bodies. The pressure impulse is defined by the integral of pressure:

$$P(x,y) = \int_{t_a}^{t_b} p(x,y)\, dt \tag{2.1}$$

where t_a and t_b are the start and finish times of the impact respectively. In this chapter, a wide range of analytical solutions are presented with some applications. Results may be computed for a range of parameters. Along with the pressure impulse solution, the total impulse, the moment and the change in normal velocity immediately after impact can all be found. The free surface shape may not always look very realistic. However, any pressure impulse contour can be taken as an alternative free surface and the value of the pressure impulse adjusted accordingly. Note how the examples indicated show very slight changes in maximum values for quite significantly different surface shapes chosen in this manner.

2.2 Mathematical model

The equation of motion describing the flow is

$$\frac{\partial \mathbf{U}}{\partial t} + \mathbf{U}.\nabla\mathbf{U} = -\frac{1}{\rho}\nabla p + g \tag{2.2}$$

where the terms on the left side represent the rate of change of momentum per unit volume and the terms on the right side represent the force per unit mass on a fluid particle. The short duration δt of the pressure impulse, of typically 0.01 seconds or less, is assumed to be much shorter than the time scale L_o/V_o where L_o is a typical length scale and V_o the velocity scale of the liquid region. Scaling of equation 2.2 with these length and velocity scales shows the gravity and nonlinear terms to be much smaller than the fluid

acceleration. These are therefore neglected, giving

$$\frac{\partial \mathbf{U}}{\partial t} = -\frac{1}{\rho}\nabla p\,, \tag{2.3}$$

where $\mathbf{U} = (U, V)$. Neglect of compressibility is justified on two grounds. The actual duration for which compressibility of water is important in the impact is much less than the total impact duration. And secondly, for wider adjustment of velocities and pressures, a compressible time scale is L_o/a where a is the sound speed and this too is much smaller than the total duration except perhaps for waves of order 10 metres high.

Integrating with respect to time,

$$\mathbf{U}_a - \mathbf{U}_b = -\frac{1}{\rho}\nabla P \tag{2.4}$$

where $\mathbf{U}_a$ and $\mathbf{U}_b$ are the fluid velocities immediately before and after the impact. For an incompressible fluid the continuity equation, $\nabla.\mathbf{U} = 0$ applies and hence P satisfies Laplace's equation:

$$\frac{\partial^2 P}{\partial x^2} + \frac{\partial^2 P}{\partial y^2} + \frac{\partial^2 P}{\partial z^2} = 0. \tag{2.5}$$

The fluid motion is modelled as an impact in a region of fraction μ of the wetted length of the rigid boundary. The liquid is enclosed by rigid boundaries and a free surface which is modelled as an idealised flat surface instead of the curved shape in reality, and this is discussed in section 2.3.

The boundary conditions on the impact wall are derived from equation (2.4). To model the wave striking the impact wall, the velocity normal to the wall before the impact is prescribed to be $U(y)$. After impact the velocity component normal to the wall vanishes, giving a boundary condition $\frac{\partial P}{\partial n} = -\rho U$ on the impact region. Outside the impact region on the rigid boundary, the fluid cannot penetrate the wall and thus the normal velocity component is zero, resulting in the boundary condition $\frac{\partial P}{\partial n} = 0$, unless the impact causes the boundary to move. On the free surface the pressure impulse is constant and is chosen to be $P = 0$, the reference level for the pressure. For simplicity of the geometry, the two-dimensional rectangular domain is chosen as the first example for detailed study, and then applied to other simple two-dimensional domains and finally to a three-dimensional rectangular domain.

2.3 Two-Dimensional Rectangular Domain

Using Cartesian coordinates (x, y), consider a liquid domain of height H and width bH. An impact zone on the rigid boundary $x = 0$ is taken to extend μH down from the free surface from $y = H$ to $y = H(1 - \mu)$. The boundary condition on $x = 0$ is thus $\frac{\partial P}{\partial x} = -\rho U(y)$ between $H(1 - \mu) \leq y \leq H$ and $\frac{\partial P}{\partial x} = 0$ between $0 \leq y \leq H(1 - \mu)$. The function for $U(y)$ is initially prescribed. For simplicity the velocity is taken as a constant U_o at all points in the impact region. The model is non-dimensionalised by introducing dimensionless space variables (x',y') where $x' = x/bH$ and $y' = y/H$.

Laplace's equation is solved by using separation of variables and Fourier analysis leading to the solution

$$P(x', y') = 4\rho U_o H \sum_{n=0}^{\infty} C_n \cos(\alpha_n y') \frac{\cosh[\alpha_n(x' - 1)b]}{\alpha_n^2 \sinh(\alpha_n b)} \tag{2.6}$$

where

$$C_n = \cos\left[\frac{\alpha_n(2 - \mu)}{2}\right] \sin\left(\frac{\alpha_n \mu}{2}\right) \tag{2.7}$$

and $\alpha_n = (n + \frac{1}{2})\pi$. A typical contour map, for a square domain of dimensions $b = 1$ with $\mu = 0.2$ is shown in figure 2.1. The peak pressure impulse is $0.114\rho U_o H$ on the

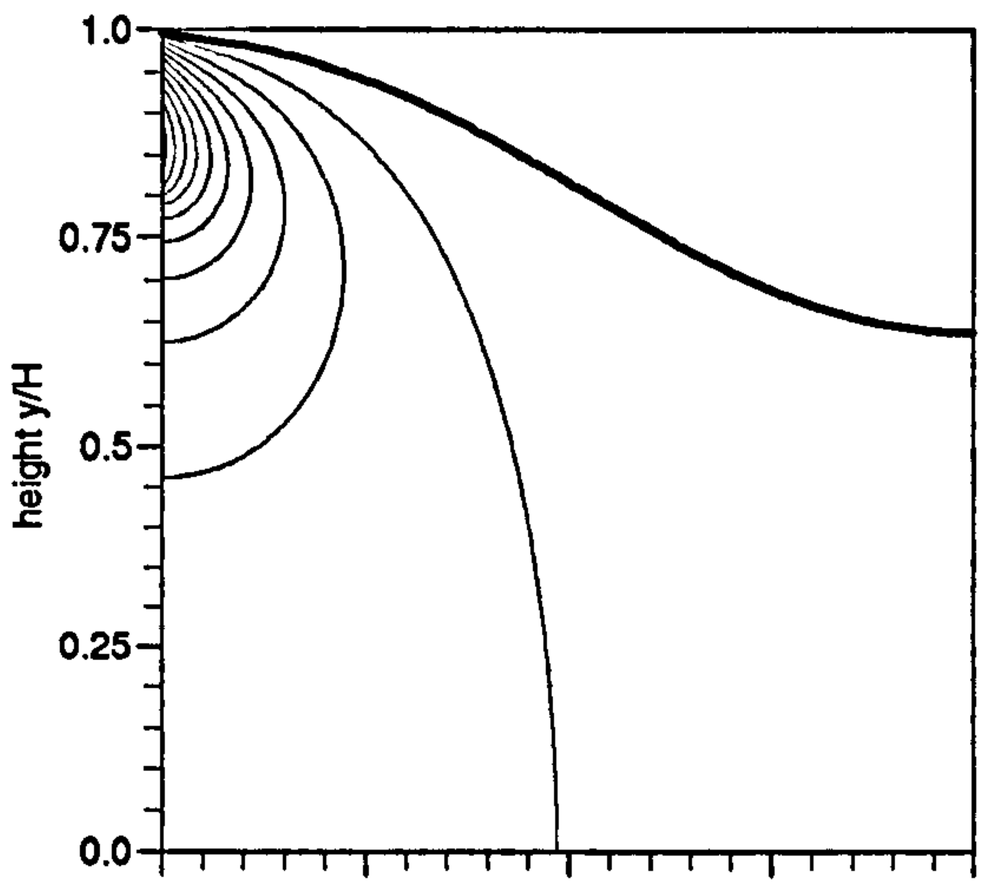

Figure 2.1: Pressure impulse contours $P/\rho U_o H$ with increments of 0.01 for a rectangular tank, width $b = 1$, with an impact of $\mu = 0.2$. A thicker contour is drawn for the value 0.01.

rigid boundary $x' = 0$ at approximately $0.86H$. There are significant pressure impulse

gradients acting along the bottom away from the impact wall which will be discussed in section 2.5. The first contour, for the value 0.01 $\rho U_o H$, has been thickened to represent an alternative free surface.

The impact wave has been modelled with a flat free surface. In reality a curved surface exists and a thicker contour has been drawn in figure 2.1 for a low value to suggest a more realistic free surface. The solution for this surface is obtained by subtracting 0.01 $\rho U_o H$ from equation (2.6) and this indicates how little the pressure impulse is changed by having a more realistic surface shape.

To study the parameter μ, the size of the impact area, figure 2.2 shows the pressure impulse for different sizes of impact region, for a domain of width $b = 1$. As the area of the impact zone increases, higher pressures are produced as portrayed in figure 2.2 for a domain of width $b = 1$. For $\mu = 1$ this corresponds to an impact region covering the

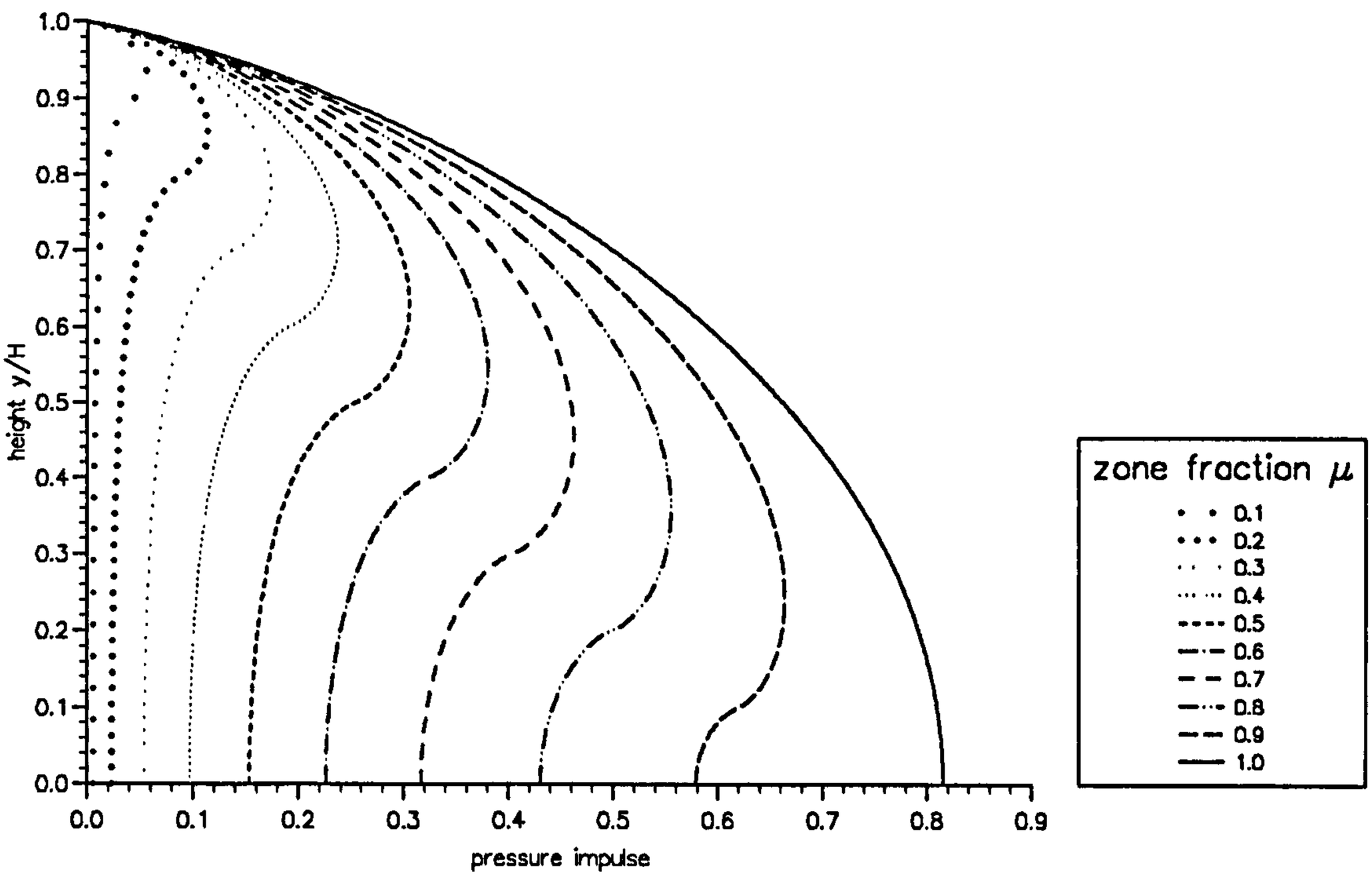

Figure 2.2: Pressure impulse $P/\rho U_o H$ for an impact in a rectangular tank of width $b = 1$ on the impact wall $x' = 0$, for the range of μ.

entire vertical wall $x' = 0$ and the highest pressures are produced near the bottom. For a small impact zone just below the surface, the highest pressures are produced near the top

of the fluid in the region of impact, then decaying further down the wall. The 'kink' in the profiles is due to the strong change in boundary condition at the edge of the impact zone.

The change in the normal velocity, V, immediately after impact can be calculated using

$$V = \frac{1}{\rho}\frac{\partial P}{\partial y} \tag{2.8}$$

to give

$$V = 4U_o \sum_{n=0}^{\infty} \frac{C_n(-1)^n \cosh[\alpha_n(x'-1)b]}{\alpha_n \sinh(\alpha_n b)} \tag{2.9}$$

Figure 2.3 shows the change in normal velocity of the free surface for part of the surface

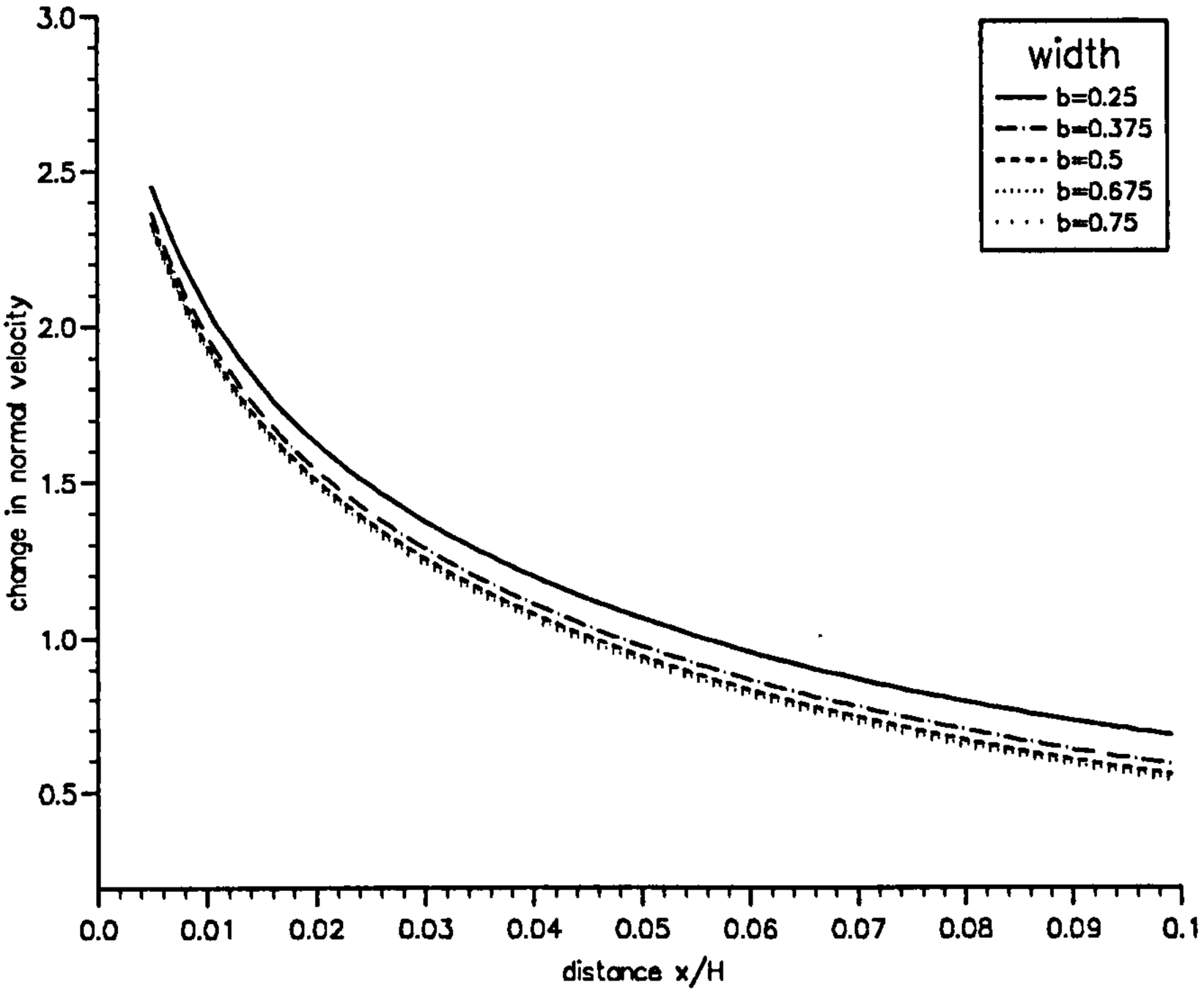

Figure 2.3: Change in the normal velocity V on the free surface $y' = 1$, after an impact of region $\mu = 0.2$ in a rectangular domain for different widths.

with the largest values near the impact wall. Due to incompatible boundary conditions at $x = 0$, where $P = 0.0$ and $\partial P/\partial x = -\rho U_o$, a logarithmic singularity occurs at this point which has not been included in the diagram. As illustrated in previous figures, a more confined domain produces higher values, in this instance the change in velocity immediately after impact. If the width of the domain, b, becomes greater than approximately

0.4, for this example with an impact region of $\mu = 0.2$, the change in the vertical velocity does not alter significantly.

The total impulse I_w on the impact wall is obtained by integrating the pressure impulse over the wall $x' = 0$:

$$I_w = 4\rho U_o H^2 \sum_{n=0}^{\infty} \frac{C_n(-1)^n}{\alpha_n^3 \tanh(\alpha_n b)}\,, \tag{2.10}$$

the moment M_h on the impact wall $x' = 0$, about $y' = 0$, for example, is

$$M_h = 4\rho U_o H^3 \sum_{n=0}^{\infty} \frac{C_n[\alpha_n(-1)^n - 1]}{\alpha_n^4 \tanh(\alpha_n b)} \tag{2.11}$$

and the moment M_v on the bed $y' = 0$, about $x' = 0$, for example is

$$M_v = 4\rho U_o H^3 \sum_{n=0}^{\infty} \frac{C_n\,[\cosh(\alpha_n b) - 1]}{\alpha_n^4 b^2 \sinh(\alpha_n b)}. \tag{2.12}$$

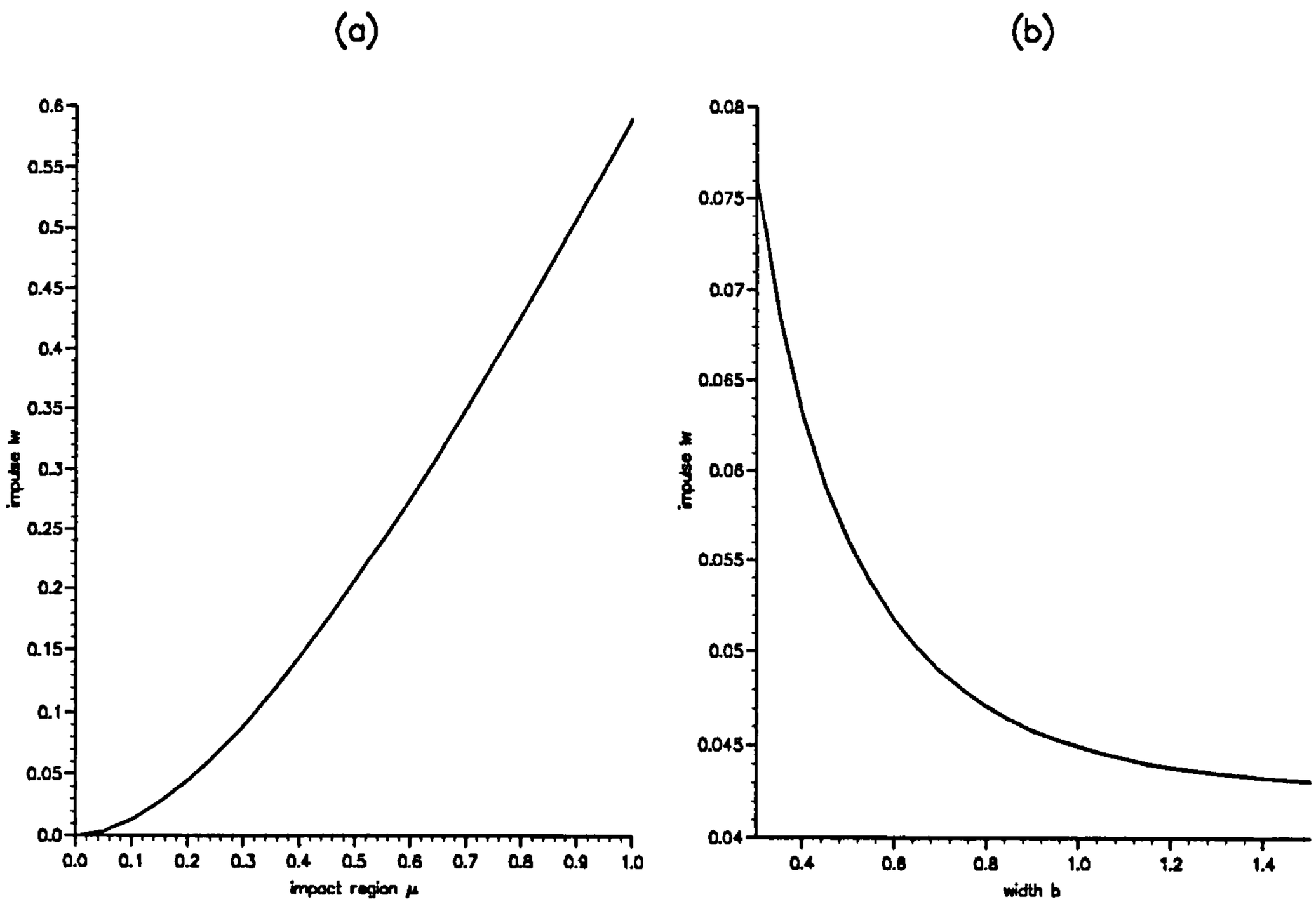

Figure 2.4: Effect of (a) impact zone size, where $b = 1$, and (b) width of container, where $\mu = 0.2$, on the total impulse I_w on impact wall $x' = 0$.

To give an example, for a rectangular tank with dimension $b = 1$ and an impact of $\mu = 0.2$, as in the figure 2.1, the total impulse on the impact wall is 0.045 $\rho U_o H^2$. The moment about $y' = 0$ is 0.029 $\rho U_o H^3$ and the moment about $x' = 0$ is 0.0093 $\rho U_o H^3$. For

a large impact covering the entire impact wall, where $\mu = 1.0$, these values would increase to 0.59 $\rho U_o H^2$ for the total impulse on the impact wall, 0.23 $\rho U_o H^3$ for the moment about $y' = 0$ and 0.21 $\rho U_o H^3$ for the moment about $x' = 0$, showing the greatest increase in the latter value. These impulses and moments are per unit length of container. Figure 2.4 shows how the total impulse I_w on the impact wall $x' = 0$ varies with the size of the impact region and the width of the tank. As expected, increasing the size of the region of impact increases the total impulse on the impact wall, and a more confined domain leads to a higher total impulse.

The effect of the width of the tank on the pressure impulse solution is shown in figure 2.5, for an impact region of size μ=0.2, for different values of b. Changing the width of a tank has little effect until it is less than approximately $0.8H$. Then as shown in figure 2.5, decreasing the width of the tank increases the pressure impulse markedly. As the domain becomes more confined, higher pressure impulses result.

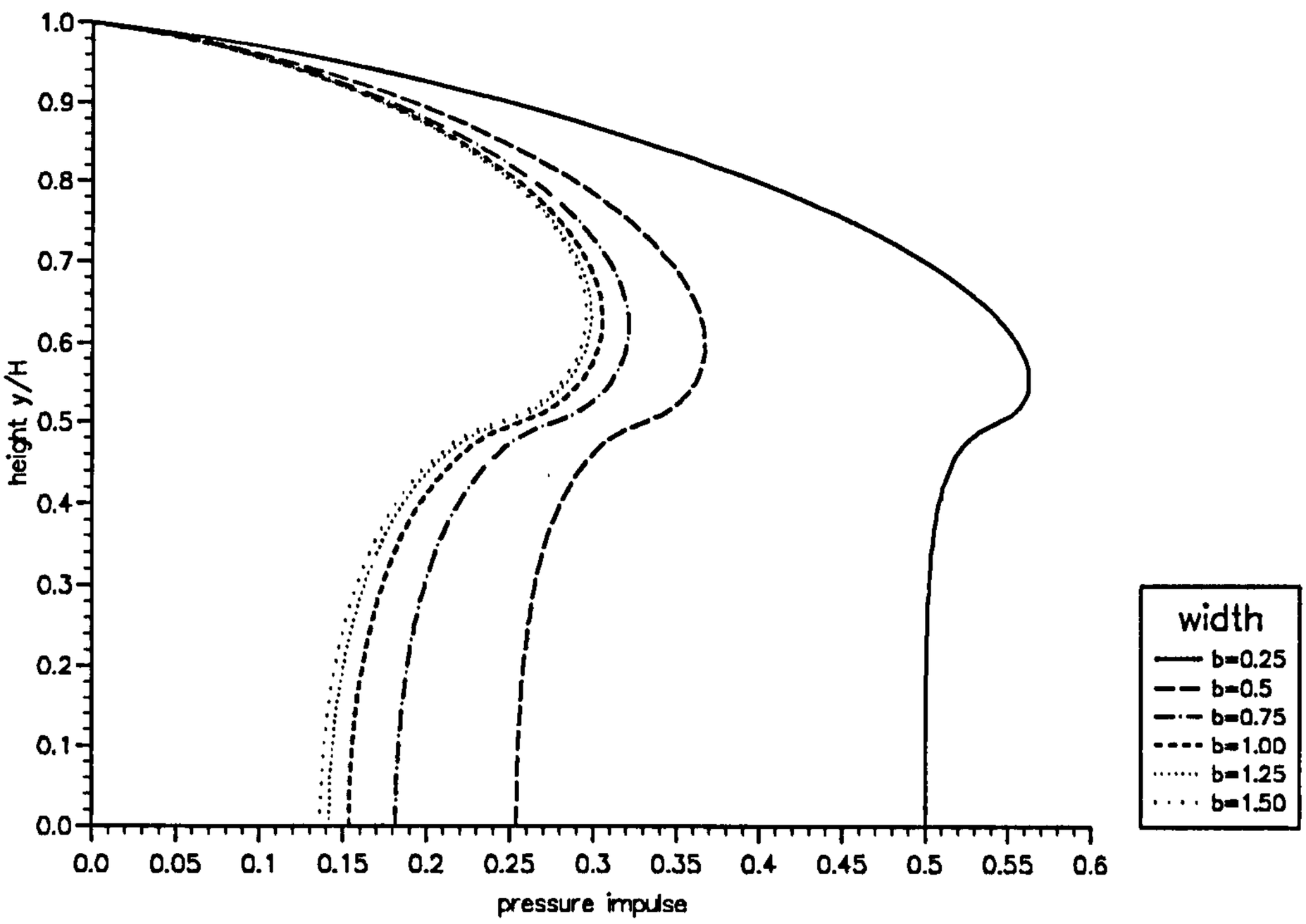

Figure 2.5: Pressure impulse $P/\rho U_o H$ on the impact wall $x' = 0$ for different widths of a two-dimensional rectangular tank with impact size $\mu = 0.5$.

The impact velocity immediately before impact has so far been modelled as a constant.

Any alternative distribution can be evaluated for an initial impact velocity. For example

$$U(y) = \frac{U_o}{\mu}[y' - (1-\mu)] \tag{2.13}$$

which decreases with depth in the impact zone. This gives the original boundary condition on $x' = 0$ at the top of the domain $y' = 1$ but zero velocity at the bottom of the impact region. The solution for the pressure impulse is now:

$$P(x', y') = 2\rho U_o H \sum_{n=o}^{\infty} \frac{[\mu\alpha_n - \sin(\mu\alpha_n)](-1)^n \cos(\alpha_n y') \cosh[\alpha_n(x'-1)b]}{\mu\alpha_n^3 \sinh(\alpha_n b)} \tag{2.14}$$

and the pressure impulse contours for an impact similar to that in figure 2.1, but with this non-constant initial velocity in the impact zone, have been displayed in figure 2.6.

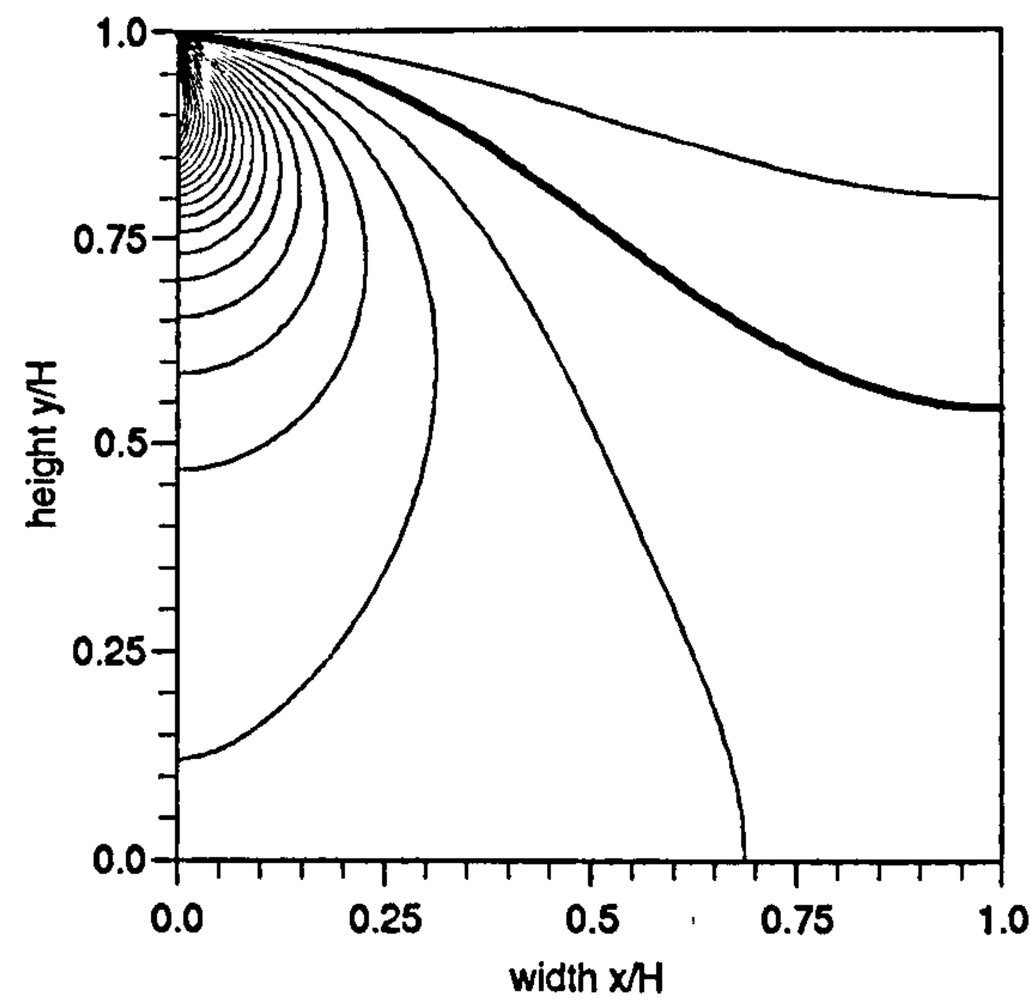

Figure 2.6: Pressure impulse contours $P/\rho U_o H$ with increments 0.002 for a rectangular tank, width $b = 1$, and with an impact of $\mu = 0.2$. A thicker contour is drawn for the value 0.004.

Contour lines with smaller increments of 0.002 have been drawn, with the value 0.004 $P/\rho U_o H$ highlighted. The peak pressure is 0.0483 $\rho U_o H$ at position 0.92 H. Comparison between these two figures show the pressure impulses are now lower in the second example due to the halving of the mean value of the velocity. The total impulse on the impact wall $x' = 0$ now becomes

$$I_w = 2\rho U_o H^3 \sum_{n=0}^{\infty} \frac{[\mu\alpha_n - \sin(\mu\alpha_n)](-1)^{2n}}{\mu\alpha_n^4 \tanh(\alpha_n b)}. \tag{2.15}$$

For a domain of dimension $b = 1$ with $\mu = 0.2$, as pictured in figure 2.1, with an impact velocity as in (2.13), the total impulse on the impact wall is 0.0164 $\rho U_o H^2$, again lower than for an impact with a constant velocity.

2.4 Two-Dimensional Circular Domains

Many liquid transportation vessels have a circular geometry rather than a rectangular shape. A simple change of coordinate system enables the motion in several two-dimensional circular domains to be studied and appropriate conformal mappings enable the study of more complex geometries. The impact velocity in this section is taken to be a constant $U(y) = U_o$ throughout.

2.4.1 Semi-Circular Domain

The motion can be studied in a circular vessel where the liquid is taken to be in the domain described by polar coordinates (r, θ) for $0 \leq r \leq R$ and $0 \leq \theta \leq \pi$ which is the cross section of a half-full circular cylindrical container. The impact zone on the rigid boundary $r = R$ extends $\mu\pi$ down from the free surface $\theta = 0$. The boundary condition on the rigid wall in the impact region is thus $\frac{\partial P}{\partial r} = \rho U_o$ between $0 \leq \theta \leq \mu\pi$ and $\frac{\partial P}{\partial r} = 0$ on the rigid wall between $\mu\pi \leq \theta \leq \pi$. Using separation of variables for Laplace's equation in polar coordinates, the pressure impulse solution describing the motion is

$$P(r,\theta) = \frac{2\rho U_o R}{\pi} \sum_{n=1}^{\infty} \frac{[1 - \cos(n\mu\pi)] \sin(n\theta)}{n^2} \left(\frac{r}{R}\right)^n \tag{2.16}$$

and the pressure impulse contours, in increments of 0.1, for an impact of size $\mu = 0.1$ are displayed in figure 2.7. An additional thicker contour line for the value 0.004 has been included to suggest an alternative free surface. The peak pressure impulse for this example is $0.175\rho U_o R$ which occurs a distance 0.236π down from the free surface $\theta = 0$ on the rigid impact wall $\frac{r}{R} = 1$. The total impulse I_w on the wall $\frac{r}{R} = 1$ can be evaluated to give

$$I_w = \frac{2\rho U_o R}{\pi} \sum_{n=1}^{\infty} \frac{[1 - \cos(n\pi\mu)][1 - \cos n\pi]}{n^3} \tag{2.17}$$

and the total impulse for the example shown in figure 2.7 for a domain with impact region $\mu = 0.1$ is 0.105 $\rho U_o R$. Differentiating with respect to θ, the change in normal velocity $V = \frac{1}{r}\frac{\partial P}{\partial \theta}$ becomes

$$V = \frac{2U_o R}{\pi} \sum_{n=1}^{\infty} \frac{[1 - \cos(n\mu\pi)]}{n} \cos n\theta \left(\frac{r}{R}\right)^n. \tag{2.18}$$

On the free surface $\theta = 0$, this can be reduced to

$$V = \frac{2U_o R}{\pi} \left\{ -\log\left(1 - \frac{r}{R}\right) + \frac{1}{2}\log\left[1 + \left(\frac{r}{R}\right)^2 - 2\left(\frac{r}{R}\right)\cos\mu\pi\right] \right\} \tag{2.19}$$

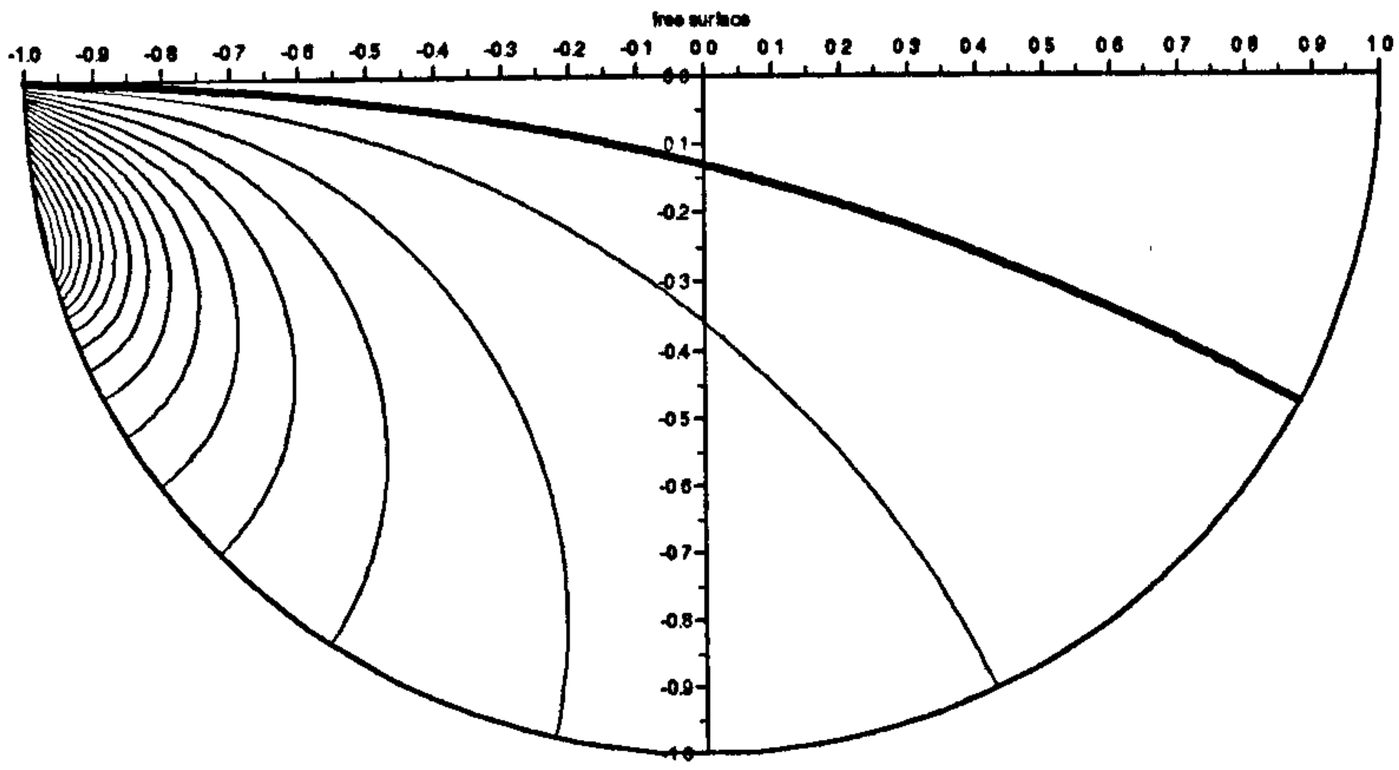

Figure 2.7: Pressure impulse contours $P/\rho U_o R$ with increments of 0.01 for a semi-circular domain with an impact region of size $\mu = 0.1$. The additional line for 0.004 has been highlighted.

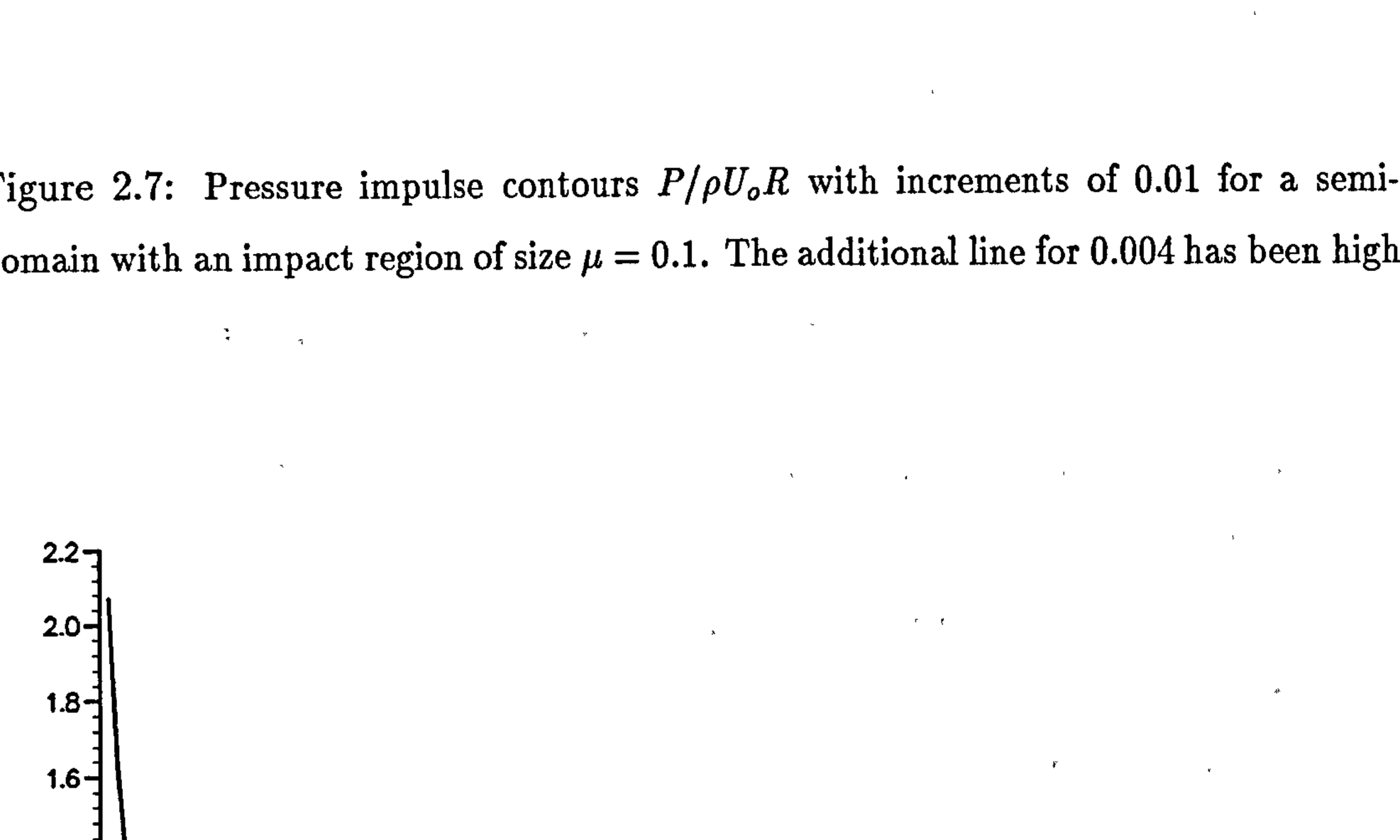

Figure 2.8: Change in normal velocity on the free surface for a semi-circular domain with impact size $\mu = 0.1$.

which gives a singularity on the boundary $r = R$. On the free surface $\theta = \pi$, (2.18) can be reduced to

$$V = \frac{U_o R}{2\pi} \log \left[\frac{\left(1 + \left(\frac{r}{R}\right)^2 - 2\left(\frac{r}{R}\right)\cos\pi(\mu - 1)\right)\left(1 + \left(\frac{r}{R}\right)^2 - 2\left(\frac{r}{R}\right)\cos\pi(\mu + 1)\right)}{\left(1 + \left(\frac{r}{R}\right)^2 - 2\left(\frac{r}{R}\right)\cos\mu\pi\right)^2} \right] \tag{2.20}$$

which further reduces to

$$V = \frac{2U_o R}{\pi} \log\left(\frac{\cos\pi\mu}{2}\right) \tag{2.21}$$

on the boundary $r = R$. The change in normal velocity of the free surface for the impact shown in figure 2.7 of size $\mu = 0.1$ has been evaluated and displayed in figure 2.8. A large change occurs near the boundary $r = R$ on $\theta = 0$, rapidly decaying until only a small change near the boundary $r = R$ on $\theta = \pi$.

2.4.2 Partially-Full Circular Domain

It is more difficult to find solutions for the motion inside a circular container that is either more or less than half-full. However it helps if the domain can be taken to form the geometrical shape of two circles intersecting at right angles, at points D and B as shown in figure 2.9. The free surface is taken to be the smaller upper circle and the rigid boundary is the lower larger circle. Let the centre of the larger circle be at A and the impact zone be the arc DE. Choosing the distance AC, where A is the centre of the larger circle as in figure 2.9, to be a length σ, where σ is a dimensionless fraction between 0 and 1, the "fill-level" of the circular container can be altered.

Let the line, AD, along the radius of the larger curve, which goes through the point of intersection of the two curves, be an angle β to the vertical, AC. This gives $AC = \sigma = \cos\beta$ and $CD = \sin\beta$, with the circumference of the lower curve, a length $2(\pi - \beta)R$ and the circumference of the upper curve a length $(\pi - 2\beta)R\tan\beta$ where R is the radius of the lower circle. Thus $\sigma = 0, \beta = \frac{\pi}{2}$ corresponds to a semi-circle and $\sigma = 1, \beta = 0$ to a full circle. To solve for the pressure impulse field inside the domain, a conformal mapping is used to map the original geometry in the $z = x + iy$ $(x = r\cos\theta, y = r\sin\theta)$ plane shown in figure 2.9 onto a semi-circle in the $w = u + iv$ $(u = s\cos\psi, v = s\sin\psi)$ plane. Thus the two points of intersection at D:$z = -\sin\beta + i\cos\beta$, B:$z = \sin\beta + i\cos\beta$ are mapped onto the points $w = -1, 1$ respectively in the w plane. The lowest point of the upper

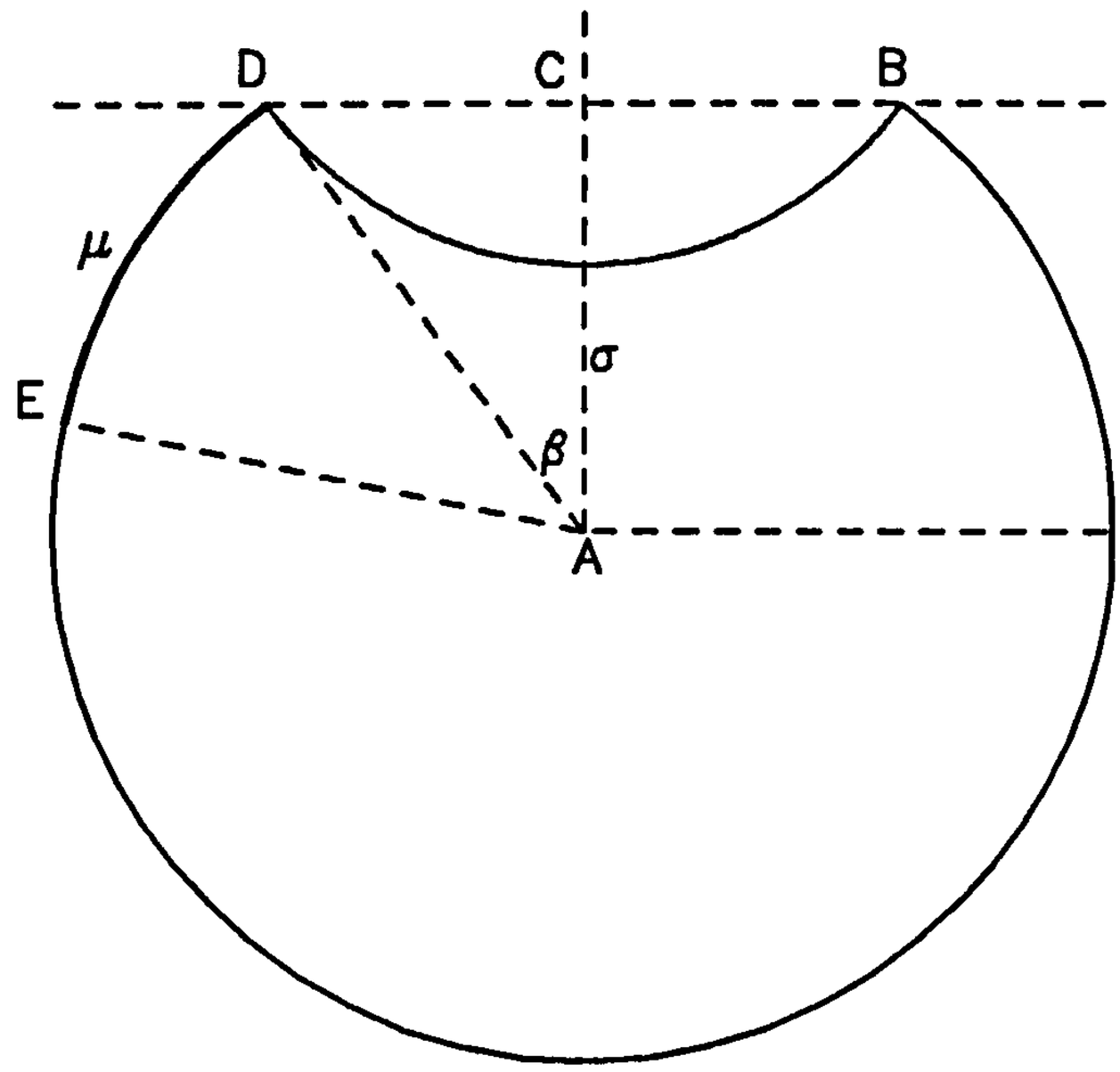

Figure 2.9: Modelling of a partially full circular container

arc, $z = i\sec\beta(1-\sin\beta)$, is mapped onto $w = 0$ and the lowest point of the lower arc, $z = -i$, is mapped onto $w = -i$. This is a bilinear (or linear fractional) transformation of the form

$$w = \frac{z(1+\cos\beta+\sin\beta) - i(1+\cos\beta-\sin\beta)}{iz(1+\cos\beta-\sin\beta) + (1+\cos\beta+\sin\beta)} \tag{2.22}$$

where the radius of the larger curve in the original plane and the radius of the semi-circle in the transformed plane have both been chosen to be 1. Thus for a semi-circle when $\beta = \frac{\pi}{2}$, $\cos\beta = 0$ and $\sin\beta = 1$, this expression reduces to $w = z$ as required.

To simplify the following expressions, let

$$K = (1+\cos\beta+\sin\beta)\,, \quad L = (1+\cos\beta-\sin\beta) \tag{2.23}$$

Then

$$w = \frac{zK - iL}{izL + K} \tag{2.24}$$

and this gives expressions for u, v:

$$u = \frac{x(K^2 - L^2)}{(K-yL)^2 + (xL)^2} \tag{2.25}$$

$$v = \frac{y(K^2+L^2) - KL(x^2+y^2+1)}{(K-yL)^2 + (xL)^2} \tag{2.26}$$

and so

$$\psi = \tan^{-1}\left[\frac{2y - \cos\beta(x^2+y^2+1)}{2x\sin\beta}\right]. \tag{2.27}$$

Thus for a semi-circle when σ=0 and $\beta = \frac{\pi}{2}$, $K = 2$, $L = 0$ this reduces to $u = x$, $v = y$ and

$$\psi = \tan^{-1}\left(\frac{y}{x}\right) \tag{2.28}$$

therefore resulting in $\psi = \theta$ as required. From the conformal mapping, returning to the original plane,

$$z = \frac{wK + iL}{K - iwL} \tag{2.29}$$

giving expressions:

$$x = \frac{u(K^2 - L^2)}{(K+vL)^2 + (uL)^2} \tag{2.30}$$

$$y = \frac{v(K^2+L^2) + KL(u^2+v^2+1)}{(K+vL)^2 + (uL)^2} \tag{2.31}$$

and

$$\theta = \tan^{-1}\left[\frac{2v + \cos\beta(u^2+v^2+1)}{2u\sin\beta}\right] \tag{2.32}$$

where for a semi-circle $\beta = \frac{\pi}{2}$, these reduce to $x = u$, $y = v$ and $\theta = \psi$ as necessary.

Boundary conditions

The smaller upper arc represents the free surface of the liquid and the larger lower arc represents the rigid container. Thus the boundary condition $P(r,\theta) = 0$ on the free surface becomes $P(s,\psi) = 0$ on $\psi = -\frac{\pi}{2}$, $\psi = \frac{\pi}{2}$ in the conformed plane. The impact zone, arc DE of length $\mu\pi$, on the rigid boundary $r = 1$ is taken to extend an angle ψ_s down from the free surface $\psi = -\frac{\pi}{2}$. The boundary condition $\left.\frac{\partial P}{\partial r}\right|_{r=1} = \rho U_o$ now becomes

$$\left.\frac{\partial P}{\partial s}\right|_{s=1} = \frac{-\rho U_o \sin\psi\cos\psi}{\cos\varsigma[A\sin\psi + B\cos\psi]} \tag{2.33}$$

where

$$\tan\varsigma = \left\{\frac{v+\cos\beta}{u\sin\beta}\right\} \tag{2.34}$$

$$A = \frac{K^2 - (\cos^2\psi - \sin^2\psi)L^2 + 2KL\sin\psi}{(K^2-L^2)} \tag{2.35}$$

$$B = \frac{-2L\cos\psi(L\sin\psi + K)}{(K^2-L^2)} \tag{2.36}$$

between $\psi = \pi$ and $\psi = \psi_s$ where

$$\psi_s = \tan^{-1}\left[\frac{y_s - \cos\beta}{x_s \sin\beta}\right] \tag{2.37}$$

with $x_s = -\sin(\beta + \mu)$, $y_s = \cos(\beta + \mu)$. When $\beta = \pi/2$, $A = 1$ and $B = 0$ and $\frac{\partial P}{\partial s}\Big|_{s=1}$ reduces to $\frac{\partial P}{\partial r}\Big|_{r=1}$ as expected. Note that for a complete circle $\beta = 0$, $A = 0$, $B = 0$, $K^2 = L^2$ and the solution cannot be found.

Pressure impulse solution

The solution for the pressure impulse inside the transformed plane can now be solved as previously for a semi-circular domain in subsection 2.4.1 and then returning to the original plane, a solution for the pressure impulse in a partially full domain is obtained:

$$P(r,\theta) = \frac{2\rho U_o}{\pi} \sum_{n=1}^{\infty} \frac{I_n}{n} \sin\left[\frac{n\pi}{2} + n\tan^{-1}(h(\theta))\right] \; [g(\theta)]^{\frac{n}{2}} \tag{2.38}$$

where

$$I_n = \int_{-\frac{\pi}{2}}^{\frac{\pi}{2}} f(\psi) \sin\left(\frac{n\pi}{2} + n\psi\right) \, d\psi, \qquad f(\psi) = \frac{dP}{ds}\Big|_{s=1} \quad \text{on} \quad -\frac{\pi}{2} \leq \psi \leq \psi_s$$

$$h(\theta) = \frac{2r\sin\theta - \cos\beta(r^2+1)}{2r\cos\theta} \tag{2.39}$$

and

$$g(\theta) = 4(1+\cos\beta)^2 \left(\frac{(2r\sin^2\beta\cos\theta)^2 + [2r\sin^2\beta\sin\theta + \cos\beta(\sin^2\beta - r^2)]^2}{[K^2 + L^2r^2 - 2r\sin\theta KL]^2}\right) \tag{2.40}$$

When $\beta = \pi/2$ for a semi-circle, $h(\theta)$ and $g(\theta)$ reduce to $\tan\theta$ and r^2 respectively, as required for the solution in a semi-circular domain.

The pressure impulse distribution has been evaluated for several different values of β, with an impact region of $\mu = \pi/10$ in each case and the contour maps are displayed in figures 2.10, 2.11, 2.12 for 'fill-levels' of angle $\beta = \pi/3$, $\pi/6$ and $\pi/9$.

The increments of 0.02 for the pressure impulse contours in each of the three figures have been taken to be the same to clearly illustrate the increase in pressure impulse as the fill-level of the container becomes greater. The pressure impulse for a half-full circular container of impact size $\mu = 0.1$ was given in subsection 2.4.1 as 0.175 ρU_o for $R = 1$. In the first example for $\beta = \pi/3$ or a fill-level of 75 %, the pressure impulse distribution is similar to that shown previously for a semi-circular domain with the maximum value

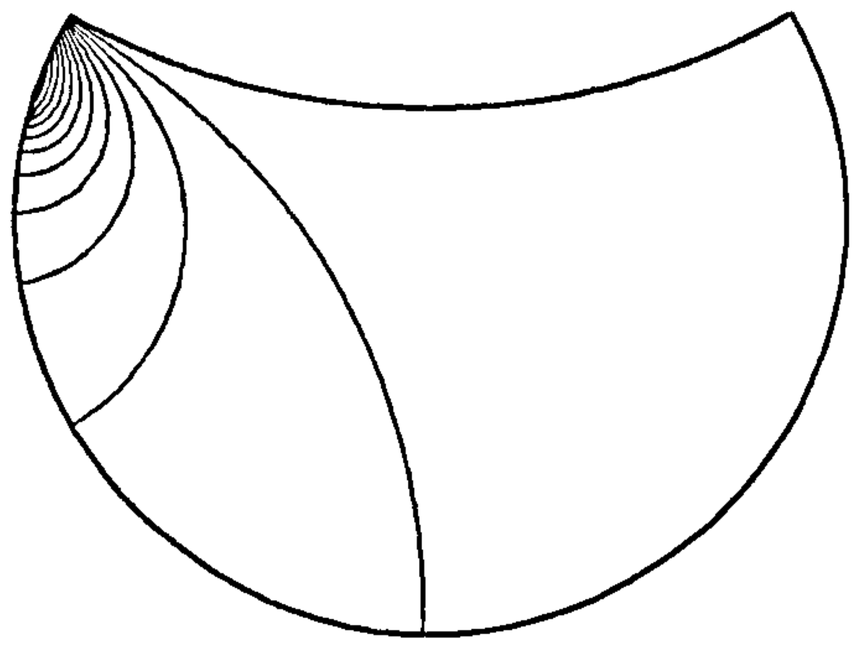

Figure 2.10: Pressure impulse contours $P/\rho U_o$ for a circular domain with a 'fill-level' of $\beta = \pi/3$ with increments of 0.02 for an impact $\mu = 0.1$.

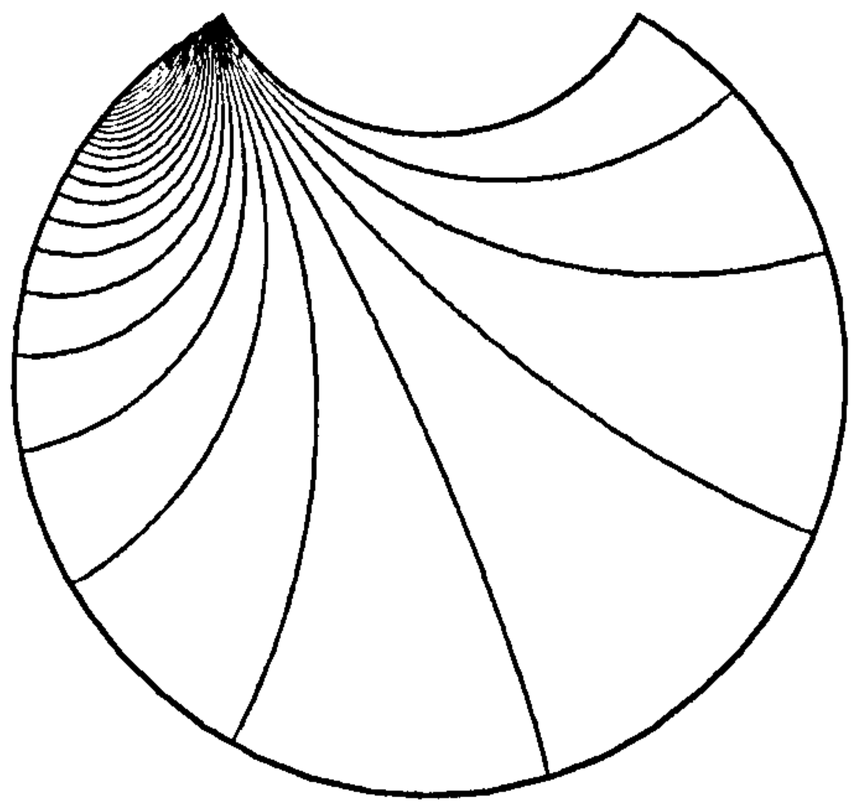

Figure 2.11: Pressure impulse contours $P/\rho U_o$ for a circular domain with a 'fill-level' of $\beta = \pi/6$ with increments of 0.02 for an impact $\mu = 0.1$.

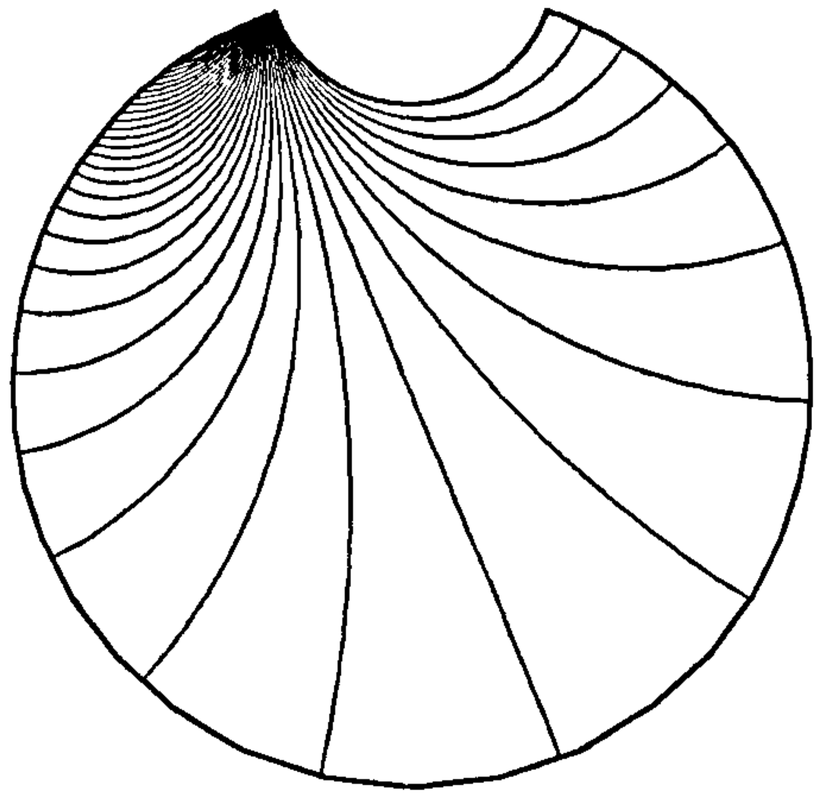

Figure 2.12: Pressure impulse contours $P/\rho U_o$ for a circular domain with a 'fill-level' of $\beta = \pi/9$ with increments of 0.02 for an impact of $\mu = 0.1$.

slighty higher at 0.236 ρU_o. In figure 2.11, for 93 % full, the pressure impulse values have increased showing a more dense region of isobars and the peak pressure impulse is now much larger than that of the previous figure at 0.515 ρU_o. For the final example shown, $\beta = \pi/9$, 97 % full, the tightly-packed contours show steep pressure impulse gradients and the peak value is now 0.717 ρU_o, thus indicating rapidly increasing solutions as the container becomes very full. This rapid change in the peak pressure impulse is shown in figure 2.13 where the maximum pressure on the wall is shown for increasing angle β. Note the logarithmic scale. The values give a sharp increase as the 'fill-level' of the domain becomes greater.

The strengthening of the pressure impulse field as σ becomes larger suggests more violent motion, thus the change in normal velocity V on the free surface immediately after impact has been evaluated using

$$\frac{dp}{d\theta}\frac{1}{r\sin\theta} = A\frac{dp}{d\psi}\frac{1}{s\sin\psi} - B\frac{dp}{d\psi}\frac{1}{\cos\psi} \tag{2.41}$$

and figure 2.14 shows the change in normal velocities on part of the free surface near the impact wall immediately after impact, for the three examples, $\beta = \pi/3$, $\pi/6$ and $\pi/9$. Again a logarithmic scale has been used. The singularity at the boundary wall has not been included. Thus as the 'fill-level' increases, along with the pressure impulses, the change in the normal velocities becomes much larger.

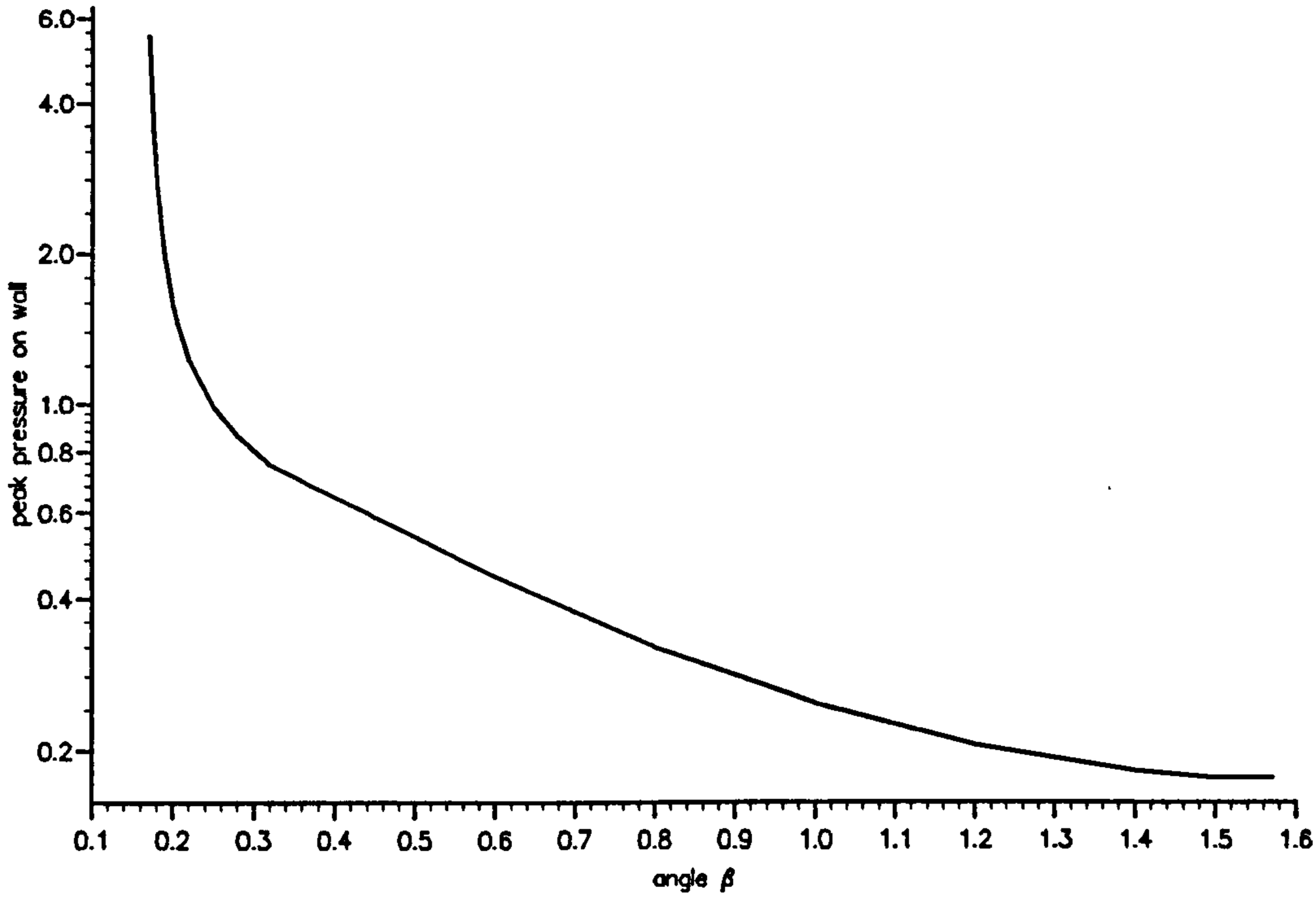

Figure 2.13: Peak pressure impulse $P/\rho U_o$ on the rigid boundary for increasing fill-levels.

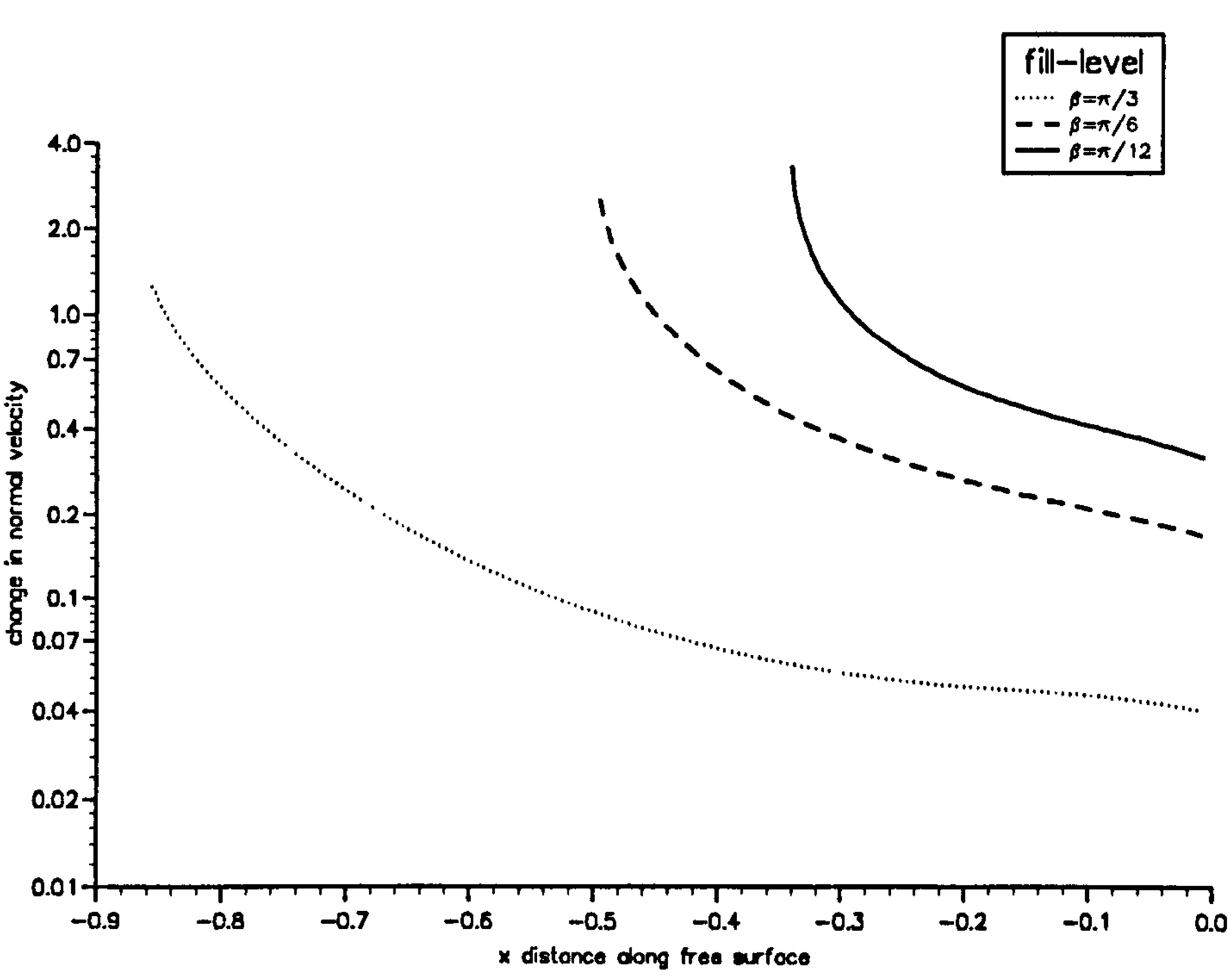

Figure 2.14: Change in normal velocity V of the free surface immediately after impact, for different values for β.

2.4.3 Semi-Elliptical Domain

Another common container shape is an elliptical container. The fluid motion in the cross section of a half-full elliptic cylindrical container can be studied using the elliptical coordinates (η, ψ) where $x = -c\cosh\eta\cos\psi$ and $y = -c\sinh\eta\sin\psi$. The curves $\eta =$ constant are ellipses with major axis $c\cosh\eta_o$ and minor axis at $c\sinh\eta_o$. The liquid is taken to be in the domain $0 \leq \psi \leq \pi$ and $0 \leq \eta \leq \eta_o$ with the region where the fluid strikes the rigid boundary $\eta = \eta_o$ to extend $\mu\pi$ down from the free surface ψ =0. The boundary condition on the impact wall, $\eta = \eta_o$, in the impact region is taken to be $\frac{\partial P}{\partial \eta} = \rho U_o$ between $0 \leq \psi \leq \mu\pi$, and outside the impact region $\frac{\partial P}{\partial \eta} = 0$ for $\mu\pi \leq \psi \leq \pi$.

Using separation of variables for Laplace's equation in elliptical coordinates, the pressure impulse solution with these boundary conditions is

$$P(\eta, \psi) = \frac{2\rho U_o}{\pi} \sum_{n=1}^{\infty} \frac{[1 - \cos(n\mu\pi)]\sin(n\psi)\sinh(n\eta)}{n^2\cosh(n\eta_o)} \tag{2.42}$$

and figure 2.15 shows the pressure impulse contours for a domain $c = 3^{1/2}$, $\eta_o = \tanh^{-1}\frac{1}{2}$ and impact region of size $\mu = 0.1$. The additional thicker contour of the value 0.002 could present a more realistic free surface and indicates well how little the more distant surface shape affects the pressure impulse. The peak pressure impulse of $0.292\rho U_o\pi$ is approximately 0.22 down from the free surface $\psi = 0$ on the rigid boundary $\eta = \eta_o$.

The total impulse on the impact wall $\eta = \eta_o$ can be evaluated to give

$$I_w = \frac{2\rho U_o}{\pi} \sum_{n=1}^{\infty} \frac{[1 - \cos(n\pi\mu)][1 - \cos(n\pi)]}{n^3\tanh n\eta_o} \tag{2.43}$$

and the total impulse on the wall for the example shown in figure 2.15 for an impact of μ=0.1 is 0.188 ρU_o.

2.5 Resultant Impulse on a Baffle

As can be seen from the pressure impulse contour map in figure 2.1, the wave impact on the wall induces a pressure impulse field with significant gradients on the bed, which has been discussed in some detail by Cooker & Peregrine (1992). Many transportation vessels contain internal fixtures which have to withstand pressure distributions due to

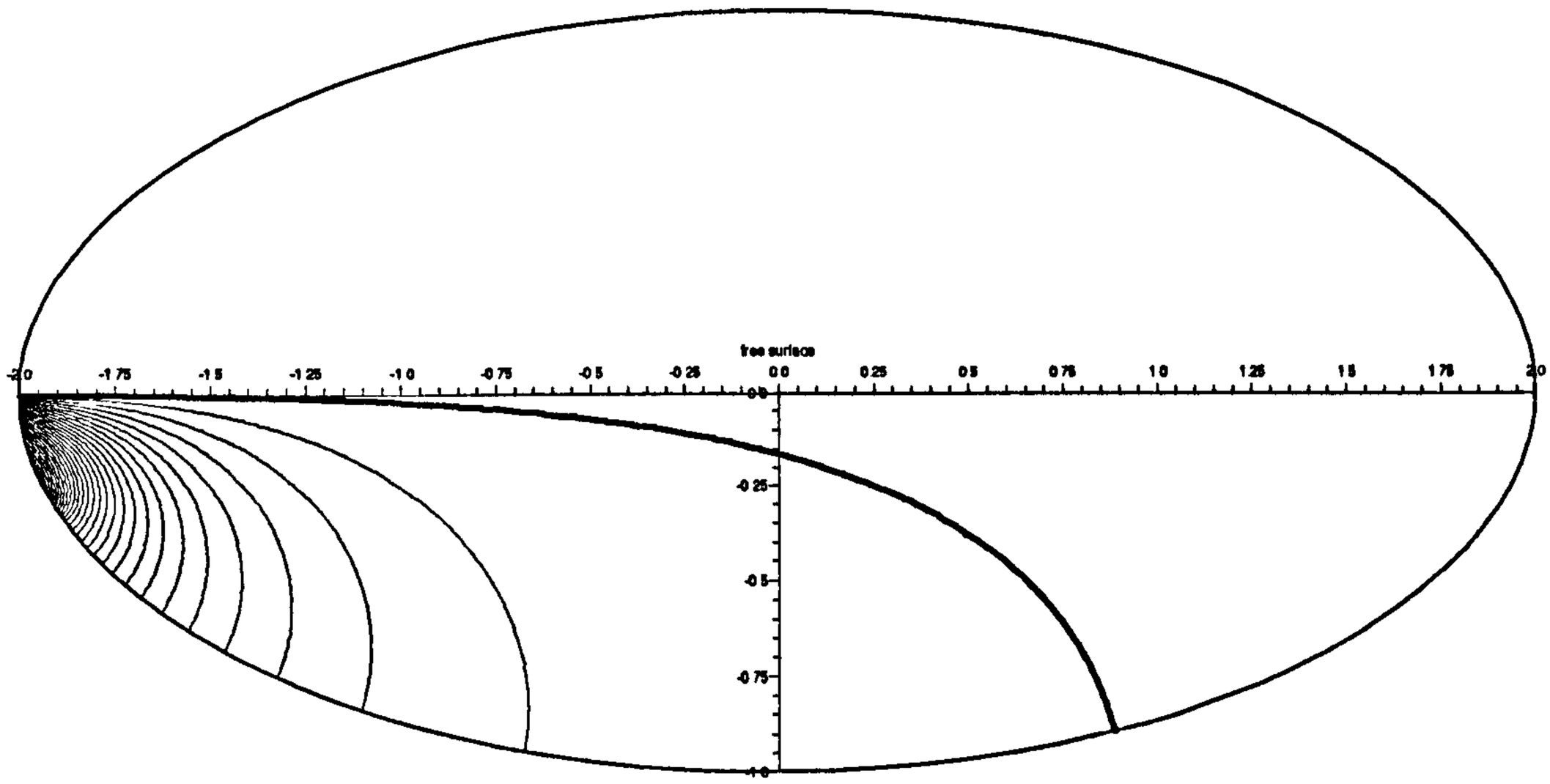

Figure 2.15: Pressure impulse contours $P/\rho U_o$ with increments of 0.01 for an elliptical tank of dimensions $c = 3^{1/2}$ and $\eta_o = \tanh^{-1}\frac{1}{2}$ with an impact region of size μ=0.1. The extra contour line for the value 0.002 has been thickened.

liquid impact. Here the total impulse on a vertical baffle on the bottom of a rectangular domain is considered.

The baffle is assumed to be much smaller than the dimensions of the wave so that near the baffle, the pressure impulse due to the wave is

$$P = P_o - Gx \tag{2.44}$$

where P_o and G are the local pressure impulse and local pressure impulse gradient respectively, both positive constants. Redefining $x = 0$ to be at the baffle and taking the baffle to be very thin, the local pressure impulse field can be found by using a conformal mapping $w^2 = z^2 + h^2$ from the original plane $z = x + iy$ to the tranformed plane $w = u + iv$ where h is the height of the baffle. This gives a solution of the form

$$P(x, y) = P_o + Af(x, y) \tag{2.45}$$

where A is a constant and

$$f(x, y) = \left\{\frac{1}{2}(x^2 - y^2 + h^2) + \left[\frac{1}{4}(x^2 - y^2 + h^2)^2 + x^2y^2\right]^{1/2}\right\}^{1/2}. \tag{2.46}$$

The field lines of ∇P near the baffle are displayed in figure 2.16.

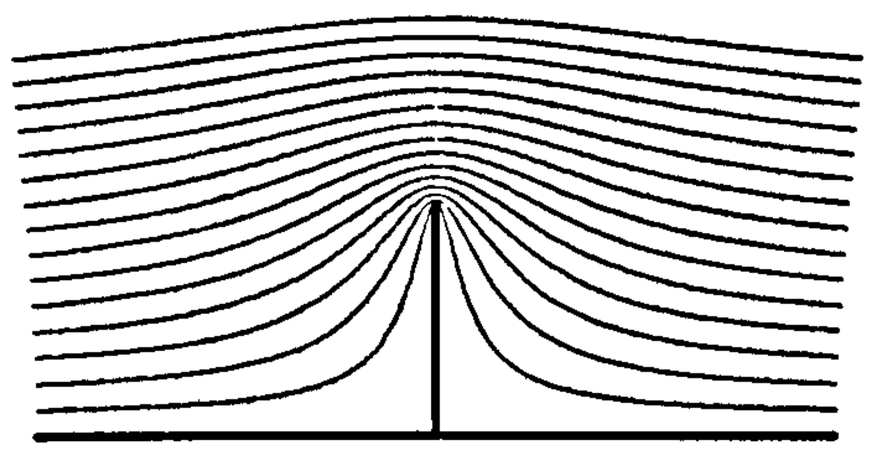

Figure 2.16: Field lines of flow in the proximity of a thin baffle

Using the boundary condition $P \to -Gx$ as $x \to \infty$, this reduces to

$$f(x,y) \approx \left\{ \frac{x^2}{2} + \frac{x^2}{2} \right\}^{1/2} \quad \text{as } x \to \infty. \tag{2.47}$$

Thus $f(x,y) \approx x$ as $x \to \infty$, giving $A = -G$. Hence the local pressure impulse field is

$$P(x,y) = P_o - Gf(x,y). \tag{2.48}$$

The resultant horizontal component of impulse on the baffle $x = 0$ is given by

$$I = 2\int_0^h P(0,y)\ dy \ = \ -2G\int_0^h (h^2 - y^2)^{1/2}\ dy. \tag{2.49}$$

Integration gives

$$I = \frac{G\pi h^2}{2}. \tag{2.50}$$

For an example, in a rectangular tank of width $b = 2$ and impact area of $\mu = 0.2$, the maximum pressure impulse gradient along the bottom of the domain is G=0.217 ρU_o at $x = 0.50H$. Placing the baffle at this point and taking a baffle height of $0.2H$, the resultant horizontal component of impulse is I=0.013 $\rho U_o H^2$.

2.6 Application for a Moveable Container

During the transportation of fluid containers, vehicle accelerations leading to brief localised impacts can affect the stability of the container as the impact can cause the walls to move. For a vehicle undergoing a turning manoeuvre there is a limiting speed beyond which the container may overturn. A sudden deceleration of a vehicle can lead to

an impact on the end wall in the direction of travel. The transverse velocity and change in angular velocity experienced by the vehicle due to the impact must be absorbed by the suspension of the system.

To apply the pressure impulse theory to a moveable vehicle containing liquid, the transverse velocity of the vehicle after impact is now taken into consideration. Considering the two dimensional cross-section of a rectangular tank, let the velocity of the container after impact be U_b horizontally. The boundary condition on the impact wall $x' = 0$ becomes $\partial P/\partial x' = -\rho(U_o - U_b)$ for $(1-\mu) \leq y' \leq 1$ and $\partial P/\partial x' = \rho U_b$ for $0 \leq y' \leq (1-\mu)$. On the opposite wall, $x' = 1$, the boundary condition is now $\partial P/\partial x' = \rho U_b$ and so the pressure impulse solution becomes

$$P(x', y') = 4\rho H \sum_{n=0}^{\infty} \{U_b(-1)^n \sin\left(\frac{\alpha_n b}{2}\right) \sinh\left[\frac{\alpha_n b}{2}(2x' - 1)\right] + U_o C_n \cosh\left[\alpha_n(x' - 1)b\right]\} \frac{\cos(\alpha_n y')}{\alpha_n^2 \sinh(\alpha_n b)}. \tag{2.51}$$

For $U_b = 0$ the solution reduces to that of a rigid non-moveable container as in equation (2.6). For U_b positive (in the direction of the initial impact and note U_o and U_b are in the negative x direction) the pressure impulse is now lower than for the stationary domain. The total impulse I_w on the impact wall $x' = 0$ now becomes

$$I_w = 4\rho H^2 \sum_{n=0}^{\infty} \left\{-U_b(-1)^n \sin\left(\frac{\alpha_n b}{2}\right) \sinh\left(\frac{\alpha_n b}{2}\right) + U_o C_n \cosh(\alpha_n b)\right\} \frac{(-1)^n}{\alpha_n^3 \sinh(\alpha_n b)} \tag{2.52}$$

For the total impulse given to the vehicle to equal its change in momentum, $I_w = MU_b$ where M is the mass of the vehicle, an expression for the change in velocity of the vehicle due to the impact can be found:

$$U_b = \frac{4 \sum_{n=0}^{\infty} U_o C_n F_n \cosh(\alpha_n b)}{\frac{M}{\rho H^2} + 4 \sum_{n=0}^{\infty} F_n (-1)^n \sin\left(\frac{\alpha_n b}{2}\right) \sinh\left(\frac{\alpha_n b}{2}\right)} \tag{2.53}$$

where

$$F_n = \frac{(-1)^n}{\alpha_n^3 \sinh(\alpha_n b)} \tag{2.54}$$

Taking moments M_y about the foot of the impact wall $y' = 0$ we obtain

$$M_y = 4\rho H^3 \sum_{n=0}^{\infty} \left\{-U_b(-1)^n \sin\left(\frac{\alpha_n b}{2}\right) \sinh\left(\frac{\alpha_n b}{2}\right) + U_o C_n \cosh(\alpha_n b)\right\} \frac{[\alpha_n(-1)^n - 1]}{\alpha_n^4 \sinh(\alpha_n b)} \tag{2.55}$$

which gives the rate of change of angular momentum. The wave impact will result in a change in the total angular momentum about $y' = 0$ and hence a change in the angular velocity.

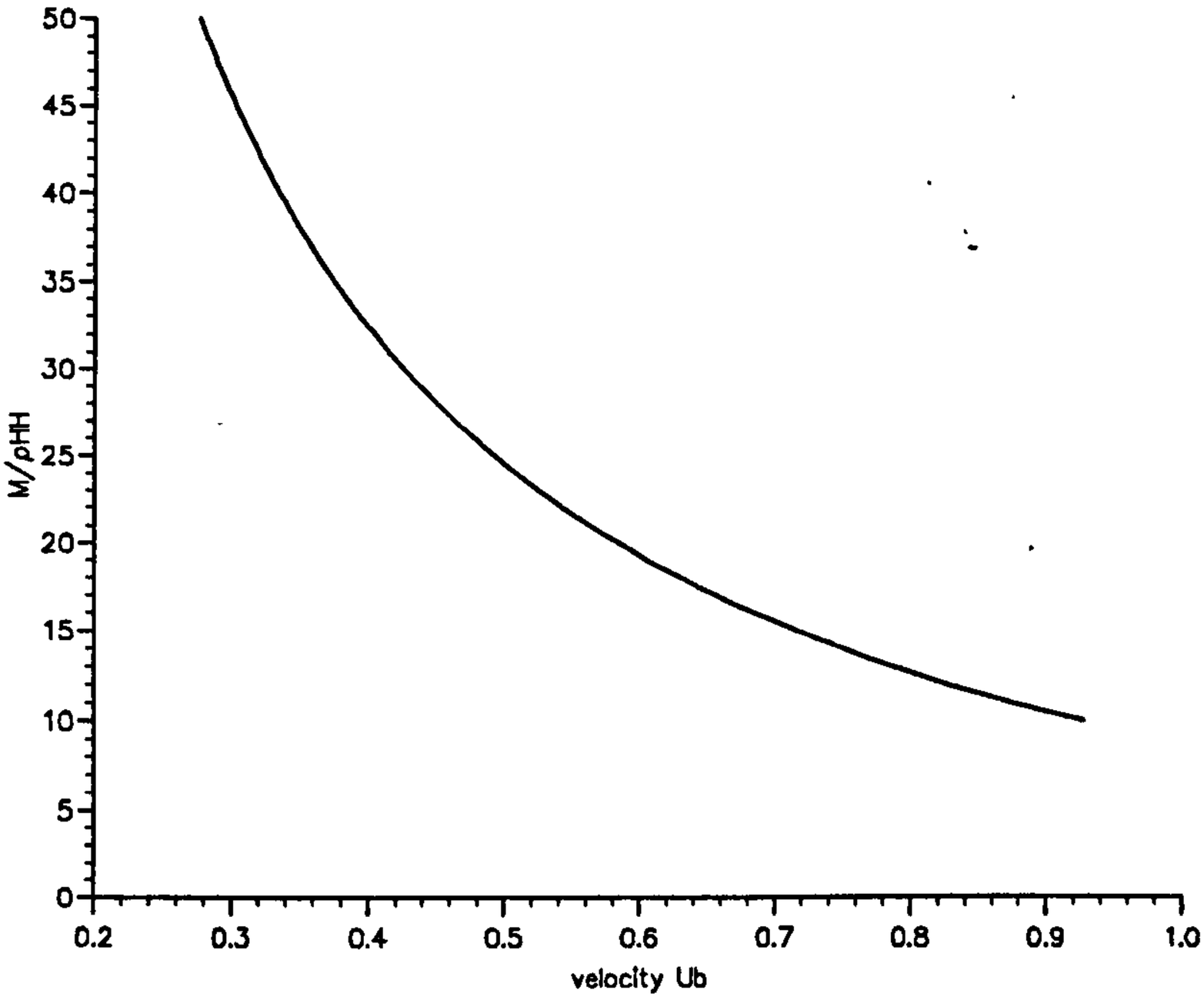

Figure 2.17: Change in velocity of vehicle due to impact with respect to the ratio $M/\rho H^2$.

Figure 2.17 shows how the change in velocity would vary depending on the mass of the vehicle, the density of the liquid and the fill-level. Not surprisingly, an impact inside a container has a greater resultant motion on a lighter container. For example, a container with liquid dimensions of H=5 m, b=1, with an impact region of μ=0.2, an impact of speed $U_o = 2\sqrt{gH}$=14 m/s and using ρ=1000 kg/m^3, the total impulse on the impact wall is 3509.9 and 4735.6 kg m/s for a mass of 2, 3 tonnes per unit length respectively. This is compared with a value of 15725.5 kg m/s for a rigid container, thus a decrease of 78 and 70% respectively. Immediately after impact, the transverse speed is U_b=1.75 m/s and U_b=1.58 m/s for a mass of 2 and 3 tonnes per unit length respectively, assuming no effect of vehicle suspension. The moment M_y for these examples is 27479.1, 29752.1 kg m^2/s^2 for 2, 3 tonnes per unit length respectively against a value of 50217.5 kg m^2/s^2 for a rigid container, a decrease of 45, 41% in each case respectively.

If the container were floating in water, e.g. as in a ship, the above calculation should include the added mass of the sway of the ship in M.

2.7 Three-Dimensional Rectangular Domain

The pressure impulse solution in a container has been evaluated and studied in several two-dimensional domains. For simplicity, when extending the theory to three-dimensions, a rectangular domain has been used. Using Cartesian coordinates (x, y, z), the liquid is considered to be enclosed in a rectangular domain of width bH, height H and length cH as shown in figure 2.18, with a free surface at $y = H$.

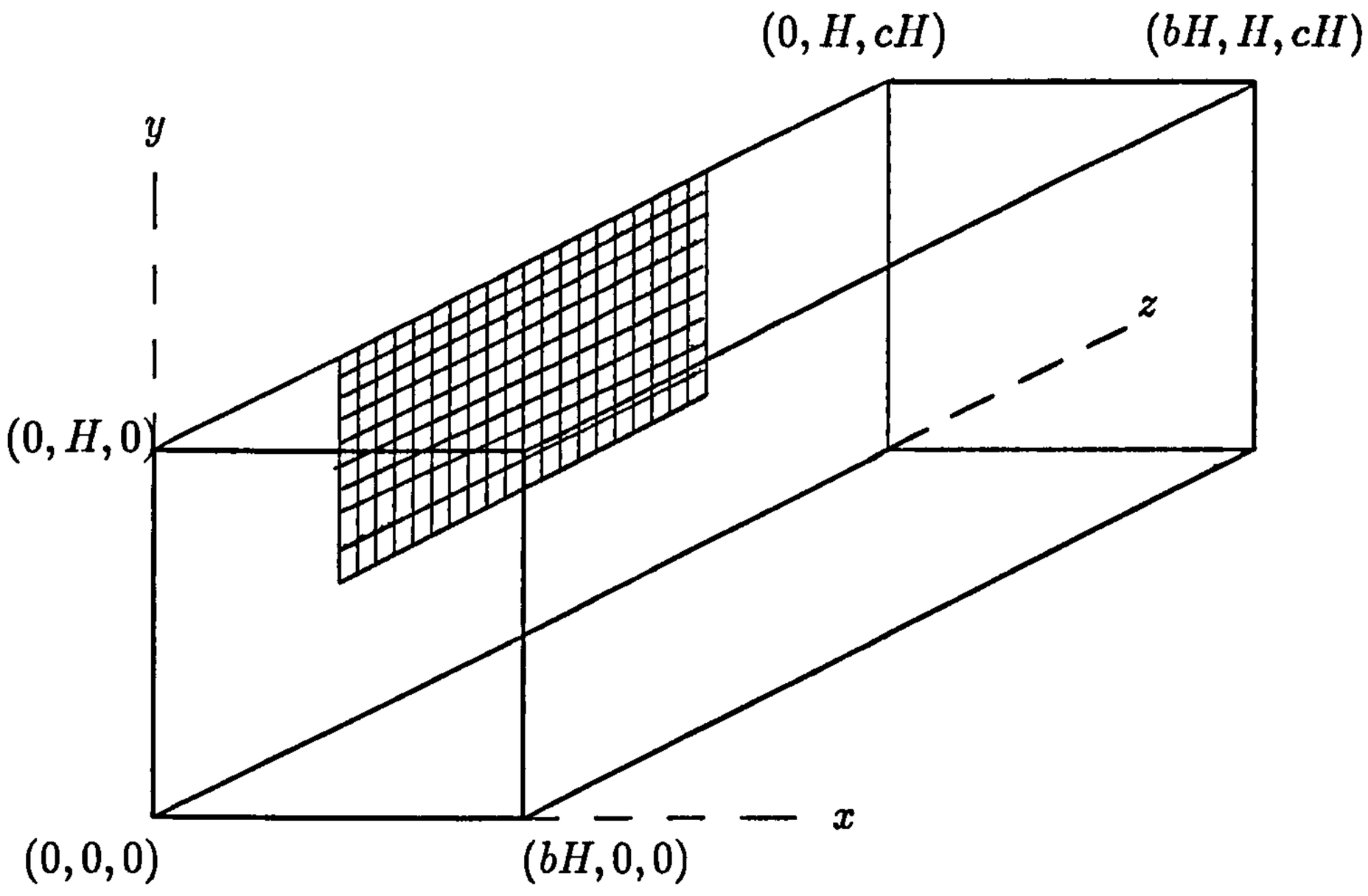

Figure 2.18: Three-dimensional rectangular tank of width bH, height H and length cH.

Positioning the impact zone on the rigid boundary $x = 0$, a region of length μH in the y-direction and length $\mu_2 cH$ in the z-direction where μ, μ_2 are dimensionless fractions between 0 and 1. The model is non-dimensionalised by introducing dimensionless space variables (x', y', z') where $x' = x/bH$, $y' = y/H$ and $z' = z/cH$. Laplace's equation $\nabla^2 P(x', y', z') = 0$ satisfying the motion is solved in the rectangular domain.

2.7.1 Pressure Impulse Distributions

Impact region on the plane $x' = 0$

Using Fourier analysis, the general solution is then of the form

$$P(x', y', z') = 4\rho U_o H \sum_{n=0}^{\infty} C_n \cos(\alpha_n y') \left\{ \frac{\mu_2 c H \cosh[\alpha_n (x' - 1)b]}{\alpha_n^2 \sinh(\alpha_n b)} \right.$$

$$\left. + \sum_{m=1}^{\infty} \frac{A D_m \cos(m\pi z') \cosh[\beta_{nm}(x' - 1)b]}{m\pi \alpha_n \beta_{nm} \sinh(\beta_{nm} b)} \right\} \tag{2.56}$$

where $\beta_{nm}^2 = \alpha_n^2 + (\frac{m\pi}{c})^2$, A is a constant, α_n, C_n are as defined in the two-dimensional case and D_m is a function of m dependent on the position of the impact zone. Four types of impact have been considered to show the effects of the position and size of the impact zone as displayed in figure 2.19.

Type I

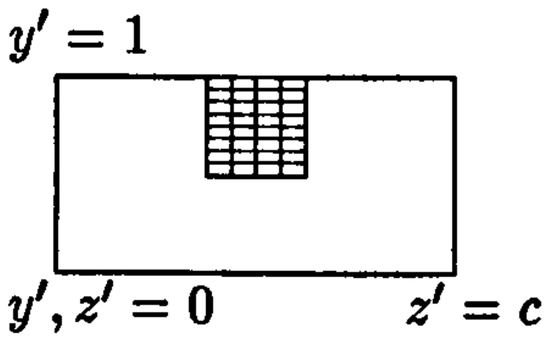

Type II

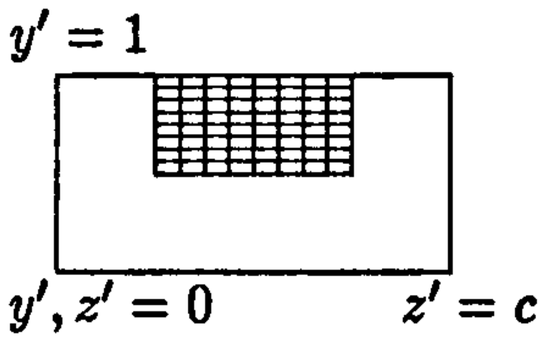

Type III

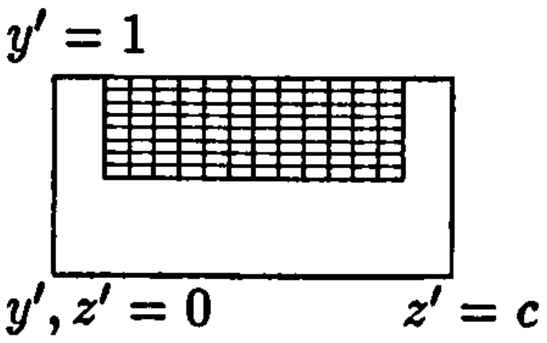

Type IV

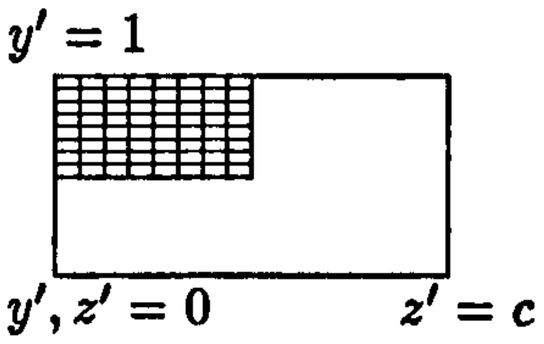

Figure 2.19: Position and size of example impact regions on the impact wall $x' = 0$. The value $\mu = 0.5$ in all cases.

For types I, II and III, the impact zone is symmetric about the plane $z' = c/2$ with μ_2 equal to 0.25, 0.5 and 0.75 respectively. For all three cases $\mu = 0.5$, $A = 4.0$ and $D_m = \sin(m\pi\mu_2/2)\cos(m\pi/2)$. For type IV the impact zone lies between $z' = 0$ and $z' = c/2$, with $\mu = \mu_2 = 0.5$, $A = 2.0$ and $D_m = \sin(m\pi\mu_2)$.

To study the effects of three-dimensions, the pressure impulse distributions have been evaluated for type II on the impact wall $x' = 0$, the side wall $z' = c$ and the bottom of the tank $y' = 0$ for a domain of dimensions $b = 1$, $c = 2$. To evaluate the solution, the

series converges satisfactorily, although not as rapidly as for a two-dimensional domain, and is truncated after a finite number of terms, of the order 100.

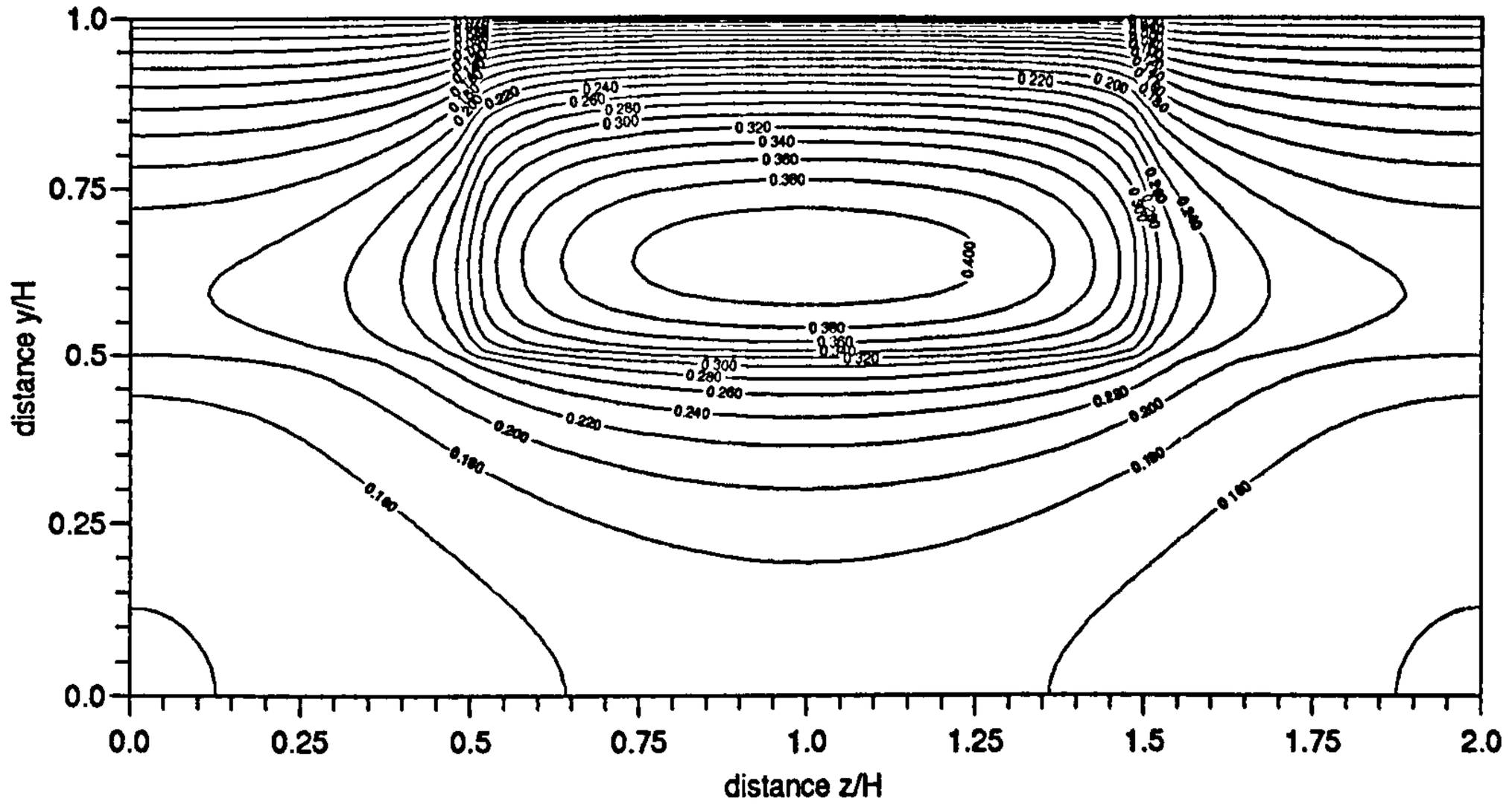

Figure 2.20: Pressure impulse contours $P/\rho U_o H$ on the impact wall $x' = 0$ for type II with dimensions $b = 1$, $c = 2$. Contour lines have been drawn with equal increments of 0.02.

The contour map in figure 2.20 shows that the impact zone produces a region of high pressure impulses which then decay over the remainder of the wall with steep gradients at the edges of the impact zone. The peak pressure impulse for this example is 0.414 $\rho U_o H$ and occurs at a height of $0.64H$.

Figure 2.21 shows the pressure impulse distribution on the wall $z' = c$ adjacent to the impact wall, with a peak pressure impulse of $0.20\rho U_o H$ at a height $0.59H$. The contour line for the value 0.02 has been highlighted to indicate an alternative free surface. As the model for type II is symmetric along the plane $z' = c/2$, the pressure impulse distribution on the side wall $z' = 0$ will be identical to that for the side wall $z' = c$. For type IV, however, as the impact is in the corner, the distribution would be expected to show higher values on the side wall $z' = 0$ and lower values on the side wall $z' = c$.

As can be seen in figure 2.22, there are again significant pressure impulse gradients acting along the bottom away from the impact wall and the maximum pressure impulse is 0.17 $\rho U_o H$ along the edge $x' = 0$.

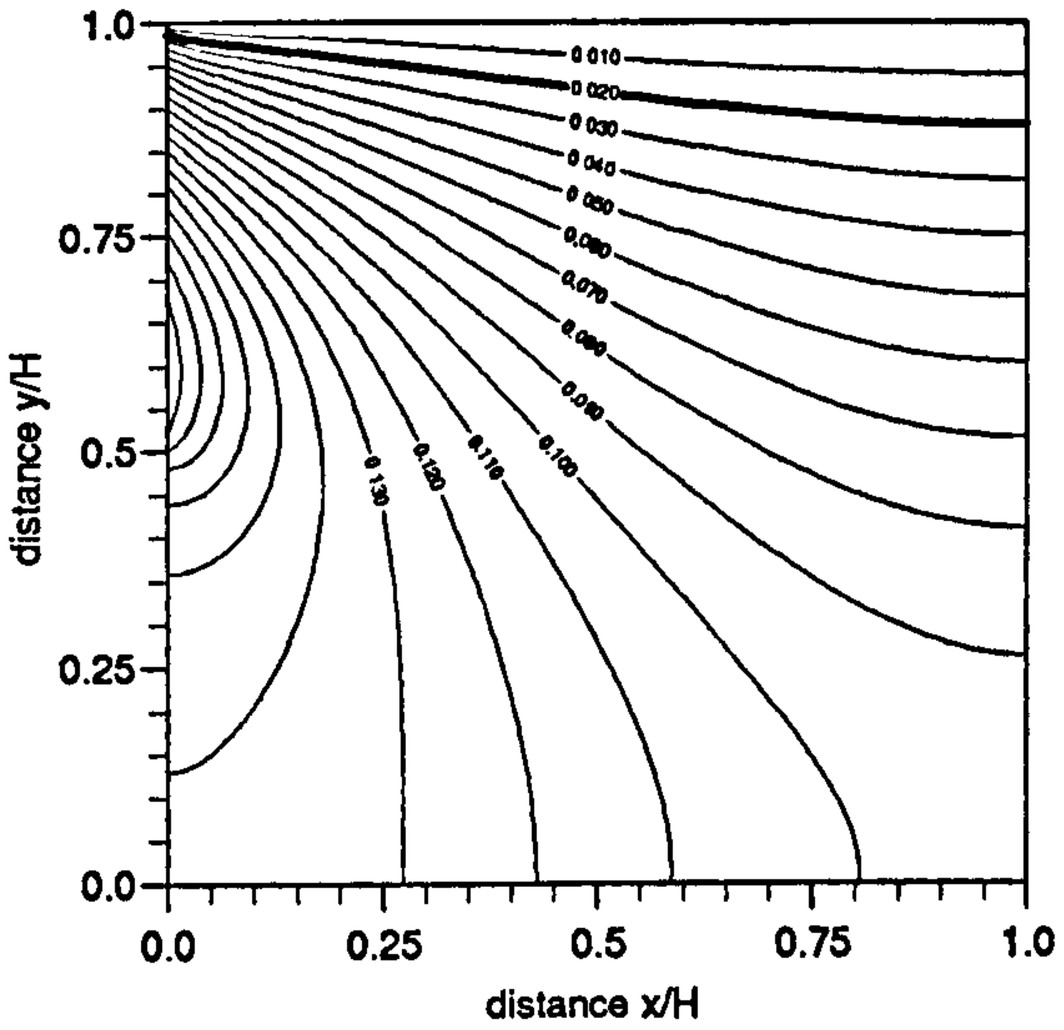

Figure 2.21: Pressure impulse contours $P/\rho U_o H$ on the side wall $z' = c$ for type II where $b = 1$, $c = 2$. Contour lines have been drawn with equal increments of 0.01. The thicker contour line for 0.02 has been highlighted.

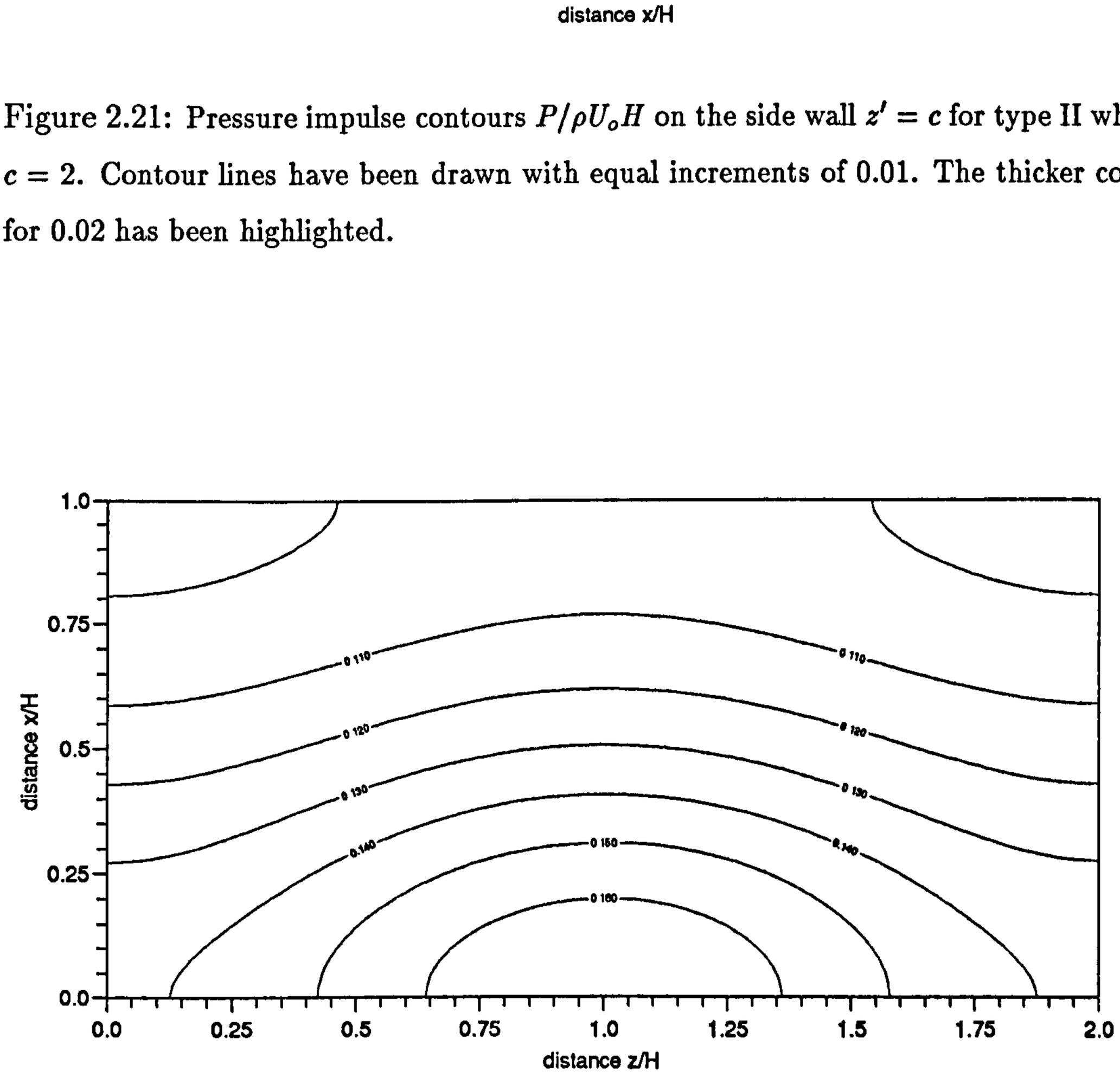

Figure 2.22: Pressure impulse contours $P/\rho U_o II$ on the bottom of the domain $y' = 0$ for type II with dimensions $b = 1$, $c = 2$. Contour lines have been drawn with increments of 0.01.

Impact region in a corner

For a truly three-dimensional impact, consider an impact in a corner on two adjacent walls, where the impact zone is now of length μ_2 in the z-direction on the plane $x' = 0$ beginning at $z' = 0$ and of length $\mu_3 = \frac{c}{b}\mu_2$ in the x-direction on the plane $z' = 0$ beginning at $x' = 0$ as shown in figure 2.23. Letting the impact region to be the same size on both walls, the velocity of the oncoming wave is now acting along the diagonal $x' = z'$ into the corner and so the impact velocity normal to each impact wall is reduced to be $U_o/\sqrt{2}$.

Type Corner

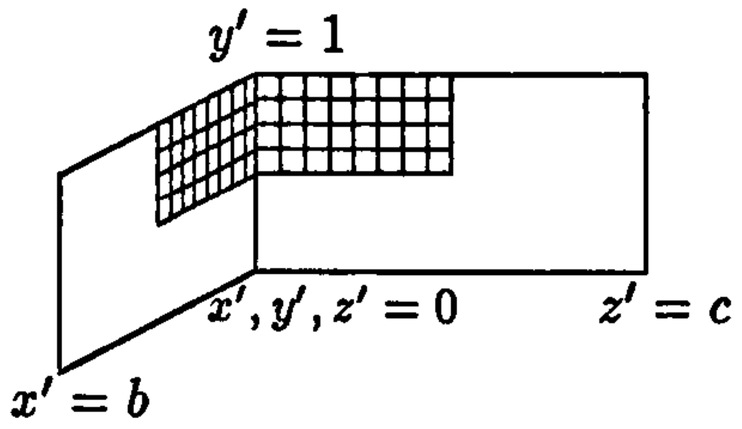

$\mu = \frac{1}{2}$ $\quad A = 2.0$

$\mu_2 = \frac{1}{2}$ $\quad D_m = \sin(m\pi\mu_2)$

$\mu_3 = \mu_2(c/b)$ $\quad D_m^* = \sin(m\pi\mu_3)$

Figure 2.23: Model for impact in a corner on two adjacent walls.

The solution for the pressure impulse distribution in type Corner now consists of a linear combination of two type IV solutions, $\frac{1}{\sqrt{2}}[P(x', y', z') + P^*(x', y', z')]$.

Proceeding as before, where the coefficients for the second part of the pressure impulse solution are now determined by the values of $\frac{\partial P}{\partial z'}$ on the impact wall $z' = 0$, gives the second part of the solution:

$$P^*(x', y', z') = 4\rho U_o H \sum_{n=0}^{\infty} C_n \cos(\alpha_n y') \left\{ \frac{\mu_3 b H \cosh[\alpha_n(z'-1)c]}{\alpha_n^2 \sinh(\alpha_n c)} \right.$$

$$\left. + \sum_{m=1}^{\infty} \frac{A D_m^* \cos(m\pi x') \cosh[\beta_{nm}^*(z'-1)c]}{m\pi\alpha_n\beta_{nm}^* \sinh(\beta_{nm}^* c)} \right\} \tag{2.57}$$

where $\beta_{nm}^* = \sqrt{\alpha_n^2 + \frac{m^2\pi^2}{b^2}}$, $D_m^* = \sin(m\pi\mu_3)$ and μ_3 is the fraction of the impact zone on z'. The pressure impulse distribution has been evaluated around the domain on the impact wall $x' = 0$, the side wall $z' = c$ and the bottom of the domain $y' = 0$ for a tank of dimensions $b = 1$, $c = 2$. This example is symmetric about the diagonal $x' = z'$.

A contour map of the pressure impulse distribution for type Corner on one of the impact walls $x' = 0$ in figure 2.24 shows a region of substantial pressure impulse values where the impact has occured, higher than those shown in figure 2.20 for type II. The

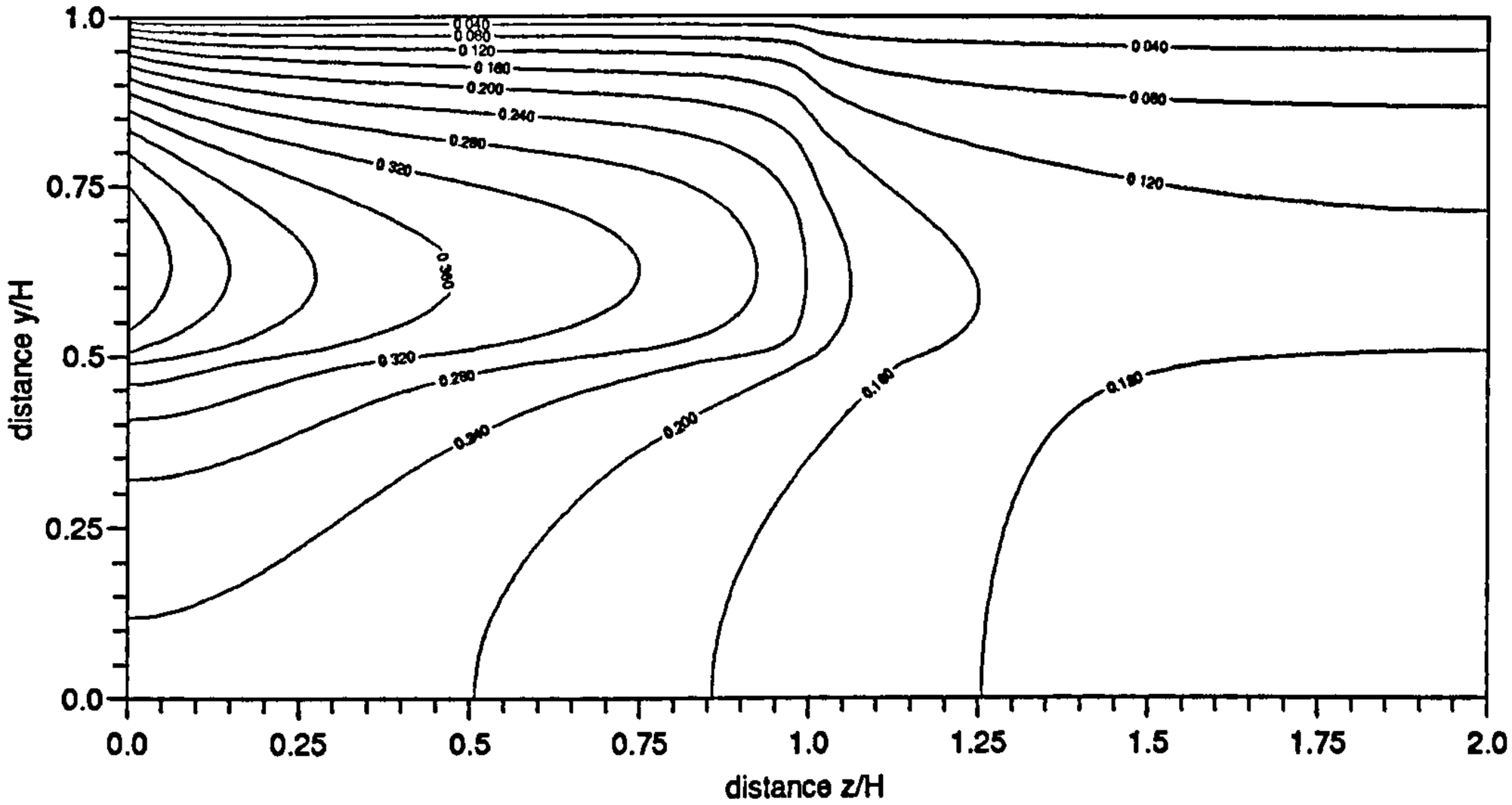

Figure 2.24: Pressure impulse contours $P/\rho U_o H$ on one of the impact walls $x' = 0$ for type Corner with dimensions $b = 1$, $c = 2$. Contour lines have been drawn with equal increments of 0.04.

maximum pressure impulse in this example is 0.52 $\rho U_o H$ at a height $0.64H$. Again a steep gradient is shown at the edges of the impact zone, although noticeable pressure impulse values are still obtained below the impact zone. As the impact occurs on the same size impact region on the two planes, the pressure impulse distribution on the plane $z' = 0$ will be identical to that on the plane $x' = 0$.

The pressure impulse distribution on the side wall $z' = c$ produces slightly lower values than for type II as the impact region is now further away. The maximum pressure impulse is $0.14\rho U_o H$ at a height $0.59H$. The thicker contour line for 0.02 indicates an alternative free surface. As the model for type Corner is symmetric along the diagonal $x' = z'$, the pressure impulse distribution on the end wall $x' = b$ as in figure 2.25 will be identical to that for the side wall $z' = c$. Thus the pressure impulse distribution on the end wall $x' = b$ will produce higher values than the end wall for type II.

The pressure impulse distributions show prominent values along the bottom of the tank for type Corner as demonstrated in figure 2.26, greater than the values obtained for type II as presented in figure 2.22.

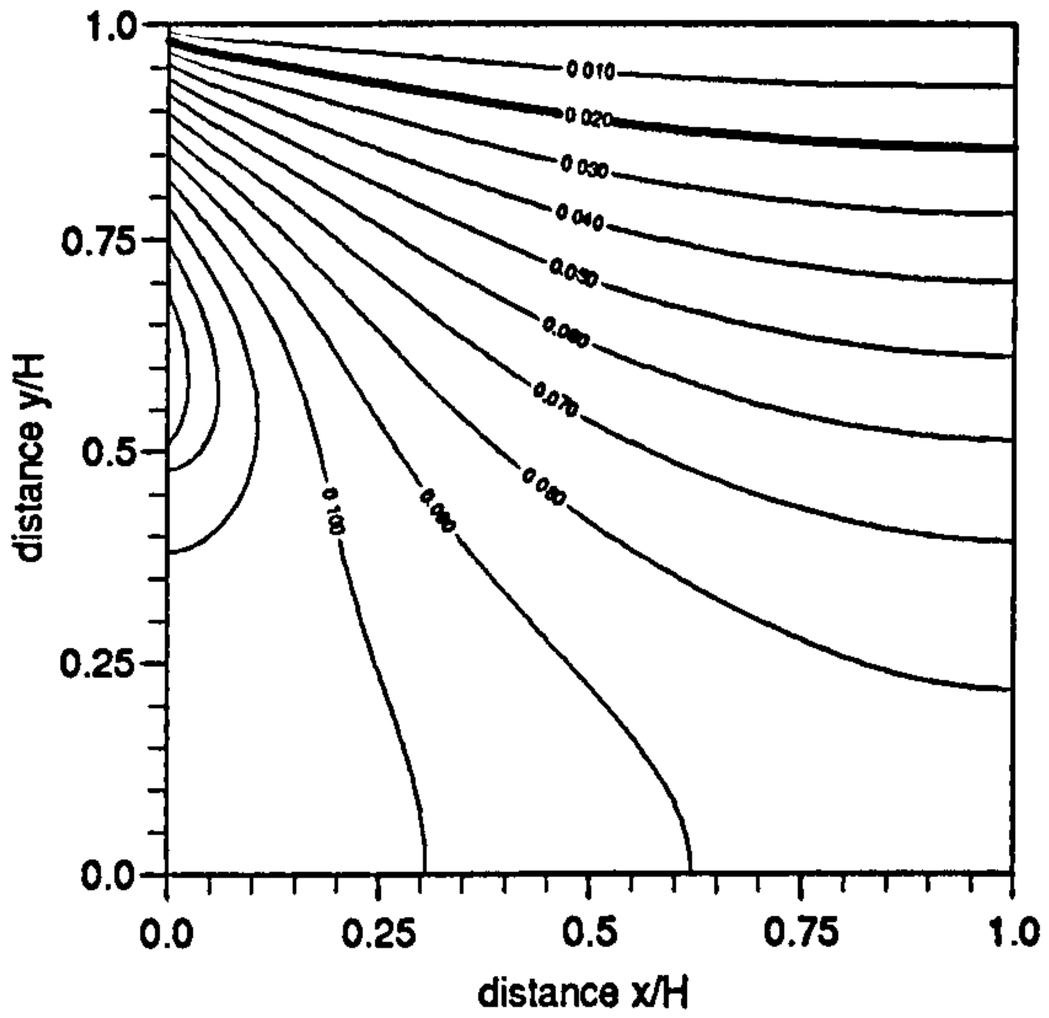

Figure 2.25: Pressure impulse contours $P/\rho U_o H$ on the side wall $z' = c$ for type Corner where $b = 1$, $c = 2$. Contour lines have been drawn with equal increments of 0.01. The contour line for 0.02 has been highlighted.

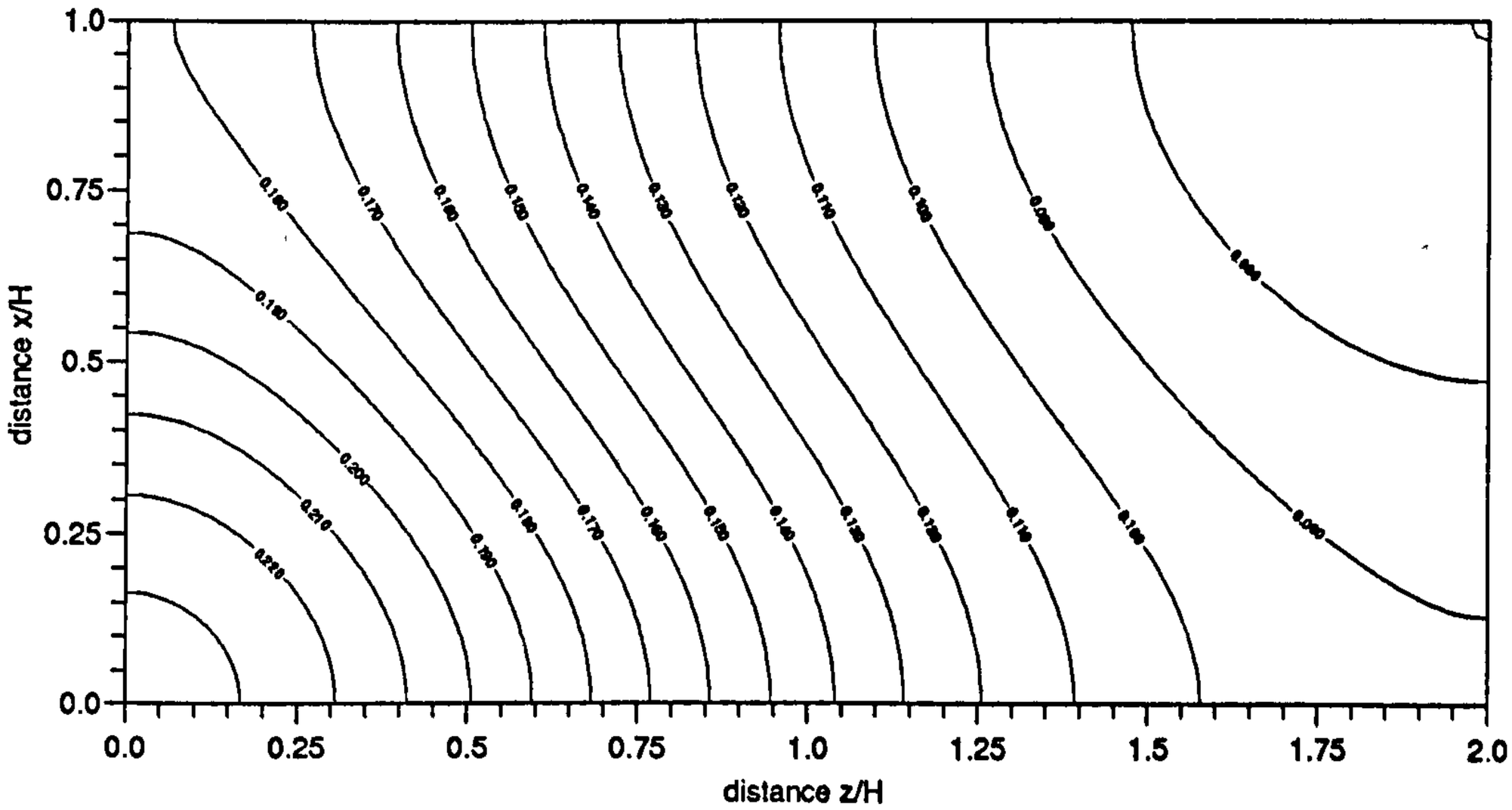

Figure 2.26: Pressure impulse contours $P/\rho U_o H$ on the bottom of the domain $y' = 0$ for type Corner where $b = 1$, $c = 2$. Contour lines have been drawn with equal increments of 0.01.

2.8 Comparisons of Geometry

From the solution for the pressure impulse, it can be seen that if $\mu_2 = 1$, the whole width of the impact wall, then the second part in the solutions for the pressure impulse becomes zero and the expression reduces to the two-dimensional solution, equation 2.6, for a model with a rigid bed and walls in a confined space. To study the effects of three-dimensions, the pressure impulses have been evaluated for the two-dimensional case, type I-IV and type Corner.

As pictured in figure 2.27, the pressure impulses will be highest in the centre of the impact area. The lowest pressure impulses are produced by type I which corresponds to the smallest impact region as expected. Comparisons between type II and type IV show the effect of the position of the impact region. In each case the impact zone is the

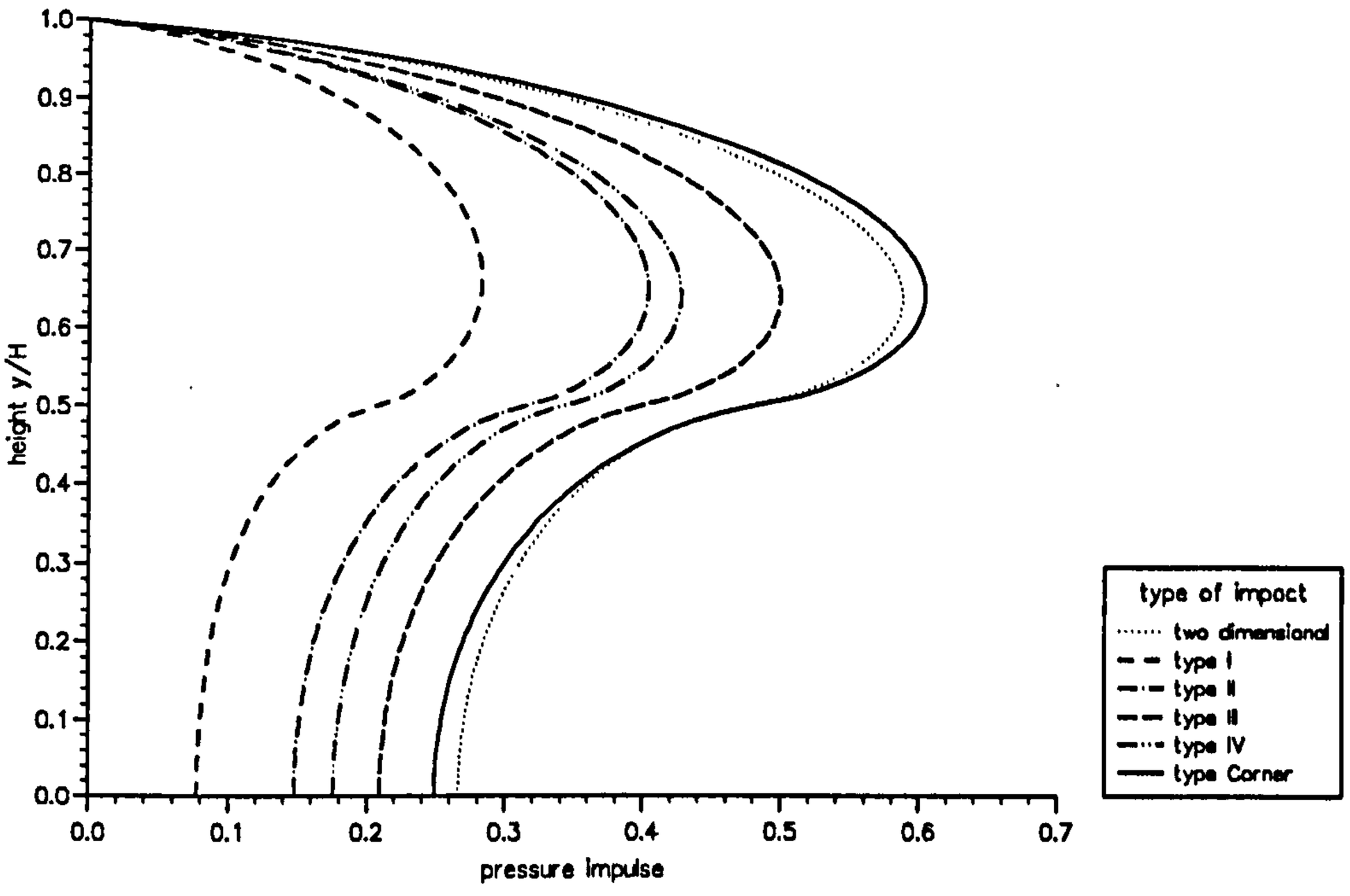

Figure 2.27: Pressure impulse $P/\rho U_o H$ on the impact wall $x' = 0$. For type I-III evaluated on the line $z' = c/2$ where $c = 2$, and for type IV and type Corner evaluated on the line $z' = 0$. The width is $b = 2$ for all types.

same size but type IV, which has the region situated next to a corner, results in slightly higher pressure impulses. Those produced by type III, which has a larger impact zone

but is situated in the middle of the tank are greater than for types II and III. The two-dimensional geometry produces the largest pressure impulses for the instances when there is impact on one wall only. For the example shown in figures 2.27, the distribution from an impact on two adjacent walls, type Corner, is similar to the pressure impulses in the two-dimensional impact. Note the pressure impulse for type Corner has been evaluated on $x' = 0$ with $\mu_2 = \mu_3 = \frac{1}{2}$ and so the impact region in both the two-dimensional and the Corner impact is of length 1 and so the similarity in solution is perhaps not surprising.

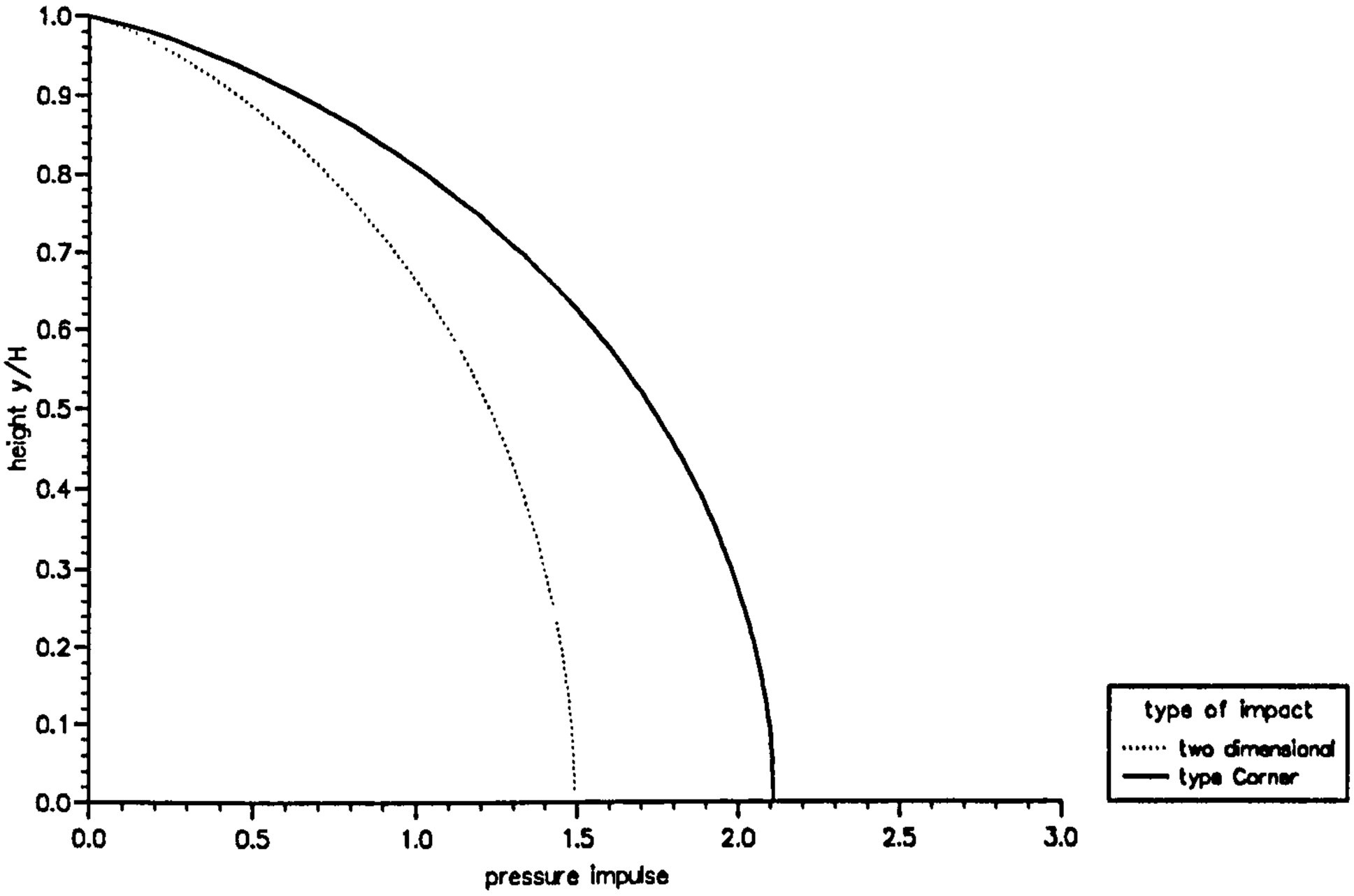

Figure 2.28: Pressure impulse solution $P/\rho U_o H$ for the two-dimensional rectangular domain and a type Corner impact, where the impact region is the maximum area, $\mu = \mu_2 = \mu_3 = 1$ for dimensions $b = c = 2$, with the impact region covering the entire impact wall(s).

For large impacts, the pressure impulse solution for the impact on two walls now gives greater values than for the two-dimensional solution. In figure 2.28, a type Corner impact has been evaluated on $x' = 0$ and this results in equal contributions for the pressure impulse from both parts of the solution. As the impact region has been taken to cover the whole of the impact walls, i.e. $\mu = \mu_2 = \mu_3 = 1$, this results in double the impact area for type Corner in comparison with the two-dimensional case.

Thus taking into account the altered impact velocity, this gives the total pressure

impulse solution for type Corner to be a factor $\sqrt{2}$ greater.

2.9 Total Impulse

The total impulse on the impact wall $x' = 0$ can be found by integrating the solution for the pressure impulse with respect to y' and z' over the whole wall. For type I-IV this reduces to:

$$I_w = 4c\rho U_o H^3 \sum_{n=0}^{\infty} C_n(-1)^n \left\{ \frac{\mu_2 cH}{\alpha_n^3 \tanh(\alpha_n b)} + \sum_{m=1}^{\infty} \frac{2AD_m \sin(m\pi/2)}{(m\pi)^2 \alpha_n^2 \beta_{nm} \tanh(\beta_{nm} b)} \right\}$$

where I_w is the total impulse on $x' = 0$. For type Corner the total impulse on the impact wall $x' = 0$ is $\frac{1}{\sqrt{2}}[I_w + I_w^*]$ where:

$$I_w^* = 4\rho U_o H^3 \sum_{n=0}^{\infty} C_n(-1)^n \left\{ \frac{\mu_3 bH}{\alpha_n^4} + \sum_{m=1}^{\infty} \frac{A\, D_m^*}{m\pi \alpha_n^2 \beta_{nm}^{*2}} \right\}$$

The solution for the total impulse on the wall $x' = 0$ for the types previously considered is portrayed in figure 2.29. As indicated from the pressure impulse solutions, the two-dimensional solution produces the greatest impulse compared with the three-dimensional results for an impact on one wall, resulting in the same solution as the three-dimensional solution when $\mu = \mu_2 = 1$ as expected. For type Corner however, the total impulse on the impact wall $x' = 0$ is less than that due to the two-dimensional solution. For an impact covering the whole of the impact wall(s), the contribution from the first part of the solution for type Corner is a factor $\sqrt{2}$ less than the two-dimensional solution as when calculating the peak pressure impulse. However the contribution from the second part of the solution, the effect of the impact on the adjacent wall on the total impulse on the wall $x' = 0$, is now not equal to the first part of the solution as previously but lower, therefore resulting in an overall lower total impulse over the whole wall.

2.10 Change in Liquid Velocity

The change in vertical velocity of the liquid immediately after impact has been calculated using

$$V = \frac{1}{\rho} \frac{\partial P}{\partial y} \tag{2.58}$$

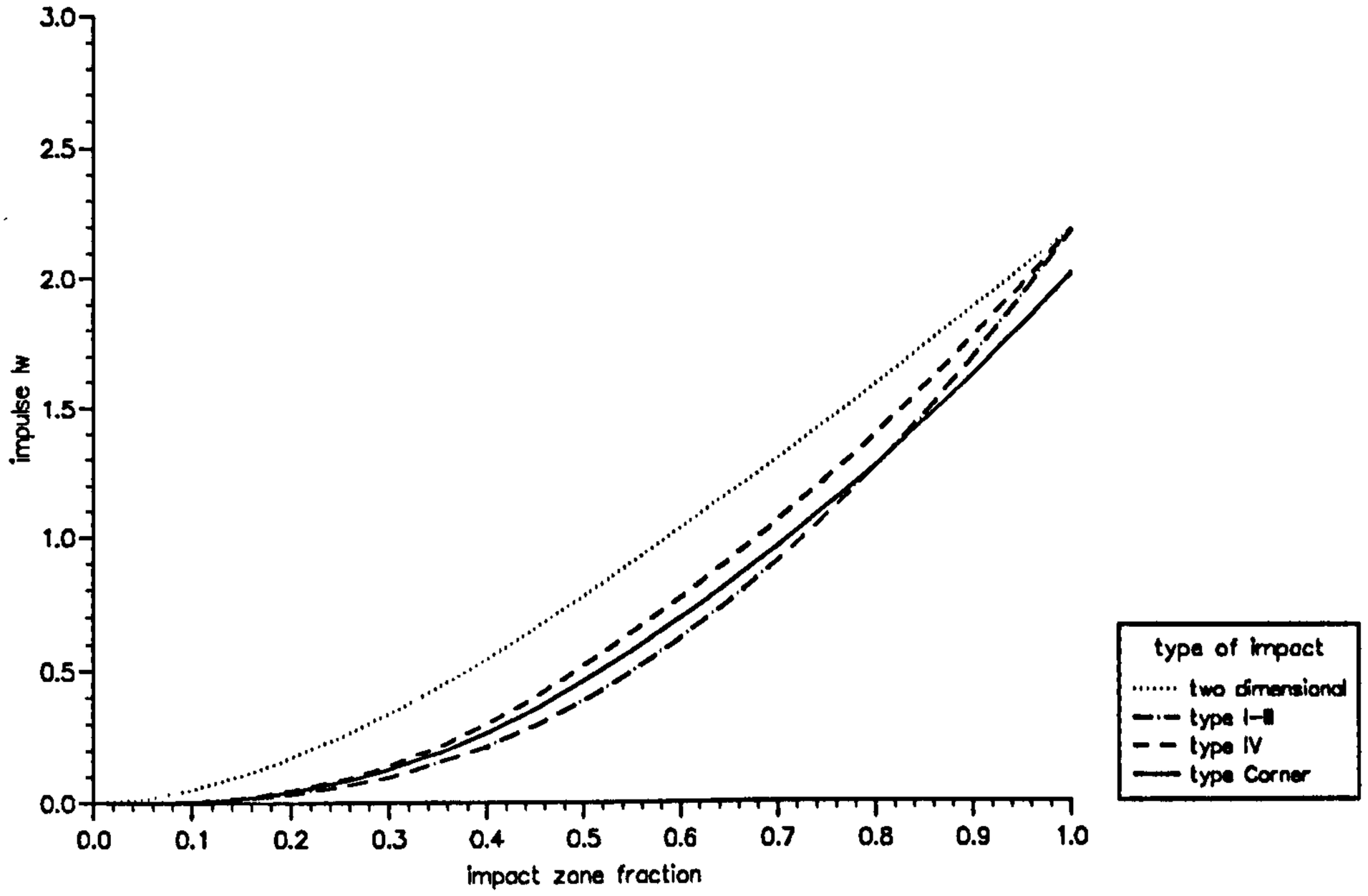

Figure 2.29: Total impulse $I_w/\rho U_o H^3$ on impact wall $x' = 0$ for the two-dimensional case and type I-IV for different values of $\mu = \mu_2$ and total impulse $(I_w + I_w^*)/\rho U_o H^3$ on the impact wall $x' = 0$ for type Corner for different values of $\mu = \mu_2 = \mu_3$ with $b = c = 2$.

as in section 2.3.

The change in vertical velocity of the free surface after the impact has been evaluated using the general expression below for the types I-IV of impacts discussed:

$$V = 4U_o \sum_{n=0}^{\infty} C_n(-1)^n \left\{ \frac{\mu_2 cH \cosh[\alpha_n(x'-1)b]}{\alpha_n \sinh(\alpha_n b)} \right.$$

$$\left. + \sum_{m=1}^{\infty} \frac{A\, D_m \cos(m\pi z') \cosh[\beta_{nm}(x'-1)b]}{m\pi \beta_{nm} \sinh(\beta_{nm} b)} \right\} \tag{2.59}$$

and for type Corner the expression for the change in vertical velocity is $\frac{1}{\sqrt{2}}[V + V^*]$ where

$$V^* = 4U_o \sum_{n=0}^{\infty} C_n(-1)^n \left\{ \frac{\mu_3 bH \cosh[\alpha_n(z'-1)c]}{\alpha_n \sinh(\alpha_n c)} \right.$$

$$\left. + \sum_{m=1}^{\infty} \frac{A\, D_m^* \cos(m\pi x') \cosh[\beta_{nm}^*(z'-1)c]}{m\pi \beta_{nm}^* \sinh(\beta_{nm} c)} \right\} \tag{2.60}$$

Immediately after impact the free surface rises with the highest change in velocities acting near the vertical wall as demonstrated in figure 2.30. Note only a small portion

of x/H has been shown. The change in vertical velocities on the free surface predicted by the two-dimensional theory are only slightly higher than those for a three-dimensional impact of type I-IV. For an impact in a corner on two walls however substantial speeds are produced over a large area. At x'=0, the expressions for V have a weak logarithmic singularity which has not been included in the graphs.

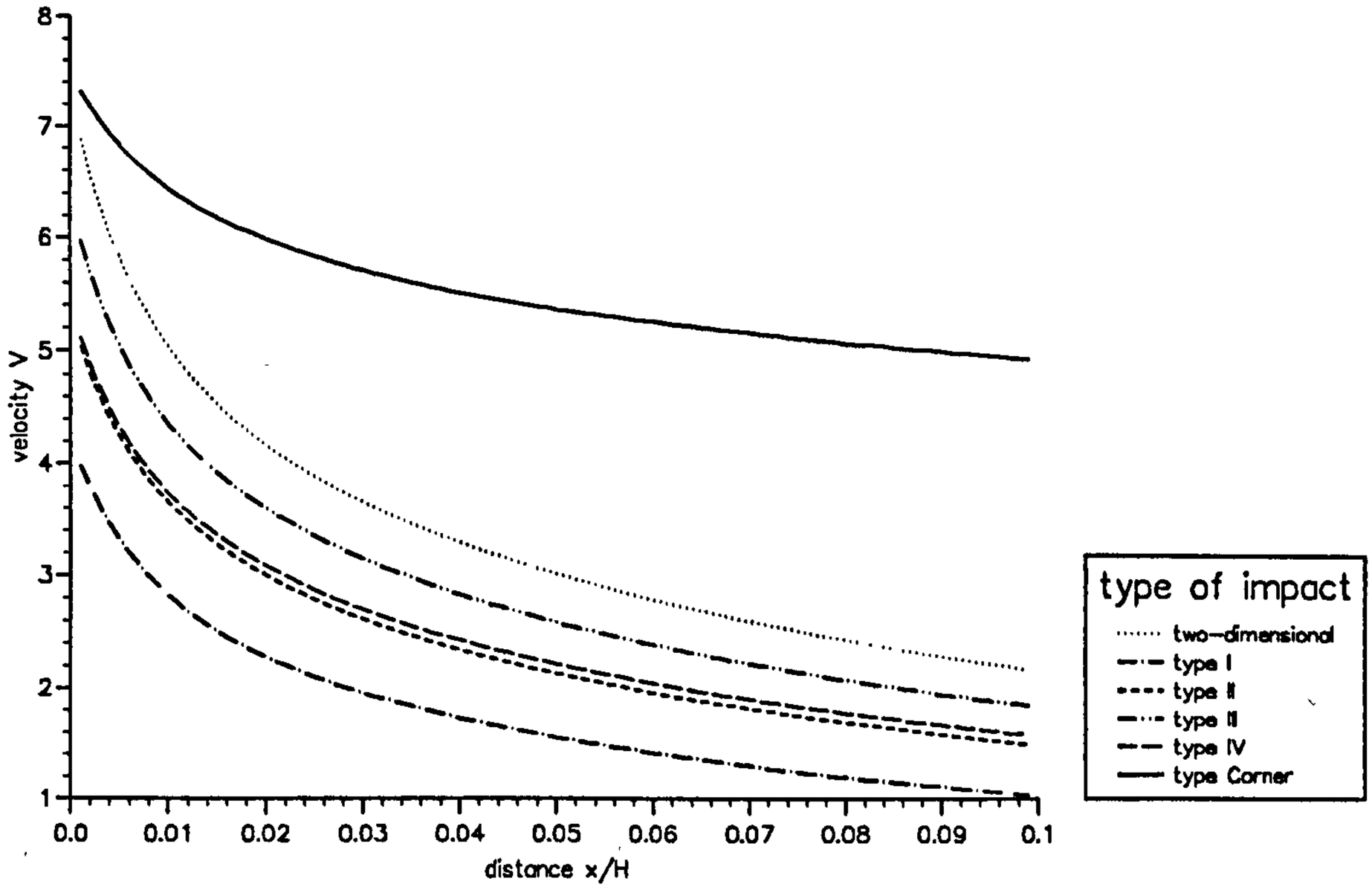

Figure 2.30: Change in vertical velocities V/U_o on free surface immediately after impact for domains with dimensions $b = c = 2$. μ=0.5 in all cases. Types I-III evaluated along $z' = c$ and type IV and type Corner evaluated along $z' = 0$.

Chapter 3

Entrained Air

3.1 Introduction

The work in this chapter explores how to model entrained air present in water-wave impacts upon a vertical wall. An initial review is provided in section 3.2 of experimental studies investigating air entrainment in water-wave impact on vertical structures. Aeration in wave impacts has been described in the laboratory experiments as either a cloud of small air bubbles in the water adjacent to the vertical structure or as a single air pocket trapped between the overturning wave and the impact wall.

Dold & Peregrine (1986) and Dold (1992) have described a numerical boundary-integral method to compute the two-dimensional motion of an unsteady, incompressible, irrotational water surface, including that describing breaking waves. Section 3.3 applies this numerical method, with appropriate initial conditions giving a prescribed surface profile and corresponding velocity potential, to model an overturning wave trapping a single air pocket between the oncoming wave front and the vertical wall. Several examples are presented with different sizes of trapped air pockets showing the change in characteristics of the motion in relation to the volume of air trapped. Two different incident waves are studied. The resulting detailed computations provide suitable initial parameters for a simple theoretical model.

Section 3.4 and 3.5 present some simple analytical modelling of the trapped air, in the form of a single bubble and as a mixture of bubbles and water. Using a conformal transformation, the trapped air pocket is modelled as a two-dimensional semi-circular

bubble and, using the method of images, the potential for the flow due to free oscillations of the air pocket is evaluated. An expression for the fundamental frequency of the bubble is obtained. The entrained air is also modelled as a rectangular bubbly mixture next to the impact wall. From the analysis, trapped modes of oscillation are found and compared with the fundamental frequencies given by the single bubble.

Video frames of small-scale experiments by Hattori & Arami (1992 and private communications) and Hattori, Arami & Yui (1994) for an overturning wave trapping an air pocket are examined in detail. These can be compared with computations from section 3.3 which provide the same size air pocket. From the analytical theory, the resulting peak pressures can be predicted and compared with those given by Hattori et.al.

The pressure impulse theory described in chapter 2 can estimate the peak pressure on the impact wall if the duration of the impact is known. By suggesting a means of estimating the timescale of the impact, the peak pressures for examples of trapped air pockets are predicted and compared with the values given by the computations. The majority of experiments undertaken to study wave impact are performed in small-scale tanks and a discussion of scaling from model to prototype completes the chapter.

3.2 Literature Review

One of the earliest investigators, Bagnold (1939), described two types of pressures that are exerted by waves on seawalls, the first due to the wave not actually breaking but deflecting the water upwards, and the second due to the breaking wave, which is of interest in this study. The experiments, undertaken in a wave tank measuring four feet by four feet, were confined to a single wave pulse driven forward along a flat bottomed channel and made to break against a vertical wall by means of a sloping beach. Bagnold recounted a breaking wave enclosing a large cushion of air between the wall and the lower part of the wavefront. The air was compressed and burst upwards with a low booming sound and spray. For a thinner air cushion, the noise was higher and sharper. Bagnold suggested the water column could be regarded as a heavy free piston which compresses the air column adiabatically. It was noted that impact pressures only occurred when air was enclosed; for no air enclosed, no noise or impact was observed. The presence of enclosed air resulted in lower maximum pressures than with no enclosed air, but these

lower pressures lasted for a longer time and over a wider area of the impact wall. The impact pressures increased in intensity with decreasing thickness of the air pocket. The high pressure peaks and maximum pressure-time areas only occurred over the area of the air cushion, below which the pressures decreased rapidly. The impulse, however, was independent of the air thickness.

An experimental investigation of the pressures exerted by waves breaking against a vertical structure by Denny (1951) provided further data in support of Bagnold's theory. The pressure measurements appeared to be constant over the area that was covered by the trapped air and decreased to a very small value in the water below. Pressure peaks were recorded whenever the waves began to break at a certain distance from the vertical structure so that the wavefront was approximately plane parallel to the impact wall.

Hayashi & Hattori (1958) undertook a series of experiments in a wave tank 14 metres long and 86 centimetres deep, using five pressure cells and a high speed motion-camera to compare the pressure readings with the behaviour of the flow. A sharp initial rise of pressure was recorded followed by a second longer period with the motion-picture showing the impact of the breaker enclosing a thick air cushion.

From his experimental results, Mitsuyasu (1966) suggested that the fluctuating pressures recorded could be attributed to the oscillations of the air cushion. The period of the pressure oscillations was in the range 1 - 12 milliseconds and was damped out within approximately 40 milliseconds. The dynamical models indicated that the greater the impact pressure intensity, the shorter its duration and period of pressure oscillation. The original adiabatic air cushion model introduced by Bagnold was extended by Mitsuyasu in an endeavour to explain the distinct damping of the pressure oscillations which had been observed. This was modelled by assuming some air was leaking upwards along the wall with the spray, reaching fairly good agreement with high intensity impact pressures, but not in cases of low intensity impact pressures.

Using a wave flume of 80 centimetres depth, an experimental investigation of shock pressures against breakwaters was undertaken by Richert (1968), who observed that the pressure measurements were directly dependent on the behaviour of the wave immediately in front of the structure. In the presence of an air cushion, the pressure readings showed an initial peak followed by damped oscillations. A thicker cushion of enclosed air gave a lower pressure reading and a longer oscillation period.

Weggel & Maxwell (1970) modelled some details of acoustic wave propagation in their experimental and numerical study, using a wave tank of depth 60 centimetres and length 30 metres, with a 1:20 slope to cause the waves to break. Six pressure transducers were placed down the impact wall. Impact pressures of two types were defined, the first with a high pressure peak at one transducer location with little or no pressure recording at neighbouring transducers, and the second type with the impact pressures occurring almost simultaneously over the entire wall. A volume of air in the form of a bubbly mixture was observed after each impact and as little as 1 percent volume of air significantly reduced the sonic speed in water. Weggel & Maxwell made the assumption in their model that the air and water were uniformly mixed as opposed to Bagnold who had considered the air and water to remain two separate entities. The maximum dimensionless pressure was found to vary inversely with the thickness of the disturbed region. One of the conclusions reached was that the wave impact problem appeared to be dependent on the value of both the Froude number and the Mach number.

For breaking waves, Führböter (1970) remarked that, after the wave begins to break, the effect of aeration cannot be ignored and questioned how far scale model tests would be able to predict prototype tests. Führböter (1986) pursued some experimental tests in two channels to compare model and prototype impact. The smaller tank used as a model was on a scale of 1:10 with the larger tank. Führböter reported that a high air content gave longer duration and weaker pressures than for low air content. Bubbles of one centimetre diameter as well as numerous very small bubbles with diameters less than 1 millimetre were observed. Führböter concluded that the aeration effect seemed to be the most important contribution to all the scale effects observed.

Ramkema (1978) verified agreements between experimental data and the linear piston model initally described by Bagnold using a one metre deep wave channel. He extended the model to include adiabatic and isothermal compression of the air and to allow for the compression of water for the full scale pressures. Attention was drawn to the damping of the oscillations, already noted by previous studies.

The complex problem of scaling from laboratory model tanks to full-scale models was reviewed by Moutzouris (1979). Three main loading factors were identified: hydrodynamic impact, water mass and air entrainment.

Lundgren (1979) produced a report outlining research needs concerning wave impact

on breakwaters and possible means of reducing the large wave impact loads that occur. The discussion on scale effects mentioned the importance of determining the influence of air entrainment.

Full-scale measurements at seawalls were studied by Blackmore & Hewson (1984) who discussed comparisons with previous experiments and formulae. The impact pressures measured were generally lower than those measured by other full-scale experiments and this was suggested to be due to the high percentage of air entrained.

Breaking wave impact on a vertical wall was one of several experimental setups studied by Witte (1988), who measured the pressure fluctuations with fourteen pressure cells placed along the impact wall. One particular case recorded showed clear damped oscillations with a period of 1.2 milliseconds. The corresponding diagrams indicated a large air pocket trapped against the impact wall. The damped oscillations occurred over the whole area of the wall and were time-synchronous which could effect the design of the breakwater if the frequencies are near to the natural frequencies of the structure. Comparison of the data with the theoretical results of Führböter gave good agreement and the experimental data showed the probability distribution of the highest pressures could be described by the log-normal distribution.

Chan & Melville (1988) undertook experiments in a long wave tank of depth 90 centimetres to describe the impact process resulting from a plunging breaker in deep water against a vertical wall. The pressure oscillations recorded were centred at the area of wave impact where the air was entrapped. They were in phase with several of the transducers up the wall, showing a decreasing amplitude away from the wave impact zone, thus indicating that trapped air dynamics play a role in determining the impact pressures. Both the frequency of oscillation and the zone where the pulsating pressures occurred appeared to be related to the volume of air trapped at impact. Locations on the wall where there was significant air entrapment gave oscillations between 300 - 800 Hertz. Reducing the amount of air trapped led to a higher oscillation frequency. Chan & Melville also conducted experiments on a smaller characteristic length-scale and recalled that the low frequency pressure fluctuations observed in the large-scale experiments were not present on the smaller scale.

In order to explore the importance of an air pocket trapped between the breaking wave and the structure, Arami & Hattori (1989) engaged in a series of experiments in a small

scale model with a still water level of 5 centimetres. The air cushion was shown to be a dominant mechanism in determining peak pressures due to breaking waves. The pressure values were recorded at intervals of half a millisecond. The high speed video recordings clearly demonstrated the wave curling over, trapping a large semi-circular volume of air against the impact wall. The frequencies recorded were in the range of 90 - 150 Hertz.

The four types of breakers that occur against a vertical structure have been summarised by Oumeraci & Partenscky (1991a) as a) turbulent bore, b) well-developed plunging breaker with a large air-cushion, often resulting in a low booming sound as noted by Bagnold, c) plunging breaker with a small air-cushion, often accompanied by a higher and sharper sound, and d) upward deflected breaker. The different types of breaker give different impact loads with different characteristics. An investigation on the effect of the entrapped air on the dynamic response of the structure was studied by Oumeraci & Partenscky (1991b) using a large scale wave flume. For large air pockets, low frequencies were recorded. The resonant frequency of the breakwaters was in the range of 5 - 20 Hertz. Oumeraci & Partenscky described swaying and rocking motions by the caisson caused by the wave impact on the structure and noted that, although the effect of the enclosed air was found to cause damping of the shock pressures, this did not necessarily apply to the dynamic response of the structure. A clear double-peak horizontal force was recorded during the experiments, the first due to the initial impact by the wave and the second due to the subsequent compression of the air pocket caused by the advancing wavefront. If the second peak had occured within the time $t < T/4$ or $3/4\ T < t < T$ where T is the period of the oscillation of the structure, whilst the caisson was moving shoreward in response to the initial peak, the overal response of the caisson could have been much greater. Oumeraci et.al. recorded the second peak to occur within the time $t < T/4$. A relationship was presented between the period of pulsations and the incident wave height. This was shown to give relatively good agreement with small and large-scale tests. The pulsation period of the entrapped air in the experiments was in the same range as the natural period of the rocking motion of the caisson used.

A laboratory study of plunging wave impacts on cylinders by Zhou, Chan & Melville (1991) showed considerable variation of the high impact pressures produced and suggested this could be partly attributed to entrained air. Impact pressures were characterized by maximum pressure peaks followed by oscillations. For two repeated runs, differences were

noted in the impact region for the impulsive pressures and frequencies of oscillations.

Tanizawa & Yue (1992) have begun numerical computations of a plunging wave trapping an air pocket against a wall for two-dimensional incompressible motion making comparisons with the experimental results of Chan & Melville and obtaining good agreement for the maximum impact pressures.

In order to determine the damping effect of air enclosure on the pressures resulting from the waves breaking against a vertical structure, Zhong, Schulz & Witte (1992) used an arrangement of grid cells placed against or very close to the breakwater, in a long wave channel of depth 1.25 metres, to represent artifical air pockets. Different sizes of grid were employed and the grid structure was either placed against the wall or with a spacing of 0.2 - 0.5 centimetres to enable water and air to escape behind the grid thus eliminating additional air content due to the grid. Up to fourteen pressure transducers were used to record the fluctuations. When the gaps between the walls and grids were sealed against air and water, damping of the maximum impact pressure was observed. The tests demonstrated that the smaller the grid size, the more prominent the effect was in reducing the peak value of impact pressures. Allowing a space of 5 millimetres between the wall and the grid resulted in an enlargement of impact pressures. Following the peak value of the maximum pressure, a secondary pressure distribution was recorded with a longer duration of the pressure history. A smaller grid size also resulted in a higher damping effect of the integral force. Schulz (1992) continued the study, calculating the impulse acting upon the structure, obtained by integrating the time history of the pressure. The results showed the impulse was amplified by the grid compared to a smooth wall. This was due to the increasing rising time of the pressure with increasing air contents.

Graham & Hewson (1992) present preliminary results of model scale measurements of the aeration caused by a wave overturning on the beach entraining a large cushion of air as it travels towards the wall. This is the turbulent bore described by Oumeraci & Partenscky. Results indicate aeration levels of the order 5 - 20 percent and frequency ranges of 100 - 300 Hertz.

Large scale model tests were undertaken by Schmidt, Oumeraci & Partenscky (1992) continuing previous work by Oumeraci & Partenscky (1991b) on the stability of the vertical structure during impact. In the instances of well-developed plunging breakers with large volumes of entrapped air, this leads to a total impact force with a large duration

time for the corresponding impact pressures. The critical instance is when the duration reaches the natural period of oscillation of the breakwater. Negative pressures were recorded, attributed to the effects of the expanded air, and double peaks found in the horizontal force history. The large volume of air entrapped led to low frequency vibrations. In addition, Oumeraci, Klammer & Partenscky (1993) studied the characteristics and pressure distributions for the four types of breaker shapes previously mentioned. The third case, described before as the plunging breaker with a small cushion of air, resulted in relatively high impact pressures occuring almost simultaneously over a large area. This case produced the impact force with the highest intensity, the pressure distribution having a high initial peak followed by oscillations. It was noted that the higher the frequencies, the smaller the air cushion appeared.

Hattori & Arami (1992 and private communications) have provided us with many details of their experiments, which were conducted in a small wave tank, including high speed video frames from which measurements can be analysed along with the corresponding pressure histories. The records from the six pressures gauges portray simultaneous smooth damped fluctuations following the inital peak value. The cases described by Hattori & Arami include large air pockets of 1-2 centimetres radius and frequencies in the region of 100 Hertz. Data presented showed the maximum peak pressure and oscillation frequency to decrease with increasing air pocket thickness. Following on from this work Hattori, Arami & Yui (1994) described various types of breaking wave impacts on vertical walls observed in their experiments. For a plunging wave trapping a thin air pocket, high impact pressures of short duration and pressure oscillations of 625 Hertz were recorded suggesting these were due to the thin layer of bubbly water compressing and expanding. For a fully developed plunging breaker, the paper described a two-dimensional air pocket of width 1.1 centimetre with corresponding oscillations of 210 Hertz. The air pocket then broke up into smaller bubbles which eventually rose to the free surface. Unlike the maximum peak pressure, the shock impulse was found to increase with the air pocket dimension.

3.3 Numerical Computations

The numerical boundary-integral method used in this thesis for computing the two-

dimensional motion of an unsteady water surface, including that for breaking waves, is found in Dold & Peregrine (1986) and later in Dold (1992).

The fluid is taken to be incompressible so that from the continuity equation with constant density this gives $\nabla.\mathbf{u} = 0$. For an irrotational flow, a velocity potential can be defined such that $\mathbf{u} = \nabla\phi$. These can be combined to give Laplace's equation:

$$\frac{\partial^2\phi}{\partial x^2} + \frac{\partial^2\phi}{\partial y^2} = 0 \tag{3.1}$$

with the boundary condition $\partial\phi/\partial y = 0$ on the impermeable bed at $y = -h$. The fluid is taken to be steady at infinity. The free surface kinematic condition, for a point on the free surface to move with the free surface, described by $(x, y) = [X(\xi, t), Y(\xi, t)]$ is

$$\nabla\phi = \left(\frac{\partial X}{\partial t}, \frac{\partial Y}{\partial t}\right). \tag{3.2}$$

The non-linear free surface dynamic condition is

$$\frac{\partial\phi}{\partial t} + \frac{1}{2}\left[\left(\frac{\partial\phi}{\partial x}\right)^2 + \left(\frac{\partial\phi}{\partial y}\right)^2\right] + gY = 0 \tag{3.3}$$

where the pressure immediately above the free surface is taken to be a constant and surface tension is neglected.

The surface profile and velocity potential are prescribed on the free surface as initial data. The domain is reflected about the bed $y = -h$ to form a symmetric flow where a point on the upper free surface has an image on a lower free surface. The free surface boundary conditions are satisfied at the free surface which moves with time. The surface of the fluid is considered to be a smooth continuous profile approximated by a set of discrete points. Then a truncated Taylor series is used to perform the explicit time-stepping for appropriately small time steps, as the convergence of the series depends on the size of the timestep. Cauchy's integral theorem is used to obtain a boundary-integral equation for the evaluation of multiple time-derivatives of the surface motion. After the unsteady surface motion is calculated, the velocity and pressure beneath the surface can be evaluated at points over a rectangular grid.

To use this numerical program to model entrained air, suitable initial conditions have been chosen to simulate a wave travelling towards a wall, steepening and overturning, trapping an air pocket between the oncoming wave and the wall. The presentation and discussion of the numerical computations has been divided into two sections where the

initial profiles of the wave have been chosen to be of the form of 1) a tanh curve and 2) a solitary wave. With appropriate initial parameters, both of these waveforms can be made to overturn. In each section, the initial data is discussed and examples given to illustrate the numerical results.

Variables are scaled accordingly: $y^* = y/h$, $x^* = x/h$, $p^* = p/\rho gh$, $t^* = t\sqrt{g/h}$, $u^* = u/\sqrt{gh}$ and $A^* = Ag$ where h is a chosen value and $*$ represents the scaled variables.

3.3.1 Computations for an overturning 'tanh' wave.

Using this boundary-integral method for a non-periodic surface, Cooker (1990) has described the motion of a wave overturning immediately before a vertical wall (with a finite depth), trapping a pocket of air against the wall. This was achieved by allowing two equal waves propagating in opposite directions towards each other to form a flow which is symmetric about a plane. This is equivalent to a single wave approaching a vertical wall. The initial data used was obtained from a tanh expression describing a long wave of elevation:

$$u(x) = -\frac{1}{2}u_o\left\{1 + \tanh\left[\frac{(x - x_o)}{s}\right]\right\} \tag{3.4}$$

where x_o is the initial centre of the wave, u_o is the initial maximum velocity, and s is a constant. The wave elevation is of the form $\eta(x) = |u| + \frac{1}{4}u^2$. The initial potential of this tanh wave, assuming it is propagating towards the wall and gentle enough to satisfy the shallow water equations, is

$$\phi(x) = -\frac{1}{2}u_o\left\{x + s\log\left[\cosh\left(\frac{x - x_o}{s}\right)\right]\right\}. \tag{3.5}$$

The long shallow water-wave steepens and breaks as it propagates into water of constant depth, for an example see the surface profiles in figure 3.1. The following examples build on the preliminary work by Cooker (1990) for an overturning wave, to study the characteristics of the motion of a trapped air pocket. The computations have to stop just before the wave jet comes into contact with the wall and so the results only describe the motion immediately before impact.

With appropriate initial parameters, three examples have been studied in this section of a wave overturning immediately in front of a vertical wall using different initial positions of the wave to give different size air pockets. This illustrates the different characteristics

of the motion due to the volume of air trapped. In this section, h is the lowest water depth at the wall. Between 250-350 discretisation points were used to describe the surface of the wave and its image, with a tolerance (the error parameter for the timestepping) of 0.00001. The initial depth is 1.0 and the wave is taken to have a large initial amplitude of 1.7 with $s = 2.0$. Surface profiles are presented for several timesteps and the pressure contours below the free surface have been evaluated for the final computed time in each case.

Example 1

The first example presented is for a wave of initial amplitude 1.7 on a depth of 1.0, with an initial distance from the wall of $x_o = 8.0$.

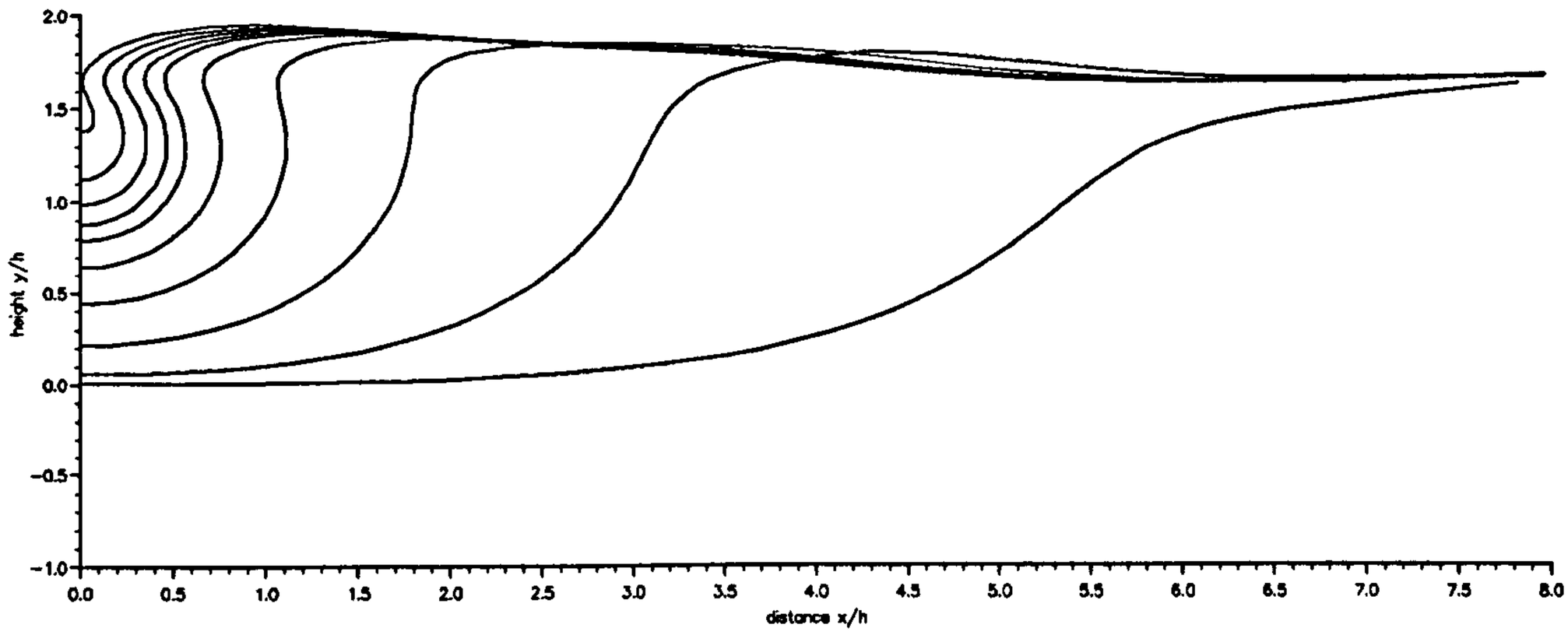

Figure 3.1: Surface profiles for a tanh waveform of initial amplitude 1.7, initial distance 8.0. s=2.0, depth 1.0, at times 1.53, 2.81, 3.45, 3.77, 3.93 and 4.01 - 4.17 in steps of 0.04.

The wavefront steepens as it approaches the wall and begins to overturn as portrayed in the time history of the surface profiles in figure 3.1. The timesteps in the numerical program and in the surface profiles shown are reduced as the wave becomes steeper, the surface curvature increases and the motion becomes more concentrated. The computations stop just before impact with the wall and a small pocket of air is trapped between the wave front and the wall immediately before impact.

The pressure field under the free surface can be evaluated and figures 3.2, 3.3 and 3.4 show the pressure contours, with the same increments of 0.4 in each case, under the free surface at the final three computed times in timesteps of 0.02, where the thickened line represents the water surface.

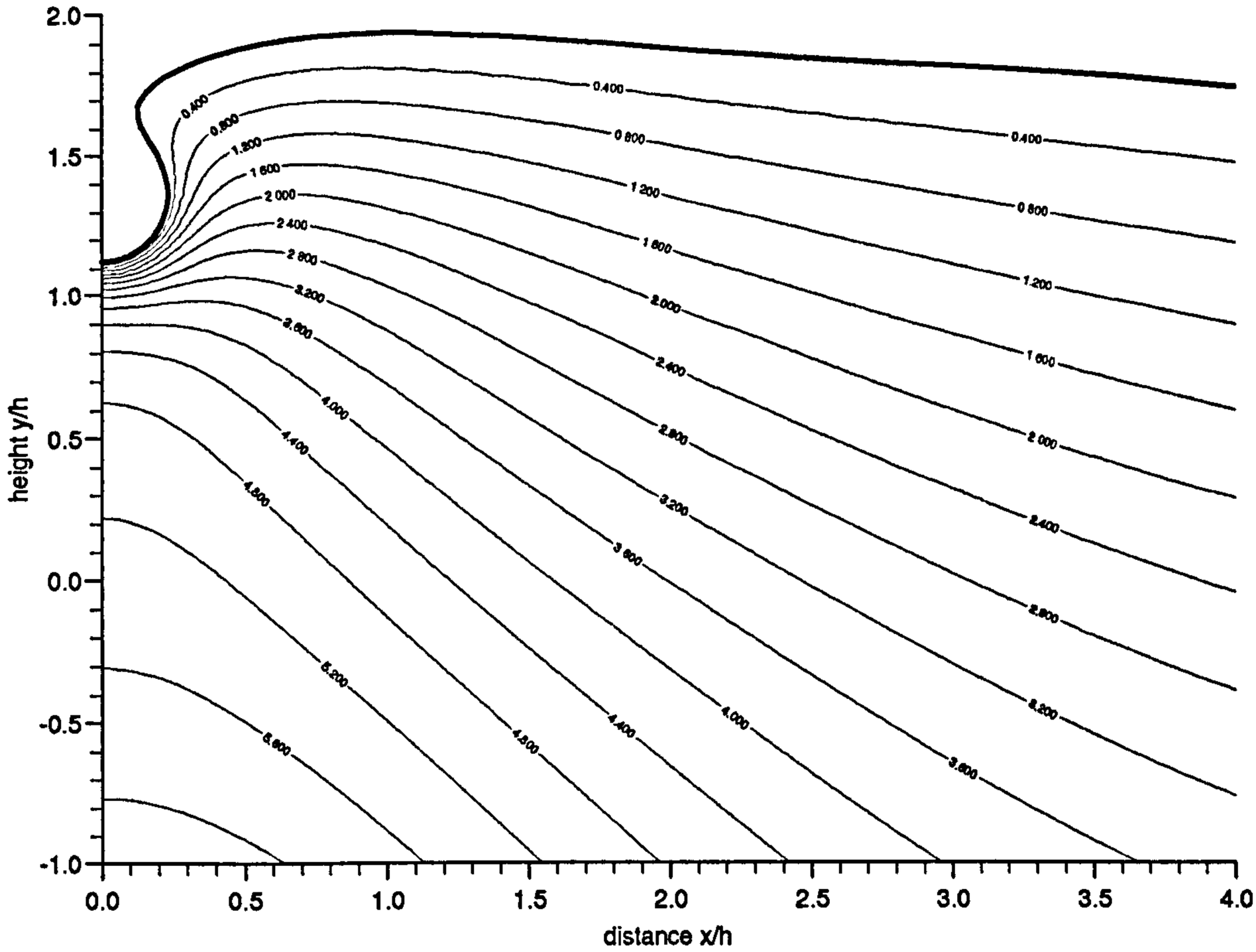

Figure 3.2: Pressure contours for a tanh waveform of initial amplitude 1.7, initial distance 8.0, s=2.0, depth 1.0, at time 4.13 with increments of 0.4.

A region of high pressure is shown near the wall in each case. Note the rapid change in the pressure field as the wave comes nearer to the impact wall. At time 4.13, the greatest pressures are found at the bed of the wall. At time 4.15, the greatest pressures are still to be found at the bed but the values have increased and the isobars near the wall have become steeper and more densely packed around the curved free surface. The pressure contour lines for the highest values continue to steepen near the wall as time increases until the final computed time, 4.17, when as well as high pressures at the foot of the wall, a region of much higher pressure is now found just below the waterline with very tightly packed contour lines. In the computations to evaluate the pressure field, a denser grid is now required to produce smooth contours. Note that no direct impact between the water

and the wall has yet occurred. The high pressures are spread over a substantial area of the domain in all three figures.

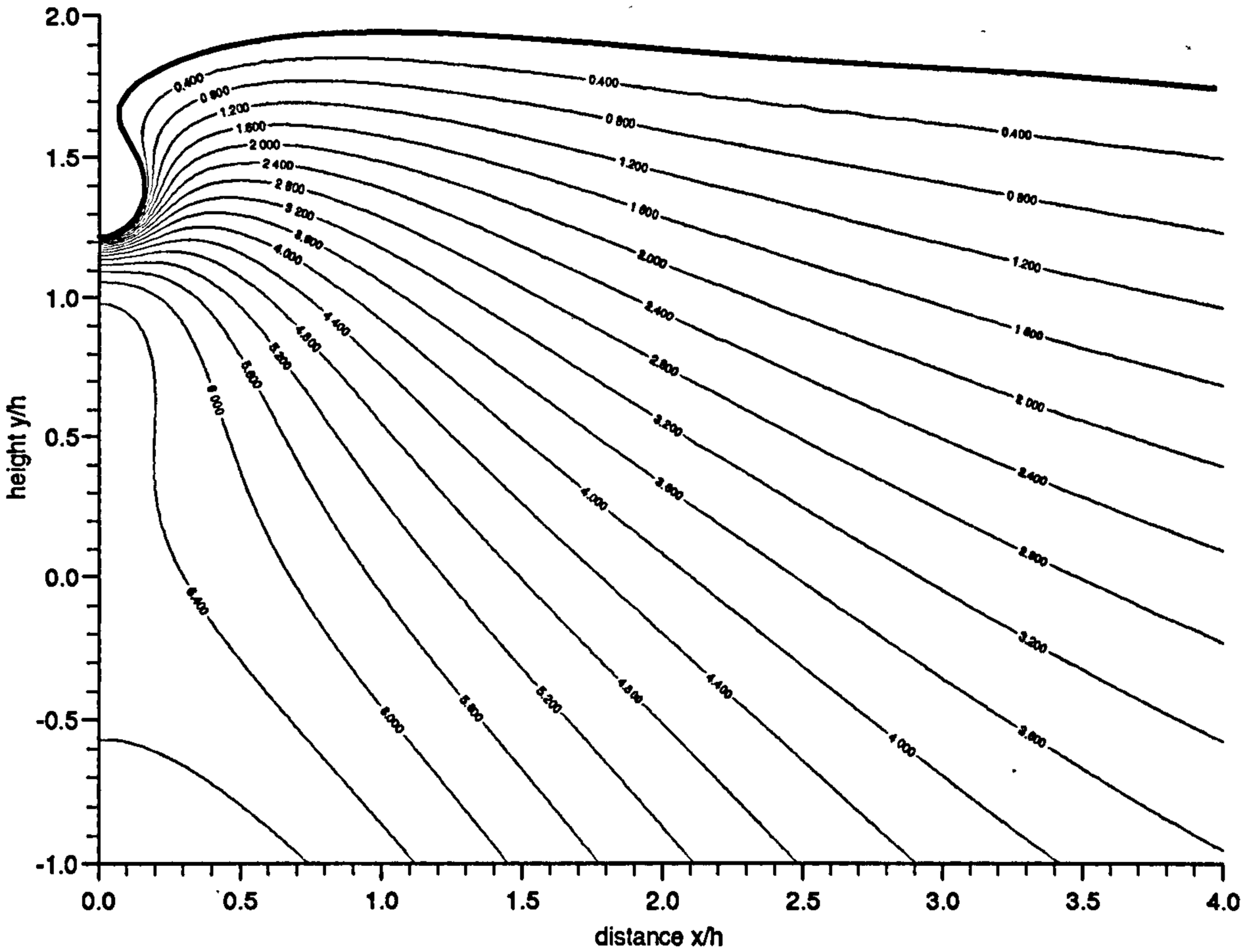

Figure 3.3: Pressure contours for a tanh waveform of initial amplitude 1.7, initial distance 8.0, s=2.0, depth 1.0, at time 4.15 with increments of 0.4.

As the overturning wave approaches the impact wall, the vertical acceleration of the waterline up the wall becomes much greater, as shown in table 3.1 for the last three computed time steps, and so near the wall the acceleration downwards due to gravity is small compared to the fluid acceleration upwards. Cooker & Peregrine (1990) describe regions of violent convergence at the wall, finding vertical accelerations greater than 1000. Table 3.1 also gives values for the maximum pressure and its position on the vertical wall in each case.

As shown in the contour maps, the maximum pressure for the first two time intervals is on the bed, but the results for the final time interval give the highest values at a vertical position of $y = 1.35h$, with the waterline at the wall just slightly higher. Note the pressures at the bed at this final timestep are still higher than in the two previous contour maps.

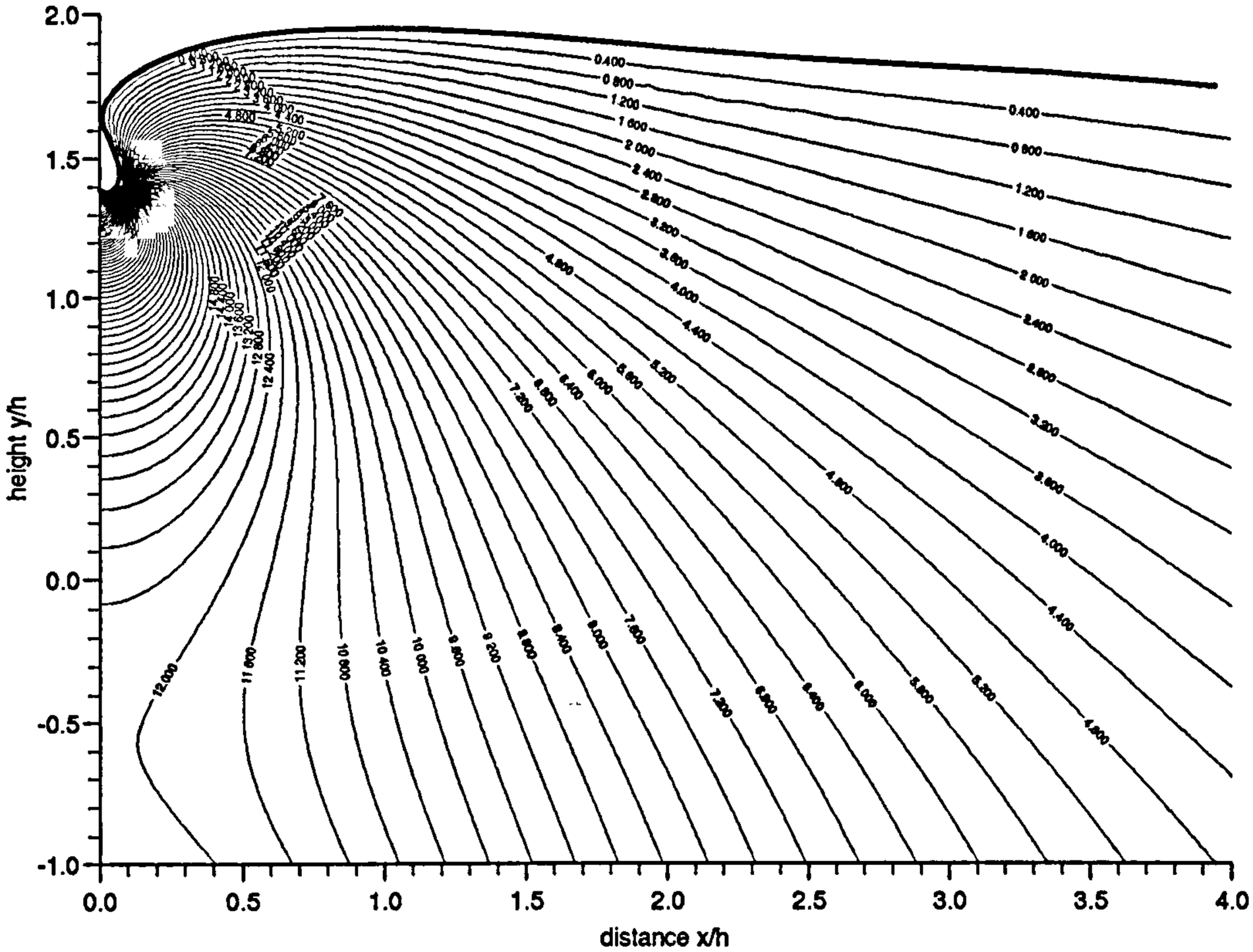

Figure 3.4: Pressure contours for a tanh waveform of initial amplitude 1.7, initial distance 8.0, s=2.0, depth 1.0, at time 4.17 with increments of 0.4.

	time	vertical acceleration of waterline at the wall	maximum pressure (on vertical wall)	position of maximum pressure
Figure 3.2	4.13	46	6.2	-1.0
Figure 3.3	4.15	120	7.2	-1.0
Figure 3.4	4.17	1701	32.4	1.35

Table 3.1: Numerical data for a wave of incident amplitude 1.7, s=2.0 and x_o=8.0 at the final three computed timesteps.

The three pressure contour maps and the data in the accompanying table illustrate that high accelerations and pressures also occur when air is trapped.

Example 2

For a similar wave of initial amplitude 1.7, s=2.0 on a depth of 1.0, the initial distance of wave from wall is now increased to $x_o = 9.0$. The time history of the surface profiles of the wave is displayed in figure 3.5, showing the wave steepening and overturning further from the wall. The waterline at the wall now lower and a larger amount of air is trapped.

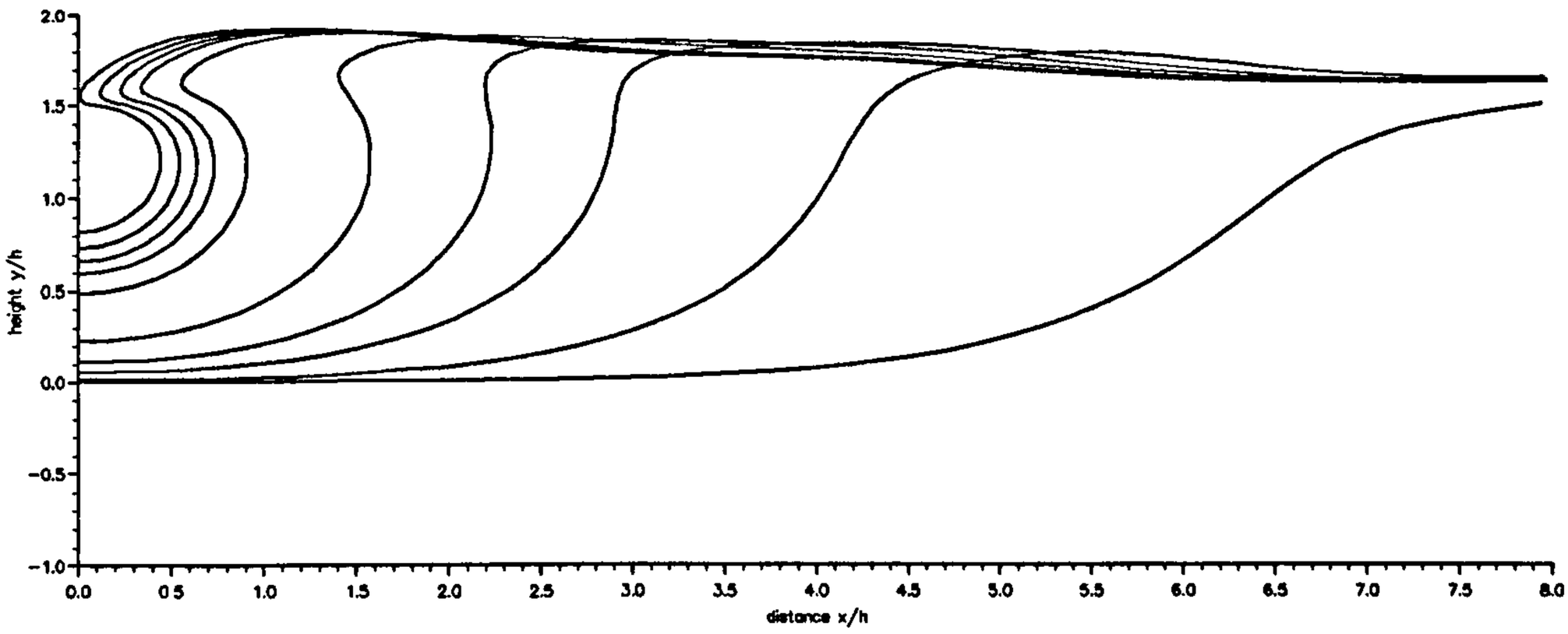

Figure 3.5: Surface profiles for a tanh waveform of initial amplitude 1.7, initial distance 9.0, s=2.0, depth 1.0, at times 1.48, 2.76, 3.40, 3.72, 4.04, 4.36 and 4.44 - 4.56 in steps of 0.04.

As can be seen in figure 3.6, the isobars show lower pressure gradients at the final computed time 4.56 than in example 1. Although increasing the size of the air pocket trapped has resulted in a decrease in the pressure values compared with example 1, the picture still illustrates a large region of significant pressures. In contrast with figure 3.4, the greatest pressures at this final computed time are now at the bed.

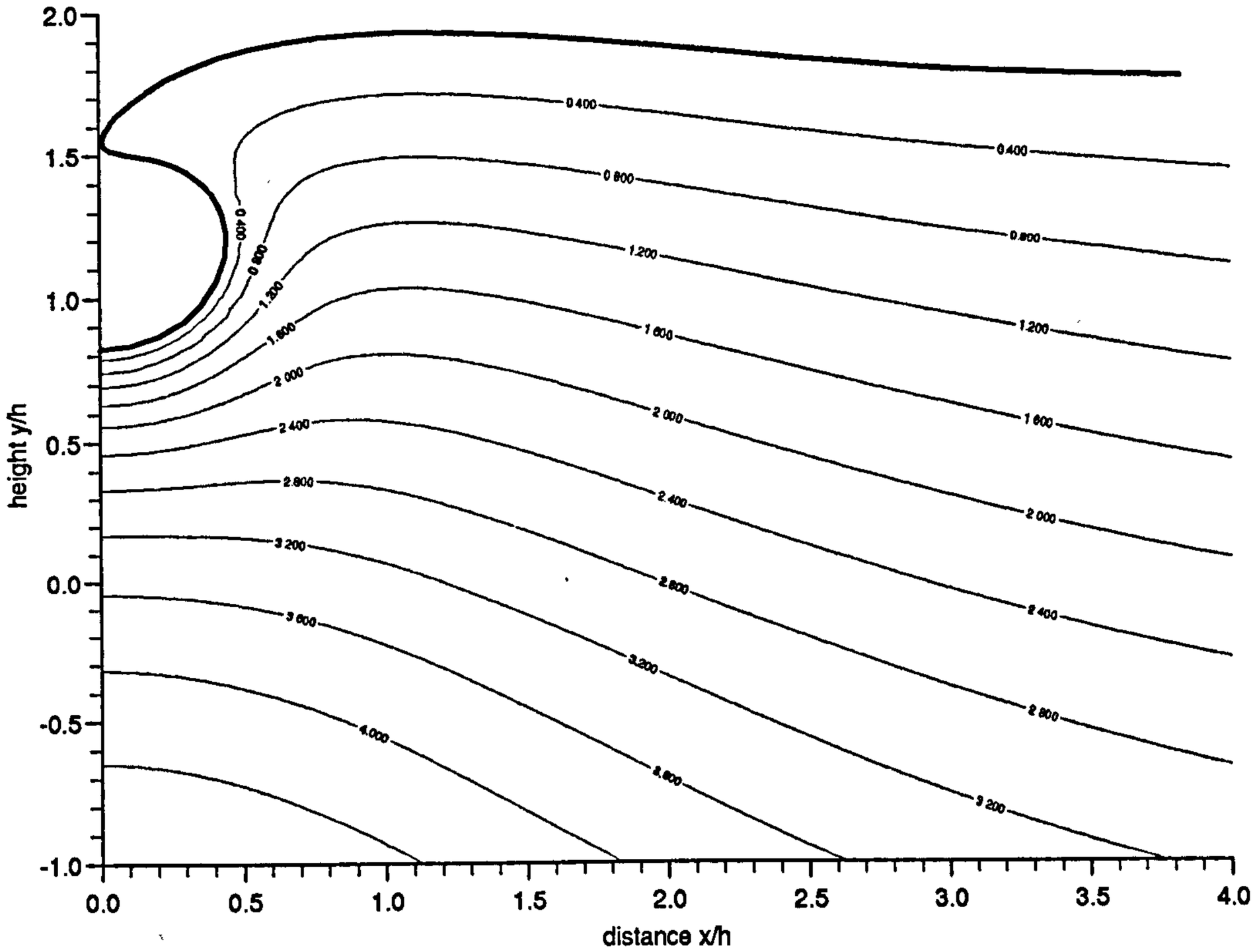

Figure 3.6: Pressure contours for a tanh waveform of initial amplitude 1.7, initial distance 9.0, s=2.0, depth 1.0, at time 4.56 with increments of 0.4.

Example 3

With a further increase of the initial distance of the wave, of initial amplitude 1.7 and s=2.0 on a depth of 1.0, from wall to x_o = 10.0, the wave now overturns further. As the waterline becomes lower, this example produces the largest air pocket at the final computed time. The surface profiles in figure 3.7 show the time history of the wave at

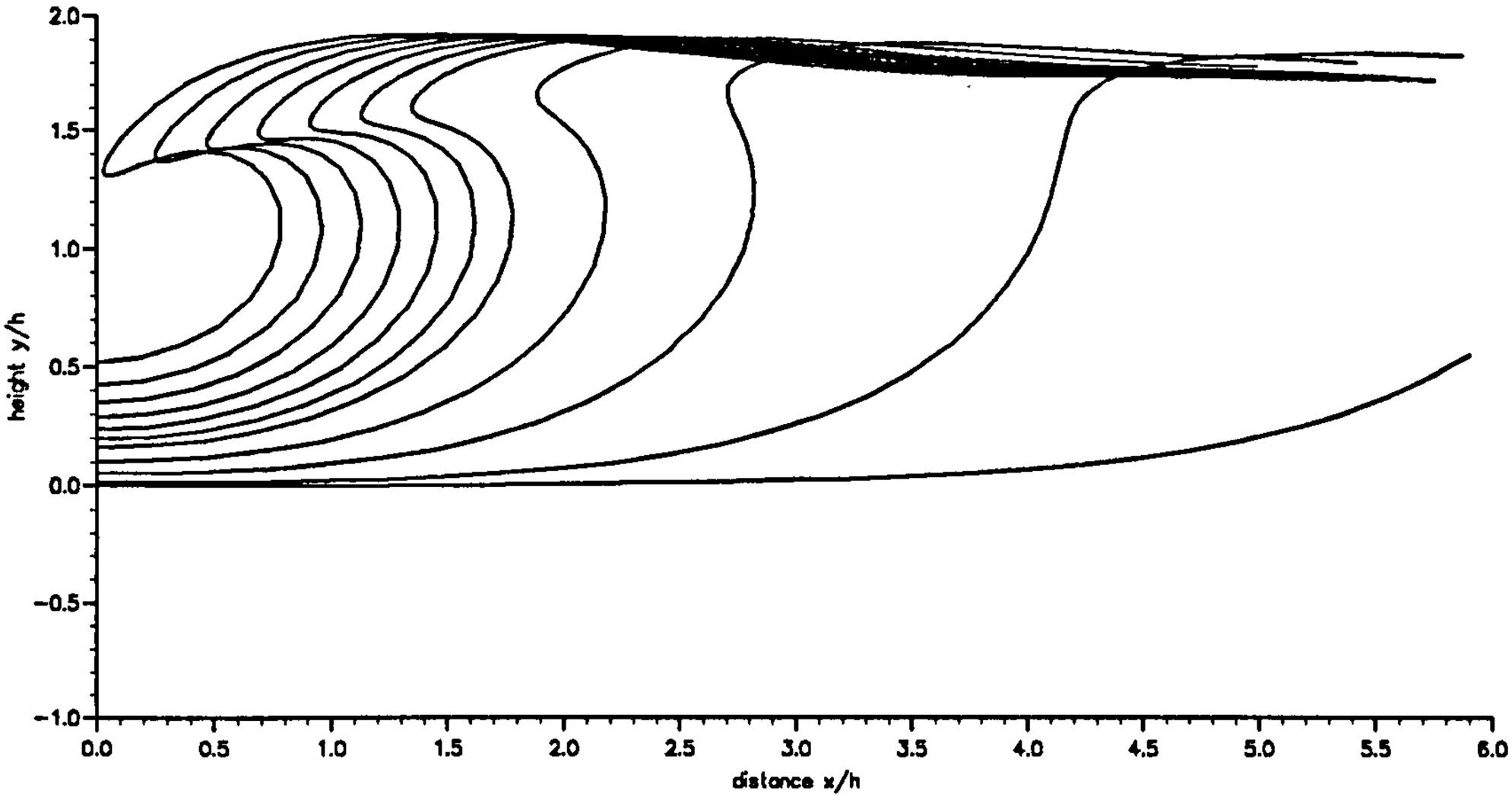

Figure 3.7: Surface profiles for a tanh waveform of initial amplitude 1.7, initial distance 10.0, s=2.0, depth 1.0, at times 2.0, 3.28, 3.92, 4.24 and 4.44 - 4.92 at steps of 0.04.

various timesteps, resulting in a large volume of trapped air just before impact. Figure 3.8 shows the pressure distribution under the free surface for the final profile before impact where lower values are given than for the previous two examples. The pressure field is now in sharp contrast with the pressure contour map in figure 3.4, as the isobars are almost horizontal and the gradients around the curved surface and along the bed are greatly reduced. As in the previous example, the contour lines show the highest pressures to be at the bed, with a peak pressure of 3.42.

Discussion

The three contour maps for the final time in the three examples show that as the

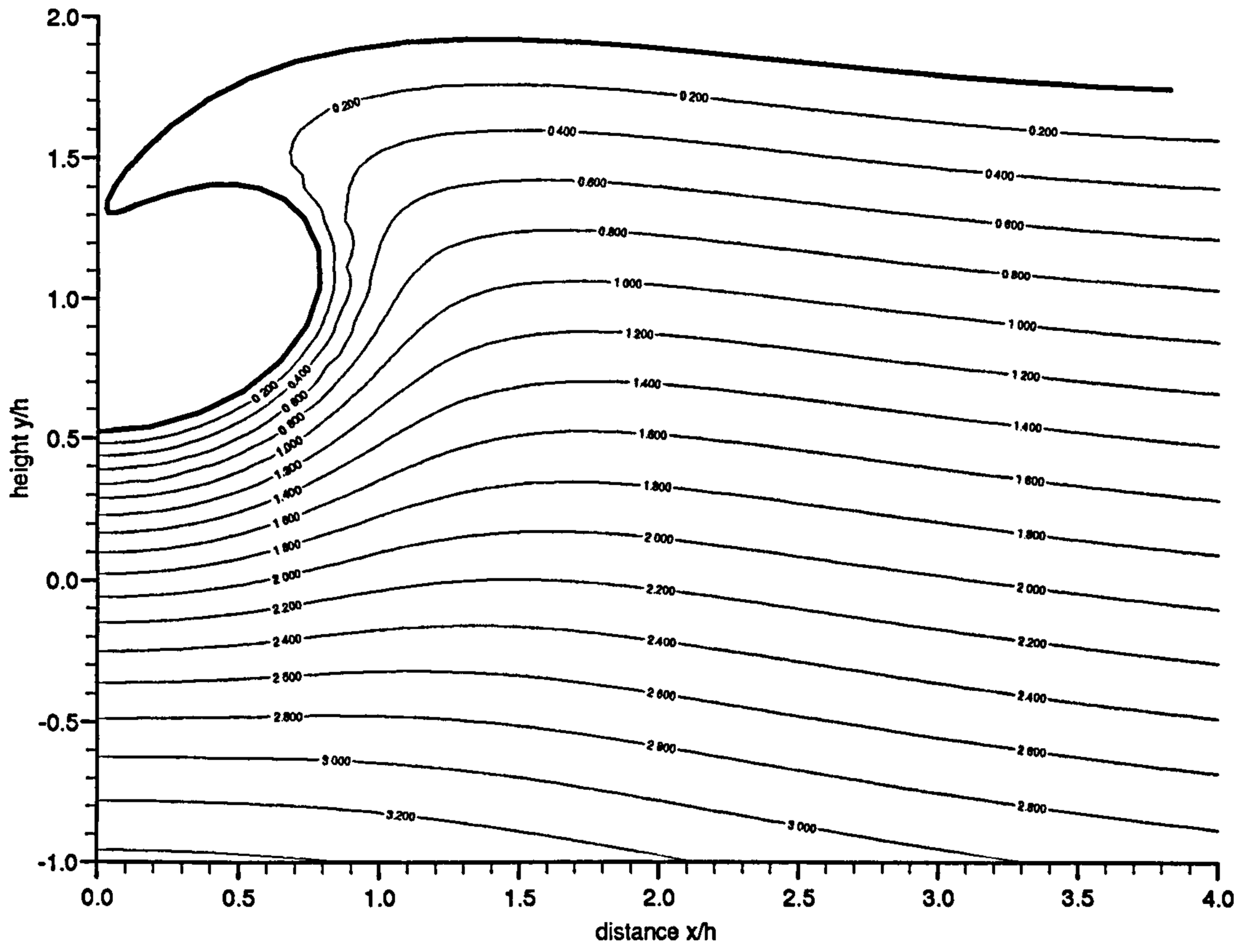

Figure 3.8: Pressure contours for a tanh waveform of initial amplitude 1.7, initial distance 10.0, s=2.0, depth 1.0, at time 4.92 with increments of 0.2.

amount of air trapped increases, the pressures decrease and the characteristics of the pressure field change. The dimensionless pressure along the bed of the domain for the three examples is presented in figure 3.9, and as shown in the contour maps, the example with the smallest air pocket has the highest values, despite the highest regions of pressure lying immediately below the free surface. Thus example 1 produces high pressures over a significant area, although these higher pressures decay much quicker. The low pressures on the bed for the largest pocket, in example 3, show a small gradual decay.

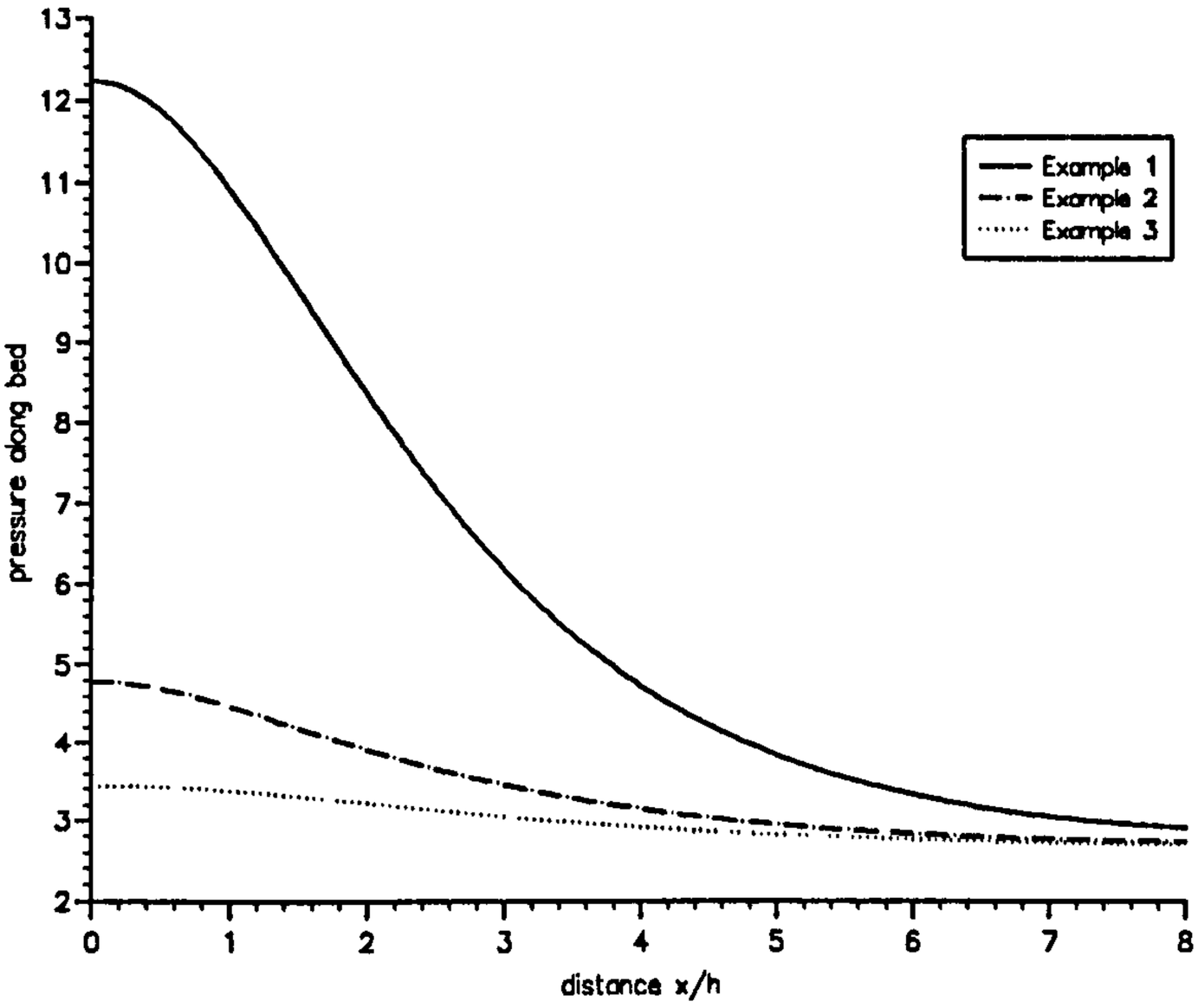

Figure 3.9: Dimensionless pressures on the bed of the domain at the final computed timestep from the numerical results for the three tanh waveform examples.

The numerical data from the final computed times enables the characteristics of the three examples to be studied and compared. As a representative set of numerical data for comparison, let the incident wave amplitude be H_o, the vertical height of the water above the bed at the final computational time be H, the vertical height of the water line in contact with the wall at the final computed time be H_w, and the vertical velocity, acceleration at this point be u_p, a_p respectively as shown in figure 3.10. The initial wave amplitude H_o is 1.7 in all three cases, but three different size air pockets result from the original placing of the wave in relation to the wall. Let the horizontal velocity at the centre line of the pocket be u_f and the horizontal velocity at the tip of the jet be u_t.

The respective parameters for the three examples from the numerical results of the final computed time are shown in table 3.2.

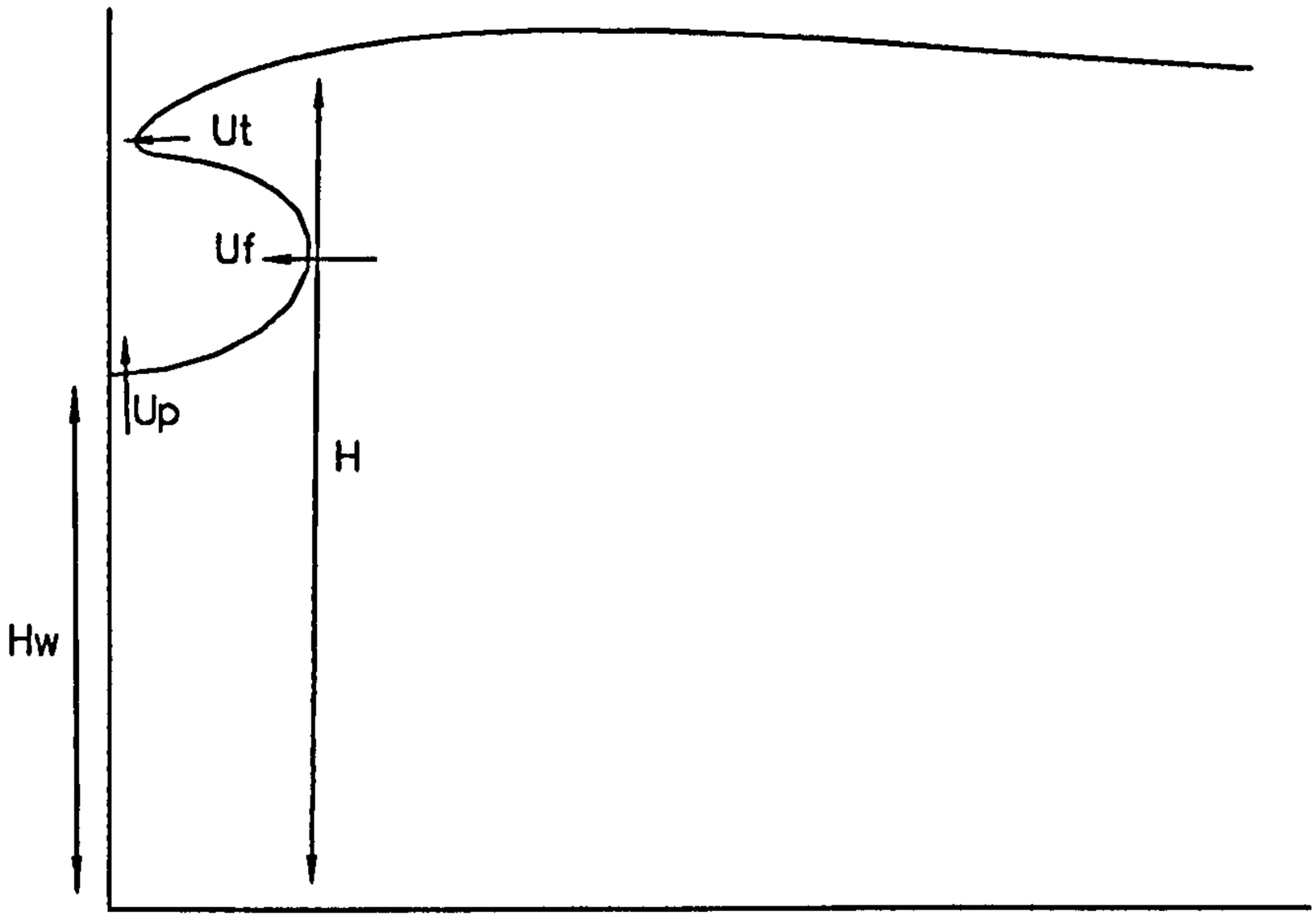

Figure 3.10: Parameters for an overturning wave

The horizontal velocity at the centre line of the bubble becomes much smaller as the radius of the pocket increases. The horizontal velocity of the tip of the jet is not significantly altered. Thus in the first two examples, the velocity of the jet tip is larger than the velocity of the centreline as noted by Hattori, Arami & Yui (1994). In addition the upward velocity of the waterline at the wall decreases rapidly with the formation of larger pockets leading to the forward velocity u_f becoming greater than the upward velocity u_p. For very small bubble sizes, large values are obtained for the vertical velocity and acceleration of the waterline. The vertical height of the waterline at the wall becomes much lower as the amount of air trapped increases resulting in the ratio H_w/H becoming smaller. These ratios are in agreement with those presented by Oumeraci, Klammer & Partenscky (1993).

The above three examples show how, for a given incident wave amplitude on a finite depth, the initial distance from the wall can be altered to give different size air pockets. Alternatively, the initial distance can remain fixed and the incident amplitude of the wave can be increased. In table 3.3, the increasing incident wave amplitude for a fixed

	Example 1	Example 2	Example 3
Wave amplitude H_o	1.7	1.7	1.7
Initial distance from wall	8.0	9.0	10.0
Pocket radius	0.071	0.445	0.784
Vertical height H	2.75	2.85	2.84
Vertical height H_w	2.390	1.823	1.522
Vertical velocity u_p	15.821	2.368	1.345
Vertical acceleration a_p	1700.7	10.93	4.09
Horizontal velocity u_f	5.35	2.69	1.99
Horizontal velocity u_t	3.06	2.81	2.77
Ratio H_w/H	0.869	0.640	0.536

Table 3.2: Comparison of dimensionless numerical data from the final computed times for the three tanh waveform examples.

incident wave amplitude	radius of air pocket	acceleration of waterline at wall
1.5	0.348	15.04
1.7	0.445	10.93
1.9	0.599	7.28
2.2	0.702	6.34
2.5	0.786	5.84

Table 3.3: Size of trapped air pocket and resulting acceleration of waterline at the wall at the final computed time for a wave of differing incident amplitudes, with s=2.0, depth 1.0 and an initial distance from the wall of x_o=9.0

initial distance from the wall of 9.0 shows an increasing size of air pocket is trapped. As expected from the previous three examples, a larger air pocket leads to a decrease in the acceleration of the waterline at the impact wall.

3.3.2 Computations for an overturning solitary wave

An alternative wave form which can be used to model an overturning wave is that of a solitary wave. The initial data is provided by a numerical method developed by Tanaka (1986), which is able to calculate the steady wave profile and appropriate velocity potential. As in the previous section, the interest lies in large amplitude waves which can overturn trapping a pocket of air against a vertical wall. Thus as for the colliding 'tanh' waves, two symmetric solitary waves are made to travel towards each other to represent a wall in the centre of the domain. By choosing a shallower depth than is appropriate for a large initial amplitude, the wave overturns in front of the wall. Again the computations stop just before impact with the wall.

Two examples from the numerical results are presented to illustrate an overturning solitary wave at a vertical wall trapping an air pocket. The computations chosen to be displayed here are for a small air pocket and a larger air pocket. Surface profiles are presented at various timesteps and the pressure distribution at the final computed time. As a shallow depth is required for the wave to overturn, a wave of dimensionless initial amplitude and depth of $0.7h$ and $0.3h$ respectively was used with between 300-400 points. To compare with results from subsection 3.3.1, h is then rescaled in the solitary wave computations by $\frac{10}{3}$, to give similar still water depth dimensions as the computations for the tanh waveforms, thus enabling better comparison of the numerical results.

Example 4

The surface profiles in figure 3.11 show a wave with initial surface conditions for a solitary wave of amplitude $\frac{7}{3}$ on a depth 1.0, an initial distance of 18.93 from the wall. The wavefront steepens and overturns as it approaches the wall, in the process trapping a small air pocket just before impact. The number of points used by the program for the final computed time was 353.

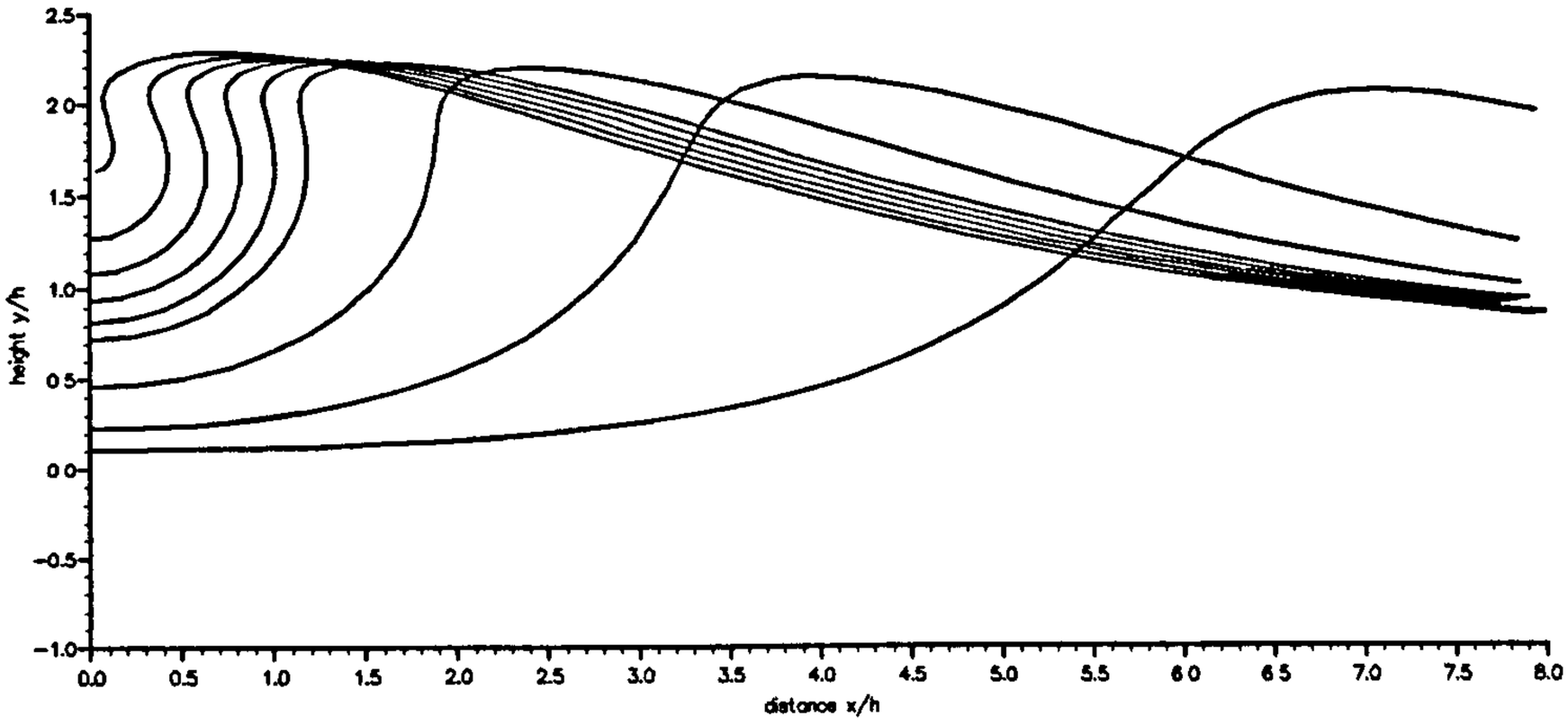

Figure 3.11: Surface profiles for a solitary wave of amplitude $\frac{7}{3}$ initial depth 1.0, with an initial distance of 18.93 at times 4.89, 6.06, 6.65 and 6.94 - 7.30 in steps of 0.073

Figure 3.12 presents the pressure distribution at the final computed time 7.30 and as can be seen from the contour map, the resulting high pressure field resembles that obtained in figure 3.4 for an overturning tanh waveform. The isobars near the impact wall are nearly vertical and a region of high pressure is produced near the bed, along with a region of higher pressures just below the waterline with tightly packed lines around the curved surface and high gradients along the bed.

Example 5

The initial distance from the wall is now increased to 20.8 for a solitary wave of amplitude $\frac{7}{3}$ and depth 1.0. The surface profiles as the wave travels towards the wall are displayed in figure 3.13. The wave is now able to overturn trapping a much larger air pocket against the wall. The final number of points used in this example was 349. Figure 3.14 displays the pressure distribution at the final computed time, 7.96. The contour map now shows the maximum pressures to be at the bed of the domain in contrast with figure 3.12. The pressure values are much lower than in example 4 and the contour lines are almost horizontal with much weaker gradients along the bed. This is consistent with the results shown in the subsection 3.3.1 in figure 3.8.

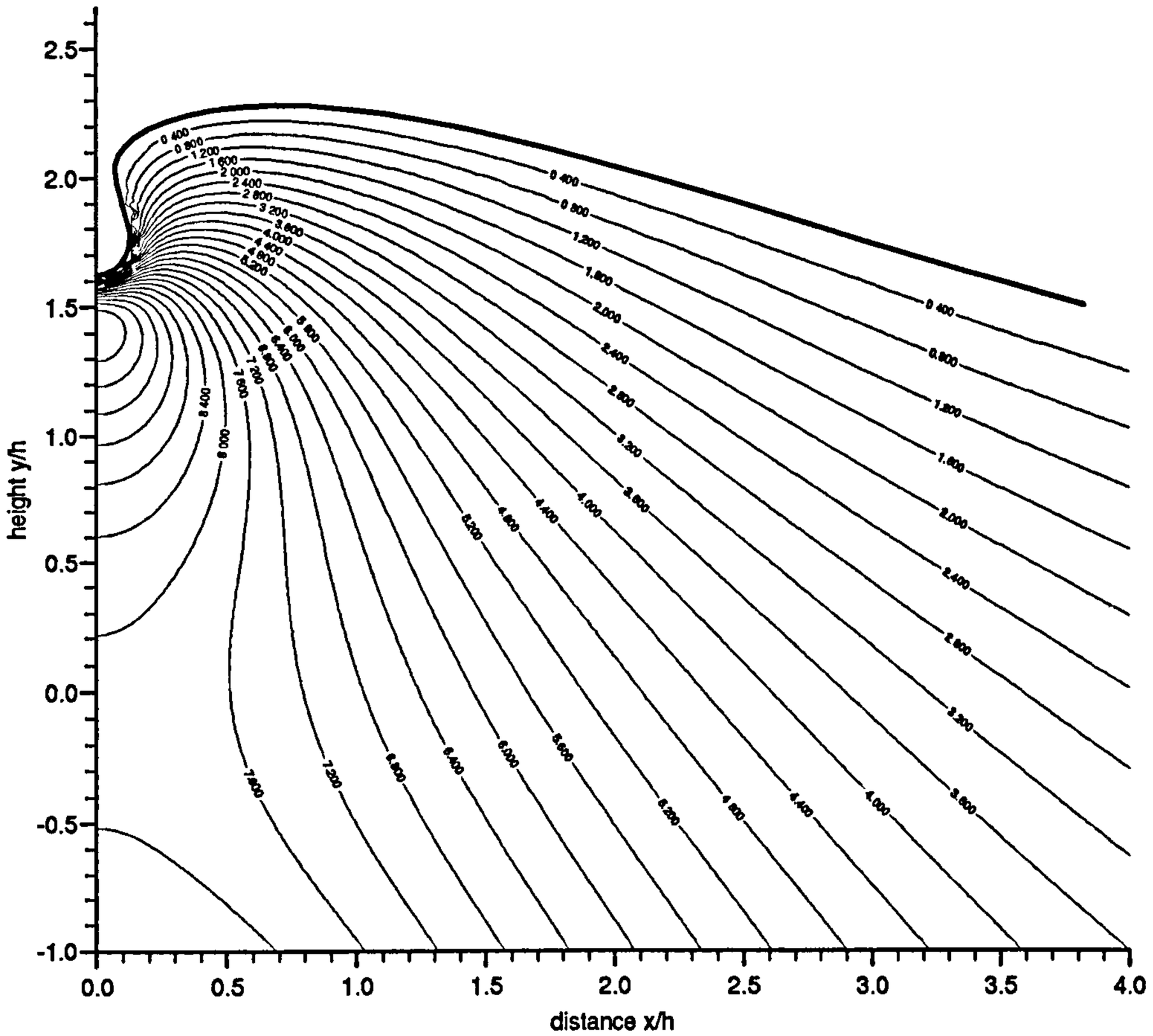

Figure 3.12: Pressure contours with increments of 0.4 for a solitary wave of amplitude $\frac{7}{3}$, initial depth 1.0 and initial distance from the wall of 18.93, at time 7.30.

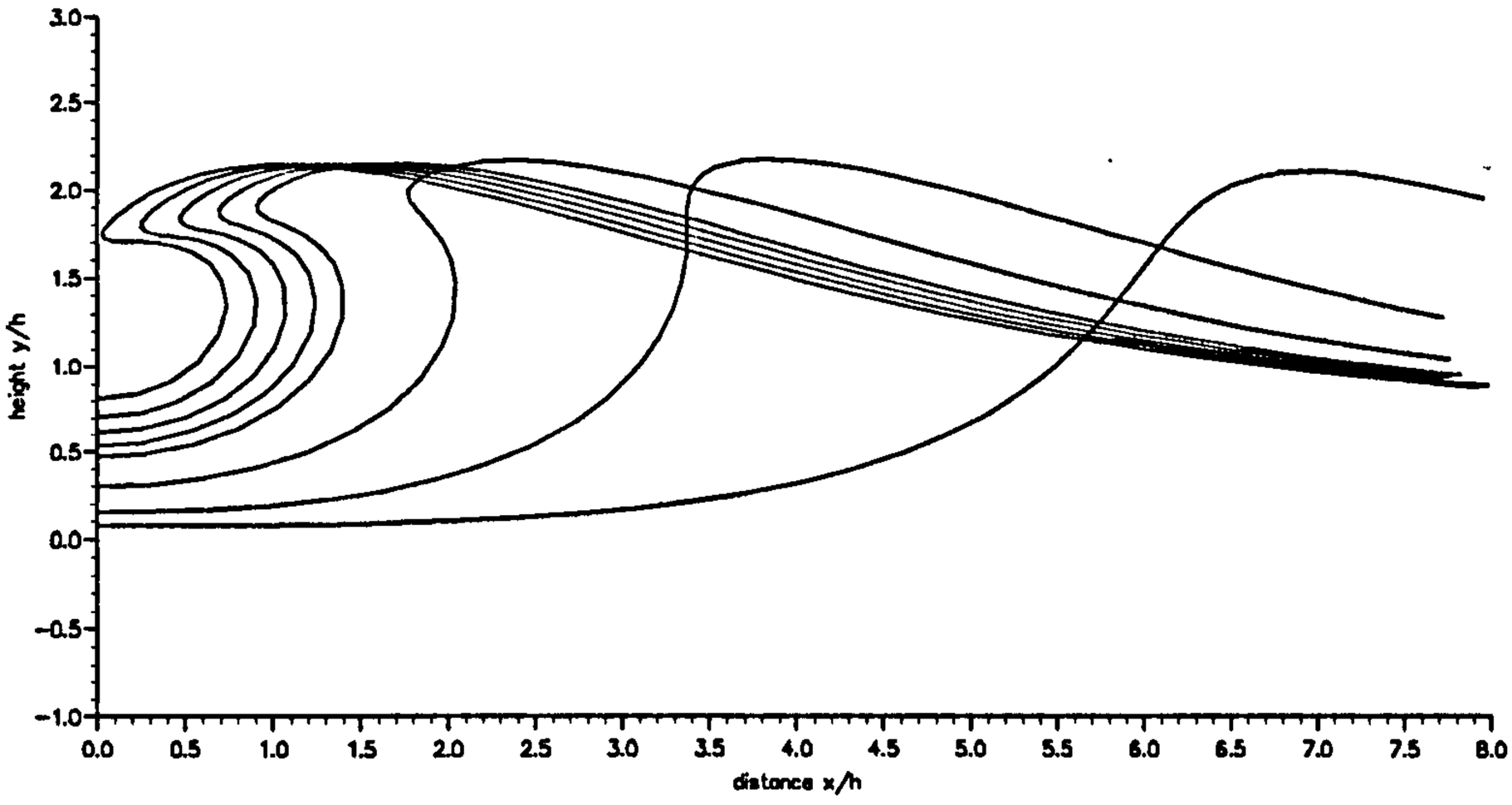

Figure 3.13: Surface profiles for a solitary wave of amplitude $\frac{7}{3}$, initial depth 1.0 with an initial distance of 20.8 at times 5.62, 6.79, 7.38 and 7.67 - 7.96 in steps of 0.073

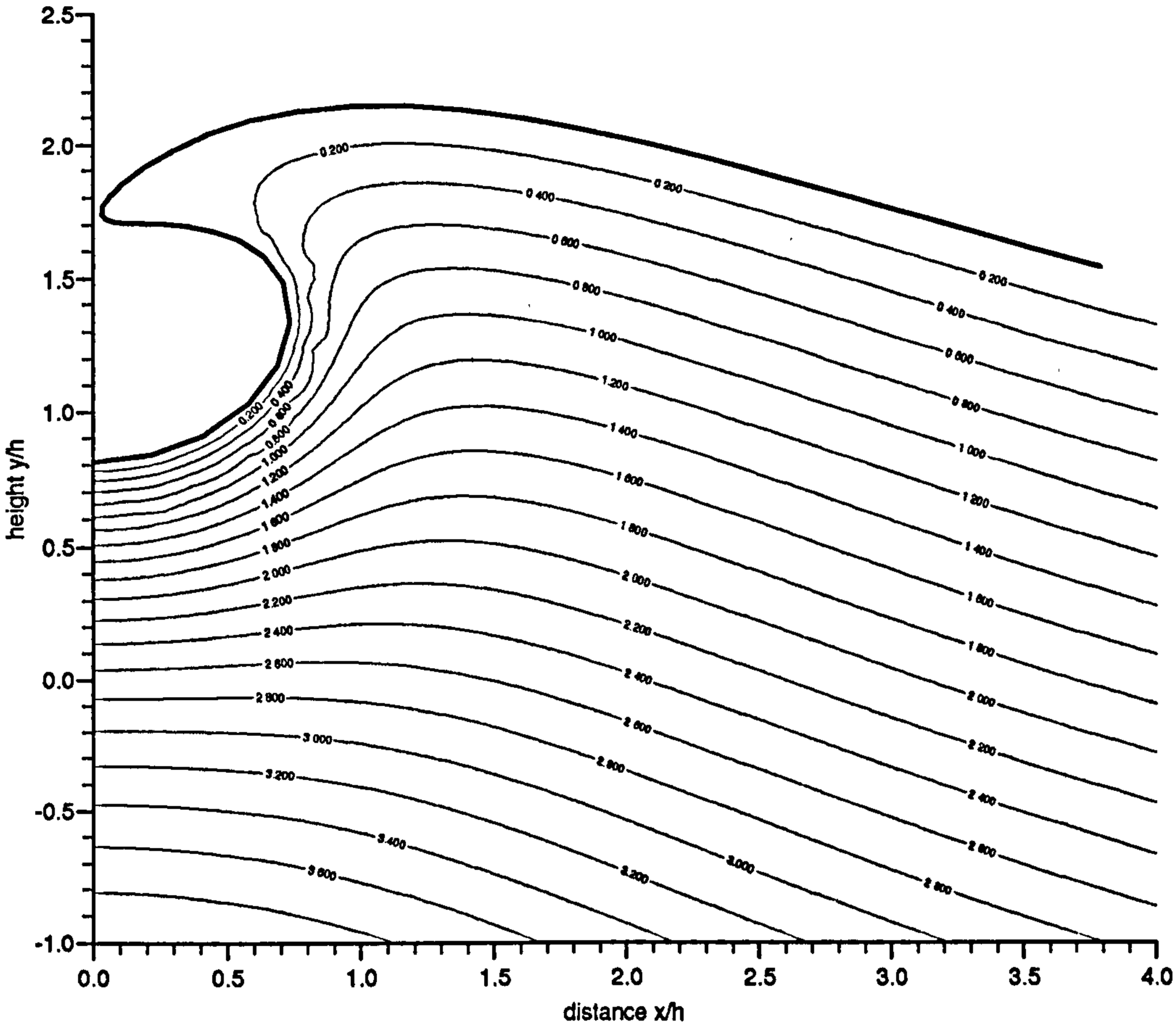

Figure 3.14: Pressure contours with increments of 0.2 for a solitary wave of amplitude $\frac{7}{3}$, initial depth 1.0 and initial distance of 20.8 at a time 9.76

3.3.3 Comparison of the two wave forms

Comparison of the five contour maps in subsections 3.3.1 and 3.3.2 shows very similar pressure characteristics for the same relative size air pockets. The highest pressure values are at the bed of the domain for the larger pockets. Areas of higher pressure are found under the free surface at the impact wall for the smaller pockets. Unlike the solitary wave surface profile, however, the tanh waveform produces an almost horizontal free surface.

The numerical data from the final computed timestep in each example gives a value for the radius of the air pocket. The numerical results from the computations for a solitary wave in subsection 3.3.2 have been compared with new computations from subsection 3.3.1 by using initial data for a tanh waveform that produces similar size air pockets as those in example 4 and 5. Thus to compare with solitary wave example 4, a tanh waveform of initial amplitude 1.9, initial distance 7.8 was used to produce a trapped air pocket of radius 0.118, and to compare with solitary wave example 5, a tanh waveform of initial amplitude 2.2, initial distance 9.11 was used to produce a trapped air pocket of radius 0.728.

Comparison of the scaled velocity and space parameters at the final time for the solitary wave examples 4, 5 and corresponding tanh waveform examples that give similar size air pockets are displayed in table 3.4. The waterline at the wall H_w and the position of the bubble d are lower in both cases for the tanh waveform. The three velocity parameters u_p, u_f and u_t agree particularly well for the larger air pocket.

	a	d	H	H_w	u_p	u_f	u_t	a_p
Solitary Wave 1	0.128	2.78	3.13	2.63	7.65	3.19	3.28	586.76
Tanh Wave 1	0.118	2.43	2.91	2.31	9.39	4.58	3.10	519.94
Solitary Wave 2	0.733	2.34	3.13	1.81	1.67	2.35	3.03	5.05
Tanh Wave 2	0.728	2.13	3.24	1.56	1.65	2.30	3.06	5.93

Table 3.4: Comparison of parameters from solitary wave computations in examples 4 and 5 scaled by $h = \frac{10h}{3}$, with tanh waveform computations that produce a similar size trapped air pocket.

Overall comparison of the numerical data reveals that the use of two different incident

waves has produced similar size air pockets with the final space and velocity parameters showing fairly good agreement, with similar characteristics - the reduction in horizontal velocity u_f at the centreline and vertical velocity u_p at the waterline and relative indifference of the horizontal velocity u_t at the jet tip.

The numerical results have illustrated how the initial parameters can affect the resulting air pocket. To model an overturning wave trapping a large volume of air, the initial distance from the wall can be increased. To model an air pocket further down under the free surface, increasing the size of the wave initial amplitude will enable the distance d to be decreased.

3.4 Theoretical modelling for a trapped air pocket

To model an air pocket trapped against a vertical wall, the presence of the free surface and rigid wall, and the cylindrical geometry of the gas pocket have to be taken into account. As the radius of the bubble is small compared with the wavelength of sound, the water is assumed to be an incompressible inviscid fluid satisfying Laplace's equation in polar coordinates:

$$\frac{\partial^2\phi}{\partial r^2}+\frac{1}{r}\frac{\partial\phi}{\partial r}+\frac{1}{r^2}\frac{\partial^2\phi}{\partial\theta^2}=0 \tag{3.6}$$

To a first approximation, an isolated oscillating circular air bubble can be represented by the flow due to an oscillating line. The complex potential for the motion consists of a logarithmic term to describe the radial flow. Suppose the bubble contains air at atmospheric pressure and that its centre is at a distance $d = H_w + a$ above the seabed where a is the radius of the air bubble as illustrated in figure 3.15. The height of the free surface after impact is H.

The fluctuations of gas pressure are assumed to be adiabatic. During the short time in which the bubble oscillates regularly, the free surface is assumed to move very little so that the flow in the impacting wave may be ignored. The vibrations of the trapped air pocket have been modelled by considering the radial oscillations of a single two dimensional bubble with semi-circular cross-section of radius a.

Take an image of the bubble above the free surface to be oscillating in anti-phase with respect to the bubble, an image below the rigid bed to be oscillating in phase, and a third

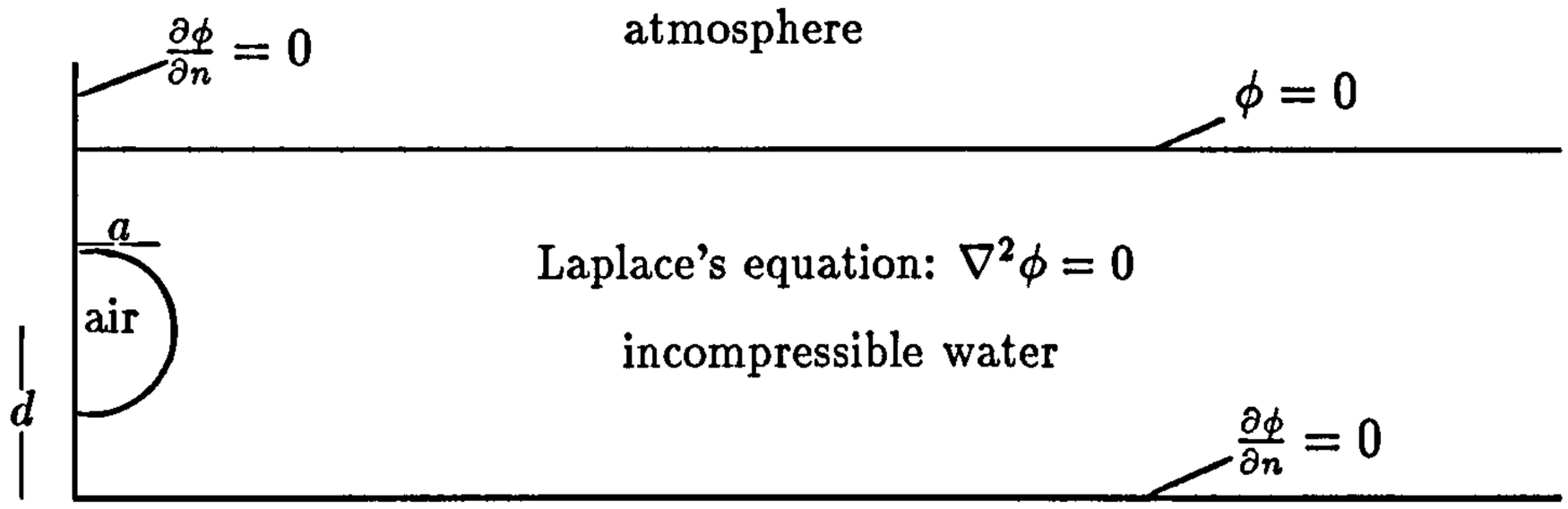

Figure 3.15: Trapped semi-circular two-dimensional bubble against a vertical wall

image below, oscillating in anti-phase, to ensure symmetry. These images then extend above and below to produce an infinite series which is summed analytically, as the motion of a combination of sources and sinks can be obtained by the addition of the corresponding complex potentials. A conformal mapping from the z-plane onto the w-plane using the transformation $w = e^{\lambda z}$, where $z = x + iy$, is the crucial step. The resulting potential for this model is

$$\Phi = -\alpha_o \log\left[\frac{\cosh(\lambda z) - \cos(\lambda d)}{\cosh(\lambda z) + \cos(\lambda d)}\right] - \alpha_1 \frac{d}{dz}\left\{\frac{e^{-\lambda z}}{\lambda}\log\left[\frac{\cosh(\lambda z) - \cos(\lambda d)}{\cosh(\lambda z) + \cos(\lambda d)}\right]\right\} \tag{3.7}$$

where $\lambda = \frac{\pi}{2H}$ and α_o, α_1 are constants. For small oscillations, the radius of the fluctuating bubble is chosen to be

$$r(t) = a + \epsilon_o \sin(\omega t) \tag{3.8}$$

where a is the equilibrium radius and ϵ_o is a small amplitude of oscillation. The pressure in the bubble is $p = p_o + p_B e^{i\omega t}$ where p_B is the pressure on the bubble surface. For a bubble with no motion, $p_o = p_\infty$ where p_∞ is the ambient pressure. Using Bernoulli's equation

$$\frac{\partial\phi}{\partial t} + \frac{p}{\rho_l} = \frac{p_\infty}{\rho_l} \tag{3.9}$$

where ρ_l is the uniform liquid density and the adiabatic equation of state,

$$(\text{pressure})\ (\text{volume})^\gamma = \text{constant}$$

where γ is the ratio of specific heats, the potential on the bubble surface $z = id + ae^{i\theta}$ can be evaluated to give

$$\phi = -\alpha_o \log\left[\frac{\lambda a}{2}\tan(\lambda d)\right] + 0(\lambda a) \tag{3.10}$$

where remaining terms do not involve volume change.

Using the linearised kinematic boundary condition across the bubble interface,

$$\frac{\partial \phi}{\partial r} = \frac{\partial r}{\partial t} \quad \text{on} \quad r = a,$$

an expression for the frequency $f = \frac{\omega}{2\pi}$ of the small oscillations can be obtained:

$$\omega^2 = -\frac{2\gamma p_o}{\rho_l a^2 \log[\frac{1}{4}(\pi a/H) \tan(\frac{1}{2}(\pi d/H))]} \tag{3.11}$$

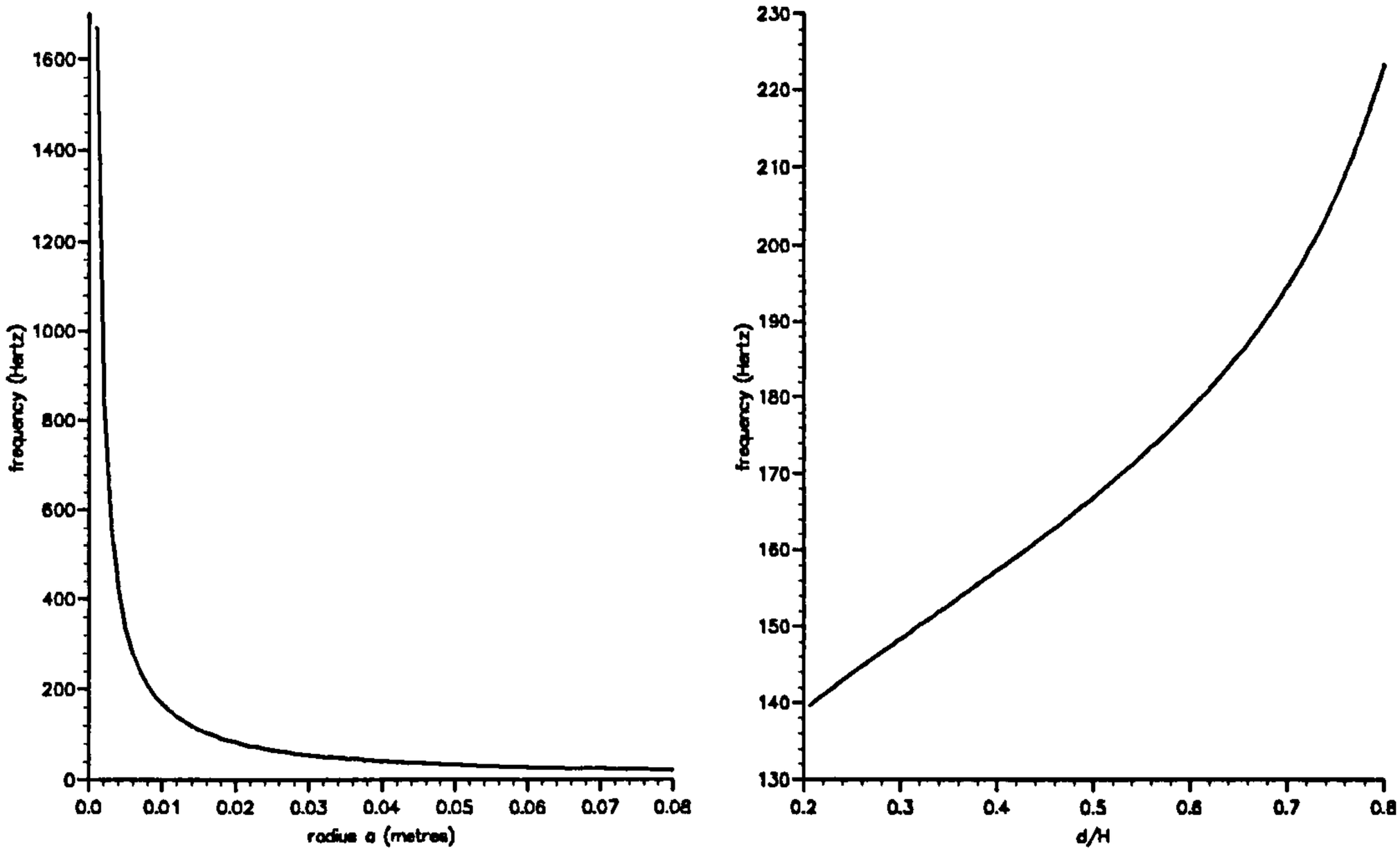

Figure 3.16: Variation of frequency f for a single cylindrical bubble with the radius a (left diagram) for $H = 2d$ and $d = 5a$ and with the ratio d/H (right diagram) for a=0.01 metres.

The frequency of the bubble is proportional to its size producing very low frequencies for large bubbles as shown in figure 3.16, where $H = 2d$ and $d = 5a$. Variation with d/H, for a bubble of radius a=0.01 metres, in the same figure shows the effect of the proximity of the rigid boundary is to lower the frequency and the effect of the free surface to increase the frequency.

i) as H becomes large

$$\omega^2 = -\frac{2\gamma p_o}{\rho_l a^2 \log\left[\frac{2ad}{R^2}\right]},$$

the frequency for a single two-dimensional bubble in the vicinity of a rigid boundary, where $R = 16H^2/\pi^2$ is a large number representing a boundary far away. This is to ensure the boundary conditions in the far field are satisfied.

ii) as d becomes large,

$$\omega^2 = -\frac{2\gamma p_o}{\rho_l a^2 \log\left[\frac{a}{2H}\right]},$$

the frequency for a single two-dimensional bubble in the vicinity of a free boundary as shown in Topliss (1991).

The pressure on the bed, calculated using equation (3.7) and $p = -\rho\partial\phi/\partial t$, shows fairly rapid decay along the bed as presented in figure 3.17. As the bubble becomes larger, the pressures becomes smaller. The pressure values on the bed due to a bubble positioned nearer the bed, $\frac{d}{H}$=0.3, are higher as expected but these values also decay faster.

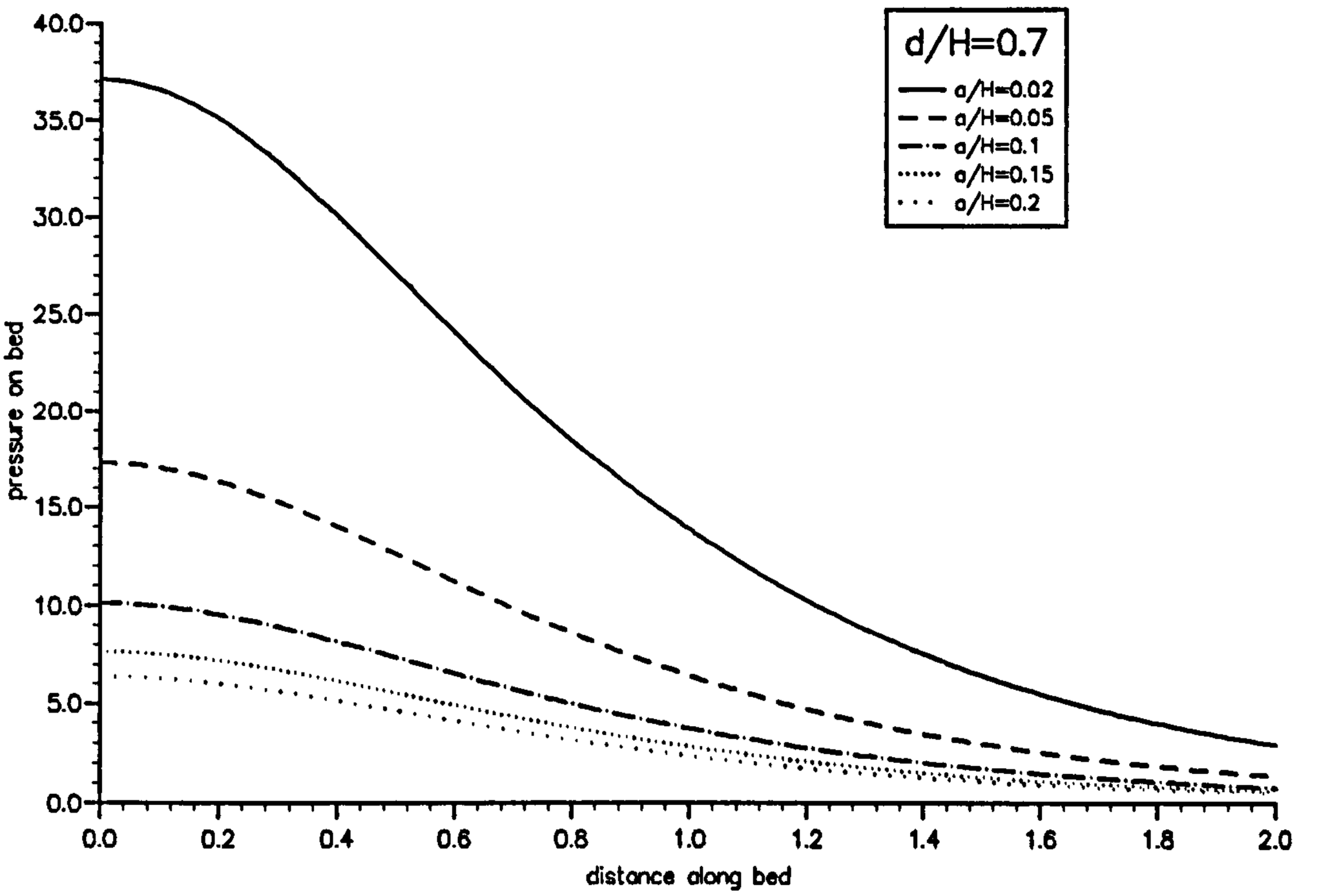

Figure 3.17: Pressure $pH/\alpha_o(\gamma\rho p_o)^{1/2}$ on the bed of the domain due to a single oscillating semi-circular air bubble.

3.5 Theoretical modelling of a bubbly mixture

3.5.1 Preliminary

The range of frequencies of oscillation which are of interest in this study are relatively low and Omta (1987) has shown analytically that the frequency spectrum of a cloud of bubbles has a peak at a frequency much lower than the natural frequencies of the individual bubbles and that this dominant frequency is mainly determined by the total gas content of the cloud. Lu, Prosperetti & Yoon (1990) presented an analysis of the oscillations of bubble clouds of simple geometrical shapes to study underwater noise emisson from bubble clouds and calculated the normal modes of oscillation in an otherwise pure fluid. Leighton (1994) gives an indepth review.

Sound velocity in air is approximately 340 metres per second; that in water is approximately 1500 metres per second. In a mixture of air and water, however, the speed of sound is dramatically reduced.

To model the sound speed in a bubbly fluid, a uniform mixture of small air bubbles is assumed. The frequency range of interest is 100 - 200 Hertz which is much lower than the resonant frequency of the bubbles. Let α be the fraction of unit volume of mixture occupied by gas, ρ_g the density of the gas and ρ_l the density of water. The density of the mixture can be written as $\rho = \alpha\rho_g + (1-\alpha)\rho_l$. The sound speed c_b in the mixture then becomes

$$\frac{1}{c_b^2} = \frac{d\rho}{dp} = \frac{(1-\alpha)}{c_l^2} + \frac{\alpha}{c_g^2} + (\rho_g - \rho_l)\frac{d\alpha}{dp} \tag{3.12}$$

where $c_l^2 = dp/d\rho_l$ and $c_g^2 = dp/d\rho_g$ the sound speed in gas and liquid respectively.

Following the approach by Hseih & Plesset (1961) and later Crighton, Dowling, Ffowcs Williams, Heckl & Leppington (1992), the sound speed c_b in the bubbly fluid is given by

$$c_b^2 = \frac{\gamma p_g}{\rho_l \alpha(1-\alpha)} \tag{3.13}$$

where p_g is the mean air pressure and γ is the ratio of specific heats. The expression is valid provided α is not too near 0 or 1. For example 1, 4 and 10 percent aeration give sound speeds of 120, 60 and 40 metres per second respectively. As a result of the aeration and hence lower sound speed, the wavelength of sound waves is much shorter than in pure water.

3.5.2 Mathematical Analysis

This model applies to the instances when a plunging wave has broken against a vertical structure creating a volume of water with many small bubbles next to the impact wall. This is now a compressible mixture.

Consider a region of uniform bubbly mixture (region 1) of height H and width L with a gas fraction α next to a vertical wall, and non-aerated water on the other side (region 2) as shown in figure 3.18. Viscosity and gravitational effects are ignored.The solid wall and solid horizontal bed are treated as rigid so that the component of displacement normal to these boundaries vanishes. As there is a large density contrast between these fluids and the air above, the pressure perturbation is taken to vanish at the free surface.

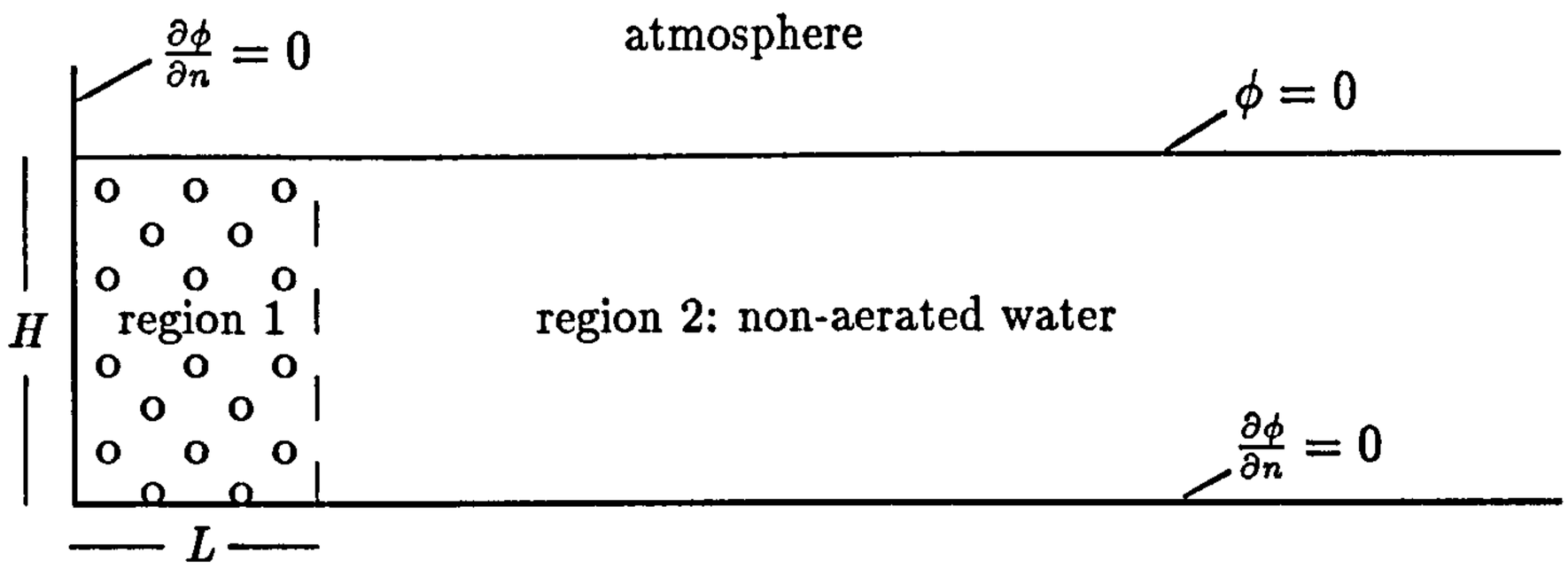

Figure 3.18: Volume of bubbly fluid next to impact wall.

For linearised theory and sinusoidally varying velocity potential $\Phi(x, y)\, e^{-i\omega t}$ this implies Φ may be taken to be zero on the free surface. Introducing a time-dependence $e^{-i\omega t}$, the reduced wave equation,

$$(\nabla^2 + k_i^2)\, \phi_i = 0 \tag{3.14}$$

where the subscripts i= 1,2 refers the regions 1 and 2 respectively and $k_i = \omega/c_i$ where $\omega = 2\pi f$ and $c_1 = c_b$, is solved by separation of variables where $\phi(x, y) = X(x)Y(y)$ with boundary conditions $\partial\phi/\partial x = 0$ on $x = 0$, $\partial\phi/\partial y = 0$ on $y = 0$, $\phi = 0$ on $y = H$ and $\phi(x, y)$ tends to 0 as $y \to \infty$.

As the free surface and the rigid bed are now totally reflecting surfaces, the fluid can be considered as an acoustic plane waveguide and a standing wave field can exist, which has a cut-off frequency $\omega_n = \frac{k_i}{c_i}$ for each mode of oscillation, below which no propagation occurs. In region 2 the sound speed is very much higher than in region 1 and therefore

ω may be less than the cut-off frequency and there will be propagation. The velocity potential for the bubbly mixture in this instance is:

$$\phi_1 = \sum_{n=0}^{\infty} A_{1n} \cos\left[\frac{(n+\frac{1}{2})\pi}{H} y\right] \cos\left[\sqrt{k_1^2 - \left(\frac{(n+\frac{1}{2})\pi}{H}\right)^2}\, x\right] e^{i\omega_n t}$$

and for the non-aerated water outside the bubbly mixture is

$$\phi_2 = \sum_{n=0}^{\infty} A_{2n} \cos\left[\frac{(n+\frac{1}{2})\pi}{H} y\right] \exp\left[-\sqrt{\left(\frac{(n+\frac{1}{2})\pi}{H}\right)^2 - k_2^2}\, x\right] e^{i\omega_n t}$$

where c_2=1500 m/s is the speed of sound in non-aerated water and A_{1n}, A_{2n} are constants.

Matching across interface at $x = L$ between region 1 and region 2 we take pressure and normal velocity continuous

$$\rho_1 \frac{\partial \phi_1}{\partial t} = \rho_2 \frac{\partial \phi_2}{\partial t} \quad , \quad \frac{\partial \phi_1}{\partial x} = \frac{\partial \phi_2}{\partial x} \tag{3.15}$$

These two equations give an expression for the frequency of modes of oscillations trapped in region 1:

$$(1-\alpha)\sqrt{\left(\left(n+\frac{1}{2}\right)\pi\right)^2 - (k_2 H)^2}$$

$$= \sqrt{(k_1 H)^2 - \left(\left(n+\frac{1}{2}\right)\pi\right)^2} \tan\left[\sqrt{(k_1 H)^2 - \left(\left(n+\frac{1}{2}\right)\pi\right)^2}\frac{L}{H}\right] \tag{3.16}$$

For a fixed volume of air and depth, a wider region will produce lower frequencies as displayed in figure 3.19. Conversely a very narrow band of bubbles against a rigid wall will produce very high frequencies. Also a higher free surface will result in lower frequencies. Estimates of the percentage of air entrained in the water mentioned in the literature are roughly in the range of 10-20 percent. As can be seen from figure 3.19, higher frequencies are obtained for lower aeration levels.

Finite tank

The model is now considered with a finite end at $x = B$ as shown in figure 3.20 and therefore represents a rigid walled container with the new boundary condition $\partial\phi/\partial x = 0$ on $x = B$.

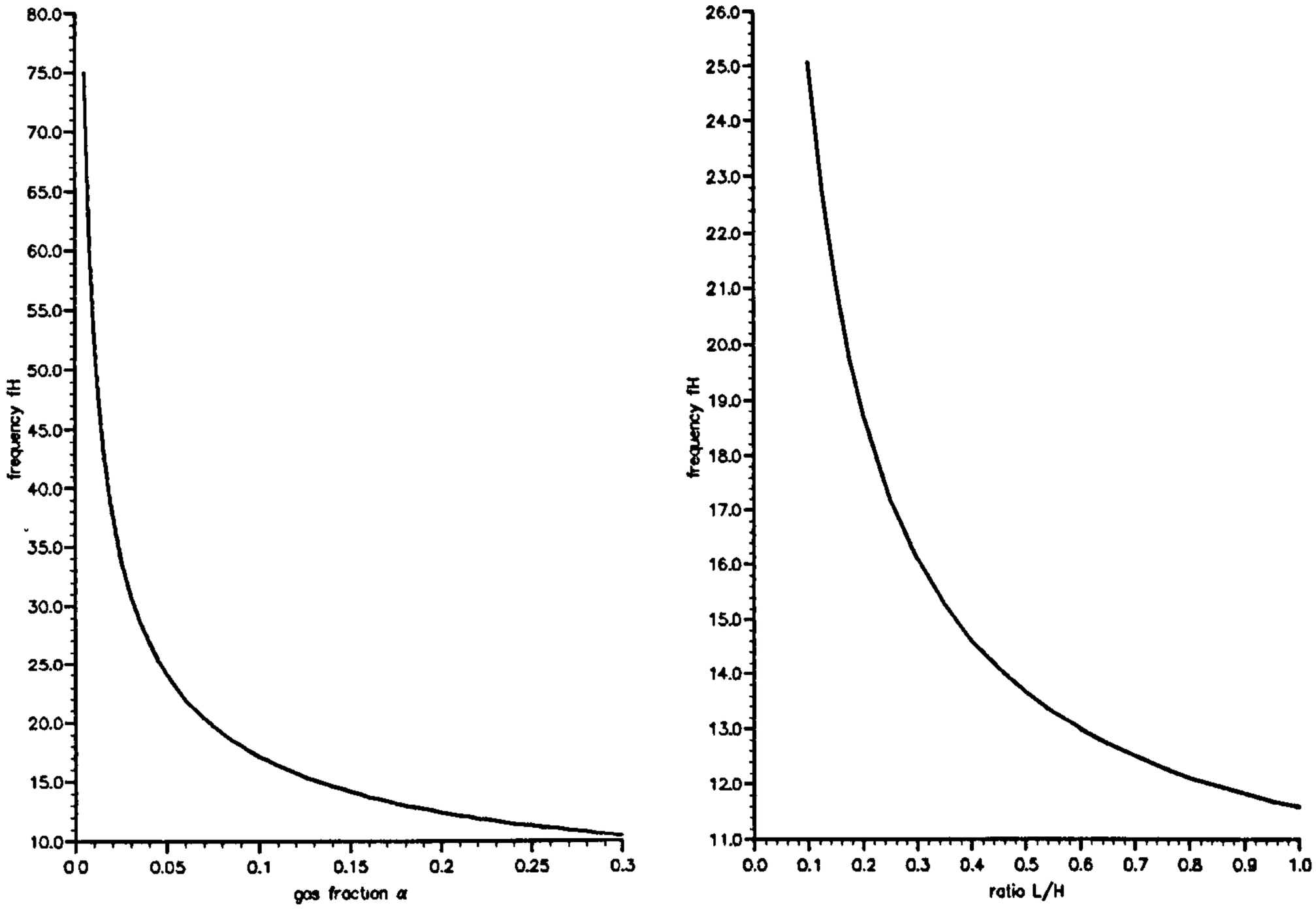

Figure 3.19: Variation of frequency fH with the aspect ratio L/H for α=0.1 (right diagram) and with the gas fraction α for $L = H/4$ (left diagram).

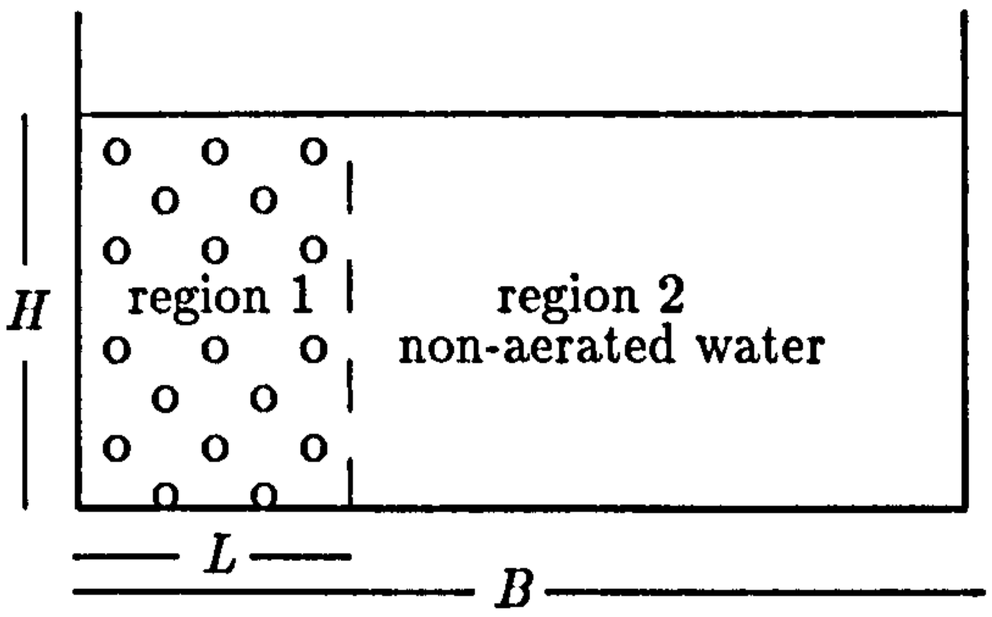

Figure 3.20: Model for a finite tank with a region of length L of bubbly fluid

Proceeding as previously, the reduced wave equation is solved by separation of variables to give

$$\phi_1 = \sum_{n=0}^{\infty} A_{1n} \cos\left[\frac{(n+\frac{1}{2})\pi}{H} y\right] \cos\left[\sqrt{k_1^2 - \left(\frac{(n+\frac{1}{2})\pi}{H}\right)^2}\, x\right] e^{i\omega_n t}$$

$$\phi_2 = \sum_{n=0}^{\infty} A_{2n} \cos\left[\frac{(n+\frac{1}{2})\pi}{H} y\right] \cosh\left[\sqrt{\left(\frac{(n+\frac{1}{2})\pi}{H}\right)^2 - k_2^2}\ (x-B)\right] e^{i\omega_n t}$$

where ϕ_1 is the potential of the fluid in region 1 and ϕ_2 is the potential of the fluid in region 2.

Again assuming pressure and normal velocity continuous across the interface $x = L$ between region 1 and region 2, an expression for the frequencies of oscillation is obtained:

$$-(1-\alpha)\sqrt{\gamma_n^2 - (k_1 H)^2} \tanh\left[\sqrt{\gamma_n^2 - (k_2 H)^2}\left(\frac{L}{H} - \frac{B}{H}\right)\right]$$

$$= \sqrt{(k_1 H)^2 - \gamma_n^2} \tan\left[\sqrt{(k_1 H)^2 - \gamma_n^2}\frac{L}{H}\right] \tag{3.17}$$

where $\gamma_n = (n + 1/2)\pi$.

As the length of the tank B tends to ∞, tanh tends to -1 and so the expression becomes as previously for a semi-infinite domain. For a small region 2, the frequency becomes close to that of a tank full of a bubbly mixture i.e when $B = L$ where the frequencies are given by $\omega H/c = \sqrt{(n+1/2)\pi)^2 + (m\pi H/L)^2}$ for $n, m = 0, 1, 2, 3, \ldots$. The frequency for an unbounded domain with $\alpha = 0.1$, $L = H/4$ and $H = 1$ metre is 17.76 Hertz. The fundamental frequency in a tank full of bubbles $B = L$, for a gas fraction of 0.1, $L = H/4$ and $H = 1$ is 9.86 Hertz thus indicating that a reduction or total loss in the length of region 2 leads to a lowering of the frequency.

In order to study the effect of the length of the tank on the fundamental frequency of oscillation, the width of the region 1 is taken to be $L = H/4$ and the length B is allowed to vary. As can be seen in figure 3.21 the fundamental frequency of the oscillations becomes relatively insensitive to the end of the tank after $B = 4L$.

3.6 Comparison of the fundamental frequencies of a single bubble and bubbly mixture

The entrained air has been modelled separately as a single bubble and also as a

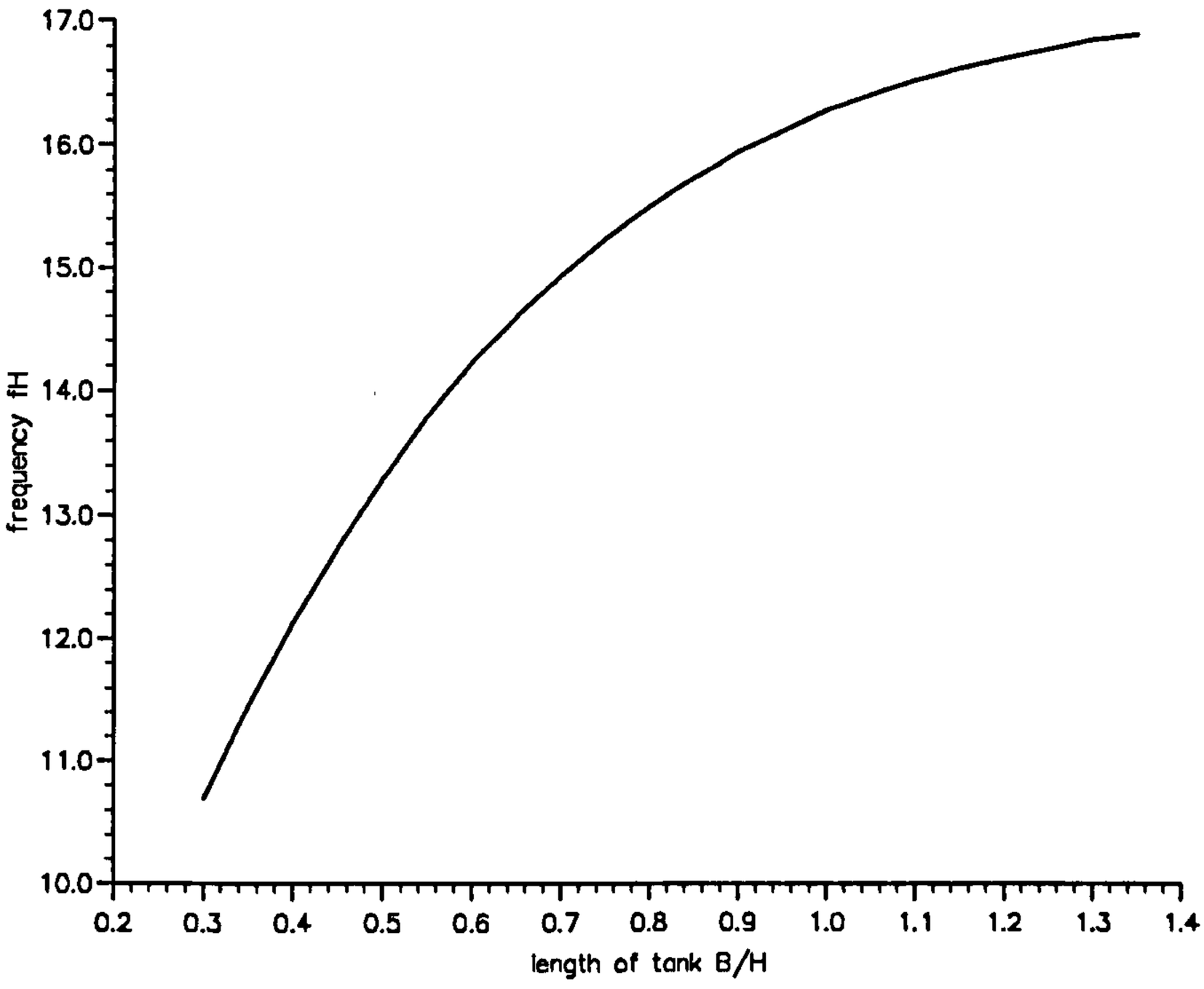

Figure 3.21: Variation of fundamental frequency fII with length of tank B/H. Width of region 1, L, has been taken to be $H/4$.

bubbly mixture. Expressions have been given in the literature, for example Omta (1987) for evaluating the fundamental frequencies of a bubble cloud which are much lower than those of the individual bubbles of the cloud in isolation. To compare the frequencies estimated for a cloud of bubbles and a single pocket, the data from the three examples of an overturning wave given by the numerical computations are used where $h = 0.1$. These have been compared with a simple expression given by Lu, Prosperetti & Yoon (1990) for a three-dimensional circular cylinder bubble cloud of dimension L

$$\omega = \frac{c_b}{2L}. \tag{3.18}$$

Let the width of the column of bubbles be equal to the radius of the two-dimensional pocket, $a = L$. Then the fraction of air in region 1 for the bubbly mixture can be estimated by $\pi a^2/2LH$.

	Example 1	Example 2	Example 3
radius/width $a = L$	0.0071	0.0445	0.0784
distance d	0.245	0.226	0.205
distance H	0.275	0.285	0.284
gas fraction α	0.041	0.245	0.434
single bubble frequency	256.2	59.5	38.8
bubbly mixture frequency	265.2	43.6	31.0
Lu et.al. frequency	668.8	42.6	24.2

Table 3.5: Comparison of frequencies predicted for a single bubble and bubbly mixtures.

The difference between the frequencies predicted by the two analytical expressions in sections 3.4 and 3.5 for the three examples in table 3.5 differ by approximately 20 percent. The single bubble frequency gives higher values for the larger bubbles. Good agreement of the frequency will be dependent on the position of the single bubble on the impact wall. The frequencies predicted by the ratio given by Lu et.al. shows good agreement for the second example, but much higher frequency for the first example with the very small air fraction and a lower frequency for the third example with the highest gas fraction where the presence of the free surface will have raised the frequencies.

3.7 Comparison of experimental data

The numerical method used to obtain a computation for an overturning wave provides many parameters. As shown in the numerical examples, choosing appropriate initial values for the amplitude of the wave and the initial distance in front of the wall, allows different sizes of air pockets to be studied. Very few experimental studies of overturning breaking waves are available in the literature, with which comparison can be made. Given experimental results, either with data showing the size of a trapped air pocket and its position under the free surface, or photographs from which these parameters can be measured, a computation can be used to model the overturning wave and produce a resulting trapped air pocket of the same dimensions. Thus when choosing a computation to compare with an individual experiment, the initial wave height H_o and distance from the wall x_o were varied until a computation for an overturning wave was achieved which gave a good match with the values for the radius a, the distance d of the bubble centre from the bed and the height H of the water after impact measured from the experimental data, primarily video frames from Hattori & Arami (1992). The numerical data for the final computed time also gives values for the normal velocities around the curved surface which can then be averaged to give a radial velocity u_r.

The numerical computations have shown a wave overturning trapping an air pocket between the wavefront and the wall, and the theory in section 3.4 models such an air pocket, providing an expression for the fundamental frequency. Once values for a, d, H and u_r have been obtained, either from a computation or, as in the next section from experimental measurements, these correspond to initial conditions for the bubble oscillations. Hence, the frequencies of the bubble can be predicted using equation (3.11), and the maximum pressure using the linearised kinematic boundary condition, $u_r = \omega\epsilon_o$, $\alpha_o = a\epsilon_o\omega$ and equations (3.9) and (3.10) to get

$$p_{max} = -\rho\omega\alpha_o \log\left(\frac{\lambda a}{2}\tan(\lambda d)\right). \tag{3.19}$$

3.7.1 Hattori & Arami (1992), Hattori, Arami & Yui (1994)

Experimental description

Hattori & Arami have provided many details of their experiments which investigate the importance of a trapped air pocket between the breaking wave and the wall. The experiments were undertaken in a small wave tank with a 1:20 bed slope to cause the wave to break. In each case the still water depth at the wall was five centimetres. High-speed video frames (200 frames per second) were taken of the fluid motion with simultaneous pressure histories. Four pressure transducers P1, P2, P4 and P6 are located vertically along the centreline of the wall at an interval of 2.0 centimetres with the first transducer P1 placed 1.0 centimetre from the bed. Two additional pressure transducers are set 1.0 centimetre (P3) below and 1.0 centimetre (P5) above the still water line and 5.0 centimetres apart from the centreline. Each transducer has a radius of 1 centimetre. The experimental data sets with the largest trapped air pockets were chosen for comparison.

The histories of the pressure, measured on the impact wall immediately after impact exhibit three stages when air is trapped. Initially the pressure rises to a peak value and is followed by an interval of regular smooth oscillations, of decreasing amplitude. These oscillations are displayed with the same frequency in all six pressure gauges. This finally develops into a more confused signal, consisting of higher frequencies with lower amplitudes, and which carries on for an indefinite time.

The photographs show a cylindrical air pocket trapped between the wave front and the structure immediately after impact. The damped oscillations recorded by Hattori & Arami decay exponentially like $e^{-\beta t}$ and the rate at which the amplitude dies away has been given in the following data sets by the logarithmic decrement, the ratio of two amplitudes of motion separated by one period. The peak pressure is presented in the dimensionless form $p^* = p/\rho g H_o$, where H_o is the incident wave height above the bed.

Comparison of data sets

Three sets of experimental data on the formation of an air pocket by Hattori & Arami have been examined in detail. In each case measurements have been taken from the video frames to obtain values for a, d, H, u_f, where u_f is the forward velocity as previously de-

fined in subsection 3.3.1. Pressure traces were given along side the video frames in the experiments. The bubble surface in the frames is not well enough defined to take measurements around the surface and so the value obtained for u_f is used for the radial velocity u_r. The video frames provided indicate a horizontal upper free surface at impact and so the computations of a tanh waveform provide the best numerical model. In addition, for a bubble nearer the bed than the free surface, a higher amplitude wave is required to model the bubble position correctly as the photographs from the small model experiments show the position of the bubble to be nearer the bed. In each of the three cases studied, a table is presented which shows the *measured* values of a, d, H and u_r obtained either from the video frames from the experiments or using a computation and the *estimated* values of f, ϵ_o, α_o and maximum p^* in each case from the theoretical analysis for a semi-circular bubble.

No. 132-3

This data set corresponds to a two-dimensional bubble of radius 0.0075 metres measured from the video frames, along with values for d and H. Comparisons are made with a computation using a wave of initial dimensionless amplitude 8.0 and a distance 6.5 from the impact wall. Using dimensional values, this corresponds to an incident wave height of 0.072 metres giving a trapped air pocket of radius 0.0075 metres with comparable values for d and H. This leads to good agreement for the predicted frequency of the oscillating bubble, although both estimates are higher than that given by Hattori et. al. The radial velocity given by the numerical computations also gives agreement with that measured from the photographs.

	d	H	f	u_r	ϵ_o	α_o	p^*
Hattori & Arami			190				38.1
From video	0.0295	0.066	221	1.0	0.00072	0.0075	43.5
Computation	0.0219	0.055	222.2	0.95	0.00068	0.0070	35.4

Table 3.6: Comparison of theory with experiment and computation for a pocket of radius 0.0075 metres.

From the experimental data, the peak pressure is recorded by P4 at approximately 38.1

with the lowest gauge P1 measuring 31. The damped oscillations last for approximately 0.015 seconds with a logarithmic decrement of 0.47 As can be seen from table 3.6, a predicted pressure of approximately 12 percent higher is obtained for the experimental parameters and 7 percent lower for the computational values.

No. 172-3

The size of the radius of the trapped air pocket from the video frames is estimated at 0.0095 metres. The computation used to produce a trapped pocket of the same size was obtained by using a wave of initial dimensionless height 5.0 and initial distance of 7.4. This corresponds to a dimensional wave height of 0.062 metres. The peak pressure recorded at P4 is 55.7 with the pressure in the lowest transducer reading 43.6. The duration of the damped oscillations is approximately 0.04 seconds with a logarithmic decrement of 0.25.

	d	H	f	u_r	ϵ_o	α_o	p^*
Hattori & Arami			210				55.7
From video	0.029	0.063	186.5	1.1	0.00093	0.01	49.0
Computation	0.03	0.061	191.5	0.99	0.00082	0.0094	39.7

Table 3.7: Comparison of theory with experiment and computation for a pocket of radius 0.0095 metres.

Table 3.7 shows the pressure values predicted by the theory for both the experiment and the computation data are lower than the maximum pressure measured by the transducers. The estimated frequency from the experimental and computational parameters is 11, 8 percent lower respectively.

No. 178-3

The third and final data set chosen has the largest trapped air pocket of radius 0.02 metres and produces the lowest pressures. A computation of a wave with initial dimensionless amplitude 7.0 with an initial distance from the impact wall of 9.0 is used to produce the required size pocket and this corresponds to an incident wave height of 0.086 metres. The highest peak pressure again measured in P4 at 22.5 whereas the pressure at

P1 is roughly 21.6. The decaying oscillations have the longest duration of 0.08 seconds with a logarithmic decrement of 0.41.

	d	H	f	u_r	ϵ_o	α_o	p^*
Hattori & Arami			106				22.5
From video	0.026	0.067	99	0.8	0.0014	0.015	28.7
Computation	0.029	0.069	101.2	0.76	0.0012	0.015	20.0

Table 3.8: Comparison of theory with experiment and computation for a pocket of radius 0.02 metres.

The values shown in table 3.8 give good agreement with the frequency given by Hattori et.al. and the estimates for the amplitudes of oscillations compare well. The pressure values show good agreement with the numerical values.

Comparison of data sets

As can be seen from the comparisons, reasonable agreement is obtained between Hattori et.al. and theoretical results, with larger bubble sizes producing lower frequencies. The measurements from the frames show that the lower surface rises more rapidly up the wall for a smaller pocket in agreement with the numerical computations. The damping of the oscillations appears to be not as strong for the largest bubble and the oscillations last longer. The slow rise of the pocket and mass of small bubbles in the video frame during the oscillations indicate little air loss initially through the surface of the water. Damping has yet to be modelled.

pressure difference with Hattori et.al.	from video	from computation
132-3	12 % higher	7 % lower
172-3	12 % lower	29 % lower
178-3	22 % higher	11 % lower

Table 3.9: Comparison of the maximum pressure estimates for the three data sets.

The pressures predicted by the theory give reasonable agreement for both the experimental and computational parameters. Table 3.9 shows the differences in the pressures estimated with those given by Hattori et.al. in each of the three trapped air pockets. The pressure differences are the percentage change between the peak pressures recorded in the data and values predicted by the theory. Differences with those from the computations are all lower.

3.7.2 Witte (1988)

Witte describes a breaking wave impact against a vertical wall and observed an air pocket trapped against the impact wall. The wave tank had a still water depth at the wall of sixteen centimetres and fourteen pressure cells. Full details are given of one case (example no.13, figure 6.3, type II). Regular oscillations are recorded in all cells of period 12 milliseconds, or a frequency of 83.3 Hertz. The peak pressure measured by Witte for this case is 57.3 kPa.

The report by Witte only contains a sketch of the wave form, indicating a sloping free surface. Thus a computation of a solitary wave is used for comparison. A solitary wave of wave amplitude $0.7h$ and depth of $0.3h$ models the wave, scaling to give an incident wave of 0.18m, with a bubble of parameters $r = 0.029$m, $d = 0.20$m and $H = 0.95$m giving a frequency of 82.7 Hertz. The maximum pressure is estimated by the theory to be 28.1 kPa which is lower than that given by Witte. However the experimental values for the parameters d and H are not available, the computation used here to model the wave may not be the most appropriate.

3.7.3 Oumeraci & Partenscky (1991)

Experimental investigations in a larger wave flume carried out by Oumeraci & Partenscky (1991) of wave breaking on a vertical structure produced a large air-cushion trapped against the impact wall. The incident wave height was 0.48 metres and approached the wall with velocity 3.3 m/s. The data in the report gives a peak pressure of 14.0 kPa.

A computation of a solitary wave is used to model the experiment due to the sloping free surface in the photographs, with dimensionless amplitude 0.6 and depth 0.2, scaled to

give a bubble of radius 0.9m, distances $d = 0.56$m and $H = 0.7$m, producing a fundamental frequency of 27.4 Hertz. The incident wave height of 0.53 metres and radial velocity of 4.6 m/s are both slightly larger than those given by Oumeraci & Partenscky, but the predicted maximum pressure of 15.8 kPa is in fairly good agreement. The forward velocity given in the literature may have been measured in an early stage of the motion, in which case it would increase as the wave became nearer the wall.

3.8 Discussion of Peak Pressures

The numerical computations in section 3.3 for overturning waves have described the pressure field of the wave motion immediately before impact but are unable to describe the actual impact of the water on the wall. Wave impact on a vertical wall has been modelled by the pressure impulse theory in Cooker & Peregrine (1990), where the appropriate solution for an semi-infinite rectangular domain is

$$P(x', y') = 4\rho U_o H \sum_{n=1}^{\infty} \frac{C_n \cos(\alpha_n y') e^{-\alpha_n x'}}{\alpha_n^2} \tag{3.20}$$

where $P(x', y')$, U_o, C_n and α_n are defined in sections 2.2 and 2.3. The two figures 3.22 and 3.23 illustrate the similarity in the contour maps for the pressure field of the final timestep of the computations in example 1 with the hydrostatic pressure subtracted out, and a pressure impulse plot using (3.20) where μ is the size of the region where air is trapped against the wall. The relation between the peak pressure and the pressure impulse is taken to be

$$p_{PK} = \frac{P(x, y)}{\Delta t} \tag{3.21}$$

where p_{PK} is the peak pressure and Δt is the short time in which the fluid pressure rises to its peak value. For the example given in Cooker & Peregrine for no entrained air, the predicted pressure of 22 ρgh from this relation agrees well with the peak pressure from the computations of 26 ρgh, where Δt has been estimated at 0.02 $\sqrt{h/g}$ from the numerical results.

To apply this theory to the computations for a trapped air pocket, an estimate for Δt must be obtained. An alternative approach has to be employed with trapped air pockets as the time Δt cannot be estimated from the numerical results and should be estimated from bubble times. Returning to the analytical theory, the fundamental frequency and

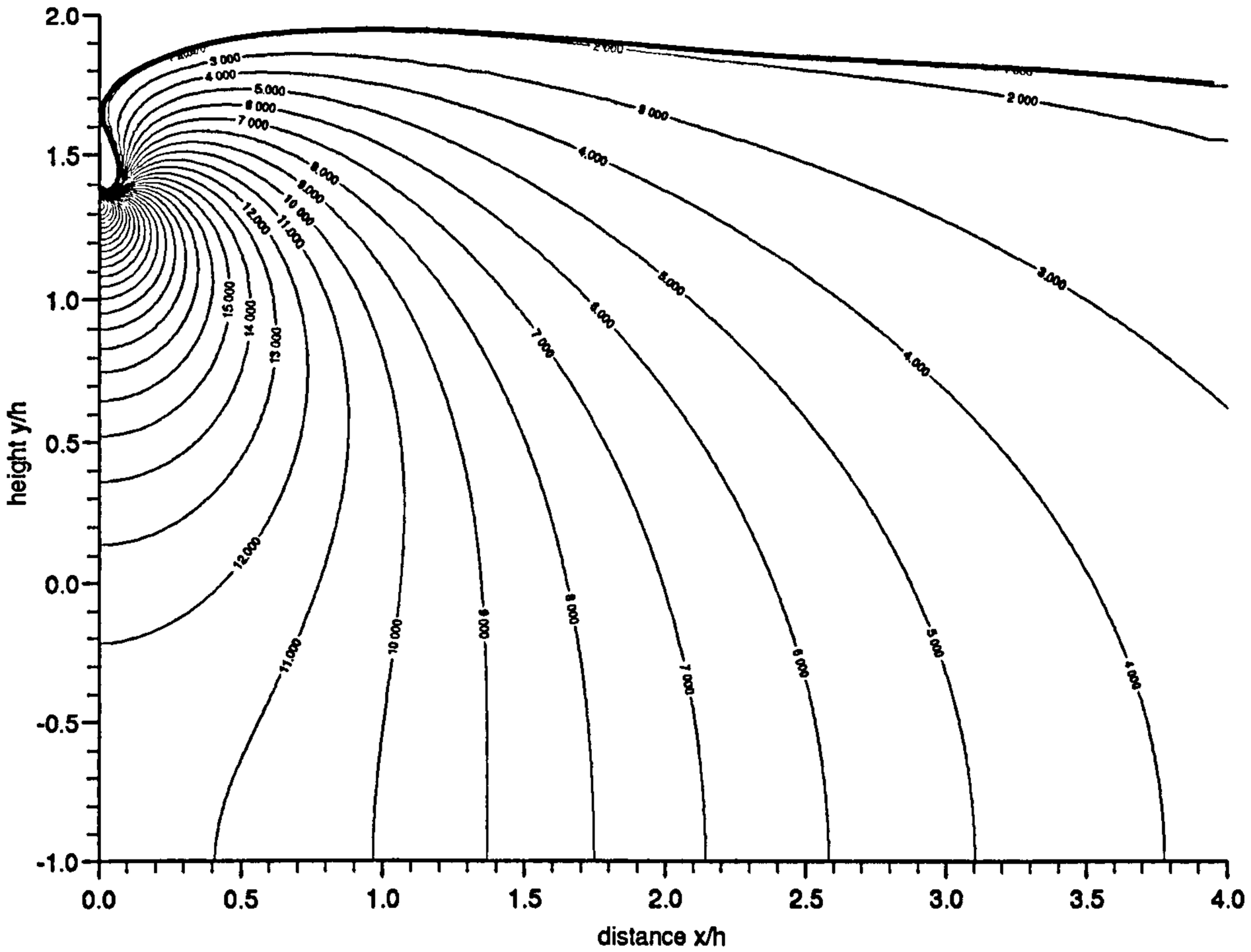

Figure 3.22: Pressure contours from figure 3.4 in example 1, with the hydrostatic pressure subtracted out.

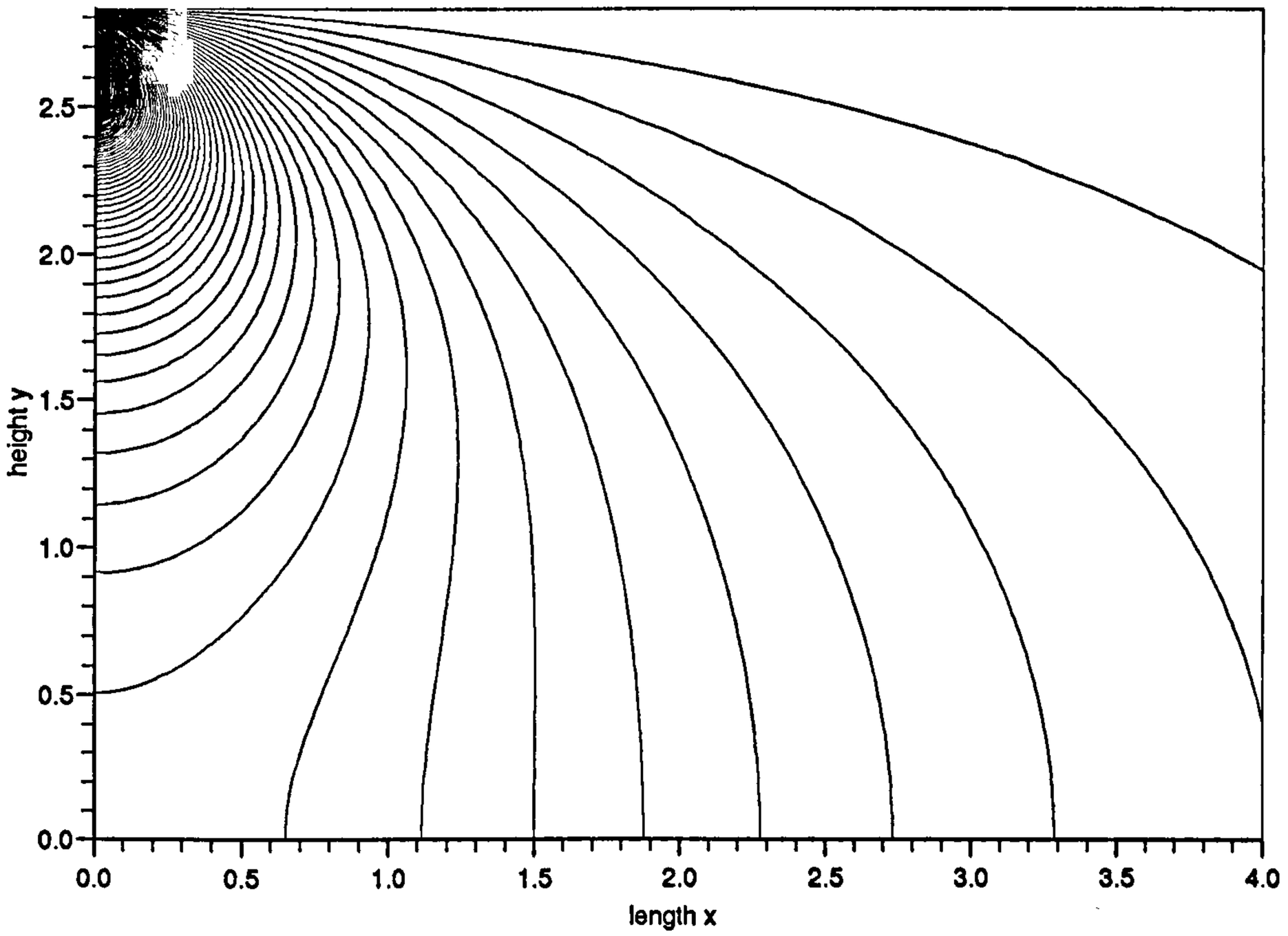

Figure 3.23: Pressure impulse contours $P/\rho U_o$ for a rectangular strip with an impact size μ=0.13.

maximum pressures of a pulsating semi-circular air pocket can be estimated. From the experimental data in Hattori et.al. pressure histories from the transducers, where large air pockets have been trapped giving clear oscillating pressures, show the rise and fall time of the initial peak pressure to be approximately half the period of the ensuing oscillations. In the three cases below, h has been taken to be 0.1.

For example 1 in the computations in subsection 3.3.1, a region of high pressure is found just beneath the waterline. Figure 3.24 portrays the pressure history along three positions on the impact wall as the wave approaches the wall in the final timesteps. A rapid

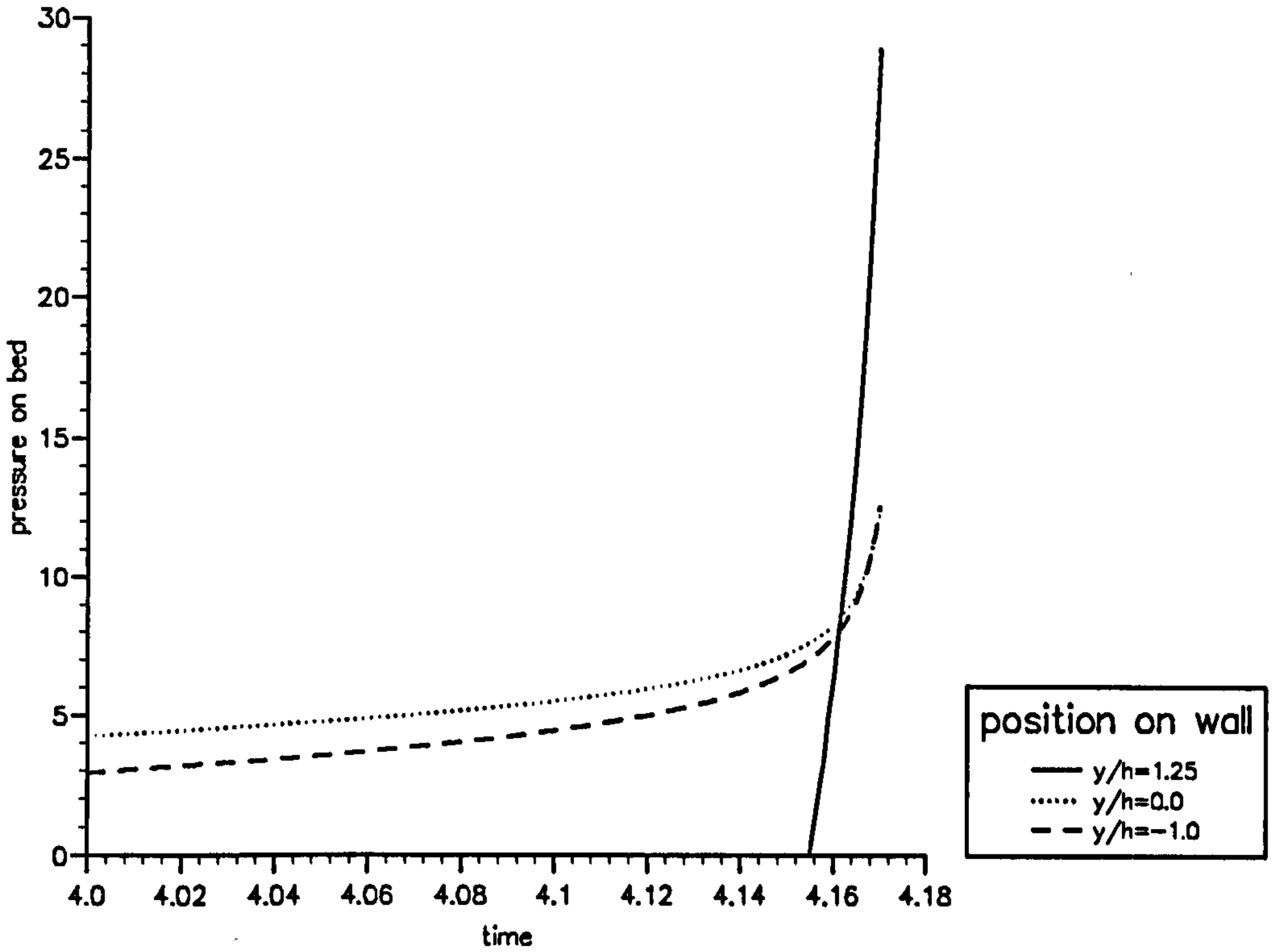

Figure 3.24: Pressure history at three positions along the impact wall for a tanh waveform of initial amplitude 1.7 and distance x_o=8.0

change of pressure is shown at the highest position $y = 1.25h$. From this third curve, the rise time of the pressure shown can be estimated at 0.0015 seconds. Given in table 3.5, the frequency of the air pocket is 256.2 Hertz, or a period of 0.0039 seconds. With a quarter of this period, in addition to the rise time of the pressures in the computation, a value for Δt can be estimated at 0.0025 seconds. The size of the impact region can

be estimated at $1 - H_w/H$=0.13 and the maximum pressure impulse for this value from equation (3.20) is 0.0731 $\rho U_o H$. From the numerical results, the horizontal component of the jet is 3.03 m/s, with the height of the wave at H=0.275 metres. Hence the maximum value of the peak pressure estimated by the pressure impulse theory is 24.4 ρ, compared with a maximum value of 28.3 ρ from the computations showing fairly good agreement.

In the two examples with larger air pockets, the computations show the greatest pressures before impact to lie at the bed of the domain and therefore the peak pressures here are less suitable for comparison with the pressure impulse theory. Thus the total value for Δt will be estimated at $\frac{1}{4}$ the period of the pulsating bubble.

For example 2, as given in table 3.5, the frequency for the air pocket is 59.5 Hertz, or a period of 0.0168 seconds. To compare with the pressure impulse theory, the size of the impact region is estimated by $1 - H_w/H$=0.36, giving a value from (3.20) of 0.305 $\rho U_o H$. The horizontal component of impact has been taken to be the forward velocity u_f, giving a value of U_o=1.802 m/s with the height of the water at 0.285 metres. With the duration of the impact at Δt=0.0042 seconds, this gives a maximum pressure from the pressure impulse theory of 37.35 ρ compared with 30.32 ρ from the theoretical expression.

For example 3, the fundamental frequency of an oscillating air pocket of dimensions given in table 3.5, is 38.8 Hertz or a period of 0.026 seconds. The size of the impact region, covering the air pocket is $1 - H_w/H$=0.464 giving a pressure impulse solution of 0.2703 $\rho U_o H$. The horizontal forward velocity u_f provides a value for U_o of 1.97 m/s and the height of the water is H=0.284 metres. With Δt taken a quarter of the period of oscillation, 0.0065 seconds, the maximum pressure from the pressure impulse theory is 23.3 ρ compared with 20.1 ρ from the analysis.

3.9 Scaling

Most experiments undertaken to investigate wave impact on vertical structures involve laboratory model-scale wave flumes. Scaling from model to prototype remains a complex and not fully understood problem. The number of parameters concerning the motion need to be identified and mathematical relationships established between the dimensionless scaling parameters.

Table 3.10 gives examples of how scale effects could vary the frequencies according to the size and position of a trapped air pocket, using equation (3.11) for the bubble frequency.

	radius a	distance d	distance h	frequency f
	(metres)	(metres)	(metres)	(Hertz)
$\times$ 1	0.001	0.05	0.05	1209.77
$\times$ 5	0.005	0.25	0.25	241.95
$\times$ 10	0.01	0.5	0.5	120.98
$\times$ 50	0.05	2.5	2.5	24.195
$\times$ 100	0.1	5.0	5.0	12.098

Table 3.10: Variation of frequencies with geometric parameters for a cylindrical air pocket where $H = 2d$.

For a wave which breaks giving a bubbly mixture, table 3.11 gives examples of frequencies which could be obtained in model and prototype dimensions, using equation (3.16).

	height H	width L	frequency f
	(metres)	(metres)	(Hertz)
$\times$ 1	0.1	0.025	3947.14
$\times$ 5	0.5	0.125	947.5
$\times$ 10	1.0	0.25	394.7
$\times$ 50	5.0	1.25	94.75
$\times$ 100	10.0	2.5	39.47

Table 3.11: Variation of frequencies with geometric parameters for a bubbly mixture with gas fraction 0.1 and $L = H/4$.

Tables 3.10 and 3.11 show that the frequency varies linearly with the geometric parameters, a property easily deduced from the equations.

When modelling the entrained air as either a single air pocket or a uniform bubbly mixture, expressions for the resonant frequencies have been obtained in each case. Pere-

grine (1994) has suggested, for order of magnitude arguments, a simpler approximation, similar to

$$\omega = (\gamma g H_a / C)^{1/2} \tag{3.22}$$

but without γ, where C is the volume of trapped air per unit length of wall (r^2 for a single bubble or LH for the mixture of bubbles), H_a is the hydrostatic head of water but here γ is included. The comparison of this formula for γ=1.0 (for isothermal bubbles) and 1.4 with the analytical expressions in each case is shown in figure 3.25. As can be seen from

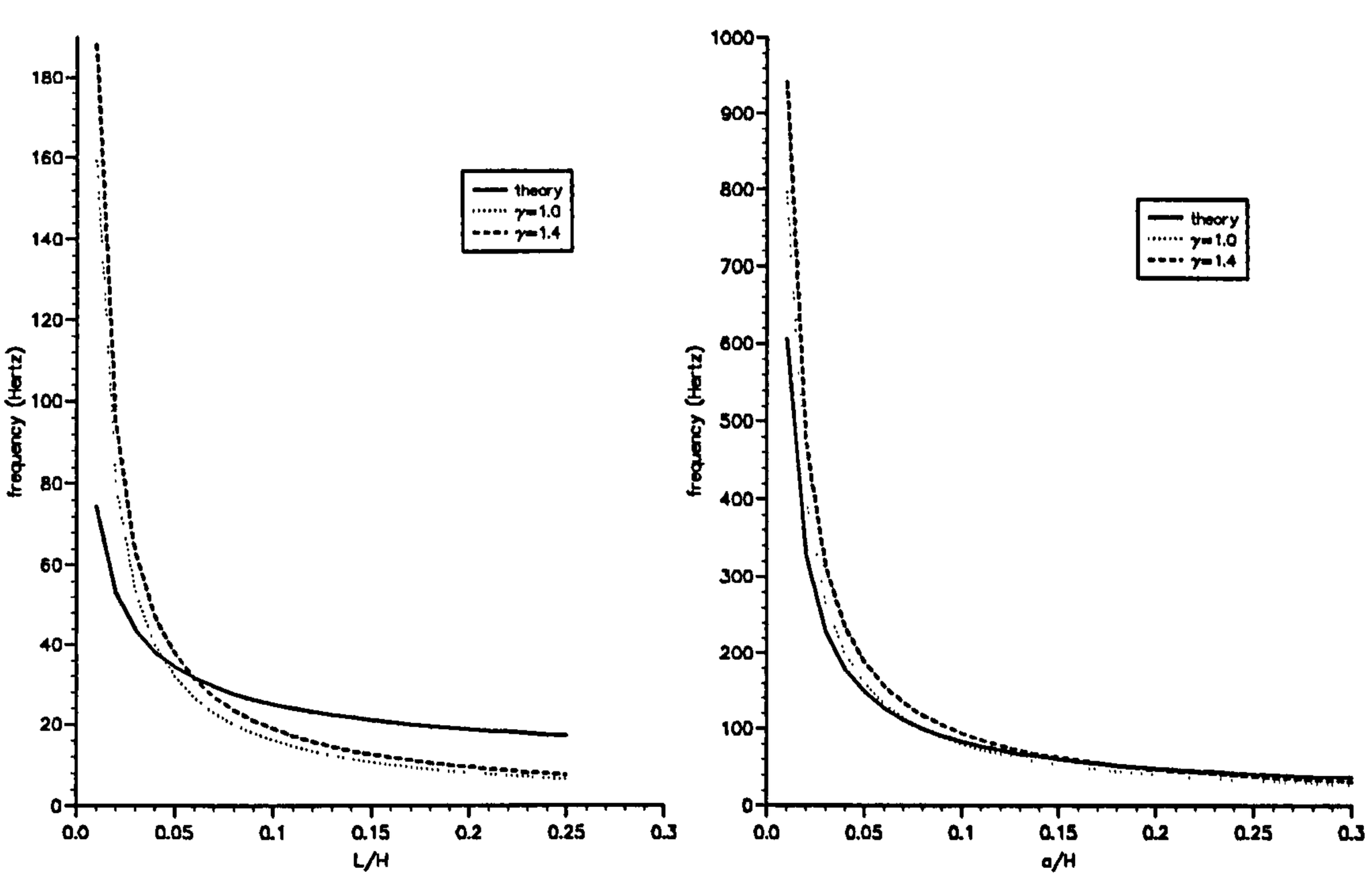

Figure 3.25: Comparison of the estimated fundamental frequencies, for a single cylindrical bubble with $\frac{d}{H}$=0.5 (right) and for a column of bubbles next to a wall with α=0.1 (left).

figure 3.25, the simplified formula presented by Peregrine is within a factor 2, particularly for the single air bubble, except for small pockets or very thin columns of bubbles.

Peregrine (1994) also presents a simple expression to estimate the maximum pressures:

$$\frac{p_{max}}{\rho g h} = \beta \left(\frac{h H_a}{C} \right)^{1/2} \tag{3.23}$$

where β is the fraction of the wall over which this impact occurs and a range in which this lies

$$0.2 \left(\frac{H_a}{h} \right)^{1/2} \leq \left(\frac{p_{max}}{\rho g h} \right) \leq 10 \left(\frac{H_a}{h} \right)^{1/2} \tag{3.24}$$

where C has been taken to lie in the range 0.01 h^2 to 0.25 h^2. To study the formulas, the maximum pressures for the three data sets studied in subsection 3.7.1 have been evaluated using equation (3.23) with the data taken from the computational parameters and compared with the results obtained previously in tables 3.6, 3.7 and 3.8.

	C	h	β	f	f	p^*	p^*
				eq(3.11)	eq(3.22)	eq(3.19)	eq(3.23)
No 132-3	$(0.0075)^2$	0.072	0.27	222.2	212.2	35.4	30.8
No 172-3	$(0.0095)^2$	0.062	0.31	191.5	167.5	39.7	25.8
No 178-3	$(0.02)^2$	0.086	0.58	101.2	79.6	20.0	26.9

Table 3.12: Comparison of estimated frequencies and pressures evaluated earlier for the data sets from Hattori et. al. using the computational parameters, and the simple estimates for frequencies and maximum pressures given by Peregrine.

The maximum pressures predicted by equation (3.23) show agreement with those predicted by equation (3.19) to within 30 percent and thus presents a much simpler calculation for rough estimates. Looking at the range for the pressures given by equation (3.23), the values C= 0.01, 0.02 and $0.05h^2$ are obtained for No 132-3, 172-3 and 178-3 respectively, giving $p_{max}/\rho gh$ to be 3.2, 4.4 and 2.1 $(H_a/h)^{1/2}$ respectively, nicely in the range given by (3.24).

Chapter 4

Reflecting Pressures in a Container

4.1 Introduction

In this chapter, the more moderate pressures resulting from large reflecting waves on vertical walls are investigated. In particular, the sloshing motion found inside confined spaces due to wave generation by external forces. These provide reflecting motions with a relatively low pressure field. In this way, some of the violent surface motions found in vehicle or vessels due to tank accelerations can be studied.

A periodic version (discussed in Dold (1992)) of the numerical boundary-integral method described in section 3.3 in chapter 3 for computing the two-dimensional motion of a water surface on a finite depth is used. By prescribing the initial data for the surface profile and velocity potential, using linear solutions for standing waves on a finite depth but with large amplitudes, large sloshing motions can be simulated. This has enabled the time histories of various surface profiles and pressure distributions beneath the water surface of large reflecting waves in a confined two-dimensional domain to be studied. Samples from the wide range of possible examples are presented.

By providing symmetric initial data, this numerical study enables the motion in a tank to be presented and the forces on the side walls due to large standing waves are evaluated.

Penney & Price (1952) have studied finite periodic stationary gravity waves and investigated the maximum height and the crest of the greatest stationary wave. They noted the crests of the waves become sharper and the troughs flatter as the amplitude is increased

and that there is no instant at which the surface is perfectly flat. The wave profile has its maximum amplitude when the water is momentarily at rest. The criterion limiting the amplitude of the waves was stated to be that the downward acceleration at the crest at the wave's greatest height must not exceed gravity. If periodic stationary waves in water of finite depth exist, their maximum amplitude will depend on depth and tend to zero as the depth is decreased. The results found a maximum crest height of 0.141 λ and trough depth of 0.078 λ where λ is the wavelength. The study included the oscillations produced when waves impinge on a vertical breakwater and two-dimensional oscillations in a deep rectangular tank. A discussion of the results from Penney & Price and a comparison with an experimental study was given by Taylor (1953), who found good agreement with his results and the calculated form of the profile of the highest wave which had an angle of very near 90 degrees.

Saffman & Yuen (1979) continued this line of investigation with numerical computations of large amplitude standing waves in inviscid irrotational fluid on deep water commencing the motion either as a release from elevated rest or by application of pressure, and found standing waves of greater height and slope than Penney & Price.

A numerical method to calculate the motion of two-dimensional standing waves was used by Mercer & Roberts (1992) to determine extremely steep standing water waves. As the crest acceleration increases, the crest height above mean level increases and the crest becomes sharper and narrower. Profiles of standing waves with a crest acceleration of 98 % of gravity were accurately obtained. Milman (1993) produced a substantial and reassuring study of the accuracy of the computations of large standing waves using this program.

The importance of slosh loads in designing tank support structures and internal tank components was studied by Abramson, Bass, Faltinsen & Olsen (1974) related to problems due to slosh loads in liquid natural gas cargo including a discussion of compressibility effects and appropriate scaling methods. The tank accelerations, liquid fill depth and tank geometry were identified as important parameters for slosh loads. In addition, the report suggested the rigidity of the fluid vessel would become an important parameter if the liquid and structural motions were to couple.

Pugh (1985) made a study of the surface profiles and velocity field of standing waves using this boundary-integral method where the surface profile used in the initial conditions

was a simple approximation given by Longuet-Higgins (1973) for a profile of a standing wave of maximum height. Sixty points were used by Pugh to describe the free surface.

The importance of parameters involved with the sloshing motions was studied by Corrignan (1992) using experimental results from scale model tests. These were undertaken in rectangular tanks partially filled with water and subjected to random excitation. Pressure measurements were taken for different fill levels and the corresponding fluid motions described: 10 percent produced a hydraulic jump together with small travelling waves, 30 percent were mainly characterized by stationary waves of relatively high amplitudes on which travelling waves were superimposed, 60 percent produced mainly stationary waves with high impacts recorded on the vertical walls and occasionally on the ceiling, 96-98 % resulted in very high pressure peaks on the ceiling close to the vertical end walls. The impact pressures were found generally to be one of two types, i) pressure peaks of high amplitudes with very short duration for example 1 ms and ii) pressure peaks of lower amplitudes with a longer duration for example 100 ms. Identical pressure peaks however were seldomly recorded showing the random nature of the sloshing phenomena.

4.2 Numerical Computations

The numerical algorithm described in section 3.3 in chapter 3 for an irrotational, inviscid, incompressible flow allows a wide range of two-dimensional water motions to be studied. For the present purpose of modelling the sloshing motions of a liquid inside a container, the numerical program has been used to perform computations with a periodic surface in a tank with finite depth by prescribing linear solutions for standing waves, but with large surface and potential amplitudes, as initial data. Standing waves are usually encountered in confined spaces and are used here to model the motion of fluid sloshing inside a rectangular container.

The superposition of two simple harmonic wave trains of equal amplitude and period travelling in opposite directions results a standing wave with vertical and horizontal oscillation. For linear waves, the surface disturbance is of the form

$$\eta = a_1 \cos x \cos \omega t. \tag{4.1}$$

where here ω is set to 2π. The surface profile is chosen in the form of a cosine curve of

amplitude $a_1 \cos x$ which varies between $-a_1$ and a_1. Where the wave has not been chosen to start from rest, the initial potential of the motion is also in the form of a cosine wave, $a_2 \cos x$ where both a_1 and a_2 are specified in the initial data. The initial data are chosen to ensure symmetry in the domain, thus representing a wall in the centre and at each end of the domain picturing two tanks. The computations allow for additional printouts at times of maximum and minimum kinetic energy levels of the water surface along with other chosen times. Eighty points have been used for the discretisation of the free surface for the initial examples.

A selection of examples of large amplitude standing waves are presented with a discussion of the characteristics of the surface profiles and pressure distributions at times of minimum and maximum kinetic energy given by the numerical method. A range of figures has been displayed to indicate some of the profiles which occur resulting from different choices of initial conditions. This is followed by a discussion of the program parameters.

4.2.1 Surface Profiles

The computations described in this subsection were undertaken using 80 points and a tolerance of 0.00001. The first two examples follow the time history of the surface profiles of a large amplitude standing wave, starting from $t = 0$. The initial conditions are for a wave of an initial surface amplitude a_1=0.6, starting from rest with a_2=0, on a depth of 1.0.

The profiles in figure 4.1 commence with a trough of amplitude -0.6 in the centre of the domain shown (initial surface amplitude 0.6 at x/h=0) which then rises up in time to give a wide crest at the final time shown, t=3.00, giving a maximum height of 0.81. The five surface profiles in figure 4.1 are presented in time intervals of 1.0, starting from t=0, where the additional profile at t=1.66 has been included. This is at a time of maximum kinetic energy.

Figure 4.2 displays a continuation of the time history of the surface profiles for this wave. Now the centre of the surface is at a position of maximum height 0.75 for the initial profile and becomes lower in time with the waterline at the sides of the domain rising. Two additional profiles represent a time of minimum kinetic energy 4.9 %, at t=3.40, and a time of maximum kinetic energy 96.6 %, at t=5.16. The final computed time is at

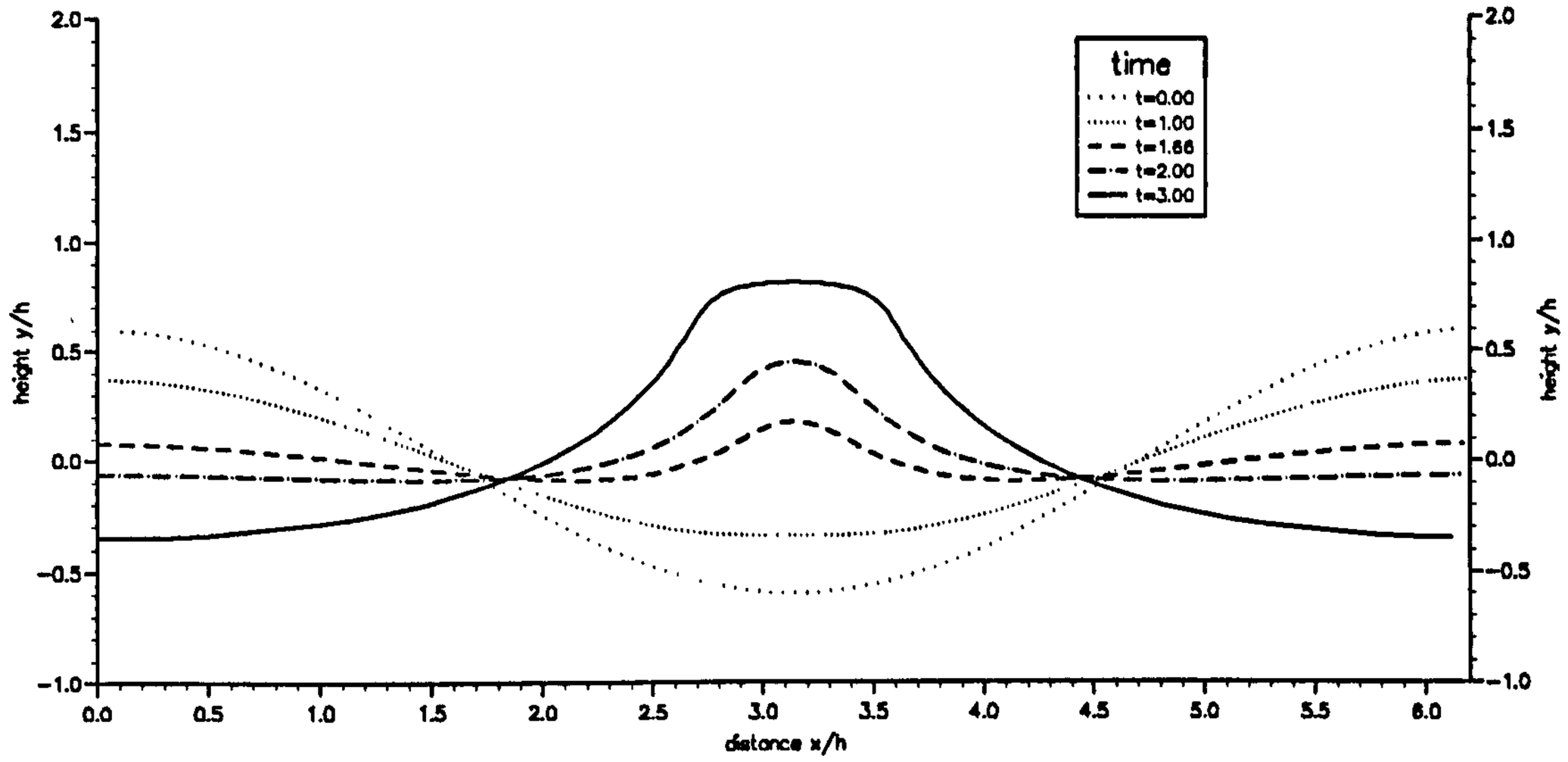

Figure 4.1: Surface profiles of a standing wave of initial surface amplitude 0.6, starting from rest on a depth of 1.0.

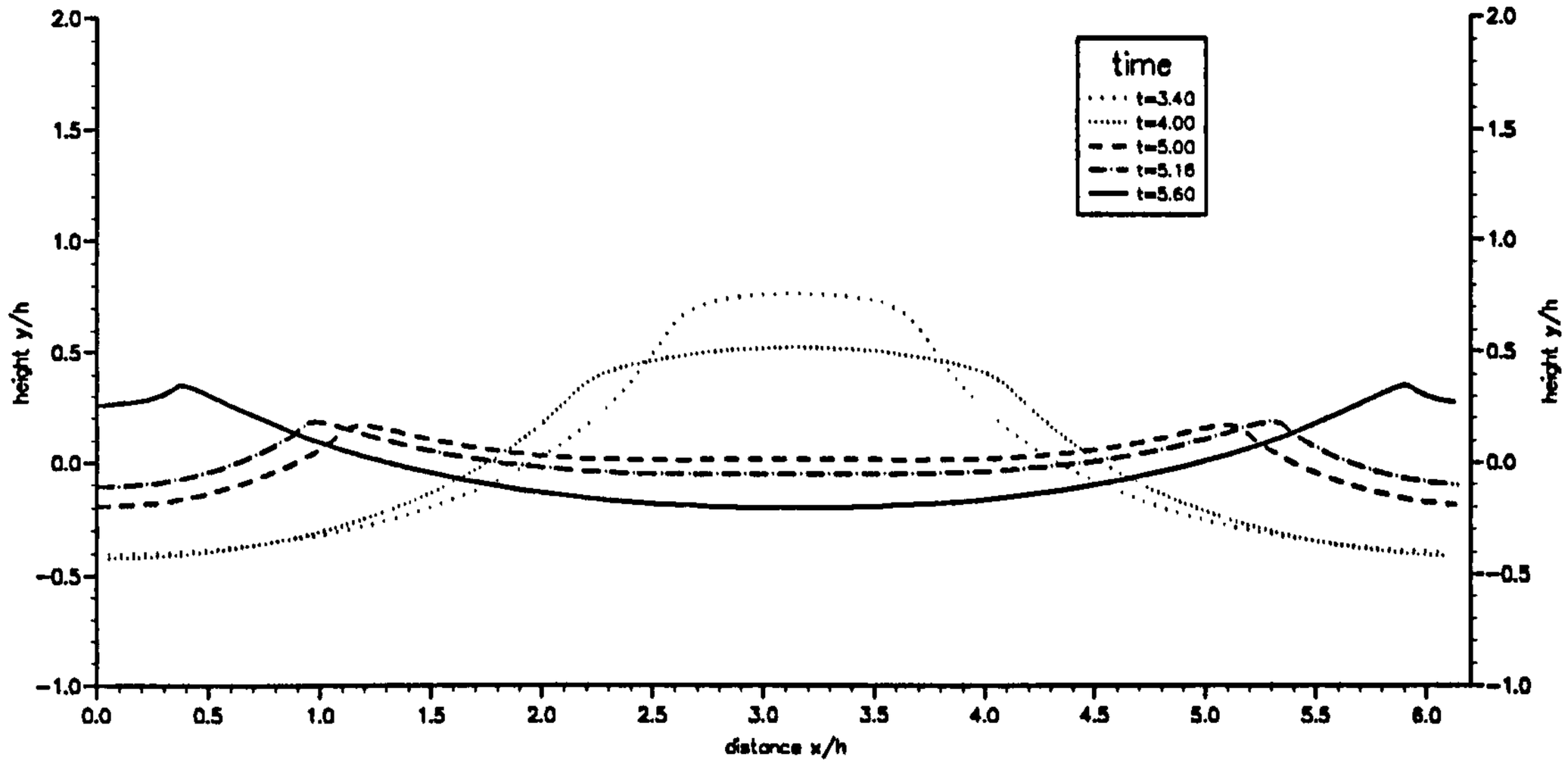

Figure 4.2: Surface profiles of a standing wave of initial surface amplitude 0.6, starting from rest on a depth of 1.0.

t=5.60 where the trough depth is at -0.21. As can be seen from the curves, a sharp corner has begun to develop and the limitations of the numerical program are reached when the height of the corner reaches 0.35. The surface profiles from these two figures show that the wave has its minimum kinetic energy when the wave has a large wide crest and its maximum kinetic energy when the wave is in a trough.

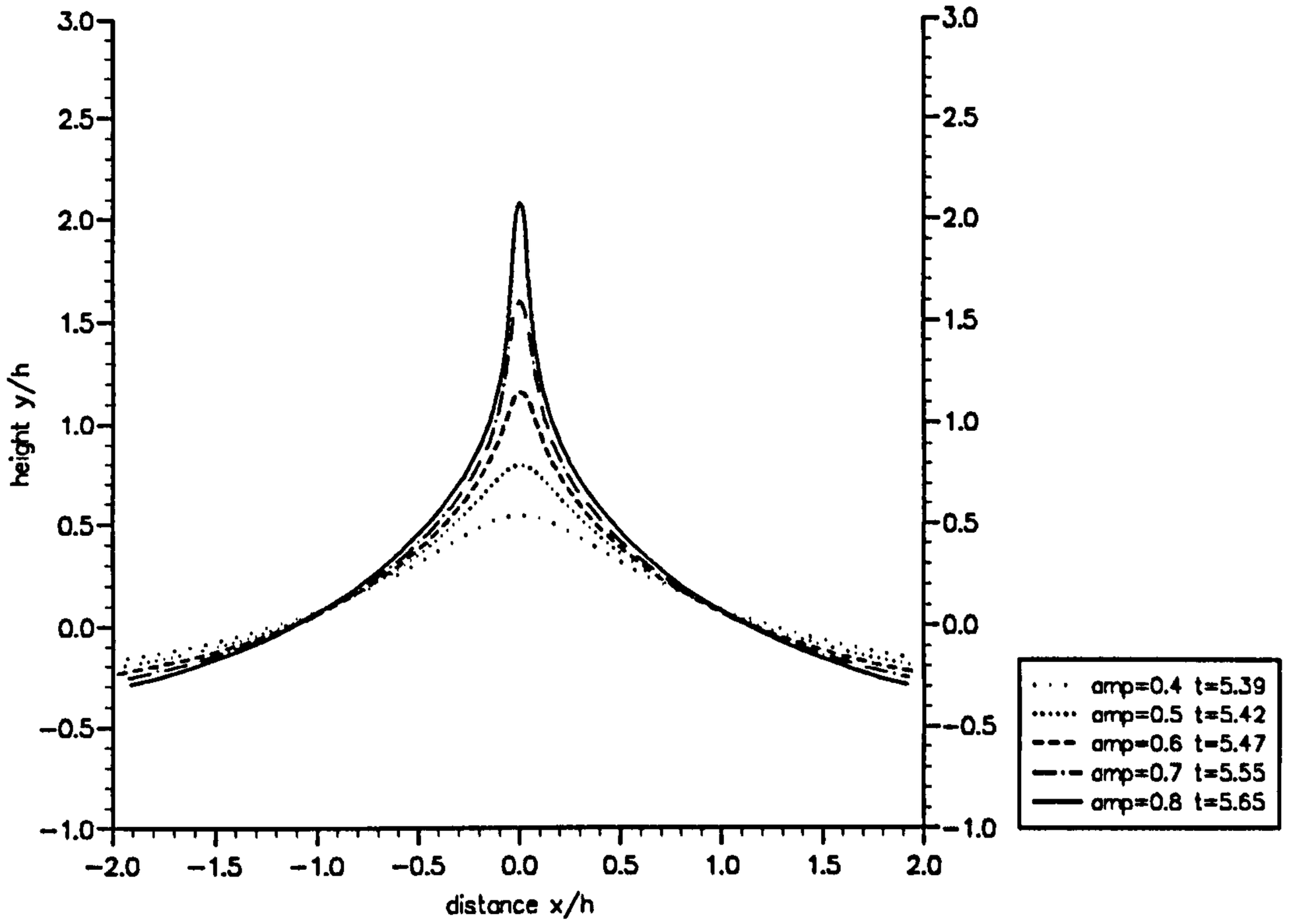

Figure 4.3: Surface profiles for a standing wave with zero initial surface amplitude and varying potential amplitude a_2 on a finite depth of 1.0.

For a standing wave with zero initial surface amplitude, a_1=0, but varying initial potential amplitude, figure 4.3 displays surface profiles of a standing wave on a depth of 1.0. The initial conditions give the potential amplitude in the form of a cosine wave, with the size of a_2 given in the legend in the figure along with the time at which this profile occurs. The surface profiles presented are at a time of minimum kinetic energy and a tall, thin jet forms for the bigger amplitudes. To help distinguish between each profile, the complete domain has not been shown.

Figure 4.4 shows a portion of the surface profile of a standing wave of zero initial surface amplitude and initial potential amplitude a_2=-0.6 at an instance of minimum

kinetic energy for different depths. A smooth crest is produced and the maximum wave height is found to increase with depth, although at a slower rate, as the depth becomes greater. After the depth is larger than 1.0, in this example, the change in profile and the time at which the minimum kinetic energy occurs becomes insignificant.

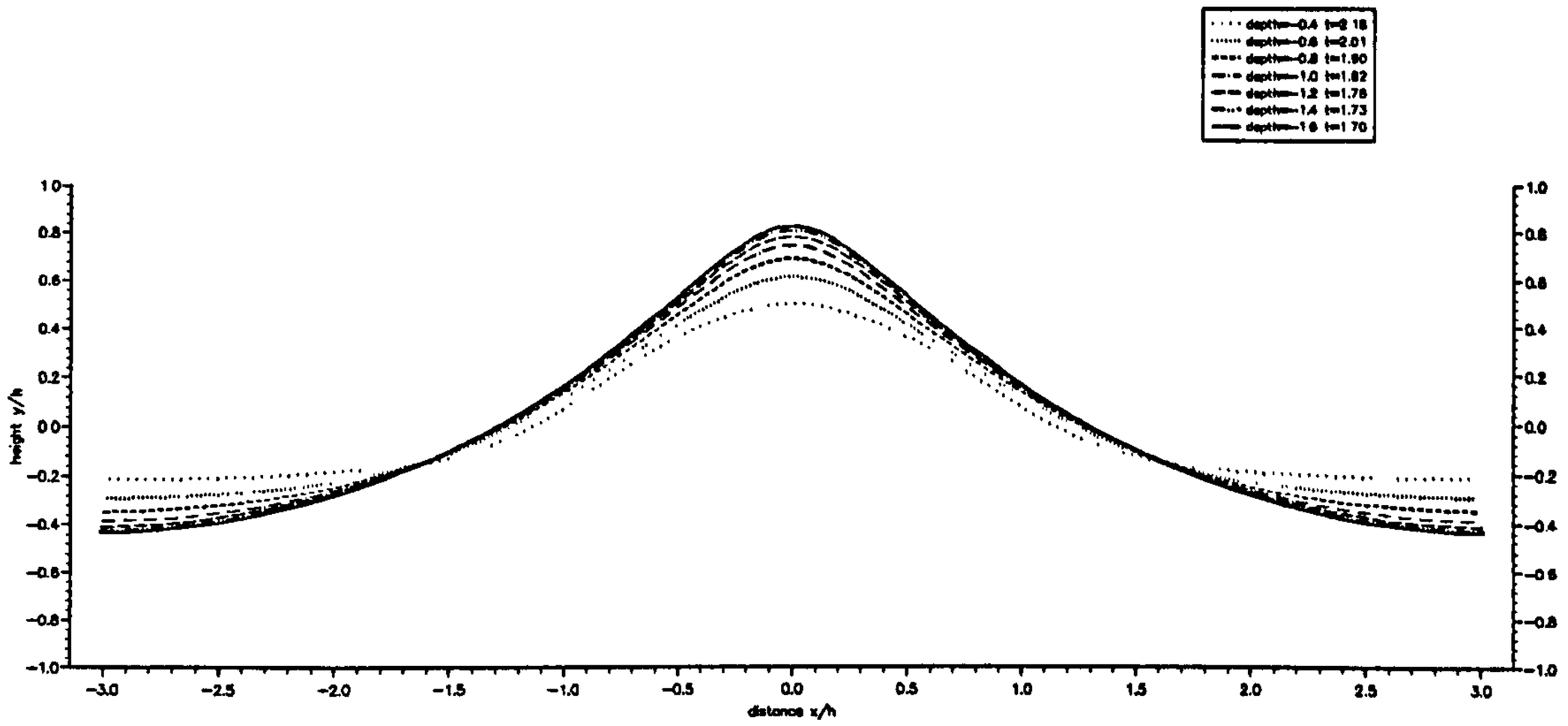

Figure 4.4: Surface profiles for a standing wave of initial potential amplitude -0.6 and zero initial surface amplitude for different depths.

The surface profiles for a wave of still water depth of 1.0, for increasing initial surface and potential amplitudes, at the first time of minimum kinetic energy are displayed in figure 4.5. In each case, the initial data given for the size of the surface amplitude is the same as that for the size of the potential amplitude, $a_1 = a_2$. As can be seen from the diagram, the instance of low kinetic energy corresponds to the wave with a wide flat-headed crest for the larger amplitudes. The corresponding crest accelerations of each wave is shown for the maximum height at the centre of the wave. This acceleration becomes greater in the downwards direction as the amplitude increases. For the largest waves the acceleration of the free surface, along the horizontal crest head at the maximum height, becomes lower at the point of symmetry than at other points. Thus for the largest amplitude 1.0, the greatest negative acceleration along the flat crest head is approximately -1.05, although at the centre point it is -0.988.

The maximum height of the crest shown in figure 4.5 is plotted in figure 4.6 along with the size of the initial amplitudes a_1=a_2. For an initial surface and potential amplitude

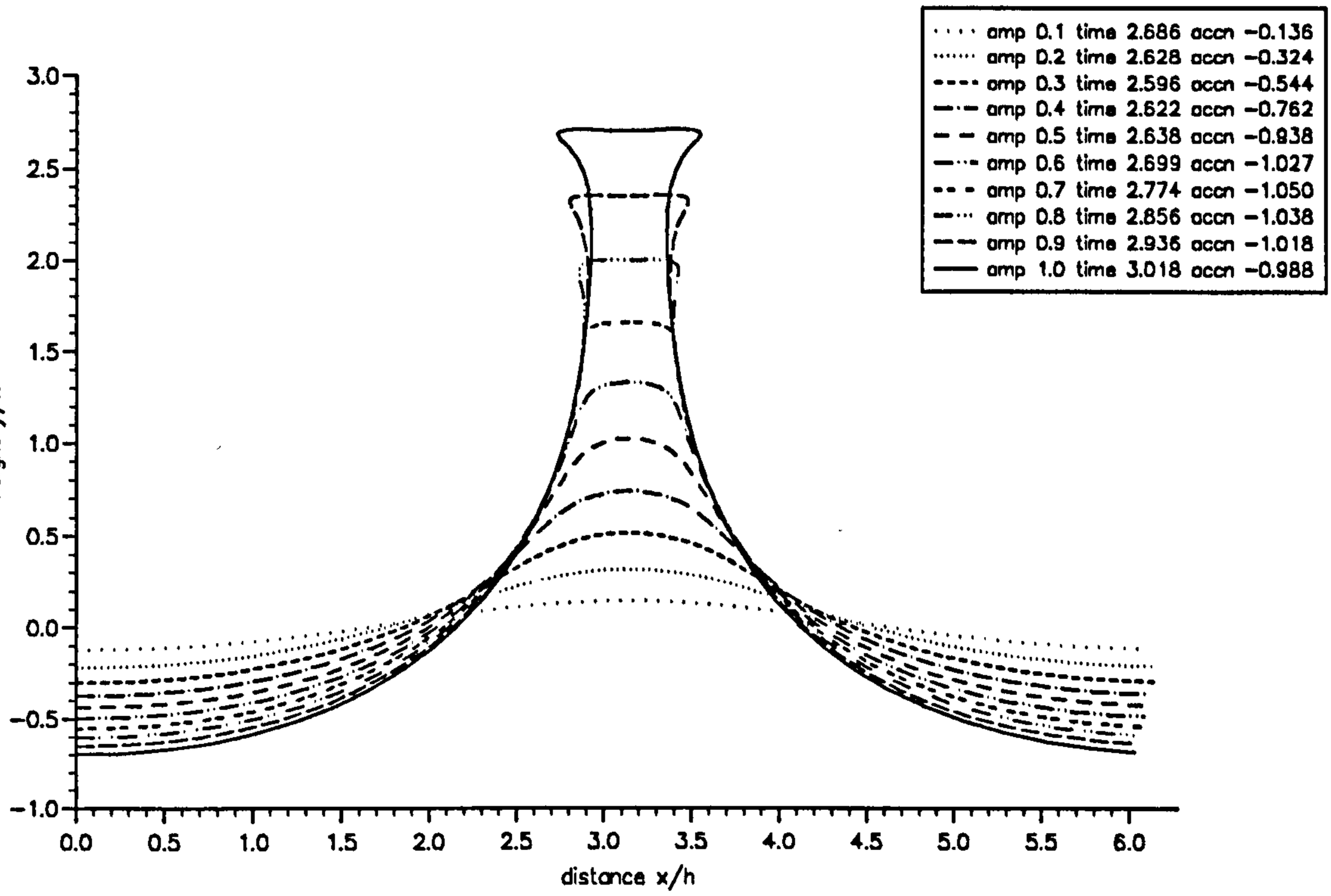

Figure 4.5: Surface profiles of large standing waves for different initial surface and potential amplitudes with an initial still water depth of 1.0, at the first time of minimum kinetic energy and the corresponding accelerations at the maximum height of the centre of the crest surface.

of 0.3, for example, the maximum waterline is 0.514, just less than double the initial amplitude. For an initial surface and potential amplitude of 0.8, the maximum waterline is 2.0, $2\frac{1}{2}$ times the initial amplitude.

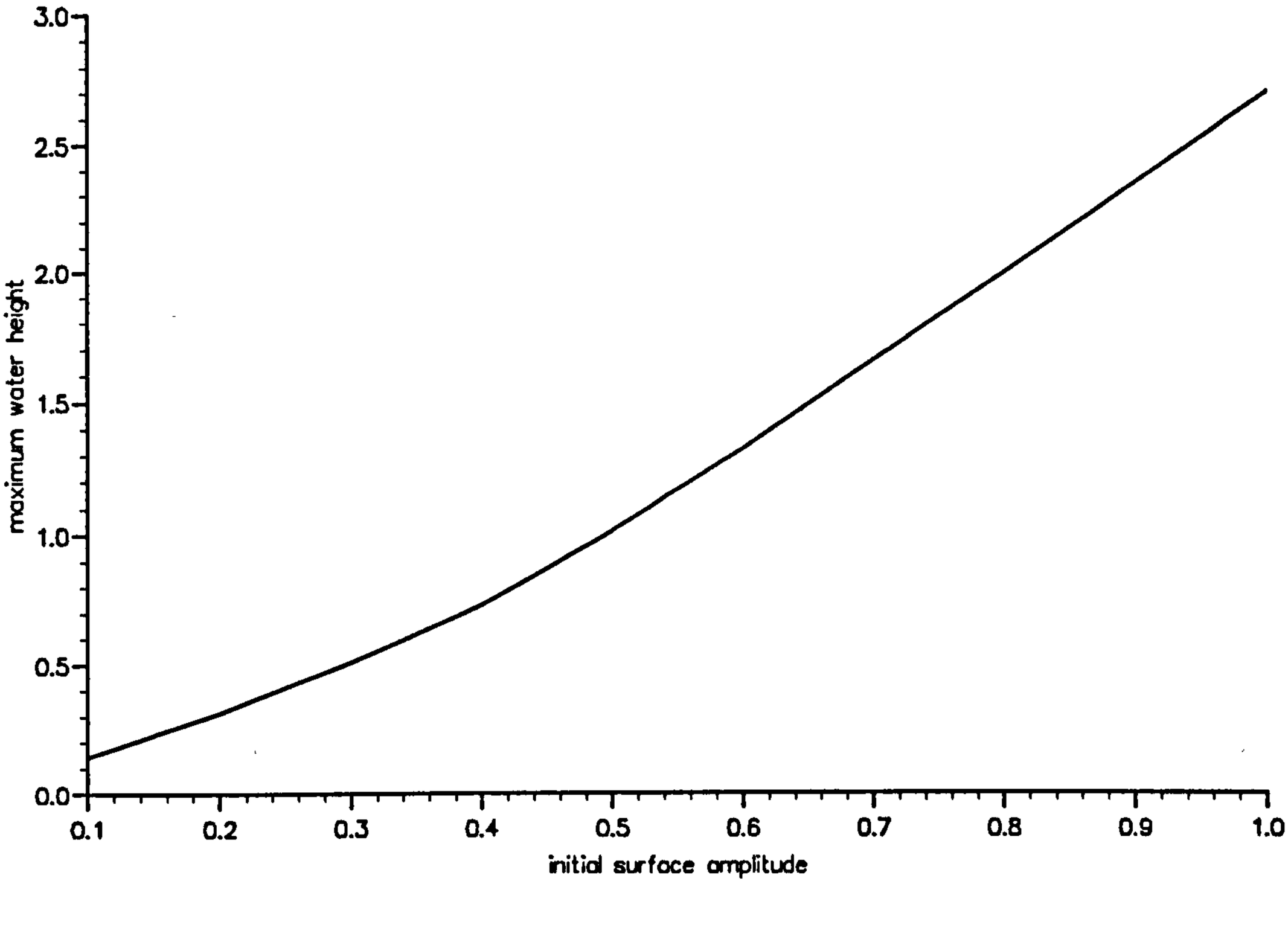

Figure 4.6: Maximum waterline for increasing initial surface and potential amplitudes on a finite depth of 1.0 at a time of minimum kinetic energy given in the previous figure.

4.2.2 Pressure Distributions.

Once the motion of the surface has been determined, the pressure field beneath the free surface can be evaluated. To study the pressure distributions beneath the surface due to the motion of the water, contour maps with the same increments for a wave of initial surface and potential amplitude both 0.8, depth 1.0, at two instants have been presented in figures 4.7 and 4.8. The first map is at an instant of maximum kinetic energy 96.3 % and the second map is at an instance of minimum kinetic energy 0.98 % .

The pressure contours in figure 4.7 at the first time of maximum kinetic energy, t=0.85, show the highest pressures at the bed in the centre of the domain. Closely packed isobars are found immediately beneath the surface and a maximum pressure of approximately 1.7

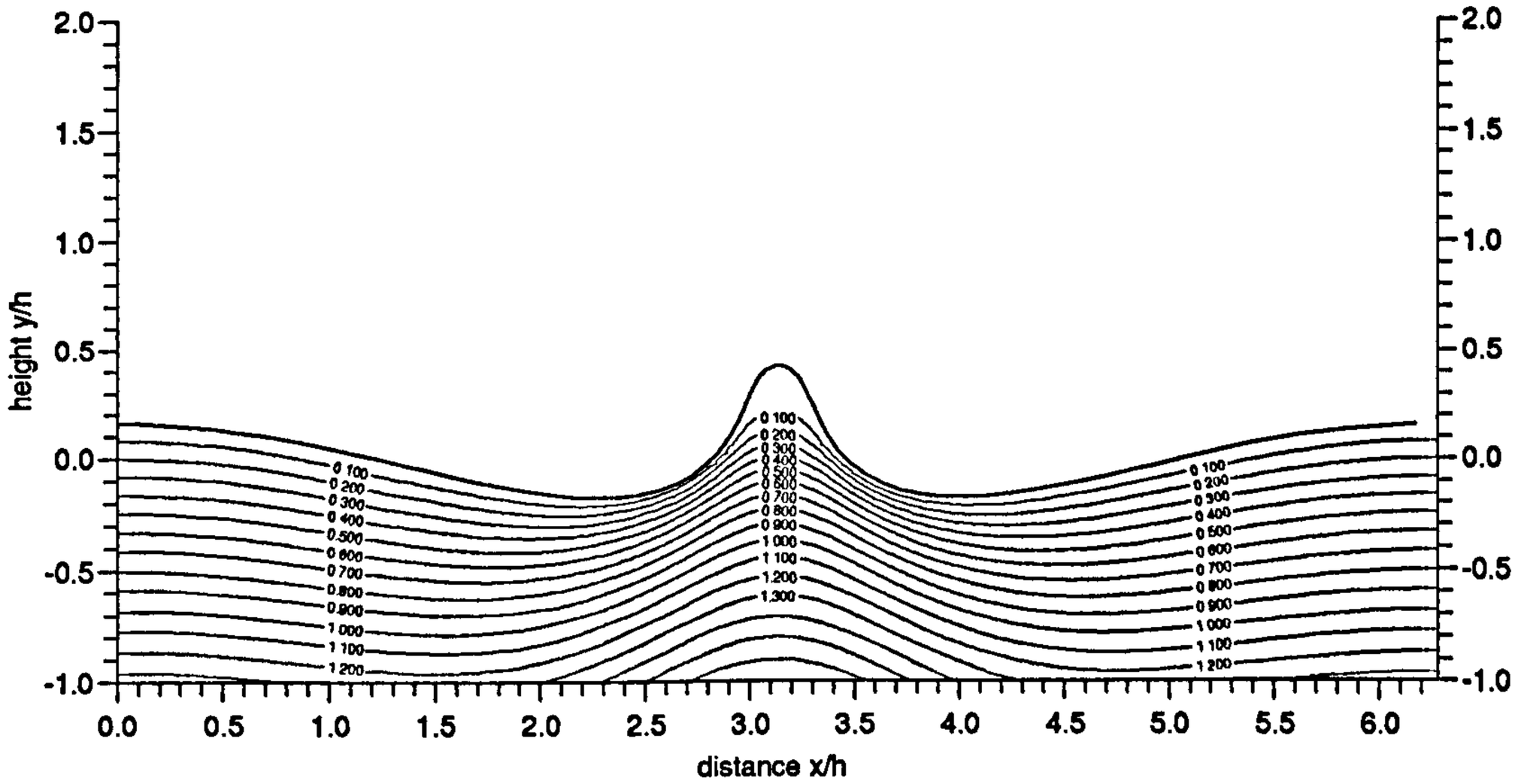

Figure 4.7: Pressure contours with increments of 0.1 for a large standing wave of initial surface and potential amplitude 0.8 at a dimensionless time of 0.85, a point of maximum kinetic energy.

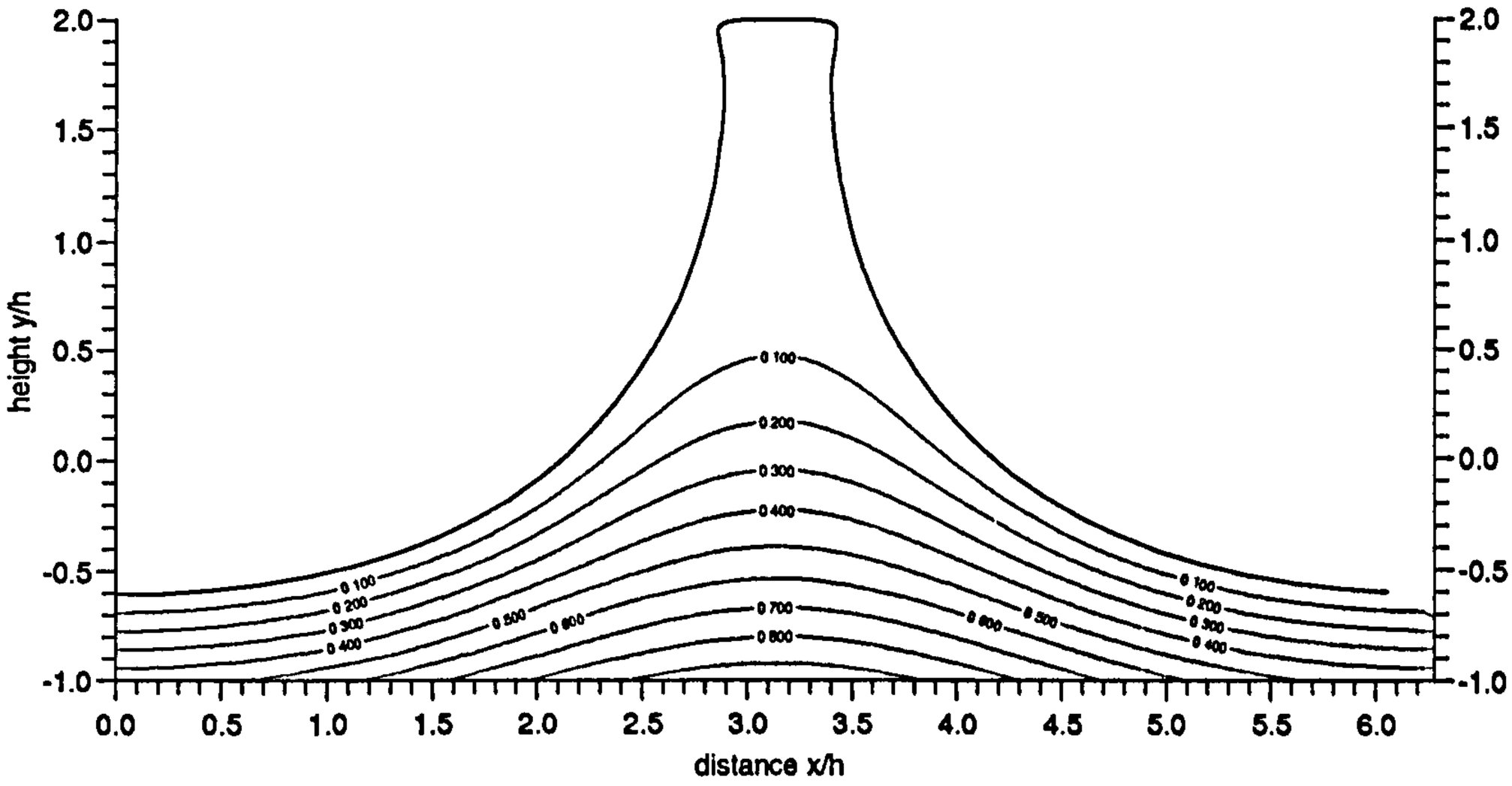

Figure 4.8: Pressure contours with increments of 0.1 for a large standing wave of initial surface and potential amplitude 0.8 at a dimensionless time of 2.86, a point of minimum kinetic energy.

on the bed.

In contrast with figure 4.7, the pressure contours at a time of minimum kinetic energy, t=2.86, in figure 4.8 reveal a lower pressure field. Less densely packed isobars are now found beneath the trough and most of the crest head contains very low pressures. At the wave's maximum height, the pressure values at the bed are lower everywhere than that in still water and the pressure gradients near the crest are very low. As a result of the symmetric initial data, a wall could be placed in the centre or edge of the domain shown in each case.

4.2.3 Motion in a tank

Due to the symmetry of the initial conditions, the flow can be considered to be bounded by a wall on any plane of symmetry, and the large amplitude 'sloshing' motion inside a tank can be modelled. For a large standing wave of initial surface and potential amplitude

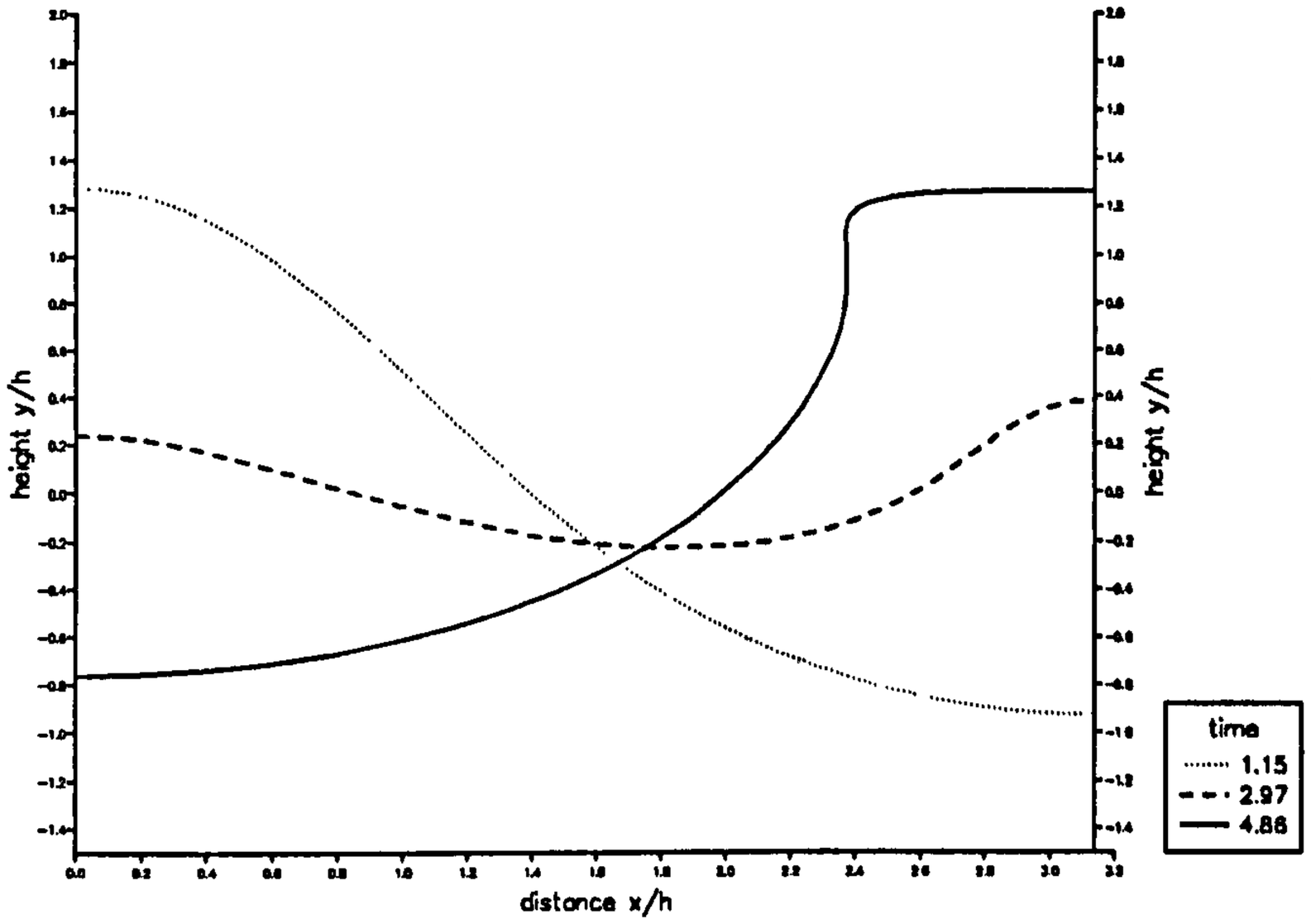

Figure 4.9: Surface profiles for a large standing wave of surface and potential amplitude 0.6 and -1.0 respectively at an initial depth of 1.5 for dimensionless times 1.15, 2.97, 4.86.

a_1=0.6 and a_2=-1.0 respectively, with an initial still water depth of 1.5, the surface profiles at two times of minimum and one time of maximum kinetic energy have been computed,

shown in figure 4.9 again using 80 points with a tolerance of 0.00001.

The first surface profile is at the first time of maximum kinetic energy in the computations, t=1.15, and the waterline is at a maximum height on the left side wall. The second surface profile at a time 2.97 shows the waterline at a much lower level and this is at the first time of minimum kinetic energy. The surface profile then rises again, this time to give a height of 1.26 on the other side of the 'tank' and this is at the second instance of maximum kinetic energy, t=4.86.

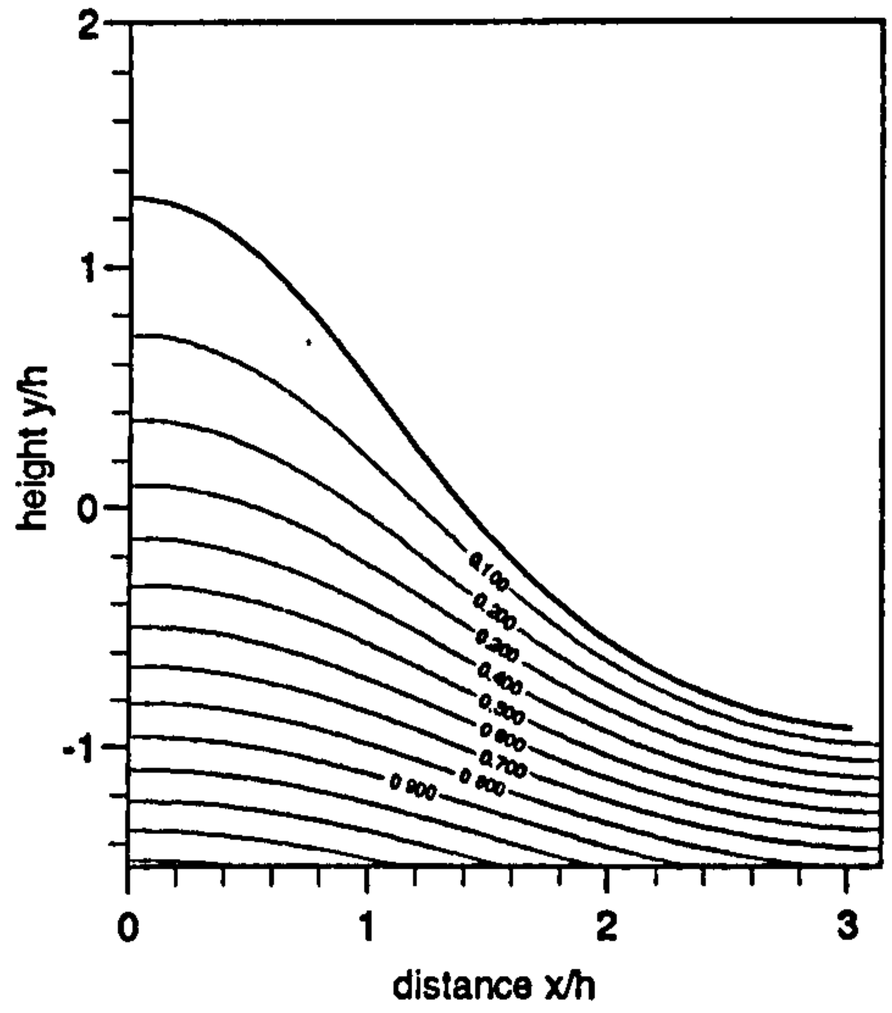

Figure 4.10: Pressure contours with increments of 0.1 for a large standing wave of surface and potential amplitude 0.6 and -1.0 respectively with an initial depth of 1.5 at a dimensionless time of 1.15, at a point of maximum kinetic energy.

The corresponding pressure field below the surface at each of the three times has been evaluated. The pressure distribution at time 1.15 is displayed in figure 4.10 and low pressure values are found, not much greater than hydrostatic pressure. In contrast, the pressure field presented in figure 4.11 now shows the isobars under the lower waterline to be much closer together with high values near the bed of the domain beneath the trough and a maximum of approximately 1.86. The pressure distribution for the final time 4.86 as portrayed in figure 4.12 shows a similar map of a low pressure field as in figure 4.10 with the maximum waterline now on the other side of the 'tank'. The crest is now wider and contains lower pressure gradients than at time 1.15. The computations for this example stop before the next instance of maximum kinetic energy is reached.

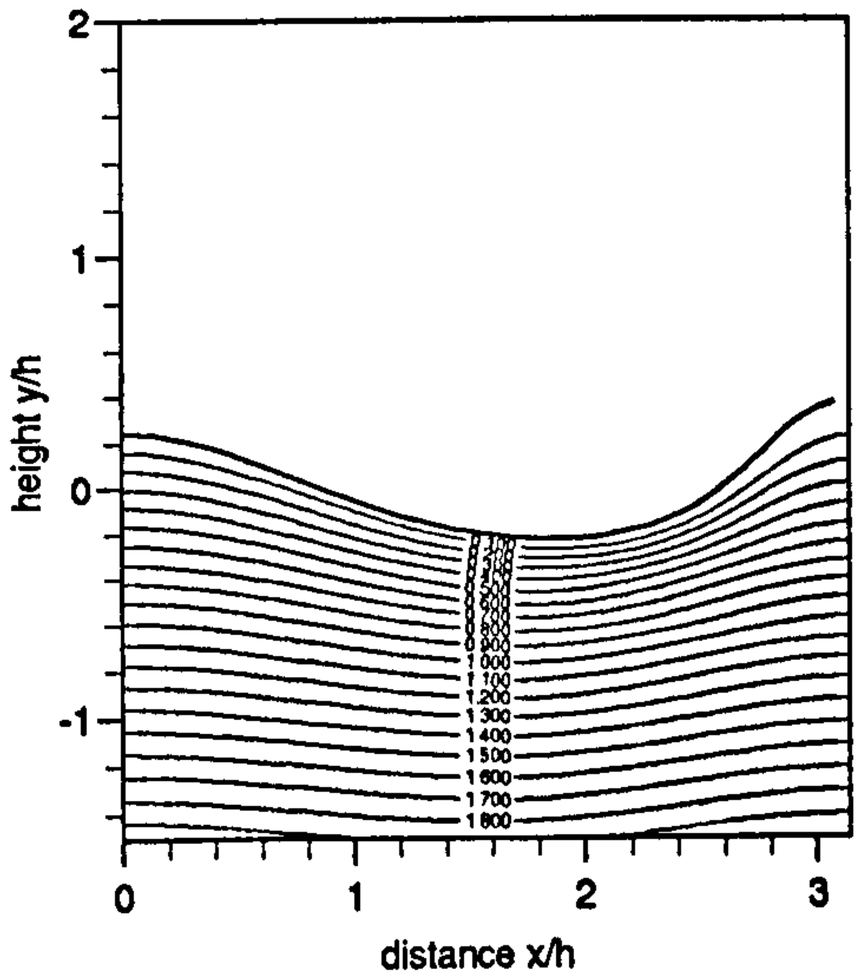

Figure 4.11: Pressure contours with increments of 0.1 for a large standing wave of surface and potential amplitude of 0.6 and -1.0 respectively with an initial depth of 1.5 at a dimensionless time of 2.97, at a point of minimum kinetic energy.

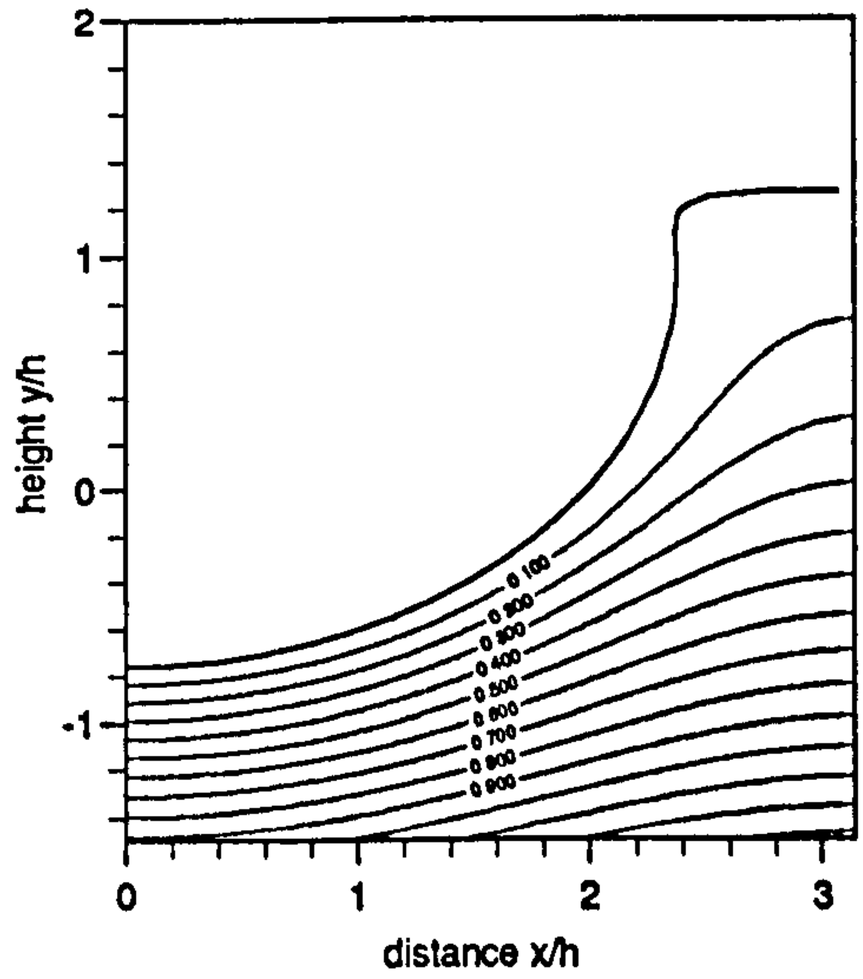

Figure 4.12: Pressure contours with increments of 0.1 for a large standing wave of surface and potential amplitude 0.6 and -1.0 respectively with an initial depth of 1.5 at a dimensionless time of 4.86, at a point of maximum kinetic energy.

4.2.4 Numerical parameters

As shown in the time history of the surface profiles in figure 4.2, the numerical model is unable to resolve corners and the program stops as the computations become inaccurate. Longuet-Higgins (1980) has presented some exact solutions of the local form of the free surface near a region of sharp curvature. Throughout the use of the numerical program in this chapter, some smoothing has been applied, using a high order smoothing formula, described in Dold (1992), applied only if the effect of 'roughness' exceeds a given value in the program. For the examples shown above, the absence of smoothing would not have altered the resulting data.

Amongst the program parameters specified at the beginning of the computations, the number of points used to discretise the free surface and accuracy required for the timesteps have to be chosen. For the preceeding examples, 80 points with a precision or parameter of 0.00001 was used. An increase in the number of points used was not found to alter the numerical results, highlighting the efficiency of the numerical method.

For large or detailed computations, the final numerical data obtained when the computations begin to fail can depend on the accuracy requested. In figure 4.13, the importance of the number of points used to describe the free surface is illustrated by the formation of a 'spike' or small jet at the final time intervals of a computation. This has been achieved by using a wave of initial surface amplitude 0.45, starting from rest with a still water depth of 2.0, and the development of a spike occurs shortly before the numerical program begins to fail. For increasing points, n=40, 80, and 120, the final surface profile for the last computed time interval in each case is shown in figure 4.13 for computations with an accuracy of 0.00001.

As the number of points used to model the free surface increases, the computations continue for longer. A close-up of the spike is shown in the upper right-hand corner of the figure. The spike becomes smaller and more well-defined as the free surface becomes lower and could be tending towards a singularity. The maximum number of points used is 120 after which the solution does not improve. Here the absence of smoothing would have resulted in the computations failing much earlier. For example, with 80 points and a tolerance of 0.00001, figure 4.13 shows the final computed time at 17.63. With no smoothing, the final computed time is 10.60, failing much earlier in a trough as the wave

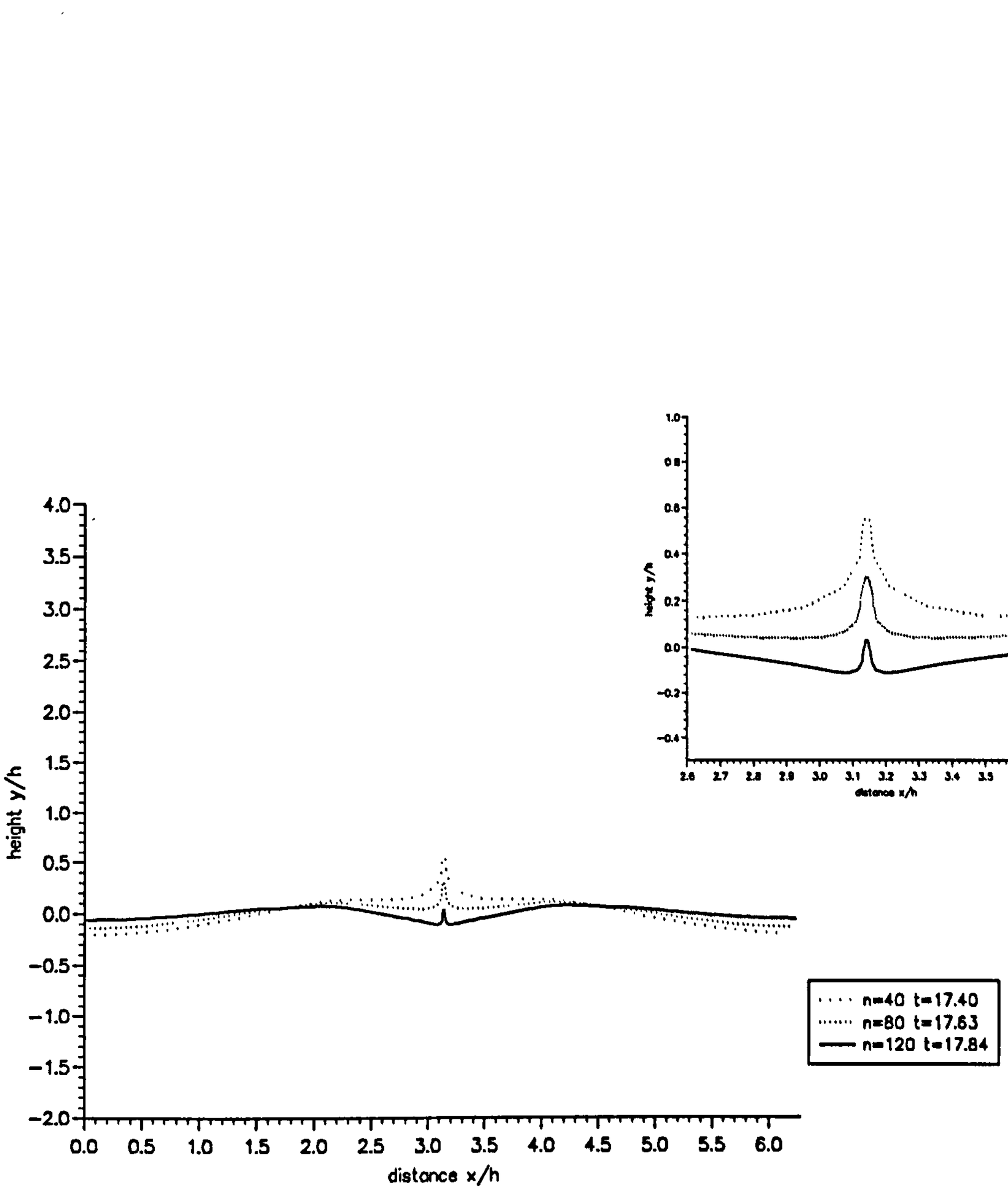

Figure 4.13: Surface profiles for a large standing wave of initial surface amplitude 0.45 starting from rest with an initial depth of 2.0 and an accuracy of 0.00001 for increasing points.

comes to a point of maximum kinetic energy.

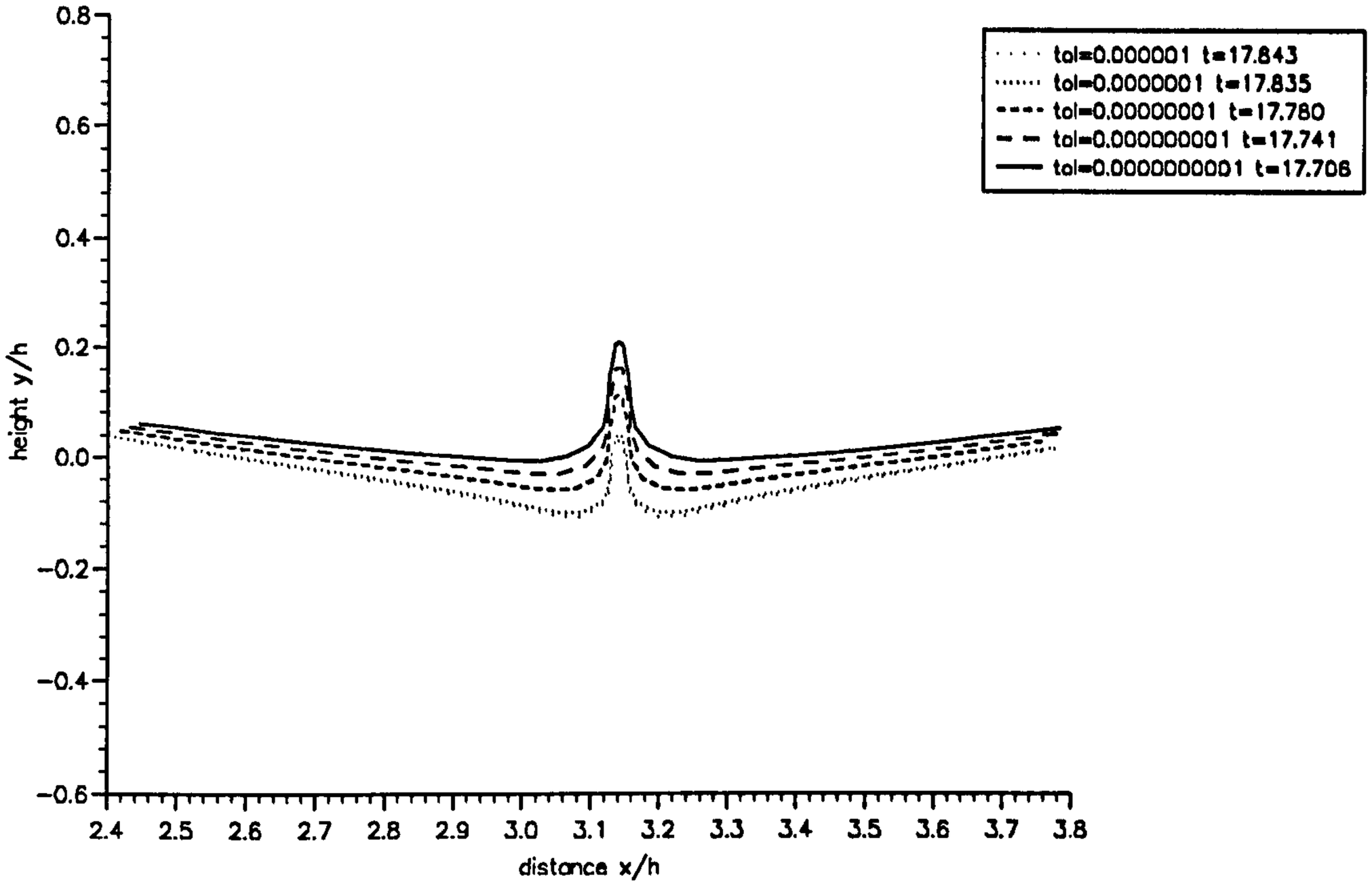

Figure 4.14: Surface profiles for a large standing wave of initial surface amplitude 0.45 starting from rest with an initial depth of 2.0 and 120 points on the surface for increasing accuracy.

Continuing with this waveform, for a wave of initial surface amplitude 0.45, starting from rest on a depth of 2.0, the last surface profile from figure 4.13, for 120 points at a time 17.84, is now the first profile in figure 4.14. Note only part of the domain is shown. Subsequent surface profiles in the figure are for increased accuracy and the computations fail earlier. The final computed time for the lowest accuracy is 10^{-5} is 17.843 whereas the final computed time for the highest accuracy, 10^{-10} is at 17.706. This increase in accuracy serves to increase the computational time with the final computation taking over 20 minutes instead of the more usual 2-3 minutes.

4.3 Forces exerted on side walls.

The pressure distributions have been shown for large amplitude motion inside a confined domain and the total force exerted on a side wall can be calculated by integrating

the pressure over the impact wall. The forces exerted on the centre wall $x = \pi$ are presented in figure 4.15 as a function of time for a standing wave of initial surface amplitudes 0.3-0.8, starting from rest on an initial still water depth of 1.0. For the larger waves, the computations fail before the final time computed. The force of still water on the wall is 0.5.

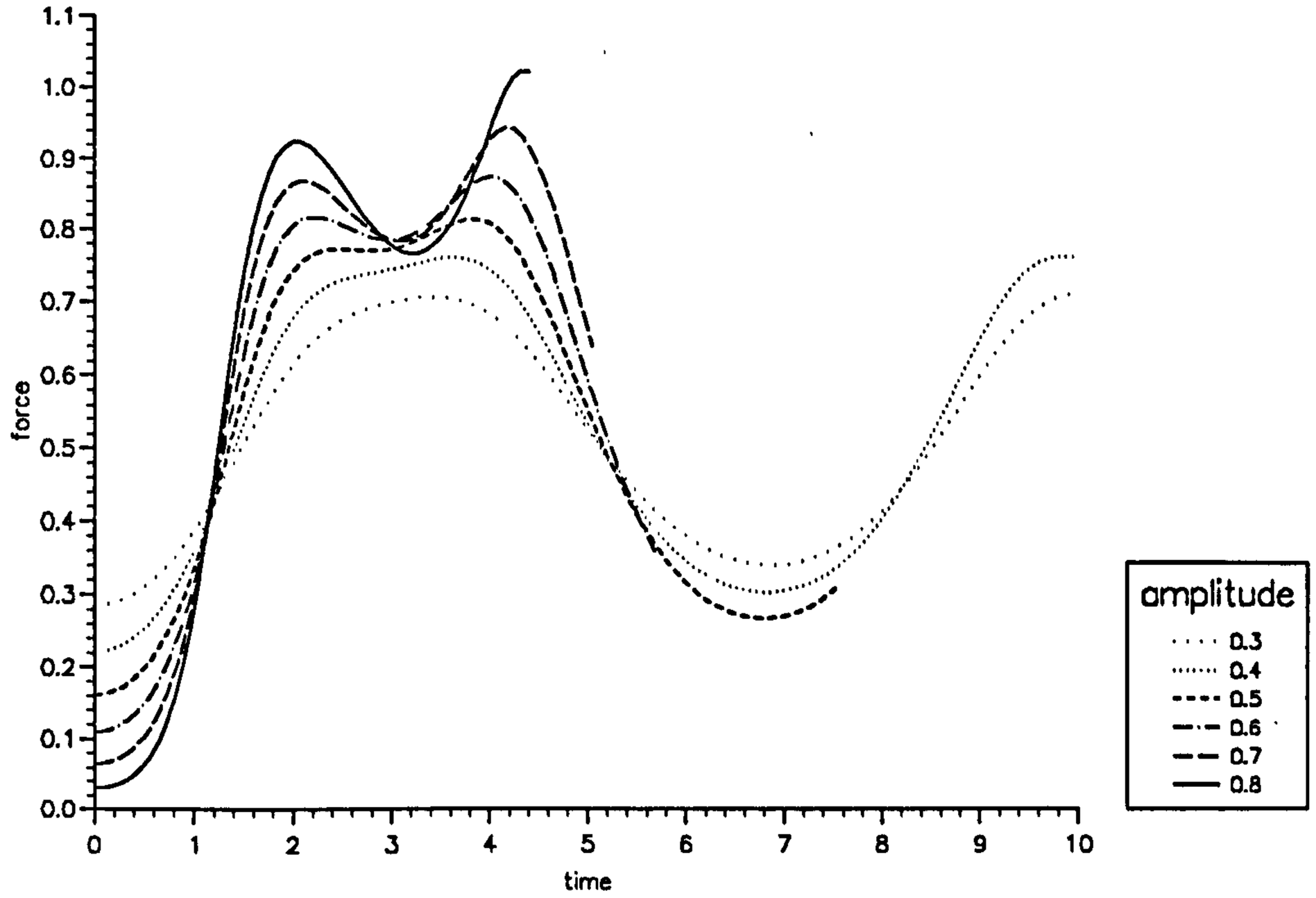

Figure 4.15: Time history of forces on the centre wall $x = \pi$ of the domain for a wave for increasing initial surface amplitudes starting from rest on a depth of 1.0.

For a large enough amplitude, a double peak in the time history of the force is obtained, portrayed in figure 4.15, of which the second peak is the larger. The maximum pressures of the standing waves occur when the waves are at the crest position on the vertical wall. The double peaks of the pressure-time curve are generated at both sides of the crest position of the wave, as noted by Nagai (1969). The maximum wave height does not coincide with the maximum force and pressures. For example, the waterline and pressure at the bed of the wall as a function of time for a large standing wave of initial surface amplitudes 0.5 and 0.9 respectively, starting from rest are presented in figure 4.16. The maximum height of the waterline occurs between the two peaks. The maximum force on the wall in each case has been shown in figure 4.17 where the peaks are shown to

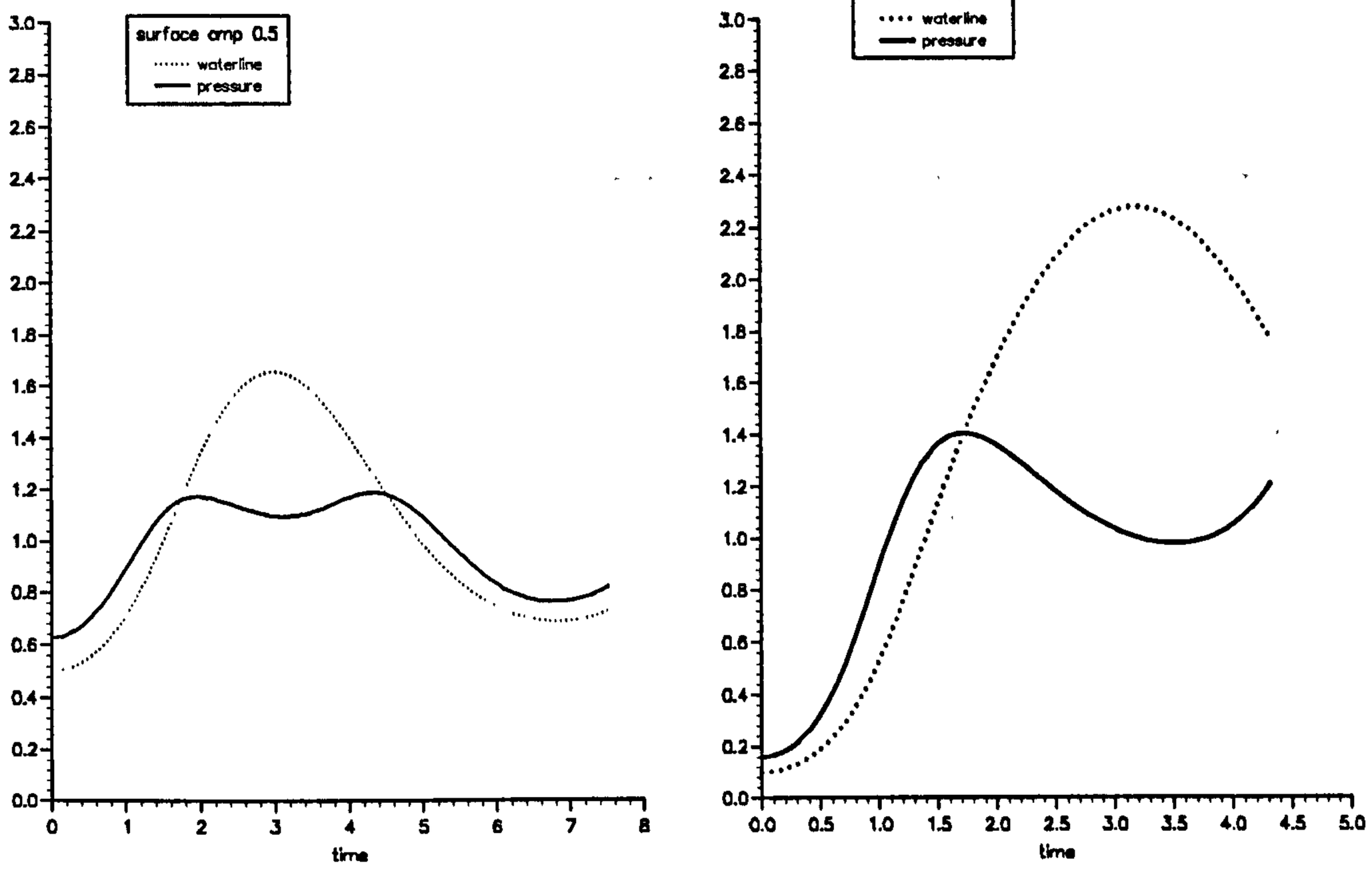

Figure 4.16: Time history of waterline and pressure at the foot of the impact wall for a wave of initial surface amplitude as indicated, starting from rest on a depth of 1.0.

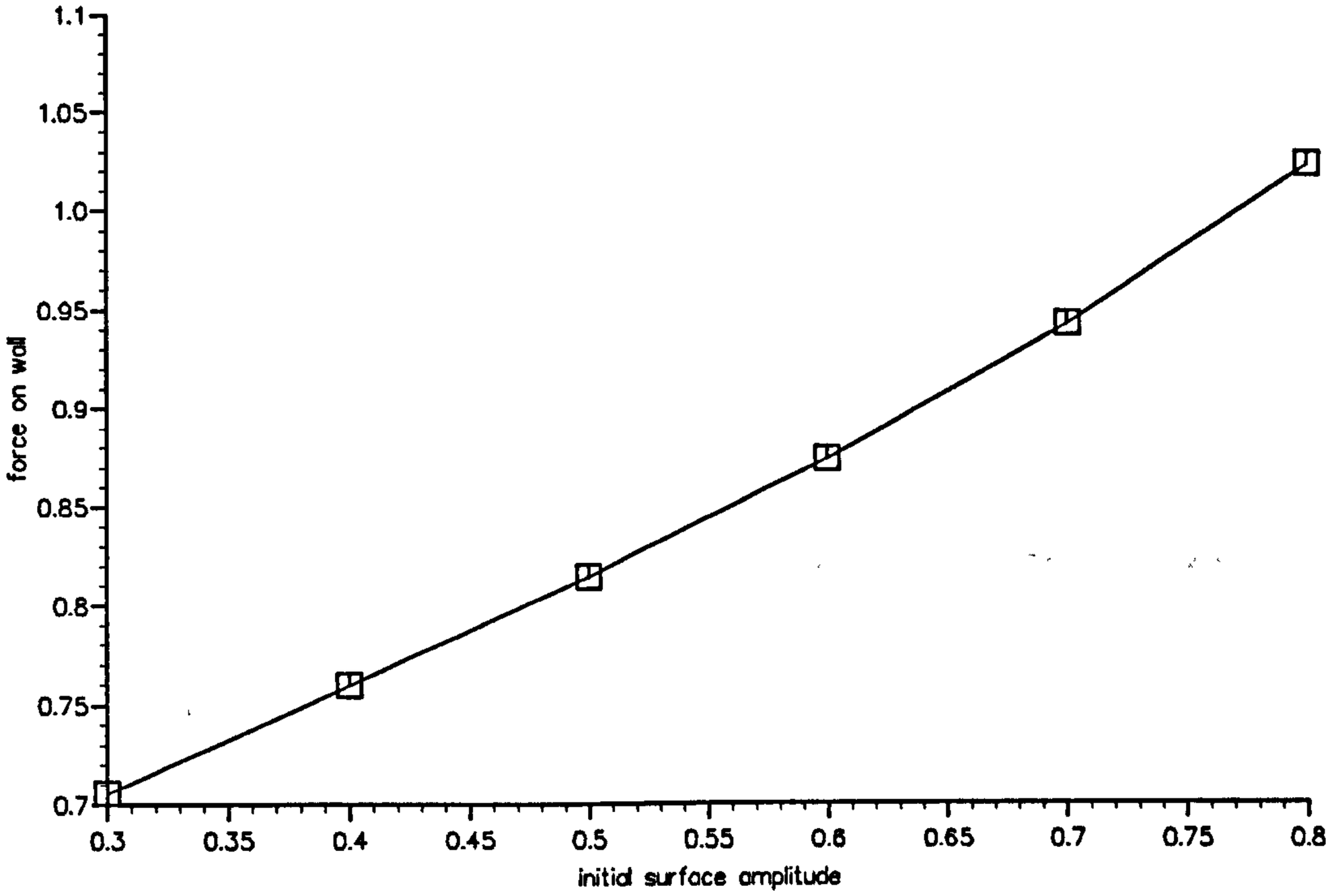

Figure 4.17: Maximum force on wall against size of initial surface amplitude a_1 on a finite depth of 1.0, where the markers indicate the points plotted.

increase linearly with the initial surface amplitude. The interpretation of the double peak is discussed in the concluding chapter.

Chapter 5

Response of a Flexible Wall to Wave Impact

5.1 Introduction

The possible damage to structures due to wave impact and the concern over the stability of liquid containers leads to the need for the study of the response of a wall to the impact of wave motion. Steep water-wave impact on breakwaters can cause the structure to vibrate or slide and the sloshing motion found inside containers can cause thin walls to oscillate. As mentioned in the introduction in section 1.4, this chapter contains the recent and current research of the author. The results have yet to be fully verified and analysed, however the importance and relevance of the subject to industrial applications merited its presence.

In this chapter, the vertical impact wall is modelled as a two-dimensional elastic plate using classic plate theory. Detailed computations describing the wave motion can provide the pressure field on the wall as a function of time. For wave impact on a vertical breakwater, the computations for a solitary wave, described in section 3.3.2 in chapter 3, are used to provide the pressure field on the wall as a function of time. The initial conditions for the numerical program are chosen to give a reflecting solitary wave, such as that illustrated in section 1.3 in chapter 1. For wave impact inside a container, computations for the sloshing motion described in section 4.2 in chapter 4 for large amplitude standing waves, provide the pressure distribution in time on a wall of a tank. The transverse

displacements and amplitudes of a vertical breakwater or a thin vertical tank wall are evaluated.

A study of the interaction of an arch dam with a reservoir was undertaken by Astley (1972) modelling the dam face as a two-dimensional plate. Using a finite element method to study various geometries, the pressure was shown to be largely determined by a relatively small volume of water and to be insensitive to the reservoir shape.

Laboratory experiments were undertaken by Kirkgöz (1990) to measure impact pressures and resulting deflections from plunging oscillatory waves which were breaking directly against a vertical wall. A 10 millimetre thick steel plate of height 0.47 metres with a built-in upper edge and simply supported lower end to represent a rubble mound base was used with a displacement transducer 0.187 metres above the lower edge. The wall deflection histories follow the same pattern as the force histories with the wall response becoming smaller as the duration of the impact force decreases. Again a time delay was shown between the pressure peak and the maximum displacement. The greatest wall deflection of 1.74 millimetres was reached after a time delay of 0.42 seconds where the peak pressure was 36.0 kPa, force of 4847 N/m^2. Kirkgöz concluded that the high magnitude forces with very short durations have only a local influence on the wall deflection histories but low impact forces which last longer produce the greatest wall deflections.

An experimental study into the dynamic response of non-rigid vertical walls to impact pressures due to breaking waves was undertaken by Hattori (1994). Measurements of the impact pressures with the simultaneous wall deflections were given. The impact wall was a plastic plate of height 0.5 metres with four different thicknesses of 0.005, 0.01, 0.015 and 0.035 metres used; the latter represented a rigid wall. The natural frequencies of the plates in water was measured and found to be 10-20 % lower than in air. The still water height was 0.05 metres and a range of differing wave impacts was considered. The dynamic response of the wall was shown to differ according to the breaking wave conditions with a large pocket of oscillating air leading to similar wall oscillations with relatively large amplitudes which continued until the entrapped air started to rise to the free surface. Examination of the experimental results was in agreement with Kirkgöz, showing the wall not to respond much to high impact pressures of short duration. In contrast, the low impact pressures caused by fully developed plunging breakers caused large wall deflections. The author concluded that the largest wall deflection occurs when

the rise time of the impact pressure is almost the same as the natural period of the wall and suggested more consideration should be given to the wall deflections by low and longer-lasting impact pressures.

Comparisons are made with the experimental data in section 5.3.1 with Kirkgöz & Mengi (1986) for wave impact on a breakwater and in section 5.4.1 with Corrignan (1993) for wave impact in a container.

5.2 Theoretical Analysis for an Unloaded Plate.

The vertical wall is modelled as a flexible two-dimensional plate of height eh and thickness s, as shown in figure 5.1 for a rectangular container, where e is some fraction greater than 1. The thickness of the plate is small compared to the height and the

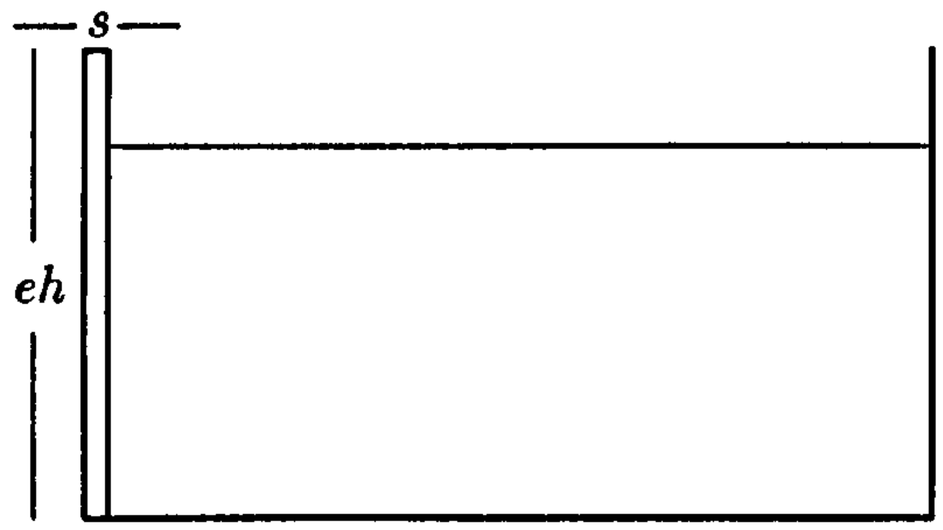

Figure 5.1: Thin wall modelled as a two-dimensional flexible plate of height eh and thickness s at one end of a partially-full rectangular tank.

plate can only bend and not twist. Let the bending moment per unit length be M_y, the shear force per unit length be Q_y and the lateral displacement of the plate be $w(y,t)$. Considering an element $s\,dy$, two equations are obtained:

$$\frac{\partial M_y}{\partial y} - Q_y = 0 \tag{5.1}$$

and

$$\frac{\partial Q_y}{\partial y} = \rho_p s \frac{\partial^2 w(y,t)}{\partial t^2} \tag{5.2}$$

where ρ_p is the density of the plate. The normal strain is given by $\eta_y = z/r_y$ where r_y is the radius of curvature and may be approximated by $-\partial^2 w(y,t)/\partial y^2$ for small deflections

and slopes. From Hooke's Law the stress is

$$\sigma_y = -\frac{Ez}{1-\nu^2}\frac{\partial^2 w(y,t)}{\partial y^2} \tag{5.3}$$

where E is Young's modulus which is a measure of the stress/strain, ν is Poisson's ratio. The bending moment due to σ_y is

$$M_y = \int_{-s/2}^{s/2} z\sigma_y \, dz = -\frac{Es^3}{12(1-\nu^2)}\frac{\partial^2 w(y,t)}{\partial y^2}. \tag{5.4}$$

Combining the two equations 5.1 and 5.2, one equation of motion satisfying the free oscillations of the plates is obtained

$$D\frac{\partial^4 w(y,t)}{\partial y^4} + \rho_p s\frac{\partial^2 w(y,t)}{\partial t^2} = 0 \tag{5.5}$$

where $D = Es^3/12(1-\nu^2)$.

Introducing dimensionless variables $y' = y/h$, $w' = w/h$, and $t' = t/\sqrt{h/g}$ where h is the still water depth, the height of the plate is $y' = e$.

To determine the natural frequencies and normal modes, the method of separation of variables is used with

$$w(y',t') = Y(y')T(t') \tag{5.6}$$

to give

$$\frac{1}{a^2 Y(y')}\frac{\partial^4 Y(y')}{\partial y'^4} = -\frac{1}{T(t')}\frac{\partial^2 T(t')}{\partial t'^2} = \omega^2 \tag{5.7}$$

where $a = \sqrt{\rho_p s h^3 g/D}$.

5.2.1 Boundary conditions

The edges of the plate can either be free, pinned or clamped. For a clamped edge, the displacement and derivative normal to the edge are taken to be zero,

$$Y = \frac{dY}{dy'} = 0 \tag{5.8}$$

thus no rotating freedom. For a pinned edge

$$Y = \frac{d^2 Y}{dy'^2} = 0, \tag{5.9}$$

for example, as in the hinge of a door. For a free end, higher derivatives are used as discussed by Timoshenko (1940) giving

$$\frac{d^2 Y}{dy'^2} = \frac{d^3 Y}{dy'^3}. = 0 \tag{5.10}$$

Three types of boundary conditions for the upper end of the plate have been considered, but in each case the bottom of the plate has been chosen to be clamped. The normal modes for each case are evaluated:

Case 1: Clamped-Free

For a plate with a fixed edge at $y' = 0$ and a free end at $y' = e$, an expression for the normal modes is obtained:

$$Y_n(y') = [\cos(\beta_n y') - \cosh(\beta_n y')] - [\sin(\beta_n y') - \sinh(\beta_n y')] \left[\frac{\cos(\beta_n e) + \cosh(\beta_n e)}{\sin(\beta_n e) + \sinh(\beta_n e)}\right] \quad (5.11)$$

where

$$\beta_n^4 = a^2 \omega_n^2 \quad (5.12)$$

and the frequencies satisfy the equation

$$\cos(\beta_n e) \cosh(\beta_n e) = -1, \quad (5.13)$$

the three solutions of which $\beta_1 e$, $\beta_2 e$ and $\beta_3 e$ are 1.875, 4.964 and 7.855.

Case 2: Clamped-Pinned

For a plate with a fixed edge at $y' = 0$ and a pinned end at $y' = e$, an expression for the normal modes is obtained:

$$Y_n(y') = [\cos(\beta_n y') - \cosh(\beta_n y')] - [\sin(\beta_n y') - \sinh(\beta_n y')] \left[\frac{\cos(\beta_n e) - \cosh(\beta_n e)}{\sin(\beta_n e) - \sinh(\beta_n e)}\right] \quad (5.14)$$

where β is as defined in equation 5.12 and the frequencies satisfy the equation

$$\tan(\beta_n e) = \tanh(\beta_n e) \quad (5.15)$$

where the first three solutions $\beta_1 e$, $\beta_2 e$, and $\beta_3 e$ are 3.927, 7.069 and 10.210.

Case 3: Clamped-Clamped

For a plate with a fixed edge at both $y' = 0$ and $y' = e$ the expression for the normal modes is as for a pinned edge at $y' = e$ as in equation 5.14, but with the frequencies satisfying the equation

$$\cos(\beta_n e) \cosh(\beta_n e) = 1 \quad (5.16)$$

where the first three solutions $\beta_1 e$, $\beta_2 e$ and $\beta_3 e$ are 4.73, 7.85 and 10.996.

5.2.2 Displacement due to pressure field

To study the response of the plate to wave impact, the pressure field on a wall as a function of time is obtained from the numerical computations, described in section 3.3 in chapter 3 or section 4.2 in chapter 4, and used as the driving term.

The dimensionless equation of motion for the displacement of the wall with the forcing term is now

$$\frac{\partial^4 w'(y',t')}{\partial y'^4} + a^2 \frac{\partial^2 w'(y',t')}{\partial t'^2} = \frac{\rho g h^4}{D} p'(y',t'), \tag{5.17}$$

where $p' = p/\rho g h$, ρ is the density of water and g is gravity. Following the general method, set out for example in Graff (1975), $w'(y',t')$ is expanded in terms of the normal modes $Y_n(y')$ described above and general functions of time $T_n(t')$,

$$w'(y',t') = \sum_{n=1}^{\infty} T_n(t') Y_n(y') \tag{5.18}$$

to give

$$\sum_{n=1}^{\infty} \left[T_n(t') \frac{\partial^4 Y_n(y')}{\partial y'^4} + a^2 \frac{\partial^2 T_n(t')}{\partial t'^2} Y_n(y') \right] = \frac{\rho g h^4}{D} p'(y',t') \tag{5.19}$$

and using $\partial^4 Y_n(y')/\partial y'^4 = \beta_n^4 Y_n(y')$,

$$\sum_{n=1}^{\infty} \left[\beta_n^4 T_n(t') + a^2 \frac{\partial^2 T_n(t')}{\partial t'^2} \right] Y_n(y') = \frac{\rho g h^4}{D} p'(y',t') \tag{5.20}$$

and so

$$\frac{\partial^2 T_n(t')}{\partial t'^2} + \frac{\beta_n^4}{a^2} T_n(t') = \frac{2\rho g h^4}{D a^2} P_n(t') \tag{5.21}$$

where

$$P_n(t') = \int_0^1 p'(y',t') Y_n(y')\, dy'. \tag{5.22}$$

Since the normal modes are orthogonal, the general functions of time then have the solution

$$T_n(t') = -\frac{2\rho g h^4}{D a \beta_n^2} \int_0^{t'} P_n(t') \sin[(\beta_n^2/a^2)(t'-\tau)]\, d\tau \tag{5.23}$$

giving the full solution for the displacement as

$$w'(y',t') = -\frac{2\rho g h^4}{Da} \sum_{n=1}^{\infty} \frac{Y_n(y')}{\beta_n^2} \int_0^{t'} \sin\left[(\beta_n^2/a^2)(t'-\tau)\right] \int_0^e p'(y',\tau) Y_n(y')\, dy'\, d\tau. \tag{5.24}$$

The wall deflections are assumed to be too small to affect the hydrodynamics.

5.3 Deflections due to wave impact on a breakwater

To study the effect of water-wave impact on a vertical breakwater, computations describing the motion of solitary waves, discussed in section 3.3.2, have been chosen to provide the pressure distribution on the wall as a function of time. In particular, the initial data has been chosen to produce a reflecting solitary wave, similar to that shown in figure 1.4 in section 1.3 in the introduction in chapter 1, where h=1.0. The numerical program was run from t=0.0-6.0$\sqrt{h/g}$ in timesteps of 0.005$\sqrt{h/g}$. Thus the computations for a solitary wave of initial amplitude 0.6 m, an initial distance 5.65 m from the impact wall on a finite depth of 1.0 m, give the pressure field on the wall from t=0.0 s to t=1.916 s, where the wave crest has reached its maximum height of 1.63 m at a time t=1.596 s.

As comparison is to be made with the results from Kirkgöz & Mengi (1986) for wave impact on a vertical breakwater, the plate has been taken to be clamped-pinned, with characteristics given by Kirkgöz et.al. Thus the plate is chosen to be made of reinforced concrete to model the breakwater, with characteristics E=30.25 GN/m^2, ν = 0.15 and ρ=2400 kg/m^3, and dimensions 3.0 metres high, 0.2 metres thick. This gives a fundamental frequency from (5.12) of 56.5 Hertz.

The deflections of a vertical plate due to the motion of a reflecting solitary wave have been evaluated. Figure 5.2 shows the smooth profile of the plate at three timesteps, before, at and after the time of maximum wave height at t=1.596 s. The maximum displacements are of the order of 2 millimetres. The three profiles indicate some oscillation of the plate.

The time history of one position at 2.0 metres up the wall is displayed in figure 5.3 showing regular oscillations in time. The displacements are largest before the maximum height, at t=1.596 s, when the water is rising up the wall, then decreasing when the water is at its maximum height and then increasing again on returning down the wall.

The regular oscillations show a period of approximately 0.08 seconds or 12.5 Hertz. The fundamental frequency of the plate in air has been calculated at 56.5 Hertz, much higher. Due to the added mass of the water, the frequencies of a plate partially submerged in water are lower, as shown in Hattori (1994). It would be extremely difficult to compute what the change would be but the results given by Hattori (1994) suggest the oscillations seen here are those of the fundamental frequency for this plate in water.

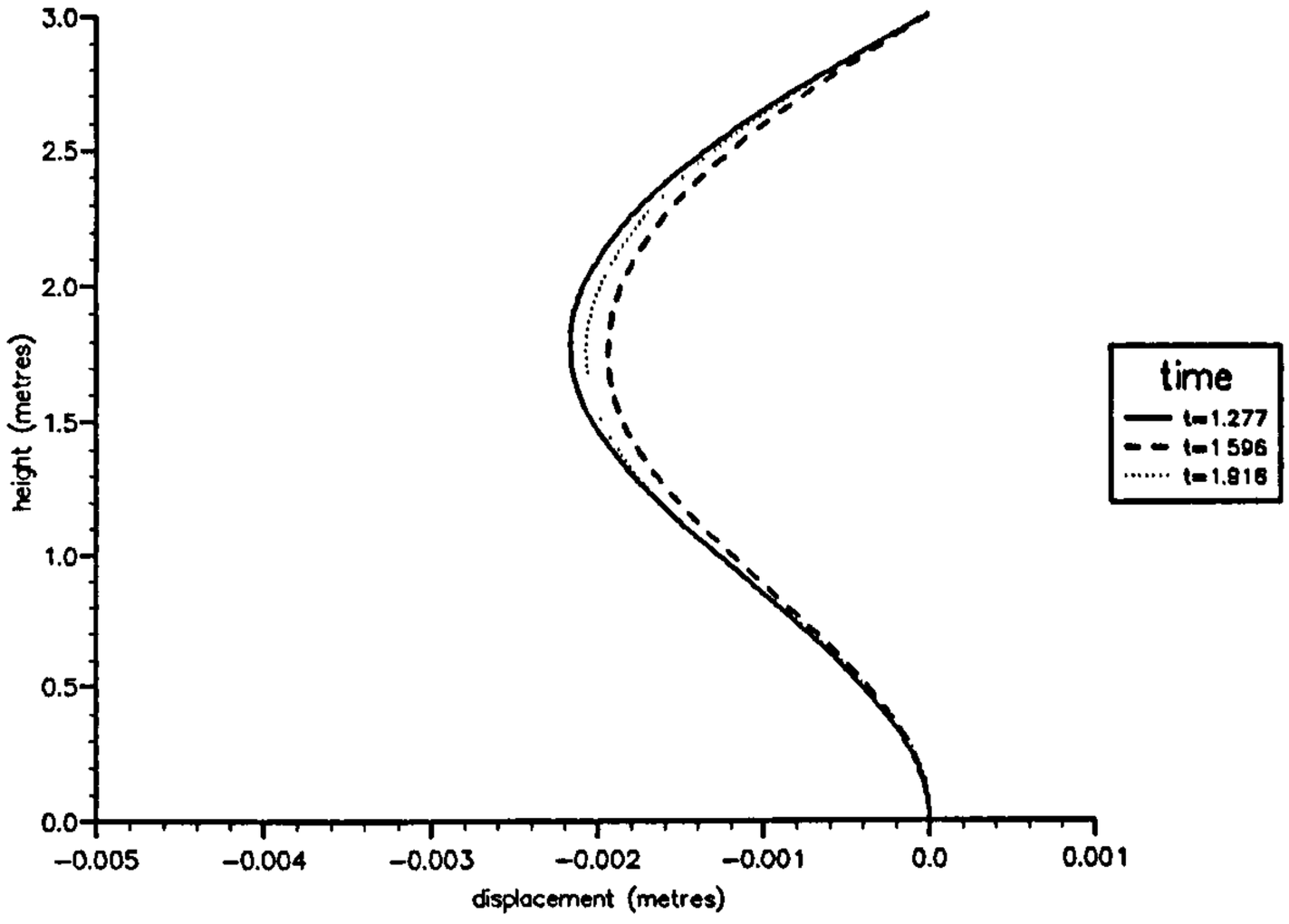

Figure 5.2: Profiles of a vertical plate of height 3.0 m, thickness 0.2 m due to the impact of a reflecting solitary wave of initial amplitude 0.6 m on a depth of 1.0 m. Horizontal exaggeration of approximately 500.

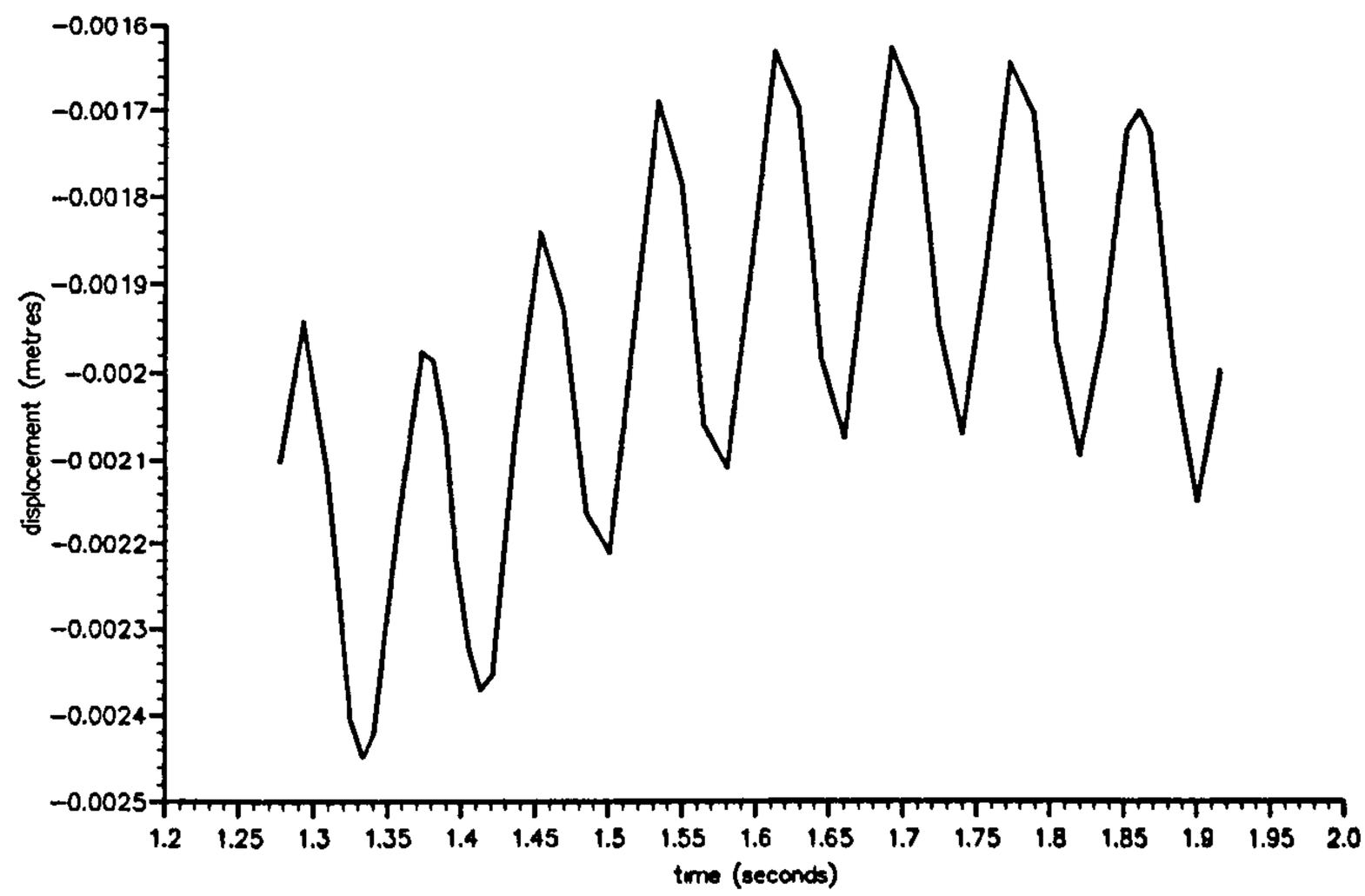

Figure 5.3: Time history of displacement w at 2.0 m on a vertical wall of height 3.0 m, thickness 0.2 m due to the impact of a reflecting solitary wave of initial amplitude 0.6, on a depth of 1.0 m.

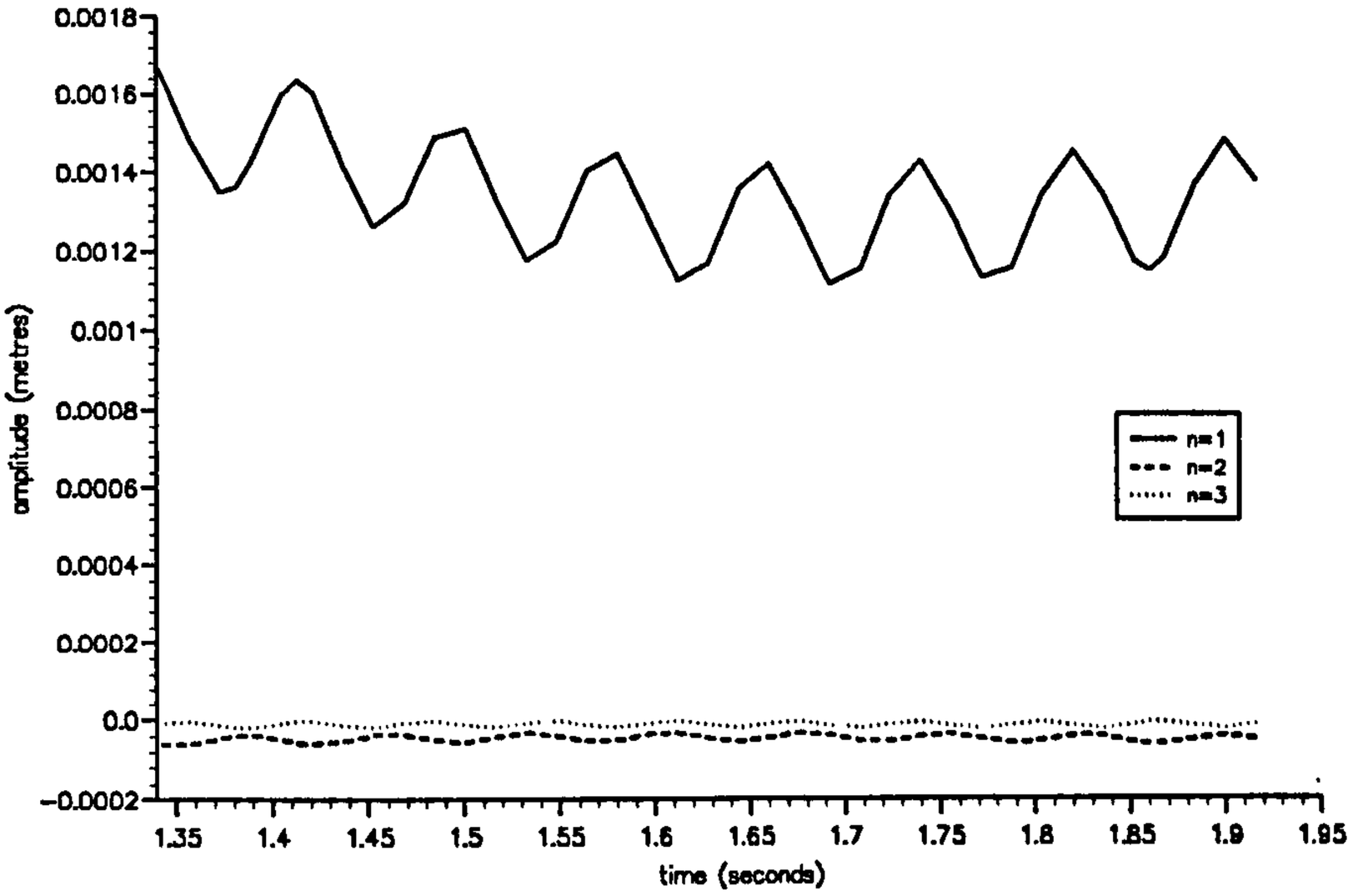

Figure 5.4: Time history of the amplitudes T_n for the first three modes for a vertical wall of height 3.0 m, thickness 0.2 m due to the impact of a reflecting solitary wave of initial amplitude 0.6, on a depth of 1.0 m.

The amplitudes, T_n, of the displacements are shown in figure 5.4 for the first few modes for part of the motion. The first mode, $n = 1$ is dominant, showing regular oscillations of period 0.08, as in the previous figure. The second and third modes show a weak oscillatory motion.

5.3.1 Comparison with experimental data: Kirkgöz & Mengi (1986)

The response of a vertical concrete caisson subject to plunging waves has been investigated by Kirkgöz & Mengi (1986). Experimental data for a plunging wave with a wave front parallel to the impact wall were used to provide the pressure field on the plate. Numerical results for the moments and transverse displacements were obtained using finite element method with a mode superposition technique.

The lower end of the plate was taken to be built in with the upper end simply-supported. The caisson of reinforced concrete has characteristics given in the previous section, with a height of 4.0 metres and thickness of 0.4 metres. The figures in Kirkgöz

et.al. show a peak pressure of approximately 300 kN/m^2 at a height of 2.47 metres.

For comparison with these results, the numerical data from the computation shown section 1.1 in chapter 1 were used with h=1.0, as this shows a steep wave approaching a vertical wall with an almost vertical wave front, and a comparable peak pressure of approximately 281 kN/m^2 at a vertical height of 2.55 metres. The data was obtained from the numerical program for times t=0.0-4.225 $\sqrt{h/g}$, in timesteps of 0.0025$\sqrt{h/g}$. As shown in figure 1.2 in section 1.1 the wave produces a thin vertical jet at the final stages of motion which rises up the wall. The jet is at its highest position up the wall at this final time after which the computations fail. Thus the initial conditions were for a tanh waveform of amplitude 1.5 m on a depth of 1.0 m a distance 7.5 m away from the wall, producing the pressure distribution on the wall from t=0.0 to t=1.349 s. The displacements have been evaluated for a clamped-pinned plate of characteristics and dimensions, given by Kirkgöz et.al., thus s=0.4 m and e=4. This gave a fundamental frequency of 63.6 Hertz.

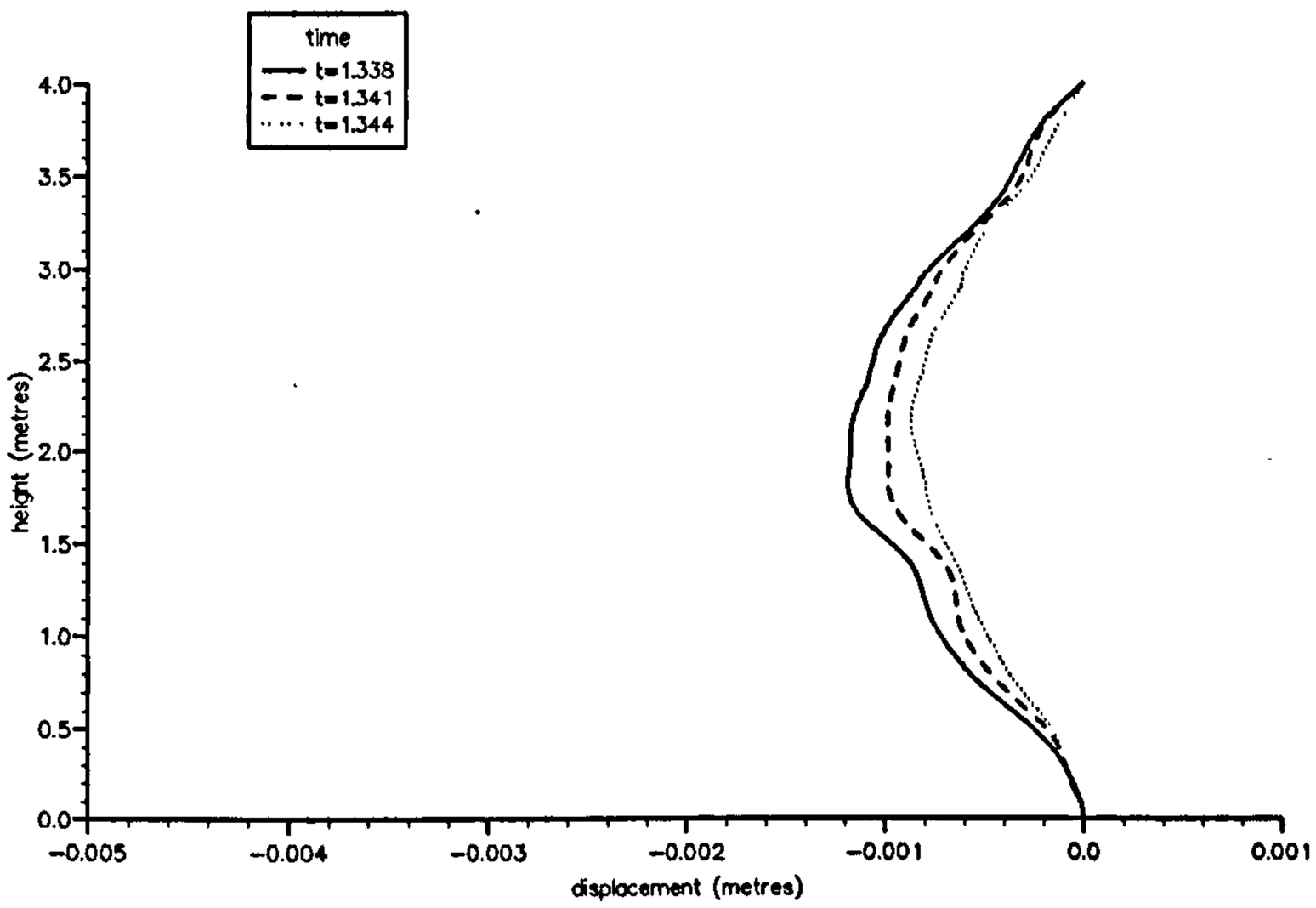

Figure 5.5: Profiles of a vertical wall of height 4.0 m, thickness 0.4 m due to a steep wave impact of initial wave amplitude 1.5 m on a depth of 1.0 m. Horizontal exaggeration of approximately 67.

The profile of the plate in response to the wave impact is shown in figure 5.5 for three times and indicate maximum deflections of approximately 1.2 millimetres, in good

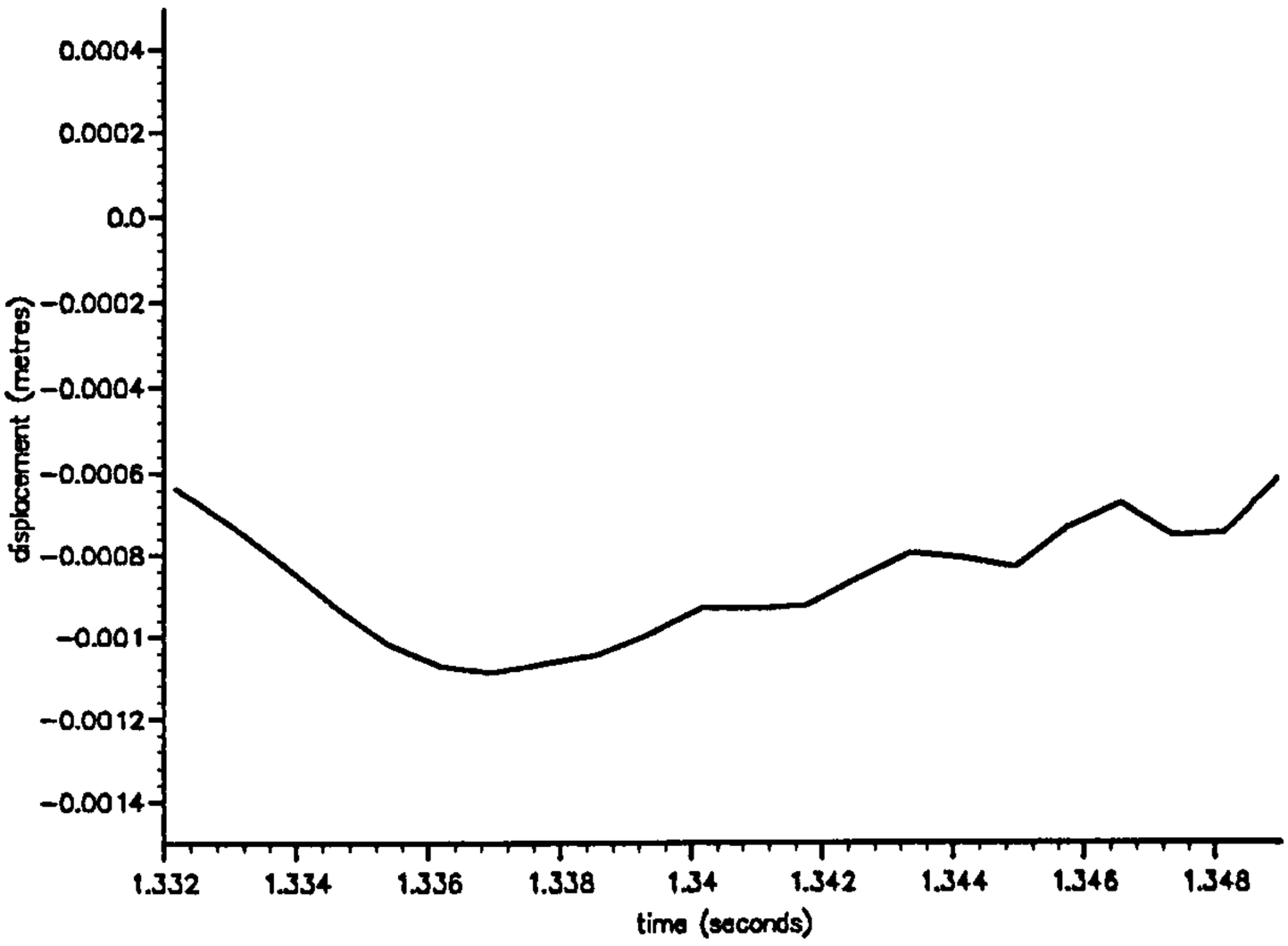

Figure 5.6: Time history of the displacement w of a vertical wall of height 4.0 m, thickness 0.4 m at position 2.47 m due to a steep wave impact.

agreement with Kirkgöz et.al. Figure 5.6 presents the displacement of one position of the wall in time, 2.47 m. The water does not reach this position until approximately 1.33 s. The wall at this point reaches its maximum deflection of 1.08 millimetres at t=1.337 s. Kirkgöz et.al. shows a value for the maximum displacement of 1.2 millimetres at 2.47 m (Node 41 in the data). After reaching the maximum displacement, the wall then appears to oscillate at a high frequency of approximately 323 Hertz. The third harmonic frequency of the plate is 430 Hertz, 25 % greater.

The amplitude of the displacement for the first few modes is displayed in figure 5.7 for part of the motion. The first mode, $n = 1$, is the dominant amplitude, rising to a peak and then decaying with some oscillation. This rise and decay can also be seen to a smaller extent in the second mode.

Due to the rapid change of the pressure field in this example, small timesteps of 0.0008 s, compared with 0.0016 s for the computation for the solitary wave, were used. Better resolution would require still smaller timesteps.

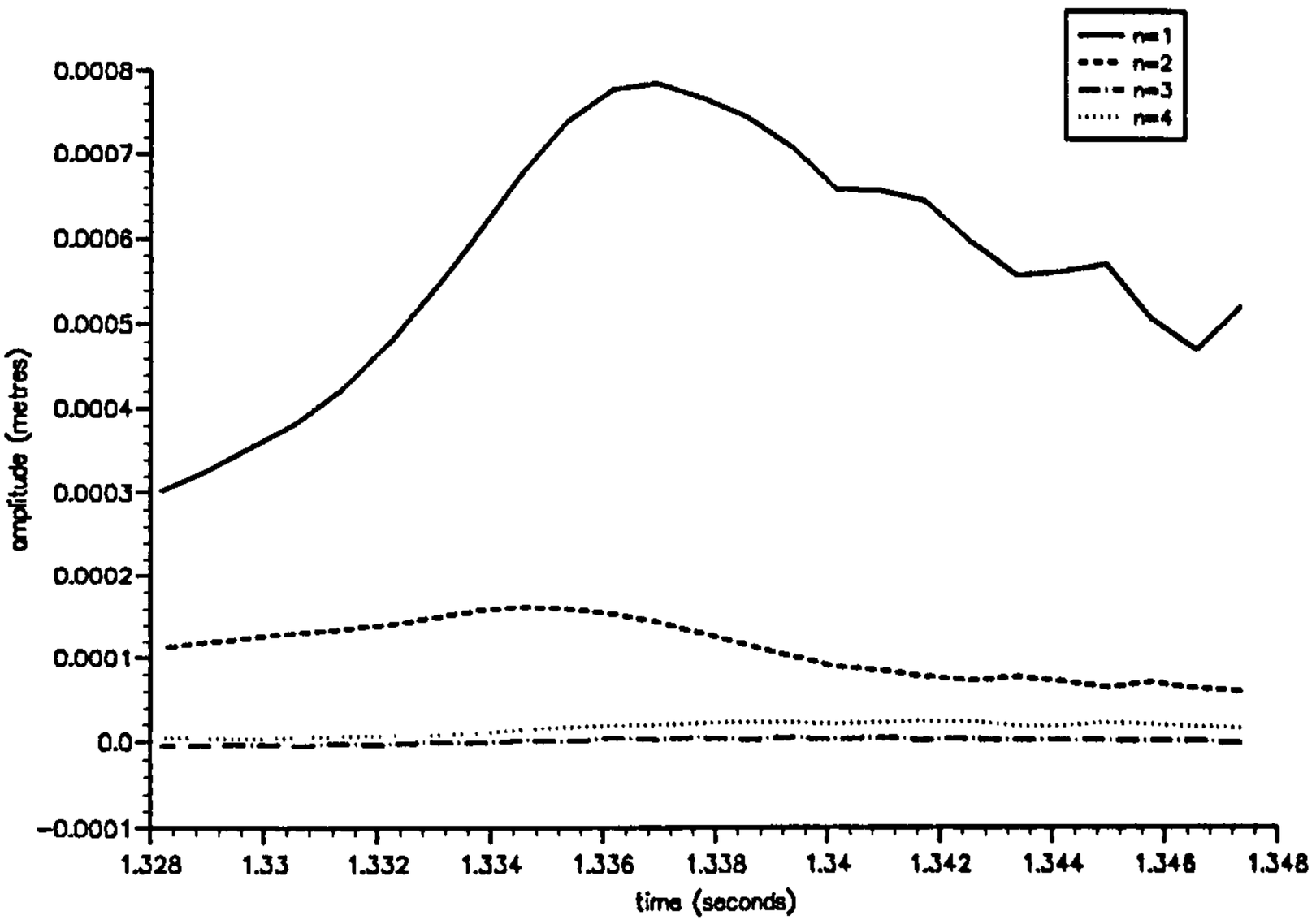

Figure 5.7: Time history of the amplitudes, T_n, for the first four modes for a vertical wall of height 4.0 m, thickness 0.4 m due to a steep water wave impact.

5.4 Deflections due to wave impact in a container

To study the response of a thin wall at one end of a container to wave impact, the numerical computations for sloshing motion in a tank described in section 4.2 are used to provide the pressure distribution on the wall as a function of time, where the plate is considered to be positioned in the centre of the domain at $x = \pi h$. Standing waves of initial surface amplitudes 0.1-0.4h, starting from rest on a depth of 1.0h were chosen. The numerical results were given from t=0.0 $\sqrt{h/g}$ to an instance of minimum kinetic energy in timesteps of 0.002 $\sqrt{h/g}$. With values h=1 and $e = 2$ this corresponds to a half full tank. For the dimensions of the elastic plate, let the thickness be $s = 0.018$ metres.

The characteristics for a steel plate are taken to be E=200 GN/m^2, ρ=7850 kg/m^3, ν=0.33 to correspond with those given by Corrignan (1993), with whose data comparisons are to be made. The deflections due to the sloshing motions have been evaluated for a clamped-free, clamped-pinned and clamped-clamped plate. For the three cases these physical characteristics give a fundamental frequency of 3.88, 17.04 and 24.7 Hertz respectively.

The pressure distribution on the wall due to the motion of the water starting from

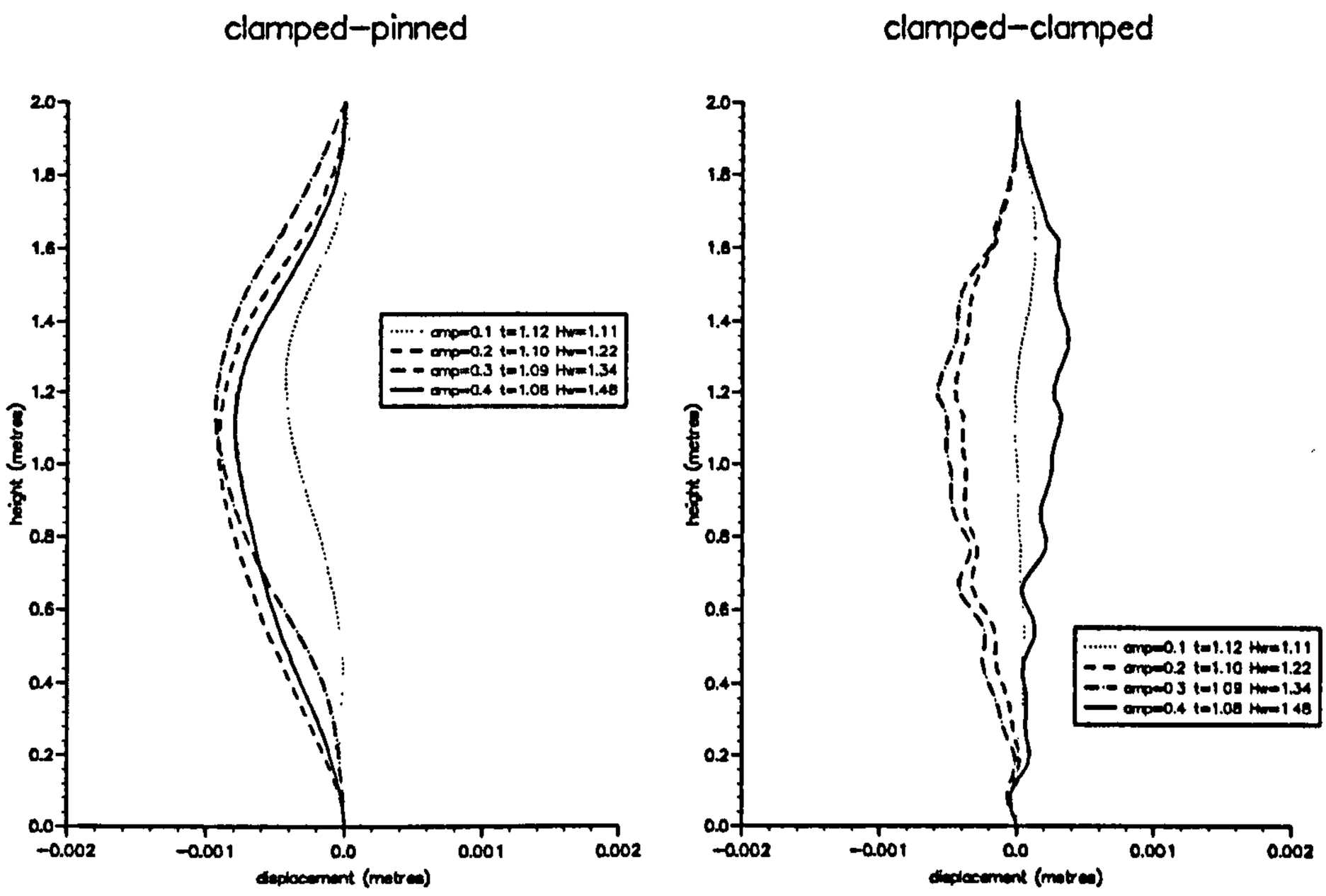

Figure 5.8: Profile of a flexible wall of height 2 m, thickness 0.018 m due to the motion of a standing wave of initial depth 1.0 m for different initial surface amplitudes on a clamped-pinned plate (left) and a clamped-clamped plate (right). Horizontal exaggeration of appproximately 500.

t=0.0 s until the final time indicated in figures 5.8 and 5.9 was obtained. The profiles of the plates shown in the figures is at a time when the waterline is at a high position on the plate at a time of minimum kinetic energy.

The clamped-pinned plate shows the smoothest profiles. The largest displacements of up to 9 millimetres are given by the clamped-free plate and high frequency oscillations can be seen. The clamped-clamped plate shows the smallest displacements in fractions of millimetres. Higher resolution profiles for this latter case could be obtained with smaller timesteps.

The deflection of the clamped-pinned plate at 1.5 metres up the wall is displayed in figure 5.10 for 0.07 seconds, showing oscillations of period 0.0064 seconds or 156.6 Hertz, along with higher frequency oscillations. The three lowest points in the figure (corresponding to the largest displacements) are at times 1.0923, 1.113 and 1.33 seconds, possibly underlying oscillations of period 0.02 or frequency of 50.0 Hertz. The 2nd, 3rd and 4th harmonic frequencies of the plate in air are 55.2, 115.2 and 197.1 Hertz.

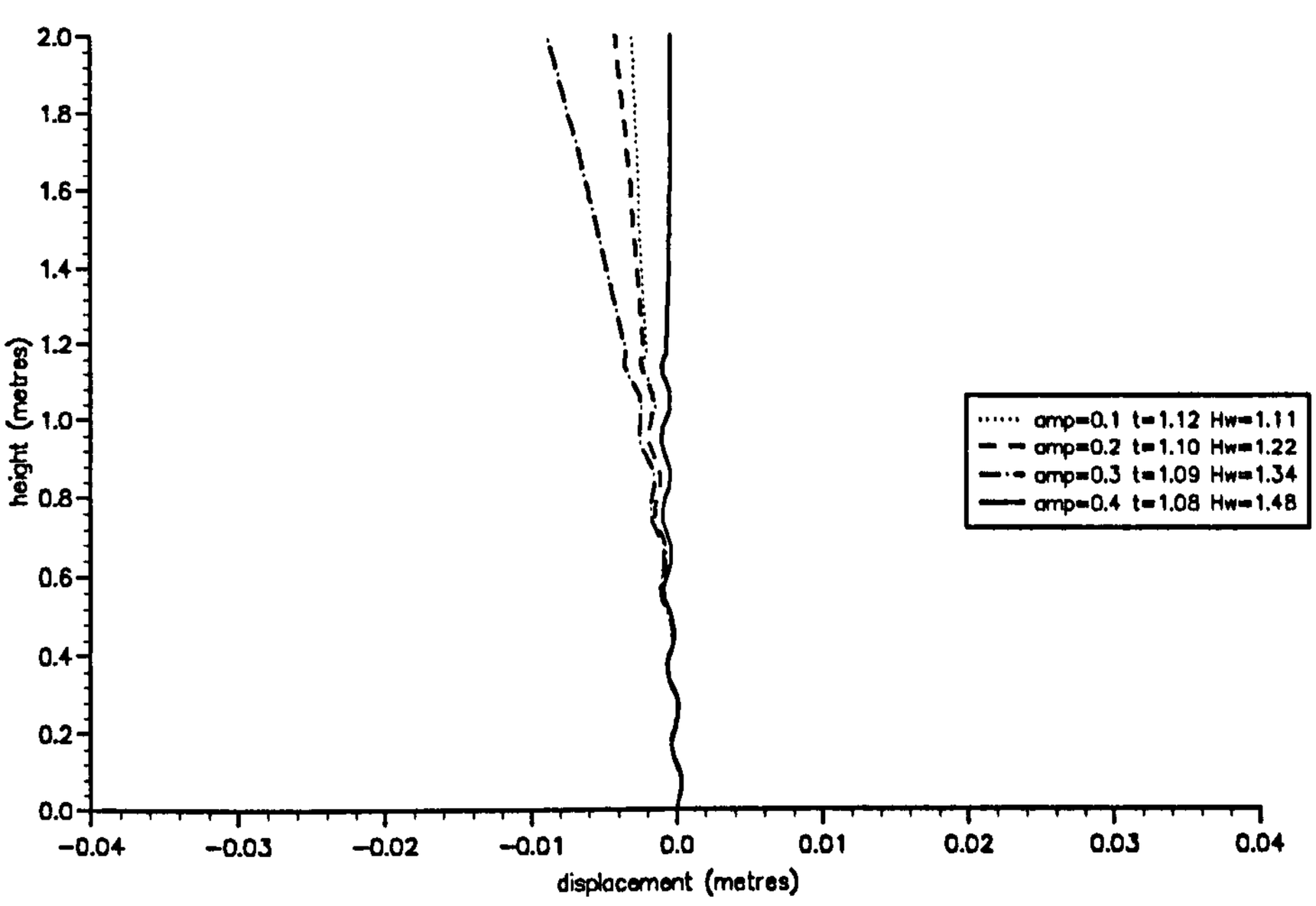

Figure 5.9: Profile of a flexible wall of height 2 m, thickness 0.018 m due to the motion of a standing wave of initial depth 1.0 m for different initial surface amplitudes on a clamped-free plate. Horizontal exaggeration of approximately 20.

Regular oscillations can be seen in all modes shown. The first and third modes have

oscillations of frequency approximately 160 Hertz and the second and fourth oscillations have a frequency of the order 500 Hertz.

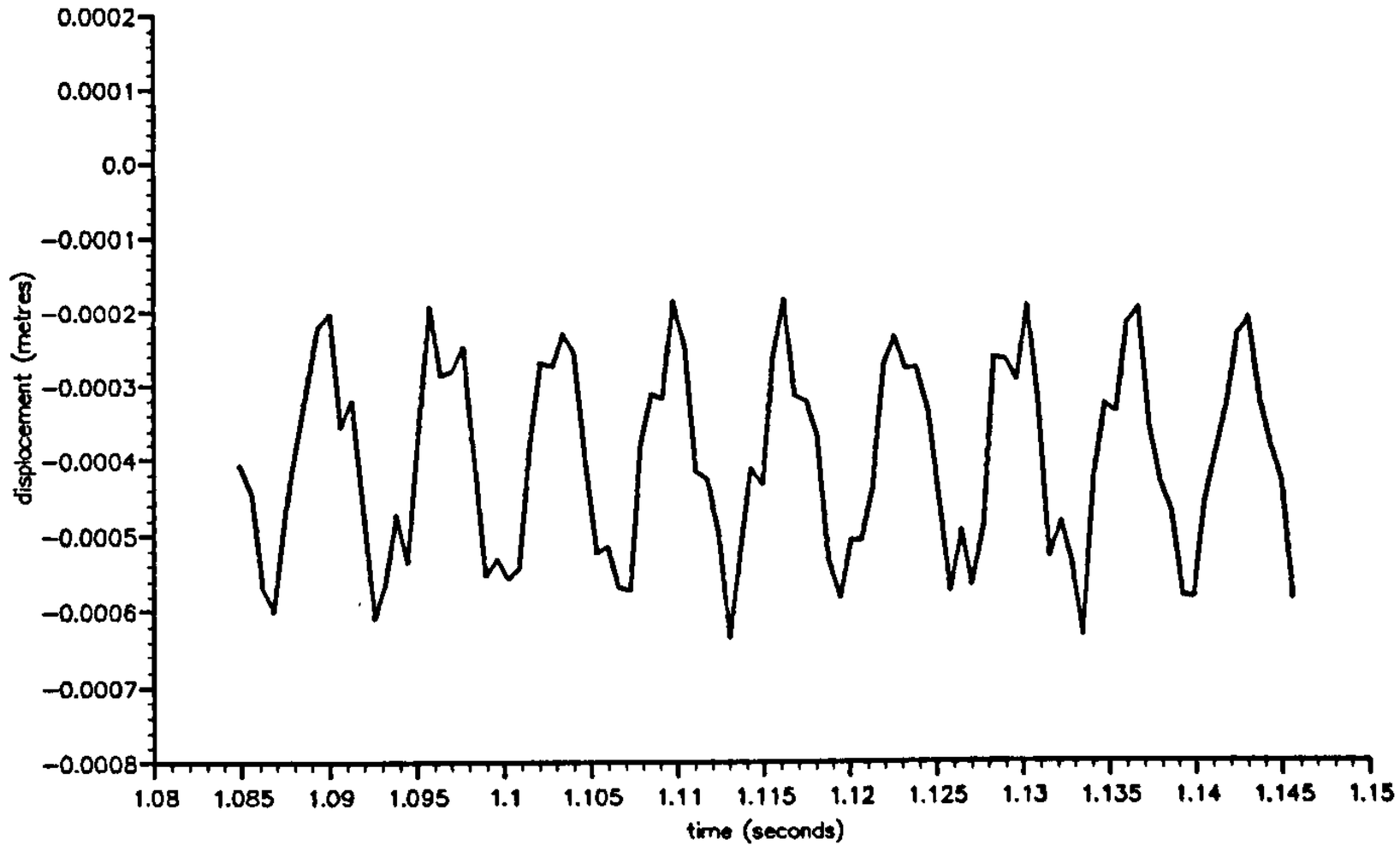

Figure 5.10: Time history of the displacement w at 1.5 m for a clamped-pinned plate of height 2.0 m, thickness 0.018 m due to a reflecting standing wave of initial surface amplitude 0.2 m on depth of 1.0 m.

The amplitudes, T_n, of the displacement for part of the time history is shown in figure 5.11.

Figure 5.12 shows the deflection of the clamped-free plate at one position, 1.5 metres, for part of the time history, 0.07 seconds. Oscillations can be seen with a period of 0.03 s or 33.3 Hertz. The 2nd, 3rd and 4th natural frequencies of the plate in air are 27.2, 68.3 and 133.7 Hertz. The frequency measured from the results could be the third harmonic frequency of the plate in water, 51 % lower.

The amplitudes, T_n, of the displacement are presented in figure 5.13. A low frequency oscillation is shown for the first, dominant mode, as seen in the time history of the displacement at one point. For the next couple of modes some oscillatory motion can be seen. For $n = 2$, the oscillations have period 0.0045, a frequency of approximately 222 Hertz.

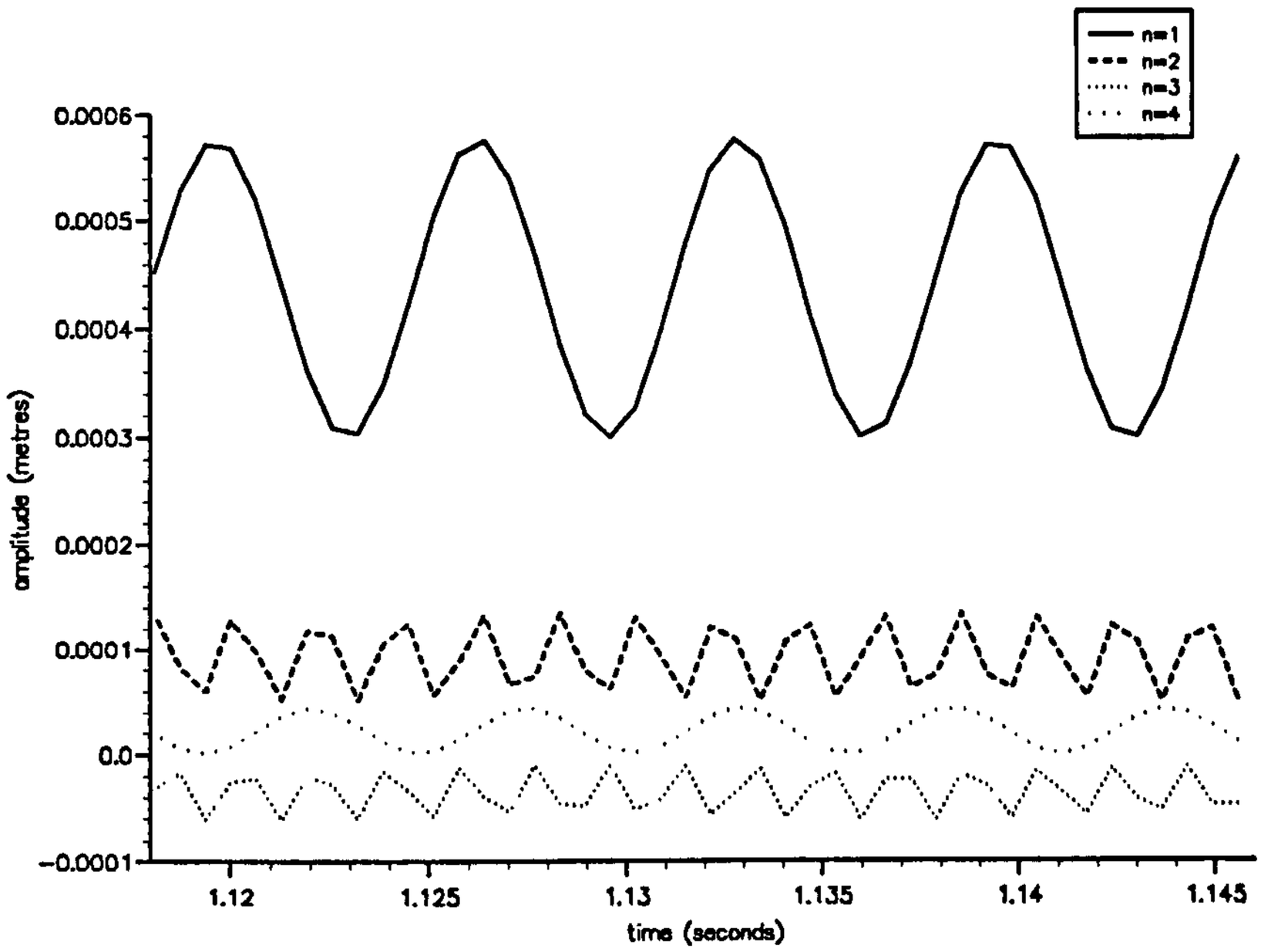

Figure 5.11: Time history of the amplitudes T_n for the first few modes for a clamped-pinned plate of height 2.0 m, thickness 0.018 m due to a reflecting standing wave of initial surface amplitude 0.2m on a depth of 1.0 m.

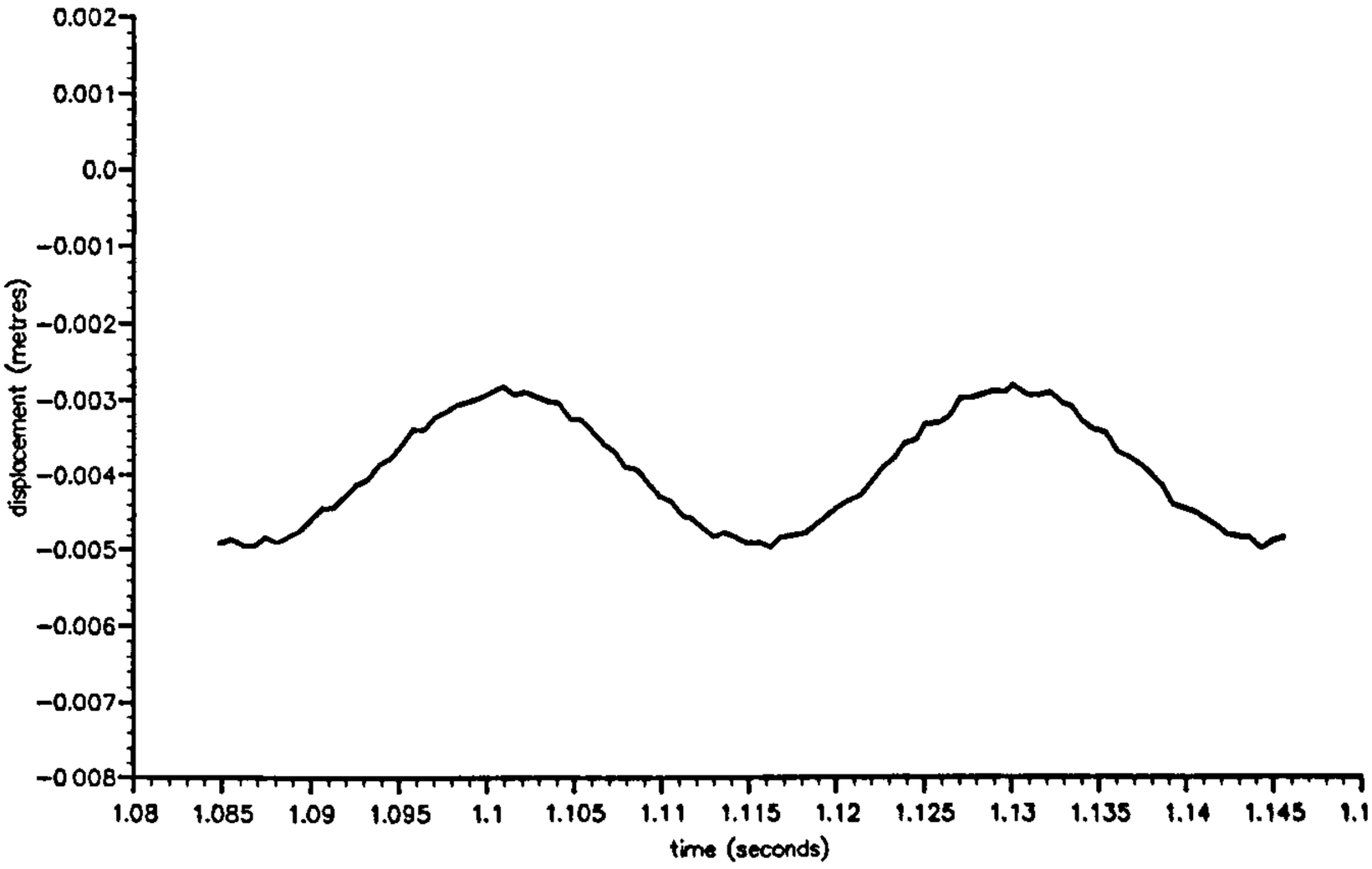

Figure 5.12: Time history of the displacement w at 1.5 m for a clamped-free plate of height 2.0 m, thickness 0.018 m due to a reflecting standing wave of initial surface amplitude 0.2 m on a depth of 1.0 m.

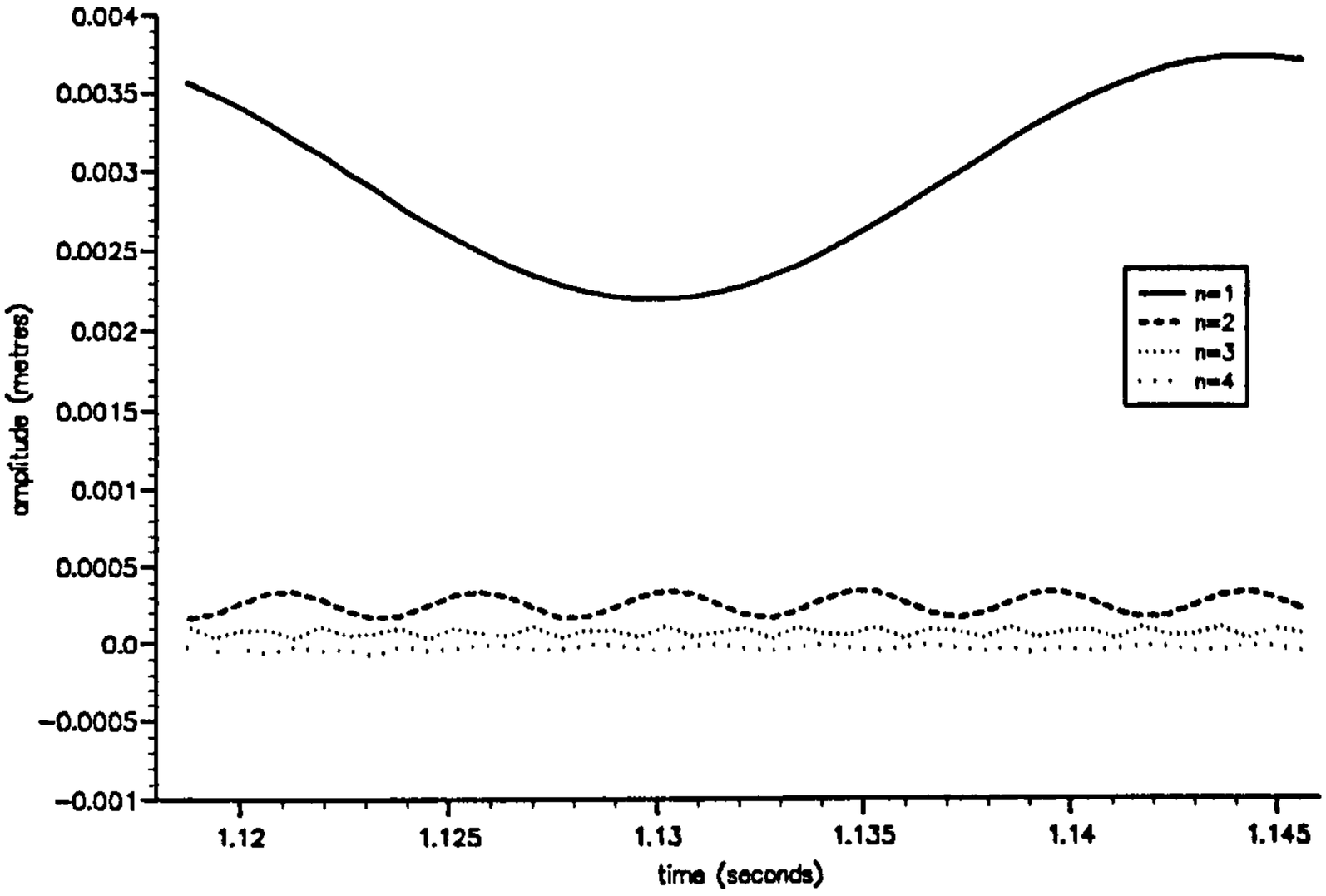

Figure 5.13: Time history of the amplitudes T_n for the first few modes for a clamped-free plate of height 2.0 m, thickness 0.018 m, for a reflecting standing wave impact of initial surface amplitude of 0.2 m on an initial depth of 1.0m.

5.4.1 Comparison with experimental data: Corrignan (1993)

Sloshing experiments have been undertaken by Corrignan (1993) to gain insight into the influence of wall flexibility. A rectangular tank of height 0.433 metres and 0.835 metres length was equipped with a vertical plate at one end clamped at the bottom with three displacement transducers fitted on. The fluid was set in motion by harmonic pitch or surge motions with the tank 60 percent full.

Measurements of the pressure loads, accelerations, displacements and strains were taken. Two plates were used in the investigation, one composed of aluminium with physical characteristics E=75 GN/m^2, ν=0.34, ρ=2800 kg/m^3 and s=0.018 m with a natural frequency of 85 Hertz, and the other composed of steel with E=200 GN/m^2, ν=0.33, ρ=7850 kg/m^3 as in the previous section with a thickness s=0.002 m giving a natural frequency of 9 Hertz. The plates were both of height 0.433 metres and as expected the second thinner plate gave larger displacements. The experimental results studied were from two displacement transducers placed 0.242 (D8) and 0.379 (D7) metres up the wall. The steel plate was used with two different weights on the top of the plate. The case with

the first (lighter) prestress showed larger displacements.

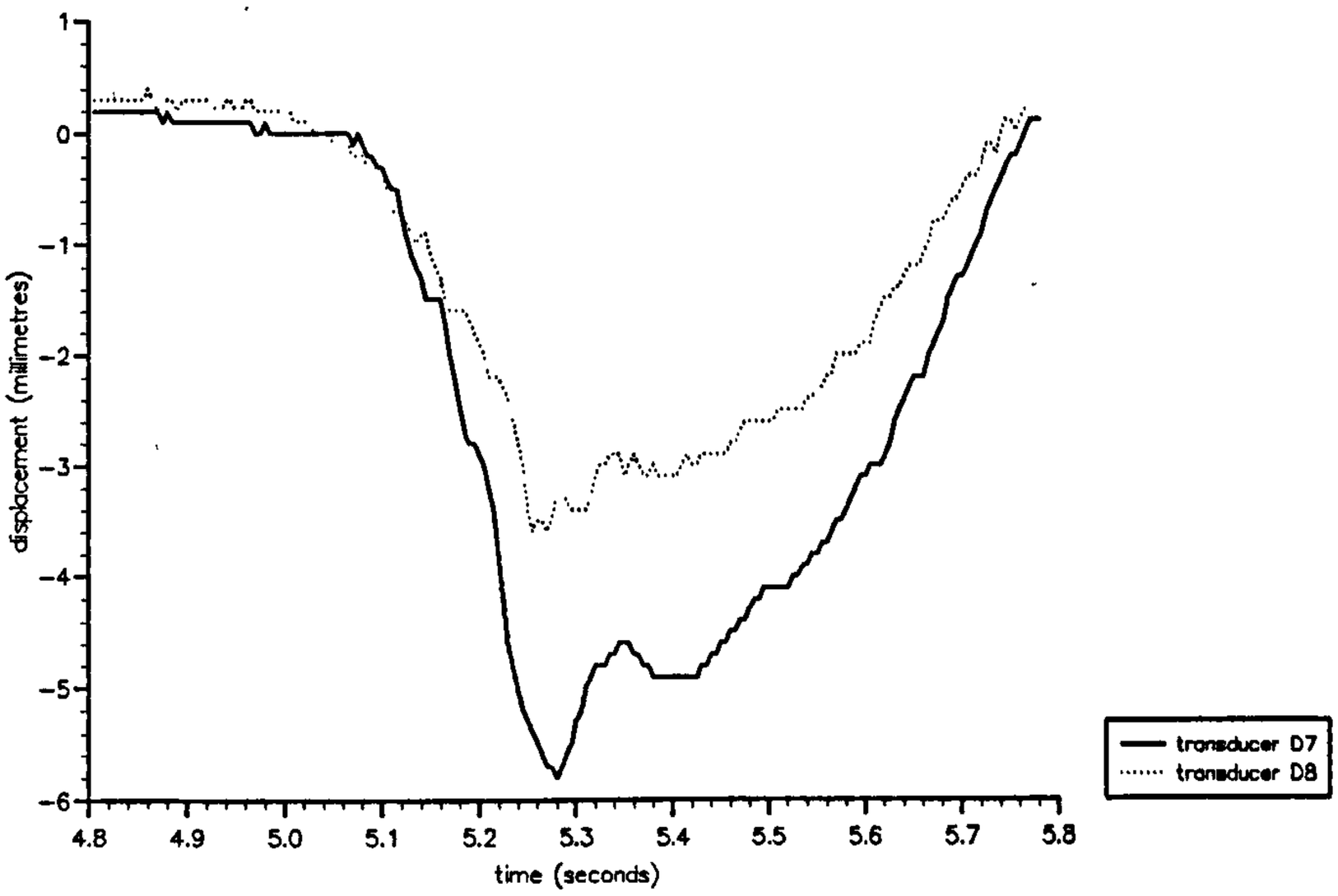

Figure 5.14: Time history of displacement of the two wall transducers on a steel plate of height 0.433 m, thickness 0.002 m from data in Corrignan (1993).

The displacements from a section of the time history from Corrignan due to an impact are presented in figure 5.14 for the steel plate with the first prestress for a wave of amplitude 0.01 metres and a frequency of 0.8 Hertz. The data for the displacements was given in timesteps of 0.005 seconds. The displacements from the two transducers show the larger deflections in the higher position. The maximum displacement occurs at a time of 5.280 seconds for the higher transducer (D7) and slightly earlier for the lower transducer (D8) at times 5.255 and 5.270. No regular oscillations of the plate were recorded.

From the video it can be seen that the water covers the entire wall for part of the motion as the wave impacts the ceiling of the tank. The displacements recorded for the second prestress were smaller (although larger than for the aluminimum plate) but continuous small amplitude oscillations of the transducer throughout the motion were recorded, in particular for the more gentle motions when no impact on the ceiling occured. From his experimental results, Corrignan concluded that the wall flexibility influenced loads on the 'flexible' wall and on the other 'rigid' ones as well implying the flow had been altered. The data taken from horizontally aligned displacement transducers verified two-dimensional motion.

Although two different prestresses were used at the top, the plate used by Corrignan was initially clamped at the bottom and free at the top, thus when modelling the plate, the clamped-free case from subsection 5.2 has been considered. Using the physical data given above, the expression 5.13 gives a fundamental frequency of 10.3 Hertz for the clamped-free plate, in fairly good agreement with Corrignan.

For the tank and plate dimensions given by Corrignan, with eh=0.433 m and s=0.002 m, numerical computations described in section 4.2 for an initial surface amplitude of $0.0376h$ where h=0.2598, were used to evaluate the pressure distribution on the impact wall.

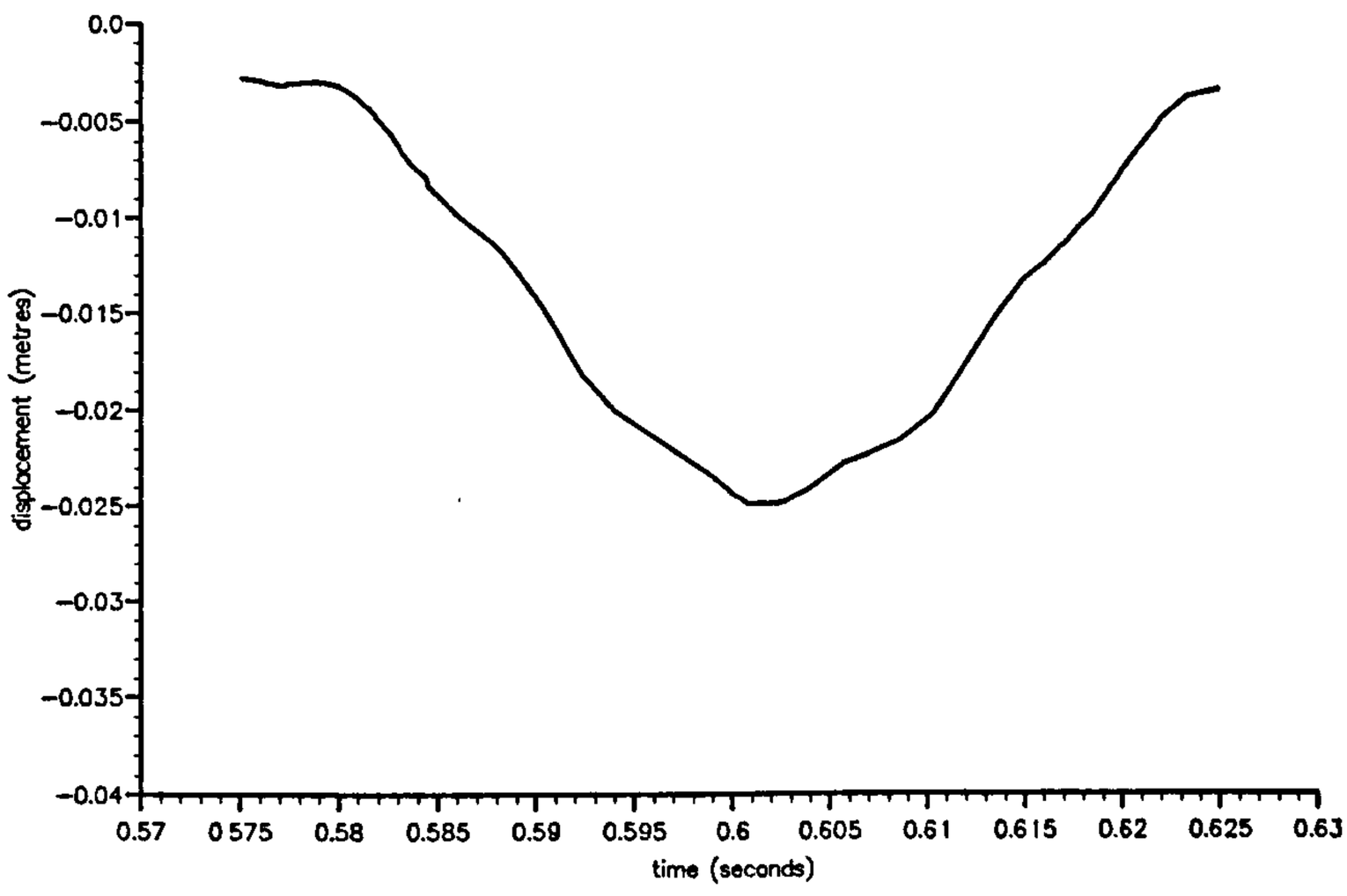

Figure 5.15: Time history of position 0.379 metres up a vertical plate of height 0.433 metres and thickness 0.002 metres due to a standing wave of surface amplitude 0.01 metres starting from rest on a depth of 0.26 metres for a clamped-free plate.

The time history for part of the motion, 0.06 seconds, at position 0.379 metres is displayed in figure 5.15. The waterline is at a maximum position up the plate at a time 0.5829 seconds. The maximum displacement of 25 millimetres is at t=0.602 s, 0.0192 seconds later. Figure 5.14 showed a maximum displacement of 5.8 millimetres. The maximum displacement recorded for the steel plate with the prestress in Corrignan was 6.7 millimetres. Thus the displacements shown in figure 5.15 for a steel plate with no prestress are larger than the experimental data for the same position.

Chapter 6

Conclusions

In this thesis, three aspects of the pressure field resulting from a moderately severe wave impact on a structure have been modelled, either in the context of coastal hydrodynamics or in a confined domain such as a transportation vessel. Finally, the resulting deflections of a non-rigid vertical wall due to wave impact have been evaluated. The following sections discuss the results and conclusions from each chapter.

6.1 Impact Pressures in a Container

The theory of pressure impulse has been used in chapter 2 to model wave impact in relation to high, short-lived pressures on a rigid wall in several two-dimensional geometries and in a three-dimensional rectangular domain to obtain general results. A high pressure impulse distribution on the impact wall arises from the idealised impact with significant pressure impulse distributions on some of the other walls during the brief motion. The size of the impact region is directly proportional to the pressure impulses evaluated, with larger regions of impact producing higher values of pressure impulse. In addition, it is shown that decreasing the width of the domain to produce a shorter tank raises the pressure impulses and the total impulse on the impact wall, and increases the change in the normal velocity of the free surface immediately after impact. Thus more concentrated motion is found in confined spaces.

With relative ease, the corresponding solution in a semi-circular and semi-elliptical domain has been found. The geometry of two intersecting circles has been used to de-

scribe a partially full circular container. The solution in this domain has produced some interesting results, showing that as the container becomes fuller, the pressure impulse distributions and change in velocity on the free surface immediately after impact becomes greater. As the fill-level becomes greater than 90 %, the solution increases rapidly along with the change in the normal velocity of the free surface due to the impact. Comparing a fill-level of 97 % ($\beta = \pi/9$) with a fill-level of 99 % ($\beta = \pi/18$), for example, gives an increase in the peak pressure of 74 %. As shown in the example, this work on pressure impulse theory can be used to evaluate the resultant velocity induced in a moveable container, of importance where a liquid impact inside a container can affect the stability of the vehicle. The resulting pressure field, where the resultant velocity is in the direction of the impact, is shown to be lower than that due to a rigid wall. The large pressure impulse gradients produced could cause damage to baffles within the containers. A simple conformal transformation has shown that the total resultant impulse on a baffle due to the impact can be calculated.

When there is impact on one wall only, the two-dimensional rectangular case predicts larger values for the pressure impulse distribution than in the three-dimensional case. For the three-dimensional case, it has been shown that the position of the impact zone itself has an effect on the forces produced with an increase as the zone becomes nearer the side wall. An impact on two adjacent walls in a corner of the rigid-sided domain has been considered and a significantly higher pressure distribution for specific large impacts has been predicted than for cases previously considered. An impact on two walls also gives substantial distributions on the other walls. This effect could have practical applications with regard to the transportation of partially full tankers. In studying the vertical velocities along the free surface immediately after impact, high values have been found for the oblique impact upon two walls.

In the model presented, a well-defined impact zone and simple horizontal velocities before impact have been considered. In reality a more complex impact velocity exists.

6.2 Entrained Air

The phenomenon of entrained air in water-wave impacts on vertical walls has been modelled in chapter 3 as both a single bubble and as a mixture of bubbles. An analytical

model for a two-dimensional bubble has been used to describe the trapped air pocket photographed during model experiments. From this theory, given the dimensions of the pocket, the fundamental frequency can be predicted. The similarity between the natural frequencies of the single bubble and the fundamental frequency of the bubble mixture for the same volume of air has been presented, thereby permitting aeration in water-wave impacts to be modelled either as a single bubble or as a bubble cloud.

Two-dimensional numerical computations for steep unsteady water-waves have been used to model an overturning wave trapping a semi-circular bubble against a vertical wall but are unable to describe the actual impact of the overhanging jet against the wall. The numerical computations were made using initial data either describing a wave of a tanh curve or that of a solitary wave which, with suitable initial parameters for the amplitude and initial distance from the impact wall, overturns as it approaches the wall. In both cases, the pressure values decrease as the amount of air trapped becomes greater. The maximum pressures immediately before impact were found to be at the bed for medium to large pockets of air, and just below the waterline for very small air pockets. Despite differing initial waveforms, the final characteristics immediately before impact are similar, in particular for moderate to large air pockets, suggesting insensitivity to the waveform far from the wall.

Numerical data from the final timestep of a computation for an overturning wave along with the analytical model of a two-dimensional semi-circular bubble have been used to study the initial motion of a trapped air pocket giving estimates for the maximum pressures. Comparison of the estimated frequencies and peak pressures with the data given by Hattori et.al. shows reasonable agreement. Where the values have been obtained using the parameters measured from the video frames, some discrepancy would be expected due to the difficulty of measuring accurately from photographs. The results using the parameters given by the detailed computations predict lower peak pressures, of between 5-30 %. This could be due to the impact of the jet on the wall raising the values in the experimental data.

The numerical results were chosen with air pockets trapped having similar parameters a, d and H as the experimental results. However the form of the wave chosen may not be the optimal form, in particular for large amplitudes. The waves in the experimental studies were made to break by means of a slope immediately in front of the impact wall.

The computations of a tanh waveform were found to provide the best comparison with the experimental data from Hattori et.al. due to the position of the bubble with respect to the rigid bed and profile of the free surface at the final computed time. The accompanying diagram in Witte (1988) and large scale experiments by Oumeraci et.al. (1991b) show the position of the bubble on the wall and the sloping profile of the free surface to compare better with the computations presented for the overturning solitary wave. In these last two studies, the limited data available has allowed rough comparisons with some success.

To estimate the peak pressures from an impact, the theory of pressure impulse described in chapter 2 has been used to estimate the peak pressure, where a value for the rise time of the pressure needs to be estimated. Section 3.8 has suggested using the natural period of the bubble.

For a small trapped air pocket the rise time of the maximum pressure can be obtained from the numerical results. This is then included with a quarter of the period of the air pocket, where the natural frequency is estimated from the analytic theory. The resulting peak pressure from the pressure impulse theory predicts a value 14 % lower than that given in the pressure field from the computations. For larger pockets, the short time duration is chosen to be a quarter the period of oscillation of a semi-circular bubble. The examples calculated show agreement within 20 % with the analytical theory in section 3.4, with the closest value of 14 % for the largest air pocket.

The pressure oscillations after the wave impact in the experimental studies display strong damping and this remains a complex problem which has not been addressed here. For the model which describes a bubbly mixture, energy from the trapped modes in the aerated region could leak into the pure water in the form of sound. Lu, Prosperetti & Yoon (1990) suggested from their experimental study that an appreciable amount of noise is likely to be emitted by clouds from such energetic events as wave breaking. The damping observed in the experimental data could indeed be due to sound radiation.

The analytical model for evaluating the trapped modes for a bubbly mixture assumed the bounding walls to be rigid. Nicholas, Roy, Crum, Oguz & Prosperetti (1994) have undertaken an experimental study to investigate the sound emissions from a circular column of bubbly liquid. This included measurements for a 'soft' or pressure-release bed compared with a rigid bed. For a boundary to considered as rigid, the natural frequencies must be much higher than those of the bubbly liquid. Thus the frequencies

of any experimental apparatus must be known in advance for good comparsion with the experiment.

The data from the experimental studies have been from fresh water wave tanks due to corrosive properties of salt water. Salt water affects the size and distribution of the bubbles and hence the natural frequencies of oscillation and pressure distributions if the volume fraction is different.

6.3 Reflecting Pressures in Containers

A study of the sloshing motion found inside containers has been undertaken in chapter 4 by using numerical computations for large amplitude 'standing' water-waves. At the maximum height the water can be in free fall for the biggest waves. This reflecting motion results in lower pressures than in the previous two chapters but of longer duration. Some of the highest pressures are found at instances of maximum kinetic energy. Very low pressures can be found in the large crest heads when the wave is at a time of minimum kinetic energy. The computations fail as the program is unable to resolve corners.

By choosing suitable initial data for symmetry, the numerical results can represent motion in a tank. Thus as the surface moves in time, the force on a side wall can be evaluated. The forces on the impact walls clearly demonstrate two maxima for the larger waves, with the maximum waterline height occuring between the two peaks. As explained in Peregrine (1994), the first peak occurs when the water rises up the wall and the vertical pressure gradient is at a maximum, accelerating the wave up the wall, and the second peak when the water comes down the wall and a strong pressure gradient is required to deccelerate it.

6.4 Response of Flexible Wall to Wave Impact

For small oscillations, the non-rigid vertical impact wall has been modelled in chapter 5 as a two-dimensional elastic plate using linearised theory. For wave impact on a vertical breakwater, using characteristics for reinforced concrete, displacements have been evaluated for impact due to a large reflecting solitary wave and due to a plunging breaker

with a much higher pressure field. For wave impact on the thin walls of a container, characteristics for a steel wall have been employed and the resulting deflections due to reflecting standing waves evaluated.

The response of a vertical wall due to a reflecting solitary wave produced displacements of 1-2 millimetres for a wall of height 3.0 metres and thickness 20 centimetres. Examination of one position of the wall in time showed oscillations of a frequency approximately 75 % lower than that of the natural frequency of the plate in air.

The response of a thin wall of a tank due to the motion of a standing wave has been evaluated for plates with a free, pinned or clamped upper end. The lower end was taken to be clamped in all cases. The clamped-free plate showed the largest displacements. The study of one position on the wall in time for both the clamped-free and clamped-pinned cases displayed oscillations in time which could be attributed to higher order harmonics of the plate.

Kirkgöz & Mengi (1986) and Hattori (1994) have both suggested that the longer-lasting more moderate pressure may be of more importance than the high peak pressures. The preliminary results in this chapter of the amplitudes of the displacements indicate that the reflecting waves, either a solitary wave on a breakwater or a standing wave in a tank, produce regular continuous oscillations. This is in contrast to the steep wave impact shown, which produced some displacement at impact and then a decay with only oscillatory motion in the first mode. The higher order modes n=3,4,.. gave negligible displacements.

To obtain accurate solutions or smooth profiles for w, a large number of timesteps is required, of the order 1000-1500, and a greater number of timesteps is required to obtain good resolution for the clamped-clamped case.

Comparison with the work by Kirkgöz et.al. for a vertical breakwater has shown good agreement. A computation for a steep water wave with a slightly lower peak pressure (approximately 20 kN/m^2 difference) has been used here for a similar plate and a slightly smaller deflection (approximately 0.12 millimetres difference) at the same position on the wall resulted.

The comparison with the experimental data from Corrignan for a thin tank wall showed some success. However, discrepancies between theoretical or numerical results and the

experimental results are expected. The prestress present in the experimental data has not been included in the modelling. Along with the effects of the prestress already mentioned, the seal glued along the top of the plate is expected to influence the results as well as the weight of the equipment on the plate. A slight initial deformation of the plate is also mentioned in the experimental description.

6.5 Future Work

In the second chapter, the pressure impulse theory has been used to describe an impact on one or two side walls of a container. For nearly full tanks with a rigid top above the free surface of the fluid, an impact can occur on the top of the tank either due to direct impact from the wave or a secondary impact due to the fluid rising vertically from the first impact against the side wall. Both these aspects could be modelled analytically.

The work presented in chapter 3 described the initial motion of a trapped air pocket. Less straightforward, the subsequent break-up of the bubble cloud and the damping of the oscillations present in experimental results has not yet been modelled.

The numerical results presented in chapter 4 for sloshing motion in a container represent a small selection of possible profiles. The initial conditions described here were for a surface elevation or velocity potential. The resulting motion due to horizontal or vertical excitation of the tank, or due to a wavemaker at one end of the tank, could be studied numerically. The liquid inside the tank was taken to be water and surface tension has not been included, which is of importance in some industrial applications.

The transverse displacements and amplitudes at a time period during which the wave is at maximum height have been evaluated in chapter 5. Aspects of the computation and presentation need to be investigated further. In all sections, only a sample of the displacements and amplitudes have been presented. The subsequent motions have yet to be examined.

The example in section 2.6 in chapter 2 for a moveable container showed a reduction in the pressure impulse field compared with the rigid case. The study of the response of a flexible plate to wave impact did not include the pressure distribution after impact but from the results in the first chapter for a moveable container, the pressure field could

display lower values than for a rigid wall.

Not investigated here, the oscillations due to the entrained air could influence wall oscillations if the frequencies are in the same range as the natural frequency of the structure.

References

ABRAMSON, H.N. (1966) The dynamic behaviour of liquids in moving containers. *NASA SP-106*

ABRAMSON, H.N., BASS, R.L., FALTINSEN, O. & OLSEN, H.A. (1974) Liquid slosh in LNG carriers. *Proc. 10th Symp. Naval Hydrodynamics* Arlington , Ed: R.D.Copper & S.W.Doroff pp 371-388

ARAMI, A. & HATTORI, M. (1989) Experimental study on shock wave pressures. *Proc. Coastal Eng. J.S.C.E* 36 (in Japanese) pp 579-583

ASTLEY, R.J. (1972) The dynamic interaction of dams and reservoirs. *Phd Thesis.* Univ. of Bristol.

BAGNOLD, R.A. (June 1939) Interim Report on wave-pressure research. *J. Inst. Civil Eng.* 12 pp 202-206

BLACKMORE, P.A. & HEWSON, P.J. (1984) Experiments on full-scale wave impact pressures. *Coastal Eng.* 8 pp 331-346

CHAN, E.S. & MELVILLE, W.K. (1988) Deep-water plunging wave pressures on a vertical plane wall. *Proc. Roy. Soc. Lon.* A417 pp 95-131

COOKER, M.J. (1990) The interaction of steep water waves and coastal structures. *Ph.D thesis* Bristol University

COOKER, M.J. & PEREGRINE, D.H. (1990) A model for breaking wave impact pressures. *Proc. 22nd Int. Conf. Coastal Eng.* Delft, pp 1473-1486

COOKER, M.J. & PEREGRINE, D.H. (1992) Wave impact pressure and its effect upon bodies lying on the sea bed. *Coastal Eng.* 18 pp 205-229

COOKER, M.J. & PEREGRINE, D.H. (1994) A mathematical model for liquid impact problems. *submitted for publication*

COOPER, R.M. (1960) Dynamics of liquids in moving containers *ARS Journal* **30** pp 725-729

CRIGHTON, D.G., DOWLING, A.P., FFOWCS WILLIAMS, J.E., HECKL, M. & LEPPINGTON, F.G. (1992) Modern Methods in Analytical Acoustics. Pub: Springer-Verlag

CORRIGNAN, Ph (1992) Results of the first test series on the influence of physical parameters. *Experimental and numerical analysis - sloshing and impact loads* **TEC-CO31-03** SIREHNA contract BREU CT/91 499

CORRIGNAN, Ph (1993) Results of the second test series - Influence of wall flexibility. *Experimental and numerical analysis - sloshing and impact loads* **TEC-CO31-05** SIREHNA contract BREU CT/91 499

DENNY, D.F. (1951) Further experiments on wave pressures. *J. Inst. Civil Eng.* 35 pp 330-345

DOLD, J.W. (1992) An efficient surface-integral algorithm applied to unsteady gravity waves. *J. Computational Physics* 103 pp 90-115

DOLD, J.W. & PEREGRINE, D.H. (1986) An efficient boundary-integral method for steep unsteady water waves. *Numerical Methods for Fluid Dynamics II* Ed: K.W.Morton & M.J.Baines pp 671-679

FALTINSEN, O.M. (1974) A nonlinear theory of sloshing in rectangular tanks. *J. Ship Research* 18 pp 224-241

FÜHRBÖTER, A. (1970) Air entrainment and energy dissipation in breakers. *Proc. 12th Int. Conf. Coastal Eng. A.S.C.E* Washington pp 391-398

FÜHRBÖTER, A. (1986) Model and prototype tests for wave impact and run-up on a uniform 1:4 slope. *Coastal Eng.* 10 pp 49-84

GRAFF, K.F. (1975) Wave motion in elastic solids. Pub:Claredon Press

GRAHAM, D.I. & HEWSON, P.J. (1992) Measurement of aeration in model-scale breaking waves. *Proc. 2nd Workshop on Wave Impact Loading of Vertical Structures.*, Plymouth. MAST contract 0032-M(JR)

HATTORI, M. (1994) Wave impact pressures on vertical walls and the resulting wall deflections. *Int. Workshop on Wave Barriers in Deep Waters.* Yokosuka

HATTORI, M. & ARAMI, A. (Oct 1992) Impact breaking wave pressures on vertical walls. *Proc. 23rd Int. Conf. Coastal Eng.* Venice, pp 1785-1798

HATTORI, M., ARAMI, A. & YUI, T. (1994) Wave impact pressure on vertical walls under breaking waves of various types. *Coastal Eng.* **22** pp 79-114

HAYASHI, T. & HATTORI, M. (1958) Pressure of the breaker against a vertical wall.

Coastal Eng. Japan pp 25-37

HSEIH, D. & PLESSET, M.S. (Aug 1961) On the propagation of sound in a liquid containing gas bubbles. *The Physics of Fluids* 4 no.8

KIRKGÖZ, M.S & MENGI, Y (1986) Dynamic response of caisson plate to wave impact. *J. Waterway, Port, Coastal and Ocen Eng.* **112** no. 2 pp 284-295

KIRKGÖZ, M.S. (1990) An experimental investigation of a vertical wall response to breaking wave impact. *Ocean Eng.* 17 no.4 pp 379-391

LAMB, H. (1932) Hydrodynamics. Pub: Cambridge university press.

LEIGHTON, T.G. (1994) The Acoustic Bubble. Pub: Academic Press.

LONGUET-HIGGINS, M.S. (1973) On the form of the highest progressive and standing waves in deep water. *Proc. Roy. Soc. Lon.* **A 331** pp 445-456

LONGUET-HIGGINS, M.S. (1980) On the forming of sharp corners at a free surface. *Proc. Roy. Soc. Lon.* **A371** pp 453-478

LU, N.Q., PROSPERETTI, A. & YOON, S.W. (1990) Underwater noise emissons from bubble clouds. *I.E.E.E. J. Oceanic Eng.* 15 no. 4 pp 275-281

LUI, A.P.-C. & LOU, J.Y.K. (1990) Dynamic coupling of a liquid-tank system under transient excitations. *Ocean Eng.* 17 no. 3 pp 263-277

LUNDGREN, H. (1991) Perspectives of structural breakwater technology *Proc. 1st Workshop on Wave Impact Loading of Vertical Structures* Hannover, MAST contract 0032-M(JR)

MERCER, G.N. & ROBERTS, A.J. (1992) Standing waves in deep water. Their stability and extreme form. *Phys. Fluids* A 4 pp 259-269

MILMAN, T. (1993) Nonlinear standing waves. *Ph.D thesis* Israel Institute of Technology.

MITSUYASU, H. (1966) Shock pressure of breaking wave. *Proc. 10th Int. Conf. Coastal Eng. A.S.C.E* Tokyo pp 268-283

MOUTZOURIS, C. (1979) Some scaling parameters of loading from wave breaking on rigid inclined structures. *Mechanics of wave-induced forces on cylinders* Ed: T.L.Shaw, Pub: Pitman pp 714-727

NAGAI, S. (1969) Pressures of standing waves on a vertical wall. *J. Waterways & Harbors Division ASCE* 95 pp 53-76

NICHOLAS, M., ROY, R.A., CRUM, L.A., OGUZ, H. & PROSPERETTI, A. (1994) Sound emissions by a laboratory bubble cloud. *J. Acoust. Soc. Am* 95 pp 3171-3182

OMTA, R. (Sept 1987) Oscillations of a cloud of bubbles of small and not so small amplitude. *J. Acoust. Soc. Am.* 82 no.3 pp 1018-1033

OUMERACI, H., KLAMMER, & PARTENSCKY, H.-W. (1993) Classification of breaking wave loads on vertical structures. *J. Waterway, Port, Coastal & Ocean Eng., A.S.C.E.* 119 no.4 pp 381-397

OUMERACI, H. & PARTENSCKY, H.-W. (1991a) Breaking wave impact loading of caisson breakwaters - Research strategy and results of small-scale model investigations *Proc. 1st Workshop on Wave Impact Loading of Vertical Structures.* Hannover, MAST contract 0032-M(JR)

OUMERACI, H. & PARTENSCKY, H.-W. (1991b) Breaking wave impact loading of caisson breakwaters - Effect of entrapped air on structural response. *Proc. 1st Workshop on Wave Impact Loading of Vertical Structures.* Hannover, MAST contract 0032-M(JR)

PENNEY, W.G. & PRICE, A.T. (1952) Part II. Finite periodic gravity waves in a perfect liquid. *Phil. Trans. Roy. Soc. Lon.* A 244 pp 254-284

PEREGRINE, D.H. (1994) Pressure on Breakwaters: A forward look *Int. Workshop on Wave Barriers in Deep Waters* Yokosuka

POPOV, G., SANKAR, S., SANKAR, T.S. & VATISTAS (1992) Liquid sloshing in rectangular road containers. *Computers & Fluids* 21 pp 551-569

POPOV, G., SANKAR, S. & SANKAR, T.S. (1993) Optimal shape of a rectangular road container. *J. Fluids & Structures* 7 pp 75-86

PUGH, D.A. (1985) The computation of the velocity field beneath steep unsteady water waves. *M.Sc Thesis* Bristol University.

RAMKEMA, C. (1978) A model law for wave impacts on coastal structures. *Proc. 16th Int. Conf. Coastal Eng. A.S.C.E.* Hamburg, pp 2308-2327

RICHERT, G. (1968) Experimental investigation of shock pressures against breakwaters. *Proc. 11th Int. Conf. Coastal Eng. A.S.C.E* London pp 954-973

SAFFMAN, P.G. & YUEN H.C. (1979) A note on the numerical computations of large amplitude standing waves. *J. Fluid Mechanics* 95 pp 707-715

SCHMIDT, R., OUMERACI, H. & PARTENSCKY, H.-W. (Oct 1992) Impact loads induced by plunging breakers on vertical structures. *Proc. 23rd Int. Conf. Coastal Eng.* Venice, pp 1545-1558

SCHULZ, K.-P. (1992) Further results on hydraulic model investigations on air enclosed by grid structures. *Proc. 3rd Workshop on Wave Impact Loading of Vertical Structures.*

MAST contract 0032-M(JR)

TANAKA, M. (1986) The stability of solitary waves. *Phys. of Fluids* **29** pp 650-655

TANIZAWA, K. & YUE, D.K.P. (May 1992) Numerical computation of plunging wave impact loads on a vertical wall, Part 2. The air pocket. *7th Int. Workshop Water Waves and Floating Bodies*

TAYLOR, G.T. (1953) An experimental study of standing waves. *Proc. Roy. Soc. Lon.* A 218 pp 44-59

TIMOSHENKO, S. (1940) Theory of plates and shells. Pub:McGraw-Hill

TOPLISS, M.E. (1991) Mathematical description of air bubbles in water. *M.Sc Thesis* Univ. of Bristol.

TOPLISS, M.E., COOKER, M.J. & PEREGRINE, D.H. (Oct 1992) Pressure oscillations during wave impact on vertical walls. *Proc. 23rd Int. Conf. Coastal Eng. A.S.C.E* Venice pp 1639-1650

WEGGEL, J.R. & MAXWELL, W.H.C. (Aug 1970) Numerical model for wave pressure distributions. *J. Waterways, Harbors & Coastal Eng. Div. A.S.C.E.* pp 623-642

WITTE, H.-H. (1988) Wave-induced impact loading in deterministic and stochastic reflection *Mitteilungen* **102** Leichtweiss Institut für Wasserbau Tech. University Braunschweig. pp ix-227

ZHOU, D., CHAN, E.S. & MELVILLE, W.K. (1991) Wave impact pressures on vertical cylinders. *Applied Ocean Research* 13 No. 5, pp 220-234

ZHONG, H.S., SCHULZ, K.-P. & WITTE, H.-H. (Feb 1992) The damping effect of air enclosure produced by grid structures on the wave impact pressure on a vertical wall. *Proc. 2nd Workshop Wave impact loading of vertical structures* Plymouth, MAST contract 0032-M(JR)